Université de Liège

centre européen d'archéométrie

Degradation mechanisms of Prussian blue pigments in paint layers

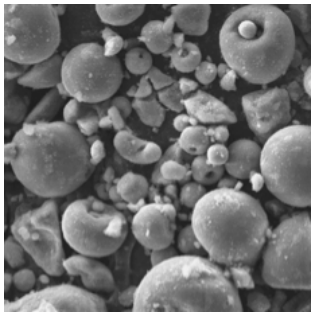
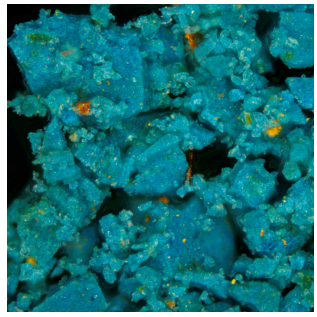
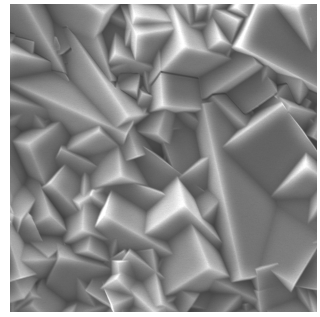

Thèse présentée par
Louise Samain
en vue de l'obtention du titre de
Docteur en Sciences

Année académique 2011-2012

Degradation mechanisms of Prussian blue pigments in paint layers

Composition du jury

Prof. Emile Biémont	Université de Liège
Prof. Bernard Gilbert	Université de Liège
Prof. Fernande Grandjean	Université de Liège
Dr. Pauline Martinetto	Institut Néel, Grenoble
Dr. Jana Sanyova	IRPA, Bruxelles
Dr. Geert Silversmit	Gent Universiteit
Prof. Philippe Walter	LAMS, CNRS, Paris

Promoteur de thèse

Dr. David Strivay
Centre Européen d'Archéométrie
Institut de Physique Nucleaire, Atomique et de Spectroscopie
Université de Liège

Collaborations

Institut Royal du Patrimoine Artistique, Bruxelles
X-ray Microspectroscopy and Imaging research group, Gent Universiteit
Departement MCMF, Institut Néel, Grenoble

Thèse présentée par
Louise Samain
en vue de l'obtention du titre de
Docteur en Sciences

Année académique 2011-2012

Remerciements

Mes années de doctorat auront été une expérience extrêmement enrichissante et une formidable occasion de dépassement personnel. Cette véritable aventure n'aurait pas été possible sans l'aide, l'intervention et le soutien de nombreuses personnes que je tiens à remercier ici.

J'adresse tout d'abord mes sincères remerciements à mon promoteur de thèse, David Strivay, pour m'avoir accueillie en 2008 au sein du Centre Européen d'Archéométrie. Mon projet de recherche n'aurait pu être mené à bien sans les moyens financiers qu'il a mis à ma disposition et les collaborations qu'il m'a aidé à établir. Je lui suis particulièrement reconnaissante pour sa disponibilité, son soutien à tout moment et sa grande générosité humaine.

Je remercie ensuite le Prof. Bernard Gilbert, le Prof. Fernande Grandjean, le Dr. Pauline Martinetto, le Dr. Jana Sanyova, le Dr. Geert Silversmit, le Prof. Philippe Walter, et le président de jury, le Prof. Emile Biémont, qui m'honorent de leur présence dans mon jury.

Je tiens à exprimer toute ma gratitude et reconnaissance envers les Professeurs Fernande Grandjean et Gary J. Long pour leur soutien inconditionnel durant ma thèse. J'ai d'abord bénéficié de leur précieuse aide et de leurs connaissances inégalées en spectroscopie Mössbauer. Ensuite, je leur dois la forme finale de cet ouvrage, qu'ils ont relu à maintes reprises et qu'ils ont corrigé en profondeur, tant sur la forme que sur le contenu. Durant ces années de collaboration, j'ai particulièrement apprécié leur sens aigu de la rigueur scientifique et leur dévouement à la recherche.

Je remercie le Prof. Robert Sporken des Facultés Universitaires Notre-Dame de la Paix de Namur de m'avoir laissé poursuivre ma thèse de doctorat dans le domaine de mon choix, sans aucune contrepartie. Je lui suis reconnaissante d'avoir guidé mes premiers pas dans le monde de la recherche. Je tiens aussi à remercier le Prof. Philippe Walter, toujours de bon conseil, qui m'a suggéré de travailler sur le bleu de Prusse.

Durant ma thèse, j'ai bénéficié du soutien du Dr. Jana Sanyova, qui a encadré ce travail de recherche depuis les prémisses jusqu'à la remise de cet ouvrage. Mes nombreuses journées passées au sein de l'Institut Royal du Patrimoine Artistique m'ont fait découvrir le monde concret de l'analyse et l'expertise picturales. J'ai beaucoup appris de par ses connaissances dans le domaine des pigments et colorants et les techniques associées à leur étude. Je remercie également Cécile Glaude pour son aide dans la préparation des coupes de peinture et leur analyse.

Je ne pourrais oublier le soutien du Prof. Bernard Gilbert, expert incontournable de la spectroscopie Raman. Ce fut un plaisir de travailler avec lui et d'en apprendre à chaque visite davantage sur les aspects théorique et technique de la spectroscopie Raman. Je le remercie tout particulièrement pour sa disponibilité, sa gentillesse et le partage sans limite de connaissances dans son domaine de prédilection.

Cette thèse est aussi le fruit de collaborations extérieures. Je remercie à ce propos vivement Geert Silversmit, Bart Vekemans et le groupe *X-ray Microspectroscopy and Imaging research group* de la Gent Universiteit, sans qui les expériences de spectroscopie d'absorption X n'auraient pas été possibles. Les campagnes de mesure à Dubble et Anka en leur compagnie font partie des bons souvenirs de mes années de doctorat.

Je suis également redevable envers l'équipe Structure et Propriétés des Matériaux Conditions Extrêmes du Département MCMF de l'Institut Néel avec qui j'ai réalisé les expériences de diffraction X à haute énergie. Je remercie plus particulièrement Pauline Martinetto et Pierre Bordet car j'ai pu compter sur leur disponibilité, leur aide constante et leur hospitalité pour l'analyse des données de diffraction X. J'espère sincèrement que la collaboration perdurera.

Au sein de l'Université de Liège, il m'a été donné de rencontrer et de travailler avec de nombreux scientifiques extérieurs au Centre d'Archéométrie. Du département de géologie, je pense notamment au Dr. Frédéric Hatert, qui a régulièrement effectué des mesures en diffraction X de poudres sur les bleus de Prusse. Au sein du département de chimie, j'adresse mes remerciements au Dr. Bruno Grignard, avec qui j'ai réalisé les synthèses du bleu de Prusse sous azote, et à Magali Brisbois, qui, outre des mesures en analyse thermogravimétrique, s'est toujours montrée disponible pour me donner un coup de main en spectroscopie Mössbauer.

Je remercie également le Prof. Raphaël Hermann qui m'a épaulée en spectroscopie Mössbauer, tant pour la mise en oeuvre de l'expérience que pour l'analyse des résultats. J'en profite aussi pour remercier le Dr. Benedikt Klobes pour son

aide en spectroscopie Mössbauer de conversion d'électrons et les expériences qu'il a menées sur les échantillons de bleu de Prusse au synchrotron PETRAIII à Hambourg.

Si ces années de thèse resteront de bons souvenirs, c'est en grande partie grâce à la bonne ambiance qui règne au sein de l'équipe du Centre Européen d'Archéométrie et de l'IPNAS. Les collègues sont devenus rapidement des amis et les bons moments passés ensemble au sein et en dehors du labo ne se comptent plus. Merci à tous, anciens et actuels membres, Gregoire, Line, Gaspard, Christophe, Muriel, François, Hélène, Stephanie, Nico, Cipriana, René, David, Thomas, François-Philippe, Catherine, Helena, Ari, John, Jérémie, André, Mathieu, Saïd, Aymeric, Michaël, en espérant n'en oublier aucun. J'adresse un merci particulier à Monsieur Weber pour tous ses délicieux vendredis spaghettis, ainsi qu'à Helena, Catherine, Ari et Stef, pour nos sorties entre filles et nos discussions en tous genres. Merci aussi à François-Philippe et Thomas, avec qui j'ai partagé le bureau, des rires comme des coups de blues. Je remercie tout particulièrement Stef, qui est rapidement devenue une amie proche et dont je ressens l'absence depuis son départ à Boston.

Mon doctorat m'a donné l'occasion de rencontrer une multitude de gens sympas, doctorants à l'Université de Liège, avec qui j'ai passé d'excellents moments. Je pense à toutes les personnes du mercredi gâteau, aux membres du Réseau des Doctorants, à Dounia, et à d'autres qui se reconnaîtront dans ces lignes. Au delà de l'université, restent les amis de longue date, François, Annick, Gaëlle, Xavier, Guillaume, pour n'en citer que quelques-uns, qui m'ont toujours encouragée, de près ou de loin. J'adresse enfin un chaleureux merci à Fabian, sur qui j'ai toujours pu compter et que j'estime énormément.

Je profite aussi de l'occasion pour remercier ma famille, mes parents et mes soeurs, dont le soutien, discret mais solide, m'est extrêmement précieux. Un merci supplémentaire revient à Hélène et Sébastien qui m'ont épargné de nombreux trajets en train entre Bruxelles et Liège en m'hébergeant chez eux.

Enfin, je termine ces lignes en remerciant Cédric, *last but not least*, qui a été ma véritable bouffée d'air durant ces douze derniers mois et sans qui ma vie serait nettement moins colorée.

Contents

Introduction

Our cultural heritage is an integral part of our society and must be preserved for current and future generations. Conservation and restoration concerns have recently become a moral duty and a full scientific research field referred to as *archaeometry*. Archaeometry is *the application of the physical and biological sciences to archaeology and the history of art*, as defined in the website of the eponymous research journal [1]. Archaeometry deals in particular with artifact studies, dating methods, use and development of non-invasive and non-destructive techniques, and conservation science. In the latter case, studying the degradation mechanisms occurring in cultural heritage objects is essential to guide restorers and conservators in making the right decision on how to best preserve these objects with respect to the initial artist's intention.

A beautiful and controversial example that illustrates the importance of understanding alteration processes in painting is the conservation issue arising from the world-wide famous *La Joconde*, painted by Leonardo da Vinci in *ca.* 1503-1506. The painting is exhibited in Le Louvre in Paris, France, and shows a yellowish aspect, which some qualify as golden, see Figure 1a. This was not intended by da Vinci, but is rather a consequence of the ageing of the varnish layer. A few years ago a group of French scientists [2][3] studied the so-called *sfumato* technique used by da Vinci to paint flesh tint. After a virtual removal of the varnish, they discovered the characteristics of the glaze technique, which was developed by the Flemish primitives and was not in use in Italy at the time of da Vinci [2]. The numerical representation shown in Figure 1b is much closer to what da Vinci painted in the sixteenth century. Although it is clear that the varnish distorts our perception of the masterpiece, the relevance of a possible intervention on the real painting is still debated.

The necessity of understanding degradation and alteration processes in a painting's materials is well established for preservation and art history issues. The task is however complex because of the highly heterogeneous character of a paint layer, which consists of a mixture of pigments and a binder on a support. All components interact and influence the ageing process of the paint layer. This thesis will

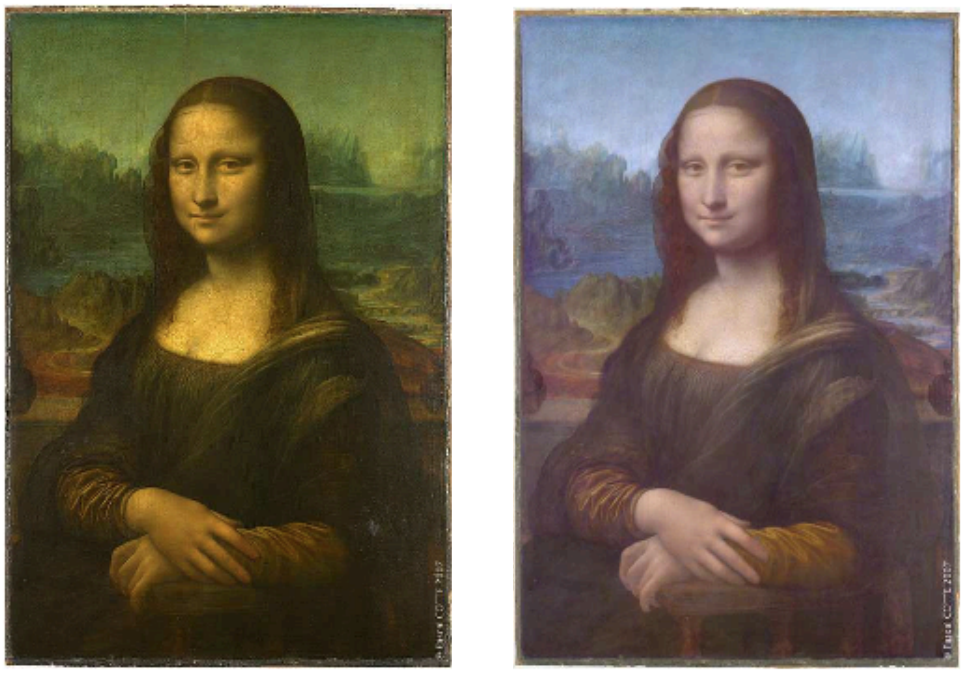

(a) **(b)**

Figure 1 *La Joconde*, **Leonardo da Vinci**, 1503-1506. Oil on poplar. Musée du Louvre, Paris. Representations of the painting, **a**, in its current state and **b**, after a virtual removal of the varnish [2].

focus on a particular pigment, Prussian blue. Prussian blue is a synthetic modern pigment, discovered in 1704 in Berlin. It had been widely used by artists until the end of the twentieth century. However, reports of discoloration had already appeared in eighteenth and nineteenth century books. To date, little attention has been devoted to the understanding of the degradation processes of Prussian blue in paint layers. The popularity of Prussian blue and its discoloration issue, whose mechanisms remain unclear, guided my choice of this research topic.

The popularity of Prussian blue is easily understood when considering the other blue pigments available at the beginning of the eighteenth century [4]. The most common blue pigments were indigo, blue ashes, azurite, and ultramarine. The first two were known to be unstable, there was a shortage of azurite in the market, and ultramarine was very expensive. Because of its low cost and its high tinting strength, Prussian blue was immediately adopted by artists. Although doubts about its permanence had already appeared in the mid-eighteenth century, its popularity did not decrease until the 1970's when Prussian blue was finally

supplanted by phthalocyanine blue. Numerous mentions in eighteenth and nineteenth century books warned against the use of Prussian blue in paintings. It is sometimes considered as very permanent and sometimes as very light fast with a tendency to fade or to turn green in the light. The eighteenth and nineteenth century literature is contradictory and even confused. To date no complete explanation of the degradation has been proposed. A better understanding of the mechanisms associated with this degradation will help in the preventive conservation and restoration of paintings in which Prussian blue was used.

Although this topic, *i.e.*, the discoloration of Prussian blue in paintings, seems to belong to art history, we tackle the problem from a scientific point of view and we propose to study the pigment at the molecular and atomic scale. Although the art historical aspect has not been excluded from this research, it should be emphasized that this thesis does not present all the historical art considerations related to the subject.

This thesis is divided in four main chapters. In **Chapter 1** the state of the art is given, with a general description of Prussian blue and its relevant properties for our research. The following three chapters deal specifically with the fading of Prussian blue. The discoloration of the pigment is undoubtedly to some extent correlated with the composition of the paint layers. However, paintings are highly heterogeneous and diversified. Therefore, in order to have a global overview of the fading we decided to first study our own synthetic samples before studying genuine paintings with Prussian blue. This choice is also guided by a practical problem: because of conservation ethics, it is quite difficult to obtain curator's authorization for analyzing and sampling works of art.

The preparation methods of Prussian blue were recognized as a contributory factor in the fading of the pigment. Empirical recipes have evolved through centuries to standardized syntheses. In **Chapter 2** we reproduce these *ancient* and *modern* preparation methods and extensively characterize the final products, with a particular emphasis on the structure of the pigment because of unresolved questions still found in the present literature.

Chapter 3 is devoted to the degradation mechanisms of Prussian blue. Paint layers were thus prepared from the laboratory-synthesized as well as commercially available Prussian blues. Different binders, additive pigments, and supports have been used in order to best mimic artistic reality. Then degradations were induced by accelerated ageing. Aged and non-aged paint layers were then analyzed in order to identify differences due to the ageing. Finally a model is proposed for the degradation mechanisms of Prussian blue.

We should not conclude this study without connecting our results to reality. In **Chapter 4**, we analyze various art objects containing Prussian blue. Some exhibit a fading, others do not. We discuss the results, on the basis of the conclusions drawn from our synthetic samples.

The choice of analytical methods are undoubtedly crucial to this work. We combined both laboratory and synchrotron radiation-based techniques. Because of its high flux, tunable wavelength, and low divergence, synchrotron radiation used in various techniques provides invaluable information that is not accessible in the laboratory. For example, synchrotron radiation allows one to investigate the crystal structure and local order of Prussian blue by using X-ray radiation with a much smaller wavelength than is available from laboratory X-ray sources. Then it becomes possible to record the total scattering signal and carry out a pair distribution function analysis to describe the short-range order in Prussian blue samples. In order to study the change of oxidation state and the local environment of the iron ions, we performed iron K-edge X-ray absorption spectroscopy. This technique also requires synchrotron radiation because a monochromatic beam with low divergence is needed to probe the absorption edge of iron. High-energy X-ray diffraction and X-ray absorption spectrosocpy were both performed at the European Synchrotron Research Facility, Grenoble, France.

In this thesis we have used various methods in order to describe as completely as possible our samples. For the determination of the elemental composition of the Prussian blues, we performed particle induced X-ray emission studies, PIXE, atomic absorption/emission and thermogravimetric analysis, TGA. The structure of the pigments has been investigated by X-ray powder diffraction and by high-energy X-ray diffraction. In order to identify the degradation mechanisms, we focussed on the color-producing intervalence charge transfer in the $Fe^{III}-N-C-Fe^{II}$ bonding pathway, a pathway that we studied with various spectroscopic techniques, namely UV-visible, iron K-edge X-ray absorption, iron-57 Mössbauer, Fourier transform infrared, and Raman spectroscopy. Optical microscopy and scanning electron microscopy were used as imaging techniques. Table 1 summarizes the analytical methods used in this thesis.

Particular attention must be paid to the impact of a measurement on the sample itself, the technique must not induce further degradation than that caused by the visible light exposure of the pigment. Moreover, when studying paint layers, the analysis depth must be taken into account because measurement by transmission gives an average of the surface and bulk information. These subtleties have their importance when interpreting the results.

In this thesis we decided to highlight the results and their interpretation rather

Table 1 Analytical methods used in this study

Techniques	**Abbreviation**	**Information**
Particle induced X-ray emission	PIXE	Elemental composition
Atomic absorption	–	Fe and K contents
Thermogravimetric analysis	TGA	H_2O content
X-ray powder diffraction	XRD	Crystal structure
High-energy X-ray diffraction	HE-XRD	Short-range order and microdeformations
UV-visible spectroscopy	–	Color
X-ray absorption spectroscopy	XAS	Local environment of iron, nearest neighbors
Mössbauer spectroscopy	–	Local environment of iron, Fe(III)/Fe(II) ratio
Fourier transform infrared spectroscopy	FTIR	Molecular vibrations
Raman spectroscopy	–	Molecular vibrations
Optical microscopy	–	Imaging down to 200 nm
Scanning electron microscopy	SEM	Topography down to 10 nm, electronic density

than the experimental aspect related to the techniques. Descriptions of the analytical methods, with the required theoretical background, and the experimental details are therefore not included in the body of this thesis but rather are given in **Appendix B**.

Chapter 1

State of the Art

Summary. *This chapter is devoted to the scientific knowledge of Prussian blue, from its invention until the present time. Prussian blue was accidentally discovered in Berlin in 1704. It was eventually shown to contain a hydrated iron(III) hexacyanoferrate(II) anion,* $\{Fe^{III}[Fe^{II}(CN)_6]\cdot xH_2O\}^-$*, with varying values of x up to 16, and various cations, such as* K^+*,* $NH_4{}^+$ *or* Na^+*. Its intense blue color arises from an intervalence charge transfer between the iron(II) and iron(III) ions when light is absorbed at ca. 700 nm. Prussian blue used as a pigment in paintings shows a tendency to either fade in the light or to turn green. The fading of Prussian blue in paint layers is commonly attributed to its electrochromic character, i.e., its capability of switching electrochemically between different colors.*

Contents

1.1 Prussian blue, a challenging material for scientists

Prussian blue has been widely studied since its discovery, as is indicated by the 2 310 000 items that appear on Google with the keyword *Prussian blue pigment*[1] [5]. Scientific publications about Prussian blue are abundant: 7978 articles are found on ScienceDirect [6] and 4844 on the Web of Knowledge [7]. Such a great interest is explained by the various properties that Prussian blue presents, *e.g.*, electrochromism, magnetism at low temperature, zeolitic character, and semiconductor behavior. This chapter deals with the different properties of Prussian blue with a special emphasis on those that are expected to influence the light fading of the pigment. First, Prussian blue is placed in its historical context, when chemistry was in its infancy. The knowledge of the compound progressively increases with the development of the modern science. Second, Prussian blue is presented as a modern material with known properties.

1.1.1 A mysterious compound

The discovery of Prussian blue is shrouded in mystery. The year 1704 is often given as the most likely date of the first synthesis. Bartoll *et al.* have recently published a chronology of the early years of Prussian blue [8]. The invention is generally attributed to a Berlin colormaker, Johann Jacob Diesbach. Initially Diesbach wanted to produce a crimson lake. Therefore he needed to precipitate an aqueous solution of the cochineal dye containing alum and iron sulfate with a basic product, *e.g.*, potash, which is potassium carbonate, in order to produce metal hydroxides [4]. Diesbach purchased the potash from a local alchemist, Johann Konrad Dippel, who provided a potash contaminated with animal oil. When Diesbach tried to prepare the desired red lake, he surprisingly obtained an intense blue product. Once Dippel discovered this accidental result, he decided to benefit from it and to perfect the synthesis in order to commercialize the blue product. These events mark the beginning of the success story of Prussian blue.

Because of our present scientific knowledge we can now explain why Diesbach obtained a blue product instead of a red lake. Prussian blue is an iron(III) hexacyanoferrate(II) complex and results from the precipitation of an iron salt and a hexacyanoferrate complex. Dippel's potash was contaminated with animal oil and thus contained, among other things, alkyl cyanides, which derive from the thermal degradation of molecules with C-N bonds, such as hemoglobin. By reacting the potash containing the mandatory cyanides with iron sulfate, Diesbach formed Prussian blue [9].

[1] If the term *pigment* is not specified in the keywords, a portion of the records concern a white nationalist pop American teenagers duo.

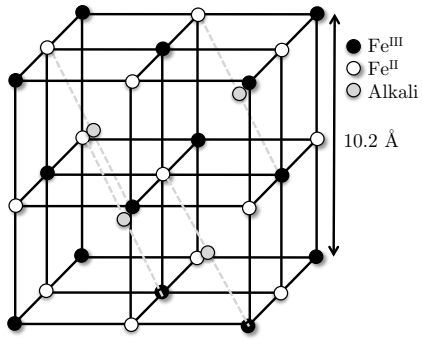

Figure 1.1 Structure of soluble Prussian blue, $KFe^{III}[Fe^{II}(CN)_6]$, elaborated by Keggin and Miles in 1936. Reproduced from [11].

The analytical composition of Prussian blue and its crystal structure have been questioned for a long time. The difficulty comes from the colloidal character of Prussian blue: it frequently adsorbs impurities such as alkali cations or organic solvents into its extremely fine particles. At this time, Prussian blue is known to contain a hydrated iron(III) hexacyanoferrate(II) anion, $\{Fe^{III}[Fe^{II}(CN)_6]\cdot xH_2O\}^-$, with varying values of x up to 16, and various cations, such as K^+, $NH_4{}^+$ or Na^+. An alkali-free Prussian blue $Fe_4^{III}[Fe^{II}(CN)_6]_3\cdot xH_2O$, which must have an increased amount of iron(III) in order to maintain charge balance, is commonly referred to as an *insoluble* Prussian blue, whereas those with alkali cations are referred to as *soluble* Prussian blues. Although all Prussian blues are highly insoluble,[2] the *soluble* appellation refers to the ease with which a *soluble* Prussian blue is dispersed in an aqueous solution to form a colloidal suspension. Though these *soluble* and *insoluble* terms are inappropriate, we will use them hereafter to distinguish Prussian blue containing alkali cations or NH_4^+ cations from those without these cations.

In 1936 Keggin and Miles determined a structure for soluble and insoluble compounds by X-ray powder diffraction analysis [11]. For the soluble variety, they proposed a cubic lattice with $a = 10.2$ Å, with an alternate arrangement of ferrous and ferric iron ions bound by the CN anions, see Figure 1.1. The alkali ions occupy the centres of some of the lattice cavities. Water molecules could also be located inside the lattice. The structure of the alkali-free Prussian blue, $Fe^{III}{}_4[Fe^{II}(CN)_6]_3$, is very similar, except that additional iron ions replace the alkali metal cations in the cavities.

The structural model of insoluble Prussian blue was finally completely re-

[2]The solubility product of Prussian blue equals 3.3 10^{-41} [10].

solved in the 1970's, with the work of Buser, Ludi, and coworkers [12]. In order to avoid the colloidal character of Prussian blue that misleads analytical data, they developed a method for growing single-crystals. The analytical composition of such crystals was close to the ideal formula with 15 water molecules, $Fe_4^{III}[Fe^{II}(CN)_6]_3 \cdot 15H_2O$. From X-ray single crystal diffraction, they developed a model consisting of a cubic Fe^{II}-CN-Fe^{III} framework where a certain number of $[Fe^{II}(CN)_6]^{4-}$ sites are vacant, see Figure 1.2. In single crystals, the vacancies do not occur at random and the cubic cell is thus primitive, with the space group $Pm3m$. However Prussian blue used as a pigment is commonly produced in the form of a fine precipitate. In this case the structure is best approximated with the face-centered cubic $Fm3m$ space group because vacancies are statistically distributed. A few years later, Herren *et al.* [13] refined the Buser and Ludi structure by studying insoluble Prussian blue by powder neutron diffraction. They distinguished two crystallographically different kinds of water molecules: six are coordinated to iron(III) at empty nitrogen positions whereas approximately eight additional water molecules occupy the center of the unit cell octants or are linked by hydrogen bonds to the coordinated water.

At present the structure of insoluble Prussian blue determined by Buser and Ludi and later refined by Herren *et al.* is commonly accepted. In contrast, the structural model for soluble Prussian blue is still debated. The commonly accepted model of Keggin and Miles has been recently revisited by Bueno *et al.* [14]. The latter claimed that the alkali cations are not inserted in the lattice cavities but are located in the $[Fe^{II}(CN)_6]^{4-}$ vacancies, similarly to the coordinated water molecules. We thoroughly study and discuss the crystal structure of insoluble and soluble Prussian blues in **Chapter 2.**

1.1.2 Prussian blue, a metal cyanide complex

With increasing chemical knowledge the synthesis of Prussian blue has become better understood. In 1749 Macquer [15] discovered potassium hexacyanoferrate by testing the chemical reactivity of Prussian blue. Hydrogen cyanide and cyanogen were first identified by Scheele in 1782 [4] and then throroughly studied by Gay-Lussac in 1815 [16]. The term cyanogen is directly correlated with Prussian blue as cyanogen came from the Greek *kuanos-gennao* which means *blue-generating.* The cyanogen discovery lead to modern transition metal cyanide chemistry.

In the periodic table, transition metals are the elements of the d-block, from group B in columns 3 to 12. They are characterized by an electronic configuration in the ground state with an incomplete d orbital occupancy. For example, the electronic configuration of iron is $[Ar](4s^2 3d^6)$. Nearly all transition metals form

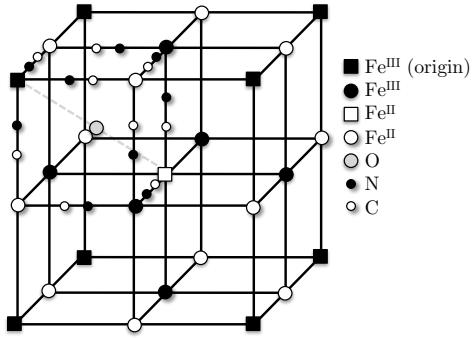

Figure 1.2 The unit cell of Prussian blue in space group $Pm3m$. The open and solid symbols indicate different crystallographic positions. More details about this structural model are given in **Section 2.2.2.** Reproduced from [12].

cyanides or complex cyanides [17]. Historically the term *complex* was given to compounds that seemed to defy the usual rules of valency. Now a complex is described as a polyatomic compound built from a central atom or cation that is bound to molecules or ions called *ligands*. The complex is characterized by its coordination number, *i.e.*, the number of ligands coordinated to the cation. Three major theories have successively tried to explain the nature of the bonding in coordination compounds: valence bond theory, crystal field theory, and ligand field molecular orbital theory. In 1962, Robin [18] applied this latter theory[3] to Prussian blue in order to explain its intense color. The following paragraphs progressively develop the concepts required to understand the type of interactions occurring in Prussian blue.

According to Pauling's **valence bond theory**, a complex arises from the reaction between the ligands and the metal or metallic ion, accompanied by the formation of a coordinate-covalent bond. In cyanide complexes, the cyanide ion is obviously the ligand. The carbon and nitrogen atoms are triply bonded, with one σ- and two π-bonds, and each atom has unshared pairs of electrons. Bonding in cyanide complexes implies the hybridization between $(n-1)d$, ns, np, and nd orbitals of the transition metal ion. For example, the ion $[Fe(CN)_6]^{3-}$ is octahedral, with the hybrid orbital d^2sp^3. The cyanides supply the bonding electron pairs. This theory predicts the magnetic properties of the complex. The $[Fe(CN)_6]^{3-}$ ion is paramagnetic because it has one unpaired electron, see Figure 1.3. However, the valence bond theory can not explain the color of complexes. Moreover, because the ligands donate electrons to the metal cation, there is a formal negative charge

[3]In fact, Robin used the ligand field theory, which can be seen as being a special case of the most general molecular orbital theory.

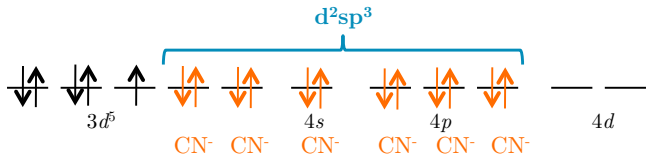

Figure 1.3 Hybridization of $[Fe(CN)_6]^{3-}$.

accumulation on the cation. This is contradictory to the principle of electroneutrality. The theory that has supplanted the valence bond theory is the **crystal field theory**, first developed in 1929 by Bethe in solid-state physics and then applied in the 1950's to the study of transition metal complexes [19].

Crystal field theory is based on the electrostatic interaction between a metallic ion and its ligands. The latter are considered as negative point charges whereas the central metal ion is positively charged. An isolated transition ion has five degenerate *d*-orbitals, *i.e.*, five *d* orbitals with the same energy, see Figure 1.4, orbitals that remain degenerate when they are placed in an electrostatic field created by a spherical distribution of six electrons. The energies of the orbitals are uniformely increased because of the repulsion between the negative charge of the metal ion electrons and the spherical distribution of the six electrons. Because of the differing symmetry of the five metal ion *d*-orbitals, see Figure 1.5, their degeneracy will be removed when the six electrons are localized at the apexes of an octahedron. The crystal field effect thus depends upon both the symmetry of the *d*-orbitals and the symmetry of the coordinated ligands. We will now restrict the explanation to the case of Prussian blue, which has an octahedral symmetry.

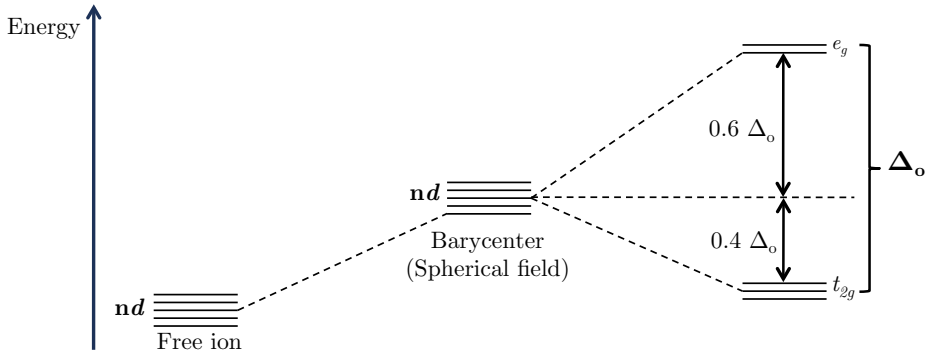

Figure 1.4 Splitting of the five orbitals in an octahedral field. Adapted from [19].

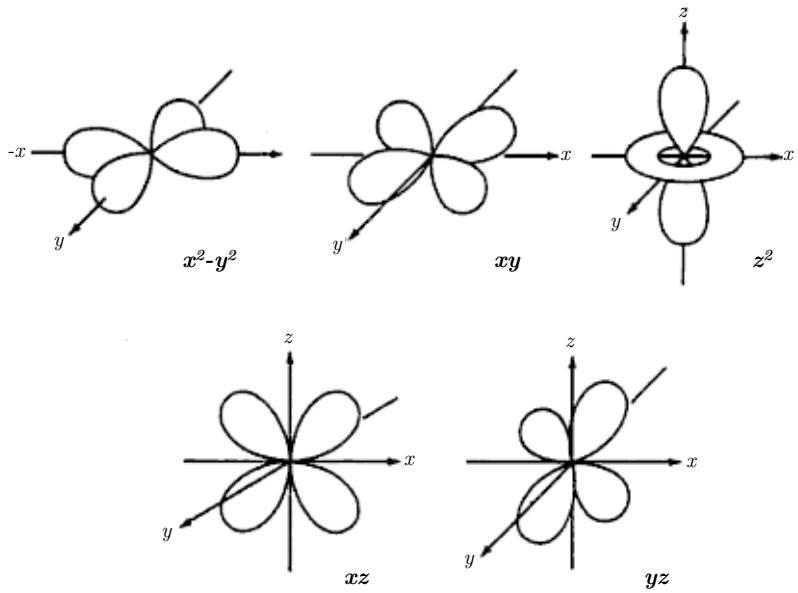

Figure 1.5 Spatial geometry of the five *d*-orbitals. Adapted from [19].

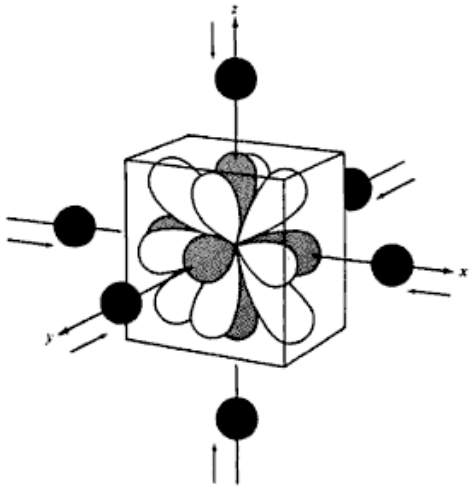

Figure 1.6 The *d* orbitals in an octahedral field generated by six ligands. The torus of the d_{z^2} orbital has not been represented. The t_{2g} orbitals are in white and the e_g orbitals in grey [19].

The spatial geometry of the five d-orbitals is shown in Figure 1.5. It is clear from Figure 1.6 that in a complex with octahedral symmetry with six ligands surrounding a metal ion, the relative energies of the d_{z^2} and $d_{x^2-y^2}$ orbitals, which point directly towards the negative ligands, are increased more than those of the d_{xy}, d_{xz}, and d_{yz} orbitals, which are spatially oriented between the negative ligands. The degeneracy of the five d-orbitals is thus removed and two groups of orbitals result, the triply degenerate d_{xy}, d_{xz}, and d_{yz} orbitals, referred to as the the t_{2g} orbitals, and the doubly degenerate d_{z^2} and $d_{x^2-y^2}$ orbitals, referred to as the e_g orbitals.[4]

The energy splitting between the e_g and t_{2g} orbitals is referred to as the crystal field splitting and is designated by Δ_o, where the o subscript stands for an octahedral crystal field. Because the octahedral field does not change the average energy of the five d-orbitals the gravity center or *barycenter* of the orbitals remains unchanged. In order to fulfill this condition for all octahedral complexes, the e_g orbitals are increased in energy by 0.6 Δ_o above the barycenter, whereas the three t_{2g} orbitals are lowered in energy by 0.4 Δ_o below the barycenter, see Figure 1.4.

The reduction in energy of the three t_{2g} orbitals in comparison with the barycenter is referred to as the *crystal field stabilization energy*, *CFSE* . The *CFSE* depends upon the electron occupancy of the d-orbitals and in octahedral symmetry, it can be calculated from [20]:

$$CFSE = (-0.4x + 0.6y)\Delta_o$$

where x is the number of electrons in the t_{2g} orbitals and y is the number of electrons in the e_g orbitals.

For a d^5 ion, such as iron(III), the fourth and fifth electrons can occupy either the higher energy e_g orbitals or be paired with two electrons in the t_{2g} orbitals. The actual configuration will be that with the lowest energy and is a function of the crystal field splitting, Δ_o, and the electron mean pairing energy, P, required to pair two electrons in the same orbital. If $\Delta_o < P$ the energy to pair two electrons is larger than the crystal field splitting and the iron(III) ion is high-spin in a weak crystal field. Inversely, if $\Delta_o > P$, the crystal field splitting is larger than the electron mean pairing energy, and the iron(III) ion is low-spin in a strong crystal field. Because the energy required to pair electrons in a $3d^5$ configuration is rather high, in other words, $P > \Delta_o$, iron(III) $3d^5$ ions in octahedral complexes are usually

[4]This notation comes from the irreducible representations arising from the symmery elements of the d-orbitals in octahedral symmetry; lower case letters are used to designate orbitals. The g and u subscripts stand for *gerade* and *ungerade*, *i.e.*, even and odd, and indicate that orbitals have either symmetric wave functions or antisymmetric wave functions, respectively. In octahedral complexes all the d-orbitals are *gerade* because of the presence of an inversion symmetry element.

high-spin, with the $t_{2g}^3 e_g^2$ electronic configuration, see Figure 1.7a. In contrast, iron(II) $3d^6$ ions experience a strong octahedral crystal field in the presence of six cyanide ligands and in this case, typically adopt the t_{2g}^6 low-spin electronic configuration. This configuration results because it is more favorable in terms of energy to pair electrons in the t_{2g} orbitals than to place them in the higher energy e_g orbitals [19], see Figure 1.7b. Thus the values of Δ_o and P determine the electronic configuration of the iron ion in these complexes. Usually these parameters are empirically determined by electronic spectroscopy. The energy splitting, Δ_o, is influenced by many factors, such as the oxidation state and the nature of the metal ion, the number and the coordination geometry, and the nature of the ligands. The *spectrochemical series* orders the ligands depending on the strength of the crystal field splitting they produce. In this series, with the exception of CO, the CN^- ligand produces the largest contribution to the crystal field.

Based on crystal field theory the color of transition metal complexes can be explained as arising from a $d-d$ electronic transition.[5] Because of the non-degeneracy of d-orbitals electrons can undergo a transition from one d orbital to another when they absorb light. If the frequency of the absorbed light is in the visible region of the spectrum, the complex has a color that is complementary to the colors absorbed [20].

Although crystal field theory effectively explains many important properties of transition metal complexes, such as their color and their magnetic behavior, the assumption of a purely electrostatic interaction between the ligands and the central metal cation is not realistic. A new theory has thus been developed in order to take into account the covalent character in the bonding interaction, this is the **molecular orbital theory**.

Molecular orbital theory considers the overlap between metal and ligand orbitals. This overlap depends on the symmetry of the complex. In octahedral first-row transition metal complexes, the metallic ion has nine valence[6] orbitals, the $3d$, $4s$, and $4p$ orbitals. Based on group theory, a purely octahedral complex is characterized by an O_h symmetry. Based on the corresponding symmetry of the orbitals, the s orbital becomes an a_{1g} orbital, the three p orbitals become the

[5] According to selection rules for electronic transitions, $d-d$ transitions in perfectly octahedral complexes are symmetry forbidden. Indeed, the first selection rule, Laporte rule, states that only transitions with a change of parity are allowed. Thus, $g \rightarrow u$ or $u \rightarrow g$ transitions are allowed whereas $u \rightarrow u$ or $g \rightarrow g$ transitions are forbidden. However this rule is not perfect and can be overridden by reduction in symmetry. In purely octahedral complexes, where all d-orbitals are symmetric, $d-d$ transitions can be observed because of asymmetric vibrations that temporarily destroy the octahedral center of symmetry.

[6] The atomic orbitals that describe the core electrons are not considered in the construction of the molecular orbitals of a complex.

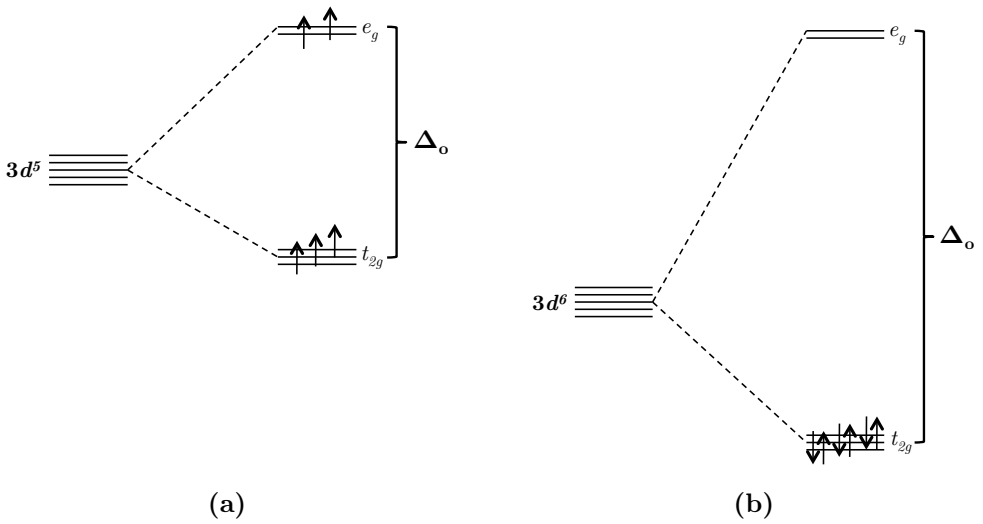

Figure 1.7 Electronic configurations of, **a**, a high-spin d^5 ion in an octahedral weak field and **b**, a low-spin d^6 ion in an octahedral strong field. Reproduced from [19].

t_{1u} orbitals, and the five d orbitals are divided into two groups, two e_g d-orbitals resulting from the $d_{x^2-y^2}$ and d_{z^2} orbitals, and three t_{2g} orbitals resulting from the d_{xy}, d_{xz}, and d_{yz} orbitals. The removal of the degeneracy of the five d orbitals is similar to that obtained by crystal field theory.

The molecular orbitals result from two types of interactions, the σ interactions, which consists of *axial* orbital overlap and the π interactions, which consist of *lateral* or *sideways* orbital overlap. The overlap requires that the overlapping ligand and metal orbitals have the same parity. So, in octahedral complexes, the σ bonding is formed by the overlap of the metal and ligand orbitals with a_{1g}, t_{1u}, and e_g symmetry. In contrast, the π bonding involves the orbitals that are perpendicular to the bonding axis, *i.e.*, the t_{2g}, t_{1u}, t_{2u}, and t_{1g} orbitals. Because the axial σ overlap is more efficient than sideways π overlap, σ interactions are stronger than π interactions.

Let us now consider the molecular orbital scheme for Prussian blue. The molecular orbitals of the cyanide ion, CN^-, are shown in Figure 1.8. The highest occupied molecular orbital (HOMO) is a σ orbital, which is the donor orbital used by CN^- for the formation of σ-bonds in Prussian blue. The lowest unoccupied molecular orbitals (LUMO) are the two π^* orbitals that will interact with the metal d-orbitals to form π-bonds [21].

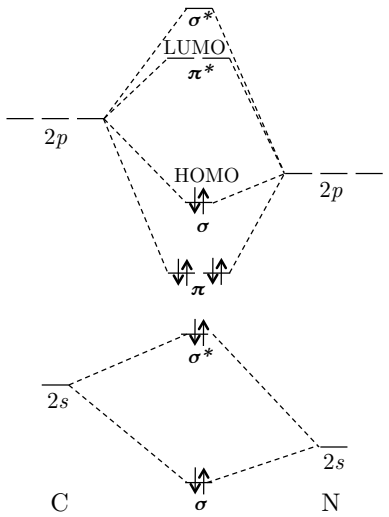

Figure 1.8 Cyanide anion molecular orbitals, reproduced from [21].

The difficulty in drawing the molecular orbital scheme for Prussian blue results from the presence of two different iron oxidation states. This *mixed valency* will be more thoroughly discussed in the **Section 1.1.3**. Thus we must first consider the iron(III) and iron(II) ions separately. Their qualitative molecular orbital diagrams are shown in Figure 1.9. It should be emphasized that there is a π interaction between the unoccupied antibonding π^* ligand orbitals and the t_{2g} metal orbitals, as is evidenced by the two black solid lines in Figure 1.9, a π bonding that affects the crystal stabilization energy, Δ_o. In $[Fe(CN)_6]^{4-}$, this π bonding from metal to ligand stabilizes the t_{2g} orbitals, lowers their energy relative to the e_g orbitals, and increases Δ_o. Thus the iron(II) ion coordinated to six carbons is consequently in a strong ligand field and is low-spin. In contrast, the iron(III) ion coordinated to six nitrogens in $[Fe(CN)_6]^{3-}$, is high-spin because its t_{2g} and e_g orbitals are destabilized by the same amount and the iron(III) ion is consequently in a weak ligand field and is high-spin.

The molecular orbitals of Prussian blue correspond to linear combinations of all six iron(III) and iron(II) t_{2g} orbitals. Let us now consider the distribution of the eleven $3d$ valence electrons of the iron(III) and iron(II) ions. Each iron ion has at least five d electrons but the localization of the eleventh is unclear, it can be in either a molecular orbital of predominantly carbon or nitrogen character. Robin removed this ambiguity in 1962 by assigning each band in the absorption spectrum of Prussian blue to a transition in the molecular orbital diagram [18].

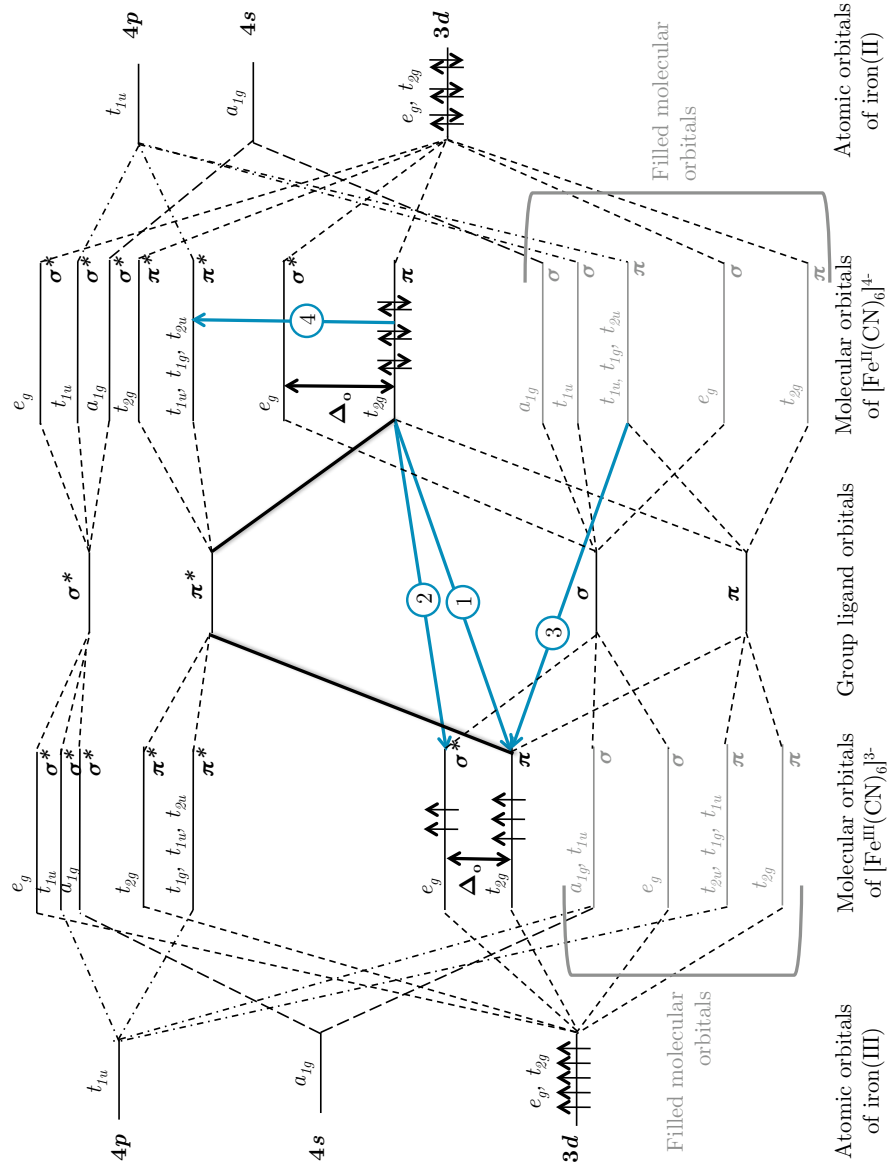

Figure 1.9 Molecular orbital scheme for iron(III) coordinated to nitrogen on the left and for iron(II) coordinated to carbon on the right. Molecular orbitals for the cyanide ion are represented in the center. The transitions in Prussian blue are labeled from 1 to 4 and shown as blue arrows. Adapted from [18], [22], and [23].

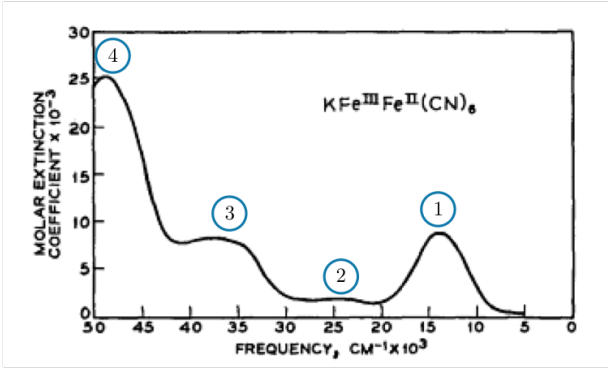

Figure 1.10 The electronic absorption spectrum of soluble Prussian blue, as a colloidal dispersion in water. The numbers from 1 to 4 indicate the absorption bands assigned to the numbered transitions in Figure 1.9. Adapted from [22].

The absorption spectrum of Prussian blue consists of four absorption bands, as is evidenced by the numbers in Figure 1.10. The blue color of Prussian blue corresponds to the 14 100 cm^{-1} transition labeled 1 in Figure 1.9, a transition that is at a wavelength of *ca.* 700 nm, and arises from the transfer of an electron from the t_{2g}^6 predominantly carbon-iron(II) ion molecular orbital to the t_{2g}^3 predominantly nitrogen iron(III) ion molecular orbital. This electron density tranfer between the iron ions bridged by a ligand is called **intervalence charge transfer**.

The weak transition located at about 24 000 cm^{-1}, labeled 2 in Figure 1.9, corresponds to the transition of an electron from the t_{2g} orbitals of iron(II) to the e_g orbital of iron(III). The strong absorption at 50 000 cm^{-1}, labeled 4 in Figure 1.9, is assigned to the iron(II) ion $t_{2g} \rightarrow CN^-$ π^* t_{1u}, t_{2u} transitions occurring in the d^6 iron(II) hexacyanide ions. Finally, Robin assigned the broad 33 000 to 37 000 cm^{-1} absorption, labeled 3 in Figure 1.9, to the CN^- π t_{1u} to Fe^{3+} t_{2g} transition.

In summary, the color of Prussian blue is produced by an intervalence charge transfer between the two iron ions in different environments. If the two iron ion sites were identical, there would not be any color-producing absorptions because there would be no energy difference between the two 3*d* orbitals associated with the two iron ions. This is the reason why ferrous ferrocyanide, $K_2Fe^{II}[Fe^{II}(CN)_6]$, is colorless and ferric ferricyanide, $Fe^{III}[Fe^{III}(CN)_6]$, is pale yellow [24]. The next section discusses the mixed valence character of Prussian blue and its resulting properties.

1.1.3 Prussian blue, the prototype of mixed valence compounds

Besides its cyanide ligands, Prussian blue has the unusual property of containing iron ions in two different oxidation states.[7] For this reason, Prussian blue is considered as the prototype of mixed-valence compounds. Mixed valency defines *inorganic or metal-organic compounds in which an element is present in more than one oxidation state* [25].

For a long time, Prussian blue prepared from an iron(III) salt solution and a potassium ferrocyanide solution was thought to be different from *Turnbull's blue*, which is prepared from an iron(II) salt and a potassium ferricyanide solution. Prussian blue was referred to as a ferric ferrocyanide, whereas Turnbull's blue was referred to as a ferrous ferricyanide. Because both exhibit the same Mössbauer spectrum and X-ray powder diffraction pattern [26][27] it was eventually recognized that Turnbull's blue was not different from Prussian blue and that both compounds were ferric ferrocyanide or iron(III) hexacyanoferrate(II).

According to the classification of mixed valence compounds proposed by Day and Robin [25], Prussian blue belongs to class 2, because the crystallographically different iron(II) and iron(III) sites are rather similar.[8] In fact, the similarity or difference between the two crystallographic iron sites of different valence determines the properties of a mixed-valence compound. In Prussian blue the energy for transferring an electron from the iron(II) to the iron(III) ion sites is only a few electron volts and gives raise to an optical transition in the visible portion of the spectrum, as explained in **Section 1.1.2**. In view of this intervalence charge transfer, one can wonder to what extent the oxidation states of iron ions in Prussian blue are mixed, or, in other words, whether the electrons associated with the optical transition are localized or delocalized. The extent of any delocalization can be estimated by the so-called *mixed valence coefficient* or *valence delocalization coefficient*, α. From the intensity of the intervalence band observed at 14 100 cm^{-1} in Figure 1.10, Robin determined a value of α of 0.10. This value indicates that the electrons associated with the optical transition are 99% localized on the iron(II) bonded to the carbon in Prussian blue, *i.e.*, only 1 % of the iron(II) electrons are delocalized and involved in intervalence charge transfer. Thus the origin of the blue color cannot be explained as an *oscillation of valence* or a resonance between the configurations

$$[Fe^{II}(CN)_6Fe^{III}]^- \leftrightarrow [Fe^{III}(CN)_6Fe^{II}]^-.$$

[7] The term *oxidation state* describes the effective number of electrons associated with a given atom in a molecule or a solid.

[8] Class 1 consists of mixed-valence compounds in which the two oxidation states of the metal occupy very different crystallographic sites. Class 3 contains compounds in which the two oxidation states occupy crystallographically equivalent sites and, hence, exhibit a non-integral valence.

Because of the weak iron ion-iron ion interaction, Prussian blue exhibits semiconductor behavior. The electronic conductivity strongly depends on the extent of hydration and the method of preparation of Prussian blue and varies from 10^{-6} to 10^{-11} $(\Omega\ \mathrm{cm})^{-1}$. The band gap is estimated to be 0.5 eV. Electron and ionic conduction in Prussian blue was not of particular interest until the discovery of its **electrochemical activity**. In 1978, Neff *et al.* [28] achieved the growth of Prussian blue thin films adhering to a platinum foil electrode by electrochemical deposition from a ferric ferricyanide solution. They then realized that the thin film had **electrochromic properties**: a change of color accompanies the electrochemical reduction or oxidation of the Prussian blue thin film [29].

The electrode with the electrodeposited Prussian blue thin film can undergo potential cycling in a K^+-containing supporting electrolyte. Electrochemical oxidation of Prussian blue yields either Berlin green, or in the case of a particularly pure form of Prussian blue, Prussian yellow, the fully oxidized form of Prussian blue:

$$K_x^+ + [Fe^{III}Fe^{II}(CN)_6]^- \rightarrow \{KFe^{III}Fe^{II}(CN)_6\}_x\{Fe^{III}Fe^{III}(CN)_6\}_{1-x} + (1-x)e^-$$

or

$$[Fe^{III}Fe^{II}(CN)_6]^- \rightarrow [Fe^{III}Fe^{III}(CN)_6] + e^-.$$

Alternatively, Prussian blue can be electrochemically reduced to form ferrous ferrocyanide, referred to as *Berlin white* or *Everitt's salt* [30], a reduction which gives a transparent appearance to the thin film:

$$[Fe^{III}Fe^{II}(CN)_6]^- + e^- \rightarrow [Fe^{II}Fe^{II}(CN)_6]^{2-}.$$

It should be noted that both the oxidized and reduced forms of Prussian blue are unstable under normal conditions because of air-sensitivity and rapidly revert to Prussian blue. All these redox reactions require electron and ion transport; in an aqueous solution of K^+, the mobile K^+ ions must provide the appropriate charge balance during reduction to the colorless Berlin white and oxidation to Prussian yellow. However many questions about these electrochromic oxidation/reduction mechanisms remain unanswered and new models have recently been proposed [14][31][32]. The electrochemistry of Prussian blue has also been investigated in the solid state, on Prussian blue powder pressed between conducting electrodes [33][34].

The ability of Prussian blue to undergo redox reactions that are accompanied by a color change has been exploited in many applications. Electrochromic devices consisting of a Prussian blue film sandwiched between electrodes of various materials, such as TiO_2, $SrTiO_3$, or organic compounds, have been designed [29][35].

Moreover, Prussian blue electrochemically synthesized on electrodes can be used in biochemical and chemical sensors, for the amperometric detection of hydrogen peroxide [36], glucose [37], or other reductants [38].

In paintings the electrochromic activity of Prussian blue is expected to play a role in the fading of the pigment. This hypothesis will be thoroughly discussed in **Section 1.2.3**.

1.1.4 Prussian blue, an inorganic sponge

Another property of Prussian blue that can influence its permanence is its zeolytic character, *i.e.*, its capability of trapping molecules inside its structure. Prussian blue can host molecules such as water or monovalent cations in the cubic voids of its structure and can thus be used as a molecular sieve or an ion exchange complex with channel diameters of about 3.2 Å [9][22].

As an ion exchange complex, Prussian blue is very useful in cases of thallium, rubidium, or cesium poisoning [39][40]. Soluble Prussian blue can exchange its cations, such as potassium, ammonium, or sodium cations, from its lattice for the radionuclide ions in the gastrointestinal tract. Prussian blue with the trapped ions is then removed by the fecal route. The process of cesium or thallium ion binding by insoluble Prussian blue is not completely elucidated. It is believed that the radionuclide ion is exchanged with either a hydrogen ion, H^+, or hydronium ion, H_3O^+, bound in the crystal lattice. Physical adsorption resulting from electrostatic forces and mechanical trapping in the crystal lattice are also considered as possible mechanisms of ionic exchange [41][42]. Because the cyanide ion is found in a hexacyanoferrate ion in Prussian blue [17], Prussian blue is completely non-toxic and can be given orally to humans.

1.1.5 Magnetic Prussian blue and its analogues

This section concludes with a discussion of the magnetic behavior of Prussian blue, although it is expected to play little role in fading of color. Prussian blue contains paramagnetic high-spin iron(III) ions and diamagnetic low-spin iron(II) ions. The effective spin-only magnetic moment, expressed in Bohr magneton, μ_B , is given by $\mu_{eff} = \sqrt{n(n+2)}$ where n is the number of unpaired electrons [19]. For Prussian blue, the theoretical effective spin-only magnetic moment of 5.92 μ_B for $n = 5$ agrees well with the experimental value of 5.98(2) μ_B obtained between 10 and 300 K. Prussian blue exhibits ferromagnetic behavior below a Curie temperature of 5.5(5) K [26]. Ferromagnetism implies a long range order of the iron(III) magnetic moments through a possible superexchange mechanism along the sequence

Fe(III)-NC-Fe(II)-CN-Fe(III).

In the 1990's, a modulation of the Curie temperature by changing the nature of the ions in Prussian blue was discovered. These so-called *Prussian blue analogues* are defined as cubic systems with the $C_nA_p[B(CN)_6]_q \cdot xH_2O$ stoichiometry, where C is a monovalent cation inserted into some unit cell octants, A is located at the corners and centers of the cubic faces and the $[B(CN)_6]$ anions occupy the octahedral sites [43]. Numerous Prussian blue analogues have been synthesized, that have interesting and diverse properties. These analogues can be high Curie temperature molecule-based magnets, such as $V[Cr(CN)_6]_{0.86} \cdot 2.8H_2O$ with a Curie temperature above room temperature [44], photomagnetic compounds, such as $C_xCo_4[Fe(CN)_6]_y$ where C is an alkali cation [45], or high-spin molecules [43]. Prussian blue analogues have been also used in inorganic/organic composite materials in order to combine unusual magnetic and optical properties [46][47]. Over the past few years interest in single molecule magnets has grown continuously and attempts have been made to tune their magnetic properties by controlling the morphology of Prussian blue analog nanoparticles [48][49][50].

1.2 Prussian blue as an artist's pigment

Prussian blue has attracted not only scientists but also artists, dyers, and printers. Prussian blue as a pigment or dye[9] has been widely used from the early 1710's to date, even though it is now often replaced by new synthetic pigments. This popularity is surprising because soon after its discovery, Prussian blue was known to have a poor light fastness. In this section a brief history of use of Prussian blue is presented. Next the degradation problems discussed in eighteenth and nineteenth century books are summarized and, finally, the current hypotheses that have been proposed to explain the fading of the Prussian blue pigment are presented.

1.2.1 History of use

The discovery of Prussian blue by Diesbach in 1704 suddenly changed the artist's vision of blue. For the first time blue became an affordable color, both commercially and artistically. At the beginning of the eighteenth century the other blue pigments, such as ultramarine, azurite, indigo, and blue ashes, were either very expensive, scarce, or unstable [4].

[9]The term *pigment* refers to an insoluble substance whereas a *dye* is soluble in water [51]. Strictly speaking Prussian blue is thus a pigment because it is not soluble in water.

It is noteworthy that Prussian blue has had many names. Some, such as Berlin blue, Paris blue or Antwerp blue, suggest the place of manufacture. Others, such as Milori blue or Turnbull's blue,[10] refer to the inventor or producer. Others describe the shade of the blue pigment with names such as bronze blue, celestial blue, or iron blue. These appellations are related to the manufacturing process that determines the composition of the pigment and, in some cases, the possible presence of extenders[11] or mixtures. For example, Antwerp blue was known to contain a mixture of Prussian blue, alumina, magnesia, and zinc oxide. Charron blue was a Prussian blue mixed with barium sulfate [53]. Synthesis of Prussian blue and the influence of such extenders on the light fastness of the pigment will be discussed in **Chapter 2** and **Chapter 3**.

The very first occurrences of Prussian blue in paintings have recently been reported by Bartoll and Jackish [8]. The earliest example is a painting by Pieter van der Werff, *Entombment of Christ*, a painting that is dated 1709. Next Prussian blue has been identified in paintings by Antoine Watteau, whose earliest painting is *La mariée du village*, dated by art historians to the beginning of the 1710s. From the 1720s the use of Prussian blue quickly spread throughout Europe and even reached America. The blue pigment has also been found in several eighteenth century art works, namely in Italian paintings by Giovanni Antonio Canal, known as *Canaletto* (1697-1768) and by Giovanni Battista Tiepolo (1696-1770), in French paintings by Jean-Baptiste Perronneau (1715?-1783), and in English paintings by William Hogarth (1697-1764), Richard Wilson (1713/1714-1782), and Thomas Gainsborough (1727-1788) [54].

In the nineteenth century, Prussian blue was used by numerous artists for easel paintings, watercolors, or pastels. Edgar Degas (1834-1917), Claude Monet (1840-1926), and Vincent van Gogh (1853-1890) were among the artists who employed the blue pigment in their art. Prussian blue has also been found in Asia, on nineteenth century Japanese paintings and in the false patina on Chinese bronzes. The popularity of Prussian blue did not decrease at the beginning of the twentieth century and Prussian blue is found in paintings by Pablo Picasso (1881-1973) and in contemporary art by Anish Kapoor (1954) [54].

Figure 1.11 shows some of the works of art of the above-mentioned painters, where Prussian blue has been identified.

Prussian blue has enjoyed great popularity worldwide. It was used not only

[10] Turnbull's blue was long considered to be a ferrous ferricyanide but was eventually shown to be similar to Prussian blue, *i.e.*, a ferric ferrocyanide. Cf. **Section 1.1.2.**

[11] An extender or *filler* is added to a pigment in order to modify its chemical or physical properties or increase its bulk volume. Extenders are usually white or lightly colored [52].

Figure 1.11 1. *Entombment of Christ*, **P. van der Weerf**, 1709, Sanssouci Gallery, Berlin. 2. *Portrait of Angel Fernandez de Soto*, **P. Picasso**, 1903, Private collection. 3. *The Graham Children*, **William Hogarth**, 1742, The National Gallery, London. 4. *A Flower, A Drama Like Death*, **A. Kapoor**, 1986, The Museum of Modern Art, New York. 5. *The Wave*, **K. Hokusai**, 1831, Metropolitan Museum of Art, New York. 6. *Bathers at La Grenouillère*, **C. Monet**, 1869, National Gallery, London.

in paintings, but also in house paint and wallpaper as well as in textile dyeing. In the beginning of the nineteenth century the importation of indigo from America by France was halted because of a maritime blockade imposed by England. Thus another dye had to be found to replace the indigo commonly used to dye the uniforms worn by French soldiers [4]. In 1811 the chemist Raymond published an efficient method to dye silk with Prussian blue [55]. This method consists of impregnating the silk with iron and then dipping the fibres in an acidic solution of potassic iron cyanide. A final bath in ammoniacal water darkened the color. A few years later, Raymond's son proposed an industrial method to dye wool. These discoveries lead to the development of a dyeing industry that used the so-called *Raymond blue*. Beginning in about 1860 new synthetic dyes appeared on the market and progressively supplanted the Raymond blue.

In the nineteenth century Prussian blue was found to be useful by the early pioneers of photography. In 1842 Sir John Herschel invented the cyanotype process, a photographic contact-printing process that used Prussian blue, see Figure 1.12. Herschel used a photosensitive coating composed of a mixture of ammonium iron(III) citrate and potassium ferricyanide. When exposed to the light, the coating undergoes a redox reaction: the iron(III) is reduced to iron(II) and the citrate is oxidized to acetone dicarboxylic acid[9][56]:

$$2\ Fe^{3+}\ (aq) + C(OH)COOH(CH_2COOH)_2\ (aq) \rightarrow 2\ Fe^{2+}\ (aq) + CO(CH_2COOH)_2\ (aq) + CO_2\ (g) + 2\ H^+\ (aq).$$

Next the iron(II) reacts with the ferricyanide to produce Prussian blue:

$$Fe^{2+}\ (aq) + [Fe^{III}(CN)_6]^{3-}\ (aq) \rightarrow [Fe^{III}Fe^{II}(CN)_6]^-\ (s).$$

After removing the unreacted chemicals with water, a tonally graduated, negative photograh in Prussian blue is obtained. The cyanotype method lead to the development of the commercial reprographic blue print process.

In the 1980's 50 000 tons of Prussian blue were annually used in Western nations [54]. In 2006 the world production was about 12 000 tons [4]. The use of Prussian blue in art works represents only 10 weight percent of the total consumption. From the 1970's phtalocyanine blue often replaces Prussian blue. Currently 70 weight percent of the production is employed in the manufacture of printing inks and carbon paper. Prussian blue, when dissolved in oxalic acid, can serve as an ink. Because its color is close to that of cyan, the Prussian blue pigment is an appropriate ink, even though its use has tended to decrease since the introduction of aniline dyes. Prussian blue is also used to color paper: the pigment is ground with a water-soluble material and then applied to the paper. Finally the remaining

Figure 1.12 Sir John Herschel, a cyanotype made in 1842 of an engraving of Mrs. Leicester Stanhope, done by Charles Rolls (1836) [56].

20 weight percent is used in agriculture to add color to fungicides.[12]

This brief history of use of Prussian blue illustrates the popularity of this pigment. However the permanence of Prussian blue had already been questioned by the mid-eighteenth century. Prussian blue used either in paintings, in dyeing, or in cyanotypes, tends to discolor with time as was reported in many eighteenth and nineteenth century books.

1.2.2 Reports and occurrences of faded Prussian blue

There are numerous reports dealing with the durability of Prussian blue as a pigment in artist's books as well as scientific studies dating from the eighteenth and nineteenth centuries. It would not be particularly relevant to present an exhaustive list of all these citations herein. Nevertheless some of them are given in **Appendix A**. Moreover, in 1994, Kirby extensively examined the early reports of fading and color change of Prussian blue [57]. The following are some of the conclusions drawn from this investigation.

According to the documentary sources of the period, Prussian blue was generally not considered to be a very durable pigment. First, Prussian blue is sensitive to alkali and therefore cannot be used in fresco paintings. Second, Prussian blue

[12]These fungicides are used by vine growers and are colored blue for historical reason. Until 1930 the traditional fungicide used in vineyards was copper sulfate, which is naturally blue. Because of its toxic nature, it has been replaced by colorless manganese or zinc ethylene-bis-dithiocarbamates colored with Prussian blue in order to respect the tradition.

shows a tendency to fade upon exposure to light and eventually to become greenish or grayish. Prussian blue is also described as a fluctuating pigment because when discolored by the light, it tends to regain its color in the dark. Because pure Prussian blue has such a deep color it was rarely used in pure form but rather diluted with some white pigment. However, the admixture of a white pigment or the presence of an extender introduced during the synthesis of Prussian blue are said to increase the discoloration. The ancient methods of preparation were thus recognized as a contributory factor in the fading, because they may introduce impurities or extenders such as alumina or barium sulfate to the pigment.

Recent studies concerning the discoloration of Prussian blue confirmed these observations that dated from the eighteenth and nineteenth centuries [58] [59]. The light fastness of Prussian blue strongly decreases with the amount of extender or white pigment mixed with Prussian blue. The nature of the white pigment seems to play little role in the degree of fading. The reversible change in color mentioned above is only observed for relatively short light exposure periods before dark storage. After a long exposure time an irreversible color change appears.

Although Prussian blue has been widely used in paintings, only a few examples of faded Prussian blue in art works have been reported. Kirby [57] specifically points out the fading of some paintings from the National Gallery in London, namely in paintings by Gainsborough, in two paintings by Richard Wilson, and in Italian School paintings, such as in *An Allegory with Venus and Time*, painted by Tiepolo in *ca.* 1754. In the latter painting the fading is easily observed in cross-sections of paint from the lightest area of Time's blue drapery, see Figure 1.13. The paint layer consists of lead white mixed with a little Prussian blue and shows a discoloration near the surface. In contrast, a cross-section from a darker Prussian blue area does not exhibit such surface fading. Faded Prussian blue was also observed in paintings by Watteau, such as *La mariée du village*, *ca.* 1710-1712 [8].

The homogeneous discoloration of Prussian blue makes the detection of faded areas difficult, unless a comparison with unexposed areas, such as those covered by the frame, is possible. For example, in *Die Hülsenbeckschen Kinder* painted in 1805 by Philipp Otto Runge (1777-1810), the fading of the sky was only discovered when the painting was unframed for restoration, see Figure 1.14.

What are the mechanisms that are involved in the discoloration of Prussian blue? Since the eighteenth century scientists have tried to explain the curious behavior of Prussian blue under light exposure. Several hypotheses have been proposed but, to date none of the hypotheses has been firmly confirmed as accounting for the color change of Prussian blue in paint layers.

Figure 1.13 *An Allegory with Venus and Time*, **G. B. Tiepolo**, *ca* 1754. National Gallery, London. At right: Photomicrographs of paint cross-sections taken from the palest tint and the darker tone of Time's drapery. Only the palest tint exhibits a fading at the surface of the paint layer, a layer that contains both lead white and Prussian blue [57].

Figure 1.14 *Die Hülsenbeckschen Kinder*, **P. O. Runge**, 1805. Kunsthalle, Hamburg. At right: detail of the painting. The sky painted with both Prussian blue and lead white pigments is faded in comparison with the areas covered by the frame.

1.2.3 Hypotheses for the discoloration of Prussian blue

In the nineteenth century, the observation that discolored Prussian blue could regain its color in the dark fascinated several scientists. Field studied the permanence of pigments and observed a discoloration in Prussian blue paint layers when exposed to strong light. The paint layers regained their color when stored in the dark. He attributed the change in color to "the action and reaction by which it (the color) acquires or relinquishes oxygen alternately." According to Field, the tendency of Prussian blue to turn green results from the formation of an iron oxide [60].

Chevreul extensively studied the degradation of Prussian blue on dyed fabrics exposed to light [61]. In vacuum darkly dyed fabrics loose their color and become brown, whereas lightly dyed fabrics turn yellow-gray.[13] However, both fabrics regain their color when placed in contact with oxygen. Similarly dyed fabrics exposed to sunlight in an ambient atmosphere loose their color and then regain it after storage in the dark. According to the chemical knowledge of the time, Prussian blue contained four atoms of iron *percyanide*, three atoms of iron *protocyanide*, and a certain amount of water. When exposed to the light, either in vacuum or in the atmosphere, Prussian blue was reduced in cyanogen and iron protocyanide. In contact with oxygen iron protocyanide was partially reoxidized in iron percyanide to yield Prussian blue.

The observations of Chevreul on fabrics dyed with Prussian blue do not completely apply to paint layers containing Prussian blue. Paint layers are indeed highly heterogeneous, consisting of a mixture of one or several pigments with an organic binder, painted on various substrates, *e.g.*, paper, wood, or canvas, substrates that could have been previously primed with a white preparation layer.

Today it is well understood that the intense blue of Prussian blue is produced by an intervalence charge transfer between the iron(II) and iron(III) ions when light is absorbed at *ca.* 700 nm. Thus, any color fading or color change corresponds to a disruption in the electron transfer pathways in Prussian blue, *i.e.*, the $Fe^{III}-N-C-Fe^{II}$ bonding pathways. In view of the known properties of Prussian blue, four mechanisms may typically affect this disruption in paint layers. These include (1) the reduction of Prussian blue, (2) the oxidation of Prussian blue, (3) ion exchange within the Prussian blue, and (4) substitution reactions within the Prussian blue.

The fading of Prussian blue in a paint layer could result from the electrochromic character of the pigment. As previously explained, Prussian blue can be either elec-

[13] Chevreul described the color as *gris nankin*.

trochemically oxidized to form an iron(III) ferricyanide, known as *Prussian yellow*, or reduced to form an iron(II) ferrocyanide, known as *Berlin white* or *Everitt's salt*. Thus the discoloration of a Prussian blue pigment could be due to a partial reduction of iron(III) to iron(II), in which some of the $Fe^{III}-N-C-Fe^{II}$ pathways would then become $Fe^{II}-N-C-Fe^{II}$ pathways and, thus, reduce the probability for intervalence charge transfer. Alternatively, the discoloration of the Prussian blue pigment could be due to a partial oxidation of iron(II) to iron(III) and similarly, the resulting $Fe^{III}-N-C-Fe^{III}$ pathway would also reduce the probability for intervalence charge transfer. These redox reactions have been extensively studied in electrochemically synthesized Prussian blue films both in the presence of an electrolyte and in the solid state.

However, the situation in paint layers is dramatically different and conclusions deduced from electrochemical studies are not directly applicable to Prussian blue pigments found in paintings. First, Prussian blue used as a pigment is not electrochemically prepared but usually results from a precipitation reaction between aqueous solutions of an iron(II) salt and a hexacyanoferrate(II) complex. As emphasized by Ellis *et al.* [62], the electrochromic behavior of Prussian blue is highly dependent upon its chemical preparation. Second, there must be a driving force to induce either the reduction or the oxidation, a driving force that does not involve the application of a voltage. The redox-reactions could be photo-induced. Photooxidation and photoreduction have been reported in nanoparticles containing both Prussian blue and a photoresponsive material, *e.g.*, the photoconductive CdS semiconductor or photochromic azobenzene molecules [46][63]. Such compounds can supply electrons upon UV/visible irradiation and induce redox processes in Prussian blue. However, such reactions in Prussian blue films or nanoparticles are reversible, whereas in paint layers a reversible fading is only observed in the short term; after a long exposure to light an irreversible color change occurs in paintings [58]. Moreover it is difficult to identify a compound in the paint layer that could play the role of the photoresponsive material.

Any ion exchange occurring in Prussian blue could also modify the probability for intervalence charge transfer. According to Ware [9][56], the color of cyanotypes can be tuned by insertion of metal cations in the lattice cavities of Prussian blue. For example the incorporation of nickel(II) ions slightly shifts the color to blue-green, whereas insertion of lead(II) ions, in the form of a solution of lead(II) acetate, shifts the color to violet-blue. For the latter lead is most likely incorporated as $Pb(OH)_2$. However such insertion of metal cations in cyanotypes occurs in aqueous solution and is probably less easily achieved in paint layers. Moreover, such a process leads to a subtle variation in the blue color, not to a discoloration.

Finally, the intervalence charge transfer could be disrupted due to a substitution reaction. In particular the substitution reaction of the weakly bonded nitrogen-coordinated iron(III) ions by other metal ions has been observed during the electrochemical oxidation of Prussian blue in aqueous solutions [64]. Another possible reaction would be the substitution of a CN^- ion by a water molecule, H_2O, leading to the formation of ferric aquapentacyanoferrate, $Fe^{III}[Fe^{II}(CN)_5(H_2O)]$. The formation of this compound has been observed during the photolysis of aqueous $Fe(CN)_6^{4-}$ solutions:

$$H_2O + [Fe^{II}(CN)_6]^{4-} \xrightarrow{h\nu} [Fe^{II}(CN)_5(H_2O)]^{3-} + CN^-.$$

The substitution is accompanied by a release of CN^- ions and an increase in the pH of the solution. This reaction is reversible if the aqueous $Fe^{II}(CN)_6^{4-}$ solutions are exposed to irradiation for a short time. A prolonged time of irradiation results in the formation of either $Fe(OH)_3$ in aerated basic solutions or Prussian blue in aerated acidic solutions [65][66].

In paint layers, because $Fe^{III}[Fe^{II}(CN)_5(H_2O)]$ is green, secondary reactions, such as other ligand substitutions or redox reactions, must occur in order to lead to a loss of color [58]. Electrochemical reduction of ferric aquapentacyanoferrate has been reported in a KCl solution and is described by the reversible redox reaction [67]:

$$Fe^{III}[Fe^{II}(CN)_5(H_2O)] + K^+ + e^- \rightleftharpoons KFe^{II}[Fe^{II}(CN)_5(H_2O)].$$

Such redox reactions have not been investigated in the solid state and are expected to be less easily achieved in paint layers because of their poor ionic conduction.

None of the above hypotheses is fully satisfactory in explaining the discoloration processes of Prussian blue in paint layers. The main objective of this thesis is thus to clearly identify the mechanism or mechanisms involved in the fading of the Prussian blue pigment in paintings.

Chapter 2

Evolution of the Preparative Methods for Prussian Blue

Summary. *Prussian blue pigments were prepared according to modern syntheses, which are based on the precipitation reaction between an iron salt and a hexacyanoferrate complex, and to ancient syntheses, which involved the calcination of dried blood for producing the hexacyanoferrate complex. The pigment particle size and the degree of ordering of the* $[Fe(CN)_6]^{4-}$ *vacancies in the Prussian blue lattice were identified as the two parameters that strongly vary with the type of modern syntheses. The Prussian blue pigments prepared according to the rather empirical ancient syntheses often contain an undesirable iron containing reaction product, identified as nanocrystalline ferrihydrite.*

Contents

2.1 Historical overview

The original recipe for producing Prussian blue was published in London in 1724 in the *Philosophical Transactions* by Woodward [68]. Dried cattle blood was calcinated with potassium hydrogen tartrate, alum, and vitriol. The resulting solution was then diluted in boiling water and treated with *Spiritus Salis*, *i.e.*, hydrochloric acid. After washing with water and filtration a deep blue pigment was obtained. At that time neither the chemical composition of Prussian blue nor the presence in blood of hexacyanoferrate and cyano groups, essential for the synthesis of the pigment, were known. It was thus very difficult to control the synthesis and the underlying chemical reaction. The proportions of reagents, the nature of the starting materials, and the temperature were among the many parameters which color makers could vary to produce a variety of hues and handling properties[1] of Prussian blue. The numerous alternative preparative methods explain the rich terminology of Prussian blues named sometimes according to the producer's name and at other times according to the place of manufacture.

In the mid nineteenth century it became possible to produce in bulk the potassium hexacyanoferrate complex from gas purification products [69]. Consequently, Prussian blue could be prepared by a completely inorganic manufacturing process, that we will now call *modern methods*, in contrast to the ancient methods that used an organic starting material. The modern methods are based on the precipitation reaction between an iron salt and a hexacyanoferrate complex and are of two types, direct and indirect, see Figure 2.1.

The direct method is a one-step process and consists of mixing a solution of an iron(III) salt with a solution of a hexacyanoferrate(II) salt. The deep blue precipitate is filtered and carefully washed with distilled water. Alternatively, a mixture of solutions of an iron(II) salt and a hexacyanoferrate(III) salt produces the so-called *Turnbull blue* considered to be a ferrous ferricyanide. In the 1960's Mössbauer spectroscopy and X-ray diffraction revealed that both reactions yield the same compound, *i.e.*, iron(III) hexacyanoferrate(II), *cf.* **Section 1.1.3**. If the iron salt is present in excess the precipitate is the insoluble variety of the pigment whereas, if the reagents are mixed in a 1:1 molar ratio or with the hexacyanoferrate present in excess, the *soluble* variety of Prussian blue is obtained.

The indirect method is the most commonly used process in the pigment industry. It is a two-step process based on the reaction between an iron(II) salt and a hexacyanoferrate(II) salt. From the solution precipitates the so-called *Berlin*

[1] Besides its coloring properties, a pigment is characterized by its chemical composition, moisture content, particle size, density, and hardness. These characteristics influence the handling properties of the pigment, such as its compatibility and dispersibility in a binder.

white, the ferrous ferrocyanide, $K_2Fe^{II}Fe^{II}(CN)_6$, which is treated with a powerful oxidizing agent such as hydrogen peroxide, or an alkali metal chlorate or chromate, to give Prussian blue. Depending on the starting reagent that is in excess, the soluble or insoluble Prussian blue is obtained.

I have synthesized Prussian blue according to modern and ancient preparative methods. Because the modern methods are expected to yield a purer Prussian blue than the ancient methods, I first describe the former and then the latter. As previously discussed, the degradation of Prussian blue is correlated with the preparative method. The main objective of **Sections 2.2** and **2.3** is thus to identify the original spectral and physical parameters that vary with the type of synthesis and that could influence the permanence of Prussian blue in paint layers.

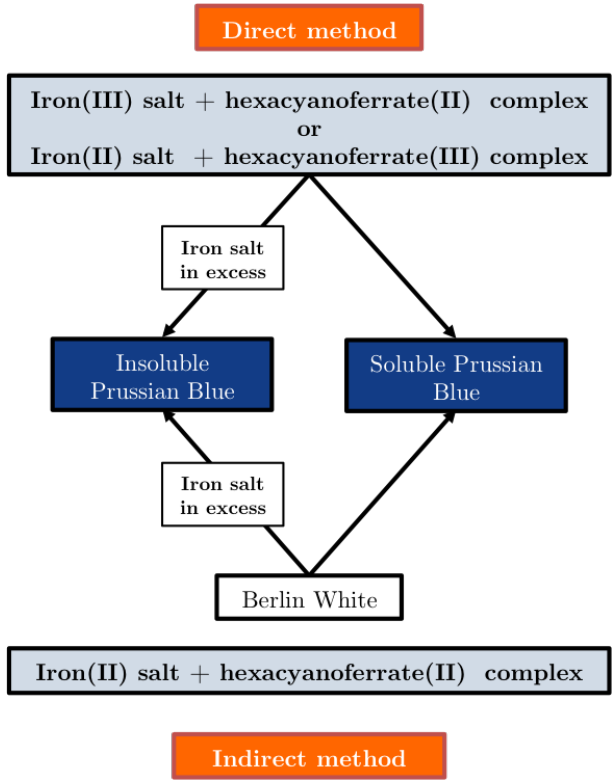

Figure 2.1 Schematic representation of the direct and indirect modern methods used to produce Prussian blue.

2.2 Modern syntheses

In this section the different types of modern syntheses that have been reproduced herein are presented. Next, the thorough characterization of both the so-obtained and commercial Prussian blues is described.

2.2.1 Preparative methods

I distinguish three types of modern syntheses, the synthesis of bulk Prussian blue reported in scientific papers, the synthesis used by the pigment industry and described in patents, and the synthesis of well-crystallized Prussian blue. Unless otherwise stated, all reagents used herein for the synthesis of Prussian blue were of reagent grade quality and obtained from Sigma-Aldrich, Steinheim, Germany.

Numerous scientific papers report the synthesis of bulk Prussian blue. Most of them date back to the 1960's and 1970's, before the interest in both electrochemically synthesized thin films of Prussian blue and Prussian blue monodispersed nanoparticles with specific magnetic, optical, and electric properties, grew. These types of syntheses are not considered herein because Prussian blue in powder is required to prepare paint layers. The usual method for synthesizing bulk Prussian blue is the direct method, consisting of mixing aqueous solutions of an iron(II) or iron(III) salt and hexacyanoferrate(III) or hexacyanoferrate(II) salts. The iron salt can be iron(II) or iron(III) chloride [70], sometimes prepared either by dissolving standard iron wire in hot concentrated $HClO_4$ [18] or by adding iron powder in hydrochloric acid [26]. The use of iron(II) or iron(III) sulfate was also reported [27].

The iron(II) or iron(III) cyanide complexes are either $K_4Fe(CN)_6{\cdot}3H_2O$ or $K_3Fe(CN)_6{\cdot}3H_2O$, respectively, depending on the iron salt used. Some authors recommend mixing the reagents by shaking before sprinkling them into water [70] in order to increase the particle size of Prussian blue, whereas others authors [26] proposed slowing the reaction by using an indirect method. Iron(II) chloride and ferrocyanide solutions were mixed to yield Berlin white. The precipitate was then rapidly oxidized by boiling the solution in air. Whatever the type of synthesis, *i.e.*, direct or indirect, the Prussian blue is thoroughly washed after precipitation with deionized water and possibly with ethanol, and then separated by centrifugation or by filtration. Atmospheric conditions and temperature during the synthesis are generally not specified; the synthesis was therefore assumed to occur in an ambient atmosphere at room temperature.

Other syntheses are described in patents for the pigment, printing ink, and paint industries. The first patents on the synthesis of Prussian blue date from

the 1850's, when the bulk production of potassium ferrocyanide became feasible [69]. From the following years to the present numerous patents have been published; a *Google Patent* search finds about 6700 patents, containing the key words *iron blue* and/or Prussian blue that have been issued since 1880 [71], whereas the United State Patent Office registered about 5600 patents, issued after 1976, with the same search criteria [72]. The industrial process leads to the production of an inexpensive high quality pigment, *i.e.*, a pigment with a pure color shade and good handling properties. These processes are usually based on the indirect method and consist of three essential steps [73], (1) the precipitation of Berlin white through the reaction of an iron(II) salt with an alkali hexacyanoferrate(II) complex, (2) the ageing or digestion of the Berlin white, and (3) the oxidation of Berlin white with an oxidizing agent to yield Prussian blue.

The synthesis generally occurs under an inert atmosphere or under a nitrogen stream in order to reduce the pre-oxidation of Berlin white [74]. The precipitate is, however, never strictly white but rather is light blue because a partial premature oxidation into Prussian blue is unavoidable [73]. The starting reagents are diverse. Iron(II) sulfate, as the iron salt, and potassium or sodium ferrocyanide, as the hexacyanoferrate(II) complex, were usually preferred because of their availability [75]. The precipitation reaction typically occurs at a temperature between 20 and 60°C. Berlin white is aged at the boiling temperature of water for a sufficiently long period, typically 90 to 120 minutes [76]. The pH of the slurry is adjusted to be between 1 to 6 by adding hydrochloric acid. Berlin white is then oxidized at a lower temperature, between 30 and 50°C, with sodium chlorate, sodium chromate, hydrogen peroxide, or potassium chlorate [77][78][79]. In order to decrease the production cost, potassium ferrocyanide has been partially or completely replaced by the less expensive ammonium salt or sodium salt. The latter is however said to yield a lower quality of Prussian blue shade of color [77]. Prussian blue can also be prepared with a calcium hexacyanoferrate, the blue precipitate is then washed with water to remove the calcium ions and finally, sodium, potassium, or ammonium cyanide is added to the pigment in order to improve its color properties [80][81].

From the literature and from patents, the parameters that apparently influence the properties of a Prussian blue pigment, such as its apparent solubility, color shade, or particle size, have been identified. They are the nature of the starting reagents, the relative proportion of the starting reagents, the atmosphere, the intermediate formation of Berlin white, and the ageing of the precipitate before oxidation. Syntheses of Prussian blue were thus carried out by varying these parameters. The general procedure is detailed below. The syntheses under a nitrogen atmosphere were carried out at the Laboratory of Macromolecular Chemistry and Organic Materials, in the Chemistry Department at the University of Liège, with

the help of Dr. B. Grignard. A blue precipitate was successfully obtained in all attempted syntheses. Table 2.1 summarizes the syntheses and the labeling of the samples.

The starting reagents were dissolved in deionized water in the appropriate relative concentration. They were mixed together under magnetic stirring. In case of an indirect process, Berlin white was formed and aged for two hours at 90 °C. Before oxidation the solution was acidified by adding hydrochloric acid. An excess of hydrogen peroxide was added to accelerate and complete the oxidation of Berlin white into Prussian blue. Filtration was difficult to achieve because of the tendency of Prussian blue to form colloidal solutions and thus centrifugation was preferred. The precipitate was thoroughly washed with deionized water and collected by centrifugation. The pigment was oven dried at approximately 55 °C for one hour and then ground into a fine powder.

The syntheses detailed in Table 2.1 produce Prussian blue as a fine precipitate. The colloidal character of Prussian blue has been the major difficulty in determining the exact composition and crystal structure of Prussian blue. In 1977 Buser *et al.* succeeded in growing Prussian blue single-crystals [12]. They prepared a solution of iron(II) and $[Fe^{II}(CN)_6]^{4-}$ in concentrated hydrochloric acid and let the crystals grow by very slow diffusion of water vapor into the solution. After eight weeks they collected cubic crystals as large as 0.15 mm on a side.

The crystal structure of Prussian blue is notoriously complex because of lattice defects and its various degrees of hydration. A new model has recently been proposed for the crystal structure of soluble Prussian blue [14]. Because uncertainties remain and because trapped ions or molecules in the cavities of the open framework of Prussian blue may play a role in its fading, I decided to reproduce the Buser synthesis and adapt it in order to produce a soluble well-crystallized Prussian blue. The procedure is described below.

Insoluble crystallized Prussian blue was prepared by separately dissolving 7.5 mmol of $FeCl_2{\cdot}4H_2O$ and 2.5 mmol of $K_4Fe(CN)_6{\cdot}3H_2O$ in 35 mL of deionized water. The two solutions were added to 430 mL of HCl (36 %) in order to obtain 500 mL of a solution containing 10 mol/L of HCl. The beaker containing this solution and another beaker containing approximately 500 mL of water were both placed in a vacuum desiccator whose stopcock was left open. The diffusion of air into the solution slowly oxidizes the iron(II) ions. After eight weeks in the dark, cubic crystals were collected by filtration. They were thoroughly washed with 2 M HCl, 0.1 M HCl, and finally with deionized water until the absence of turbidity was observed upon addition of $AgNO_3$. The sample is labelled A80.

Table 2.1 Labels and details of the synthesis of bulk Prussian blues

Label[a]	**Starting Reagents**			**Precipitation**				**Final product**
	Nature	C, mol L^{-1}	Atmosphere	T,°C	Precipitate	Ageing, h	Oxidizer	Expected composition
B148	$FeCl_2$	0.40	N_2	50	Berlin white	2	H_2O_2	$Fe_4[Fe(CN)_6]_3{\cdot}xH_2O$
	$K_4Fe(CN)_6{\cdot}3H_2O$	0.10						
B149	$FeCl_2$	1.00	N_2	50	Berlin white	2	H_2O_2	$Fe_4[Fe(CN)_6]_3{\cdot}xH_2O$
	$K_4Fe(CN)_6{\cdot}3H_2O$	0.25						
B139	$FeCl_3{\cdot}3H_2O$	1.00	N_2	RT	Prussian blue	0	–	$Fe_4[Fe(CN)_6]_3{\cdot}xH_2O$
	$K_4Fe(CN)_6{\cdot}3H_2O$	0.25						
A39	$FeCl_3{\cdot}6H_2O$	0.24	ambient	RT	Prussian blue	0	–	$Fe_4[Fe(CN)_6]_3{\cdot}xH_2O$
	$(NH_4)_4Fe(CN)_6{\cdot}3H_2O$	0.08						
A148	$FeCl_2$	0.10	N_2	50	Berlin white	2	H_2O_2	$KFe[Fe(CN)_6]{\cdot}xH_2O$
	$K_4Fe(CN)_6{\cdot}3H_2O$	0.10						
A147	$FeCl_2$	0.10	N_2	50	Berlin white	0	H_2O_2	$KFe[Fe(CN)_6]{\cdot}xH_2O$
	$K_4Fe(CN)_6{\cdot}3H_2O$	0.10						
A180	$FeCl_2$	0.10	ambient	50	Berlin white	2	H_2O_2	$KFe[Fe(CN)_6]{\cdot}xH_2O$
	$K_4Fe(CN)_6{\cdot}3H_2O$	0.10						
B63	$FeCl_2$	0.10	ambient	50	Berlin white	0	H_2O_2	$KFe[Fe(CN)_6]{\cdot}xH_2O$
	$K_4Fe(CN)_6{\cdot}3H_2O$	0.10						
B147	$FeSO_4{\cdot}7H_2O$	0.10	N_2	50	Berlin white	0	H_2O_2	$KFe[Fe(CN)_6]{\cdot}xH_2O$
	$K_4Fe(CN)_6{\cdot}3H_2O$	0.10						
B137	$FeCl_3{\cdot}6H_2O$	0.10	N_2	50	Prussian blue	2	–	$KFe[Fe(CN)_6]{\cdot}xH_2O$
	$K_4Fe(CN)_6{\cdot}3H_2O$	0.10						
B138	$FeCl_3{\cdot}3H_2O$	0.10	N_2	RT	Prussian blue	0	–	$KFe[Fe(CN)_6]{\cdot}xH_2O$
	$K_4Fe(CN)_6{\cdot}3H_2O$	0.10						
B142	$FeCl_2$	0.10	N_2	RT	Turnbull's blue	0	–	$KFe[Fe(CN)_6]{\cdot}xH_2O$
	$K_3Fe(CN)_6$	0.10						
A65	$FeCl_3{\cdot}6H_2O$	0.10	ambient	RT	Prussian blue	0	–	$KFe[Fe(CN)_6]{\cdot}xH_2O$
	$K_4Fe(CN)_6{\cdot}3H_2O$	0.10						
B145	$FeCl_2$	0.10	N_2	50	Berlin white	2	H_2O_2	$NaFe[Fe(CN)_6]{\cdot}xH_2O$
	$Na_4Fe(CN)_6{\cdot}3H_2O$	0.10						
B146	$FeCl_2$	0.10	N_2	50	Berlin white	2	H_2O_2	$NH_4Fe[Fe(CN)_6]{\cdot}xH_2O$
	$(NH_4)_4Fe(CN)_6{\cdot}3H_2O$	0.10						
B140	$FeCl_3{\cdot}6H_2O$	0.10	N_2	RT	Prussian blue	0	–	$NH_4Fe[Fe(CN)_6]{\cdot}xH_2O$
	$(NH_4)_4Fe(CN)_6{\cdot}3H_2O$	0.10						
B141	$FeCl_3{\cdot}6H_2O$	0.10	N_2	RT	Prussian blue	0	–	$NaFe[Fe(CN)_6]{\cdot}xH_2O$
	$Na_4Fe(CN)_6{\cdot}3H_2O$	0.10						
A43	$FeCl_2$	0.10	ambient	RT	Berlin white	0	H_2O_2	$NH_4Fe[Fe(CN)_6]{\cdot}xH_2O$
	$(NH_4)_4Fe(CN)_6{\cdot}3H_2O$	0.10						

[a]The labels refer to the specific page number of my laboratory notebooks where the details of synthesis are given.

The procedure used to prepare soluble well crystallized Prussian blue containing K^+ ion is identical to that for insoluble Prussian blue, except for the proportion of starting reagents. Equimolar quantities, namely 5.0 mmol of $FeCl_2{\cdot}4H_2O$ and 5.0 mmol of $K_4Fe(CN)_6{\cdot}3H_2O$ were used. The ageing time was reduced to three weeks. The label of the sample is A74. Similarly soluble well crystallized Prussian blue containing NH_4^+ was synthesized by using 5.0 mmol of $FeCl_2{\cdot}4H_2O$ and 5.0 mmol of $(NH_4)_4Fe(CN)_6{\cdot}xH_2O$, obtained from Fluka with a purity of $\geq$ 85 %. The ageing time was three weeks. The sample is labeled A76.

Commercial Prussian blues were obtained in order to compare their properties with those of the laboratory-synthesized Prussian blues, see Table 2.2. Insoluble Prussian blue and soluble Prussian blue were purchased from Sigma Aldrich, Steinheim, Germany. Prussian blues, sold for artistic purpose, were obtained from two artist materials suppliers, Winsor & Newton, Harrow, Middlesex, England, and Blockx SA, Nandrin, Belgium. The origin of the Prussian blue obtained from Winsor & Newton could not be identified, whereas the Prussian blue obtained from Blockx is a microcrystalline ammonium iron(III) hexacyanoferrate(II) designed for use in the coloration of fungicides and sold by Degussa, Frankfurt, Germany, under the registration VOSSEN-BLAU® 750 LS. Finally, a Prussian blue stored since 1948 in the inventories of the Royal Institute for Cultural Heritage, Brussels, Belgium, and manufactured by Winsor & Newton, was obtained.

Table 2.2 Labels of commercially available Prussian blues

Synthesis[a]	**Origin**	**Expected composition**
C01	Winsor & Newton	$Fe_4[Fe(CN)_6]_3{\cdot}xH_2O$
C02	From the KIK-IRPA inventories From Winsor & Newton	unknown
C03	Sigma-Aldrich	$Fe_4[Fe(CN)_6]_3{\cdot}xH_2O$
C04	Provided by Blockx Produced by Degussa	$NH_4Fe[Fe(CN)_6]{\cdot}xH_2O$
C05	Sigma-Aldrich (Fluka)	$KFe[Fe(CN)_6]{\cdot}xH_2O$

[a] C stands for commercial. The numbering is arbitrary.

In total twenty-one laboratory-synthesized Prussian blues, including three well-crystallized Prussian blues, and five commercial Prussian blues were at my disposal for analysis. In order to help the reader, I used a color code to distinguish the varieties of Prussian blue. In plots, insoluble Prussian blues are displayed in blue, soluble Prussian blues containing potassium ions in orange, soluble Prussian blues containing ammonium ions in purple, and finally soluble Prussian blues containing sodium ions in pink. In addition to the label, some parameters relative to the synthesis for laboratory-synthesized Prussian blues are also given as *DM* or

IM, for the direct method or the indirect method, *air* or N_2, for the atmosphere under which the synthesis occurred, *no ageing* or *2 h ageing* for the ageing time of the precipitate. The following subsections are devoted to the characterization of these samples. The goal is to identify the role that the various parameters in the synthesis play in determining the properties of Prussian blue.

2.2.2 Analytical characterization

Although each attempted synthesis has led to the formation of a blue precipitate, the composition of this blue precipitate as well as the absence of any other undesirable reaction products must be verified. In particular the following questions must be answered before any further analysis. (1) Is the blue precipitate Prussian blue, *i.e.*, a ferric ferrocyanide complex? (2) Which variety – soluble or insoluble – of Prussian blue is the precipitate? (3) What is the degree of hydration? (4) Are there any impurities present in the sample?

Iron-57 transmission Mössbauer spectroscopy is the technique of choice to undoubtedly identify a ferric ferrocyanide complex as well as to determine if other possible iron compounds are present. Mössbauer spectroscopy is an iron selective non-destructive technique that does not require a complex sample preparation. The Mössbauer spectrum provides bulk information and is relatively easy to interpret on the basis of published data on Prussian blue. Because of the sensitivity of the Mössbauer spectrum to the iron oxidation state, the distinction between the soluble and insoluble forms of Prussian blue, based on the iron(II) to iron(III) ratio should be possible. However a Mössbauer spectrum does not provide a quantitative elemental composition and therefore atomic absorption and flame emission spectroscopy were used to measure the exact iron and potassium weight percent in selected Prussian blues. The degree of hydration was evaluated by thermogravimetric analysis. Then particle induced X-ray emission analysis was performed to detect any impurities present in the samples.

Identification

Mössbauer spectroscopy was used as a screening technique to confirm the formation of Prussian blue and identify its variety. The physical concepts of the method, the description of the spectrometer, and relevant experimental details are given in **Appendix B.2.3**.

The Mössbauer spectra obtained at 295 K are shown in Figures 2.2 and 2.3. All spectra were fitted with two Lorentzian components, either two singlets or

one singlet and one doublet. Two singlets were used when fits with doublets lead to quadrupole splittings that were smaller than the experimental line width or even smaller than the minimum natural line width of 0.195 mm/s. The resulting spectral parameters, *i.e.*, two isomer shifts, δ^{II} and δ^{III}, two full line widths at half-maximum, Γ^{II} and Γ^{III}, one quadrupole splitting, $\Delta E_Q^{\mathrm{III}}$, and one percent area, A^{II}, with $A^{\mathrm{III}} = 100 - A^{\mathrm{II}}$, are given in Table 2.3.

The isomer shift is the shift of the center of the spectral component from zero velocity, defined as the center of absorption of α-iron powder. The isomer shift[2] results from the overlap of the non-point iron-57 nuclear charge distribution and the s-electron density at the nucleus. The isomer shift is proportional to the difference between the s-electron density at the nucleus in the absorber and in the standard. Iron(II) and iron(III) ions with formal $3d^6$ and $3d^5$ electronic configurations exhibit different isomer shifts not because of a difference in their ns-electronic populations but because the additional $3d$ electron in iron(II) provides additional screening of the s-electron density at the nucleus. As a general rule, the typical room temperature iron(II) and iron(III) isomer shifts are as follows. High-spin iron(II) ions exhibit isomer shifts between 0.8 and 1.2 mm/s, whereas low-spin iron(II) ions exhibit isomer shifts between 0.0 and 0.3 mm/s. High-spin and low-spin iron(III) ions both exhibit isomer shifts between 0.0 and 0.5 mm/s. A comparison of these shifts with the natural line width of 0.195 mm/s indicates that the identification of high-spin iron(II) ions is very easy and the distinction between the other ionic forms is more difficult. The identification becomes even more difficult in the presence of covalent metal-ligand bonding. For example, $[\mathrm{Fe^{II}(CN)_6}]^{4-}$ and $[\mathrm{Fe^{III}(CN)_6}]^{3-}$ exhibit very similar isomer shifts ranges of -0.05 to 0.00 and $+0.05$ to $+0.08$ mm/s, respectively [82]. Both ions have quasi-identical charge states because the cyanide ligands, which are strongly bond to the iron nucleus, shield the nonbonding t_{2g} electrons [27]. The observation that interelectronic repulsion is lower in complexes than in free ions is called *nephelauxetic* or *cloud-expanding effect* [19].

Because Prussian blue is a ferric ferrocyanide complex, the two components in its Mössbauer spectrum can be assigned as follows. The singlet with an isomer shift of approximately –0.1 mm/s is assigned to the low-spin iron(II) ion and the singlet or doublet with an isomer shift of approximately 0.4 mm/s is assigned to the high-spin iron(III) ion.

[2]Mathematical expressions for the isomer shift and the quadrupole splitting are given in **Appendix B.2.3**.

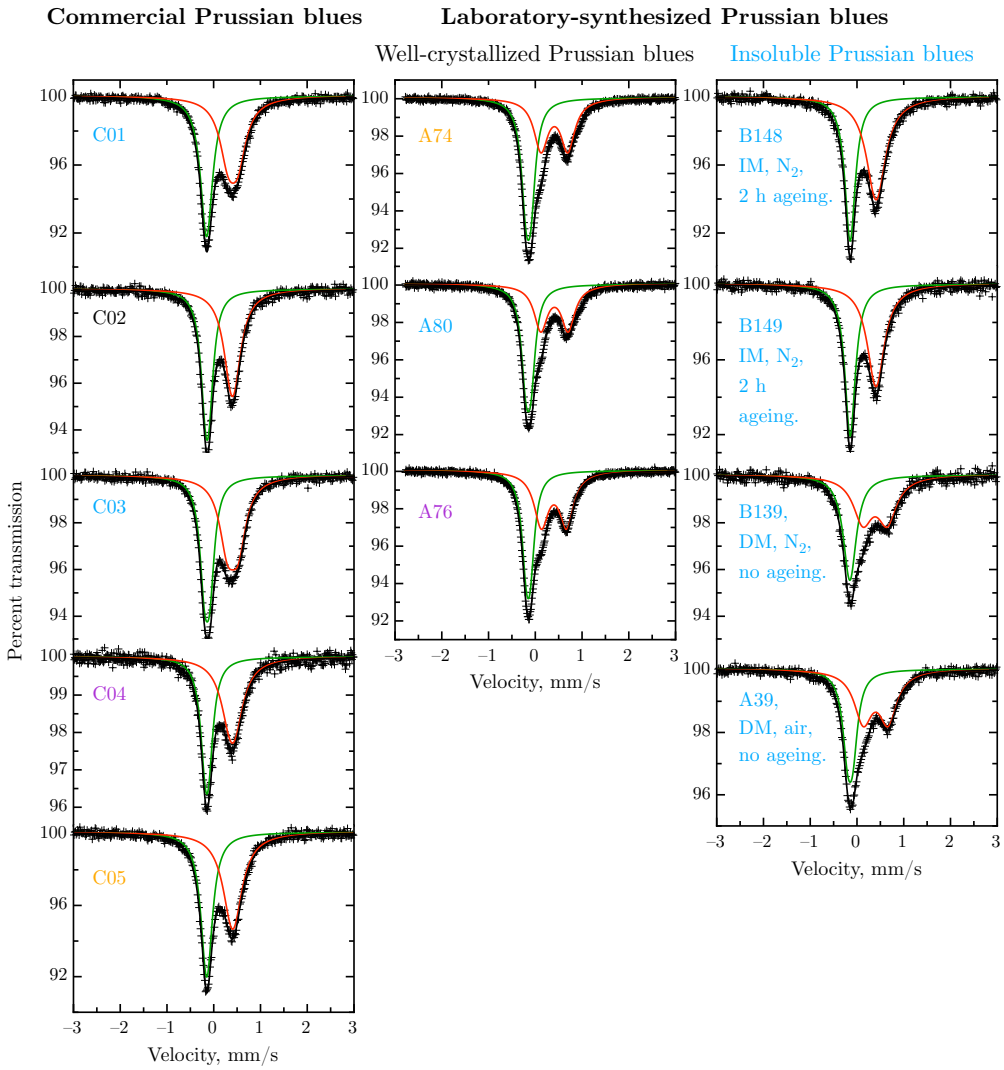

Figure 2.2 The 295 K Mössbauer spectra of commercial and laboratory-synthesized well-crystallized and insoluble Prussian blues. The green and red solid lines represent the iron(II) and iron(III) spectral components, respectively.

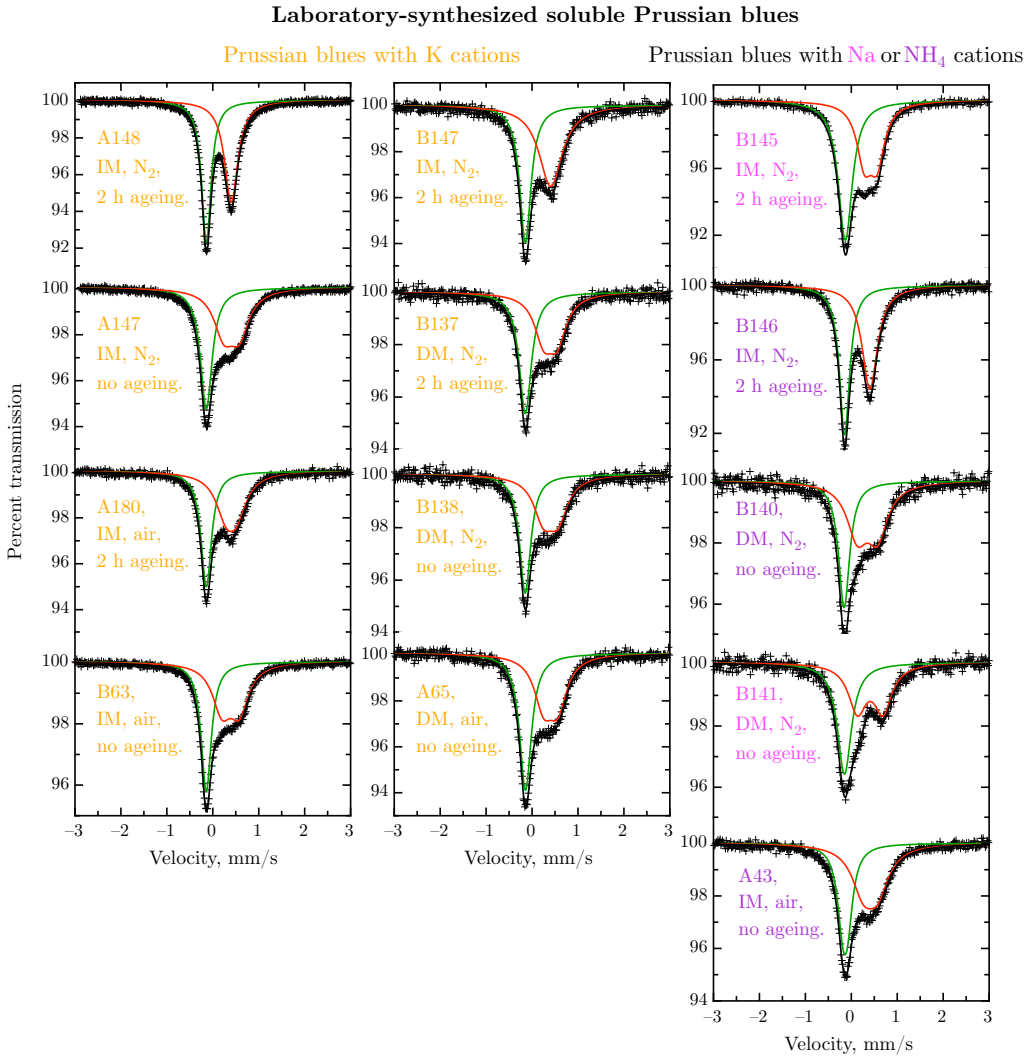

Figure 2.3 The 295 K Mössbauer spectra of soluble laboratory-synthesized Prussian blues. The green and red solid lines represent the iron(II) and iron(III) spectral components, respectively.

Table 2.3 Mössbauer spectral parameters of commercial and laboratory-synthesized Prussian blues at 295 K

Labels	Synthesis	δ^{II}, mm/s[a]	Γ^{II}, mm/s[b]	A^{II}, %[c]	δ^{III}, mm/s[a]	Γ^{III}, mm/s[b]	ΔE_Q^{III}, mm/s
C01		-0.150(1)	0.312(3)	48(1)	0.415(2)	0.44(1)	–
C02		-0.138(1)	0.276(3)	49(1)	0.405(2)	0.41(1)	–
C03		-0.139(1)	0.306(1)	49(1)	0.413(3)	0.403(1)	0.226(1)
C04		-0.147(1)	0.28(1)	47(1)	0.401(3)	0.50(1)	–
C05		-0.150(1)	0.300(4)	48(1)	0.406(2)	0.49(1)	–
A74	IM, HCl, $\sim$ 500 h ageing	-0.153(1)	0.282(2)	48(1)	0.395(2)	0.404(3)	0.607(2)
A80	IM, HCl, $\sim$ 1350 h ageing	-0.154(1)	0.278(2)	48(1)	0.393(2)	0.405(5)	0.622(3)
A76	IM, HCl, $\sim$ 500 h ageing	-0.151(1)	0.269(2)	47(3)	0.396(1)	0.376(3)	0.545(2)
B148	IM, N_2, 2 h ageing	-0.146(1)	0.270(4)	43(1)	0.409(2)	0.49(1)	–
B149	IM, N_2, 2 h ageing	-0.146(1)	0.271(4)	47(1)	0.406(2)	0.44(1)	–
B139	DM, N_2, no ageing	-0.153(3)	0.34(1)	45(1)	0.39(1)	0.50(2)	0.52(1)
A39	DM, air, no ageing	-0.147(1)	0.310(4)	44(1)	0.392(5)	0.47(1)	0.54(1)
A148	IM, N_2, 2 h ageing	-0.139(5)	0.255(1)	49(1)	0.400(10)	0.356(2)	–
A147	IM, N_2, no ageing	-0.141(5)	0.29(1)	45(3)	0.404(3)	0.52(1)	0.340(4)
A180	IM, air, 2 h ageing	-0.141(1)	0.273(4)	45(1)	0.400(4)	0.53(2)	0.23(1)
B63	IM, air, no ageing	-0.144(5)	0.24(1)	41(3)	0.377(4)	0.51(1)	0.385(5)
B147	IM, N_2, 2 h ageing	-0.145(2)	0.30(1)	45(1)	0.408(5)	0.62(1)	–
B137	DM, N_2, 2 h ageing	-0.146(3)	0.32(1)	49(2)	0.40(1)	0.48(3)	0.30(1)
B138	DM, N_2, no ageing	-0.149(2)	0.29(1)	46(2)	0.41(1)	0.52(3)	0.32(1)
A65	DM, air, no ageing	-0.142(2)	0.31(1)	48(1)	0.41(1)	0.49(2)	0.31(1)
B145	IM, N_2, 2 h ageing	-0.130(2)	0.367(4)	54(1)	0.423(3)	0.40(1)	0.277(5)
B146	IM, N_2, 2 h ageing	-0.145(1)	0.269(3)	49(1)	0.404(2)	0.41(1)	–
B140	DM, N_2, no ageing	-0.154(3)	0.29(1)	40(3)	0.35(2)	0.55(3)	0.44(2)
B141	DM, N_2, no ageing	-0.149(3)	0.37(1)	49(2)	0.41(1)	0.47(2)	0.56(1)
A43	IM, air, no ageing	-0.131(2)	0.35(1)	47(1)	0.43(1)	0.57(2)	0.30(1)

[a]The isomer shift, δ, is referred to α-iron powder at 295 K. [b]Γ is the full line width at half-maximum. [c]$A^{III} = 100 - A^{II}$.

The high-spin iron(III) component is a doublet, with a quadrupole splitting of 0.25 to 0.62 mm/s. The quadrupole splitting results from the interaction between the iron-57 excited state nuclear quadrupole moment and the electric field gradient created at the nucleus by the non-spherical charge distribution in its environment. The quadrupole splitting can be qualitatively interpreted as a measure of the charge asphericity in the iron nuclear environment. In Prussian blue as in other cyanide complexes, the electric field gradient has two contributions, the lattice contribution from the ionic charges of the iron neighboring ions and the valence electronic contribution from the $3d$ electrons of the iron ion. Because of the symmetry around the low-spin iron(II) ion, the lattice contribution is zero and, because the t_{2g} orbitals are each fully occupied by two electrons with antiparallel spins, the valence electronic contribution is also zero. Hence, a singlet is observed for the low-spin iron(II) component. Because in the high-spin iron(III) ion the five $3d$ orbitals are all equally occupied with one electron, the electronic contribution is zero and there is only a small lattice contribution to the electric field gradient. Hence, a doublet with a small quadrupole splitting is observed for the high-spin iron(III) component.

The values in Table 2.3 and the line shape profiles in Figures 2.2 and 2.3 clearly show that the iron(III) quadrupole splitting shows a strong dependency upon the preparative method, a dependency that is emphasized in Figure 2.4. The laboratory-synthesized Prussian blues whose synthesis included an ageing time of Berlin white of two hours, *i.e.*, B148, B149, A148, A180, B147, B145, and B146, have a smaller than 0.3 mm/s iron(III) quadrupole splitting. These small values are comparable to those observed for the commercial Prussian blues. Well-crystallized Prussian blues, *i.e.*, A74, A76, and A80, exhibit a large quadrupole splitting, that may be attributed to the ordering of vacancies in the crystal structure. At this point of the discussion it is not clear why the other laboratory-synthesized Prussian blues, *i.e.*, B139, A39, B63, A147, B137, B138, A65, B140, B141, and A43 have a relatively large quadrupole splitting in comparison with the commercial Prussian blues.

Another interesting spectral parameter is the iron(II) percent area, A^{II}, because the iron(III) to iron(II) ratio is different for soluble and insoluble Prussian blues, *i.e.*, one for the soluble and 4/3 for the insoluble form, see Figure 2.5. The experimental ratio are, however, quite different from the expected values, for both commercial and laboratory-synthesized Prussian blues.

It should be emphasized that spectral parameters are temperature dependent. Therefore, the spectra have been recorded at low temperature for some Prussian blues and the temperature dependence of their spectral parameters has been studied, see Figure 2.6. As the temperature decreases from 295 to 85 K, both isomer

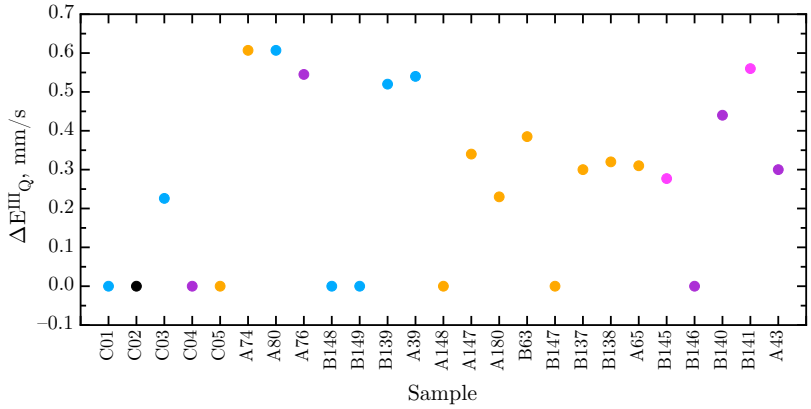

Figure 2.4 The quadrupole splitting ΔE_Q of iron(III) for all Prussian blues. The $\Delta E_Q^{\mathrm{III}}$ strongly varies according to the method of preparation. The error bars on the values are smaller than the size of the data points.

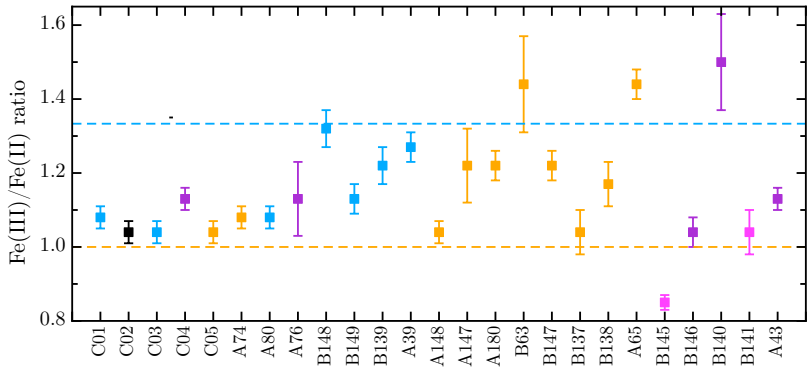

Figure 2.5 The iron(III) to iron(II) ratio for all Prussian blues. The orange and blue dotted lines indicate the expected values of 1.0 for the soluble, and 4/3 for the insoluble Prussian blue ratios, respectively. The error bar corresponds to the error propagation of the uncertainties on A^{II}.

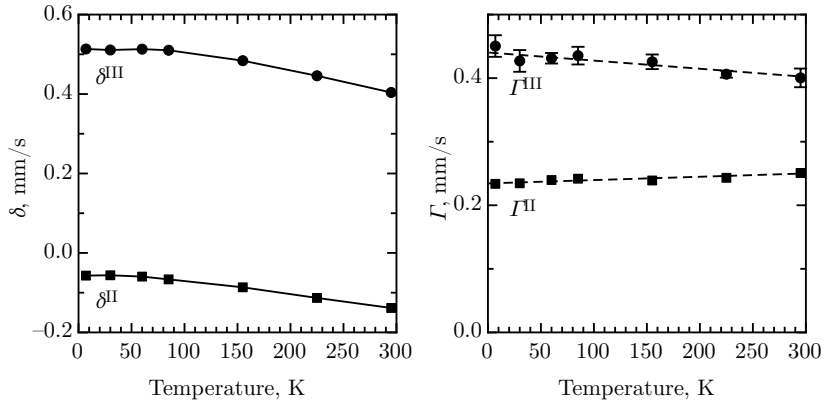

Figure 2.6 The temperature dependence of the spectral parameters for the commercial Prussian blue, C02. Except for the line width of iron(III), the error bars are smaller than the size of the data points. The dashed lines correspond to a linear best fit for the line width.

shifts become more positive as a result of the second-order Doppler shift. In contrast, the line widths are essentially temperature independent and the iron(III) quadrupole splitting remains zero at all temperatures. Below 5 K Prussian blue becomes ferromagnetic, see **Section 1.1.5**, resulting in a complex, magnetically split, Mössbauer spectrum. This splitting results from the interaction between the nuclear magnetic moment and the magnetic field generated by the electrons. This magnetic behavior at low temperature will not be discussed herein.

In conclusion, the Mössbauer spectra show that ferric ferrocyanide complexes have been synthesized. However their observed iron(III) to iron(II) ratio does not always correspond to the expected value based on the chemical formulae of insoluble and soluble Prussian blues. Quantitative chemical analyses are required to understand these differences, see below. Moreover large variations in the iron(III) quadrupole splitting are observed depending on the sample preparative method. Because the quadrupole splitting depends upon the symmetry of the charge distribution around the iron(III) nucleus, both the crystal structure and local ordering must be studied, as is discussed in **Sections 2.2.3** and **2.2.4**.

Elemental composition

The expected iron, potassium, and water weight % contents in the insoluble, $Fe_4[Fe(CN)_6]_3{\cdot}xH_2O$, and the soluble, $KFe[Fe(CN)_6]{\cdot}xH_2O$, and $NH_4Fe[Fe(CN)_6]{\cdot}xH_2O$, Prussian blues are given in Table 2.4. The observed weight % iron and potassium contents in the commercial and laboratory-synthesized Prussian blues were deter-

Table 2.4 Iron, potassium, and water weight % contents calculated from the theoretical chemical formulae of insoluble and soluble Prussian blues, as a function of hydration, x.

Theoretical formulae	**Fe, wt %**	**K, wt %**	**H_2O, wt %**
$KFe[Fe(CN)_6]\cdot xH_2O$			
$x = 1$	34.39	12.04	5.54
$x = 5$	28.15	9.85	22.68
$NH_4Fe[Fe(CN)_6]_3\cdot xH_2O$			
$x = 1$	36.78	–	5.93
$x = 5$	29.73	–	23.96
$Fe_4[Fe(CN)_6]_3\cdot xH_2O$			
$x = 14$	35.18	–	22.68
$x = 16$	34.08	–	25.11

mined by atomic absorption and flame emission spectroscopy with an accuracy of 0.01 weight %, respectively. The measurements were carried out by B. Belot and J. Otten, in the Geology Department at the University of Liège. A brief description of the techniques and experimental details are given in **Appendix B.2.1**. The results for some selected Prussian blues are shown in Figure 2.7. The observed iron and potassium weight % contents are compared with the expected contents, calculated from the chemical formulae of the insoluble and soluble Prussian blues.

Almost all Prussian blues, except A180 and B63, have a slightly higher iron weight % content than is expected from the theoretical chemical formula. In contrast, the potassium weight % content is lower than expected. The C02 Prussian blue obtained from the Royal Institute of Cultural Heritage, Brussels, contains a non-negligible amount of potassium and thus belongs to the soluble variety. Finally, it should be noted that C05, a soluble Prussian blue purchased from Sigma Aldrich, does not contain any potassium. Because C05 is very easily dispersed in water, it seems to be soluble and presumably contains another type of alkali, the nature of which was not determined herein.

Thermogravimetric analyses and differential scanning calorimetry were used to estimate the weight % water content in selected samples. The measurements were performed with a Netzsch instrument in the Chemistry Department at the University of Liège. The samples were placed in an alumina crucible and a heating rate of 2°C/min was applied. Figure 2.8 shows the thermogravimetric and differential scanning calorimetry curves recorded between room temperature and 1000°C for commercial insoluble, C03, and soluble, C02, Prussian blues.

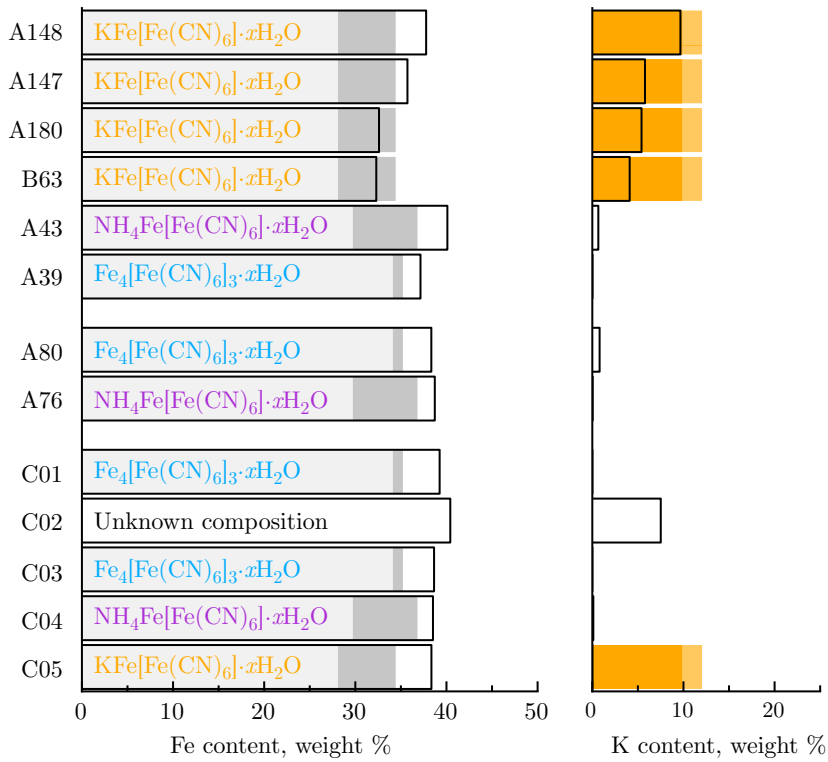

Figure 2.7 The iron and potassium weight % contents, black rectangles, determined respectively by atomic absorption and flame emission spectroscopy in Prussian blues. The colored bars correspond to the values calculated from the theoretical chemical formulae as reported in Table 2.4, in gray for the iron cations and in orange for the potassium cations.

The first weight loss of 7.7 and 4.4 % for insoluble and soluble Prussian blues, respectively, presumably correspond to the loss of water molecules. Two types of water molecules are found in Prussian blue, the water molecules coordinated to the iron(III) ions and those located in the lattice cavities of the crystal structure [13]. Among the uncoordinated water molecules a further distinction can be made between the zeolitic water molecules adsorbed in the cavities and the water molecules that are hydrogen bonded to the coordinated water molecules. In particular hydration conditions of the Prussian blue sample – several cycles of heating followed by air rehydration – these three kinds of water molecules can be distinguished by thermogravimetric analyses because they evaporate at a different temperature, at 65, 95, and 125°C for zeolitic, hydrogen-bond, and coordinated water molecules, respectively [83][84]. Ganguli *et al.* [83] noted that the degree of hydration in Prussian blue strongly depends upon the period of air exposure and

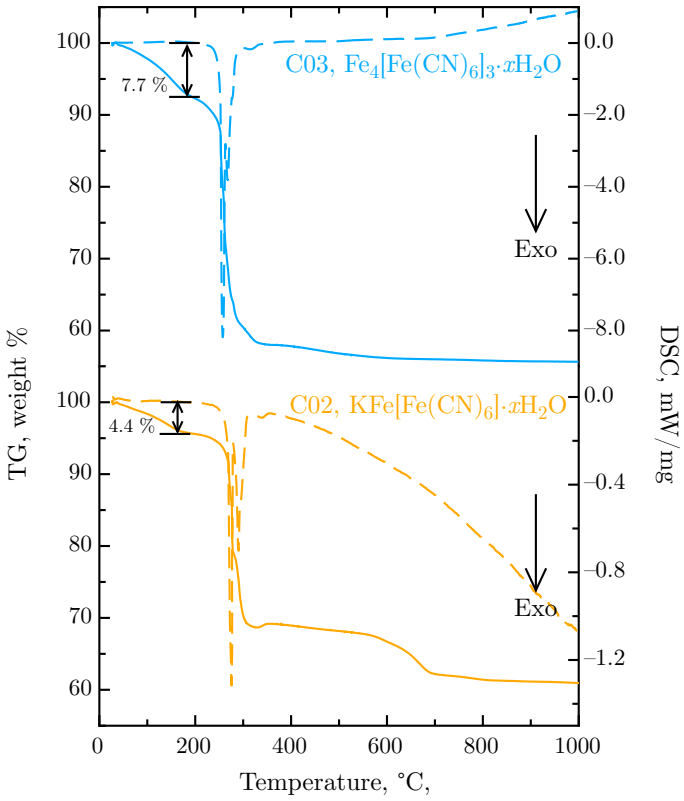

Figure 2.8 Thermogravimetric analysis, solid line, and the differential scanning calorimetry, dashed line, of commercial insoluble, C03, and soluble, C02, Prussian blues.

the ambient humidity.

In 1999 Imanishi *et al.* reviewed the thermogravimetric behavior of insoluble Prussian blue [85]. An insoluble Prussian blue sample was prepared according to the direct modern method and dried in air at 40°C for one week before the thermogravimetric analysis. The authors reported the loss of the zeolitic water molecules at temperatures up to 200°C. On the basis of the weight of the sample at 200°C the stable phase composition was calculated as $Fe_4[Fe(CN)_6]_3 \cdot 5.89\ H_2O$. The remaining six water molecules at 200°C were considered to be coordinated to the iron(III) ions and were removed by further heating the sample to 250°C, leading to a lattice collapse. According to the latter study, the weight loss from room temperature to *ca.* 175°C in both commercial insoluble, C03, and soluble, C02, Prussian blues, can be assigned to the loss of uncoordinated water molecules located in the lattice cavities of the crystal structure. Consequently, the second

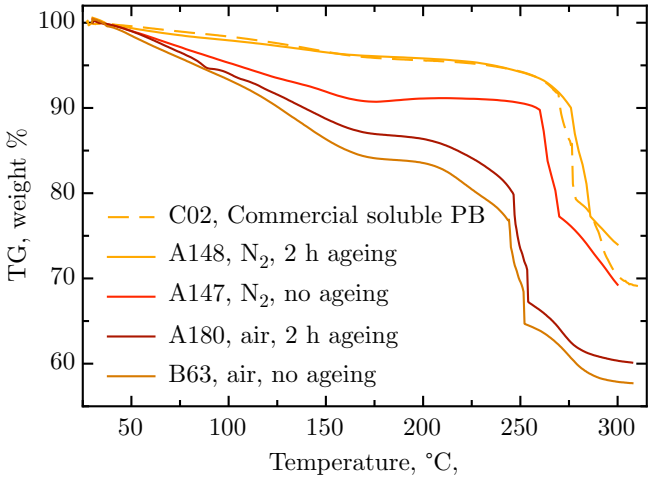

Figure 2.9 Thermogravimetric analysis of laboratory-synthesized potassium cation containing soluble Prussian blues prepared as described in the legend. The dashed curve for the commercial soluble Prussian blue, C02, is included for comparison.

weight loss of 4.0 % for insoluble Prussian blue, which occurs from *ca.* 175 to 250°C, corresponds to the loss of the remaining coordinated water molecules. In soluble C02 Prussian blue, the second weight loss of 1.4 % is difficult to assign and could result from the loss of the potassium cation located in the lattice cavities.

The strong exothermic process in the differential scanning calorimetry curve at 260 and 278°C for insoluble and soluble Prussian blues, respectively, is assigned to the loss of the cyanide anions [86]. No further significant weight loss occurs above 350°C in the insoluble C03 Prussian blue. The residual product at 1000°C is dark brown and consists of a mixture of iron oxides, a mixture that has been used as a brown pigment in the eighteenth and nineteenth centuries [55][87]. The weight loss of 7.0 % at *ca.* 600°C accompanied by a continuous exothermic process, that is observed in the soluble C02 sample could correspond to a crystallographic rearrangement in these iron oxides with the loss of oxygen ions.

Because the goal of the thermogravimetric analyses and differential scanning calorimetry was the determination of the water content in the Prussian blues, it was decided to restrict the temperature range to 300°C in order to decrease the measurement time. The results for the laboratory-synthesized soluble Prussian blues containing potassium are shown in Figure 2.9. Clearly, the thermal behavior of C02 and A148 are very similar. Sample A148 has been prepared according to a preparative method described in patents, *i.e.*, the indirect process occurring under

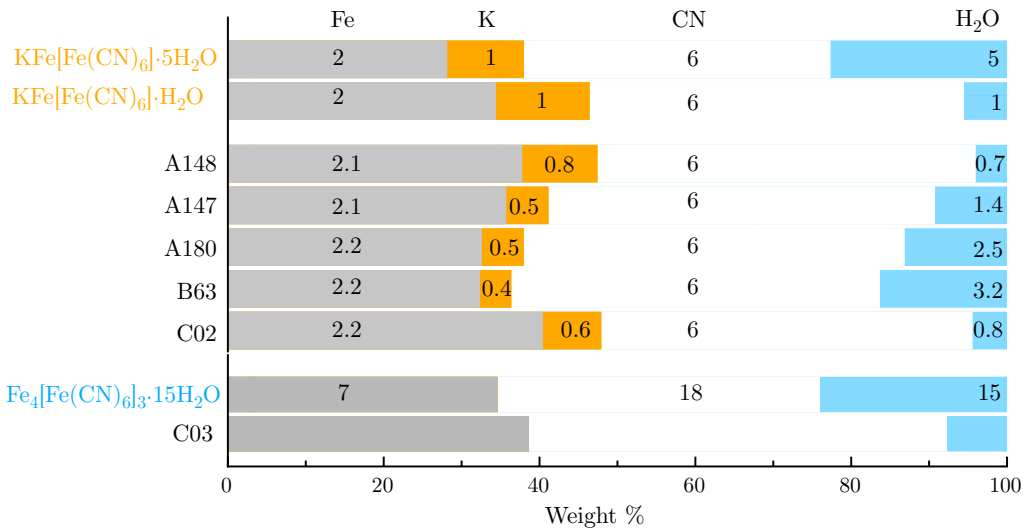

Figure 2.10 A graphical representation of both the number and weight percent of the ions and water molecules present per mole of insoluble and soluble Prussian blues. The values have been obtained with the assumption of charge neutrality, the presence of only iron and potassium cations and cyanide anions, and water; the presence of any impurities has been assumed to be negligible.

nitrogen and including an ageing time of Berlin white of two hours. Presumably, C02 was similarly prepared.

From both the weight % content of iron, potassium, and water and the iron(III) to iron(II) ratio obtained from Mössbauer spectroscopy, the number of cyanide anions and iron and potassium cations per mole found in a Prussian blue can be determined. A similar calculation for ammonium or sodium containing soluble Prussian blues has not been carried out because of the lack of data concerning the $NH4^+$ or Na^+ cationic content. Charge neutrality requires the presence of the correct number of iron and potassium cations and cyanide anions and the absence of any other ionic components. The theoretical composition of insoluble and soluble Prussian blues, as well as those of several laboratory-synthesized and commercial samples, is shown graphically in Figure 2.10.

For each of the laboratory synthesized Prussian blues, the number of potassium cations is lower and the number of iron cations is higher than expected, see Figure 2.10. The same is observed for the commercial, C02, soluble Prussian blue and, further, the water content is relatively small in all of these cases. These observations suggest that the theoretical formula $KFe^{III}[Fe^{II}(CN)_6]\cdot xH_2O$ is not exactly

Table 2.5 Composition of starting reagents and commercial Prussian blues determined by particle induced X-ray emission analysis.

	Element, wt %[a]							
Compound	**Fe**	**K**	**Cl**	**Na**	**Al**	**Si**	**P**	**S**
Sarting reagents								
$FeCl_2$	43.5(4)	–	54.2(3)	0.8(1)	0.8(1)	–	–	–
$FeCl_2{\cdot}4H_2O$	42.3(4)	–	54.6(3)	1.2(2)	1.3(1)	–	–	–
$FeCl_3{\cdot}6H_2O$	33.2(3)	–	62.7(3)	1.2(2)	1.7(1)	–	–	–
$K_4[Fe(CN)_6]{\cdot}3H_2O$	15.0(2)	41.6(2)	0.4(1)	–	–	–	0.5(1)	–
$(NH_4)_4[Fe(CN)_6]{\cdot}yH_2O$	24.1(2)	1.0(1)	7.1(1)	–	–	–	–	–
Laboratory-synthesized Prussian blues								
A65	35.8(3)	11.8(1)	2.0(1)	–	–	–	–	–
A39	40.8(3)	–	1.9(6)	–	–	–	–	–
A43	41.5(3)	–	–	–	–	–	–	–
Well-crystallized Prussian blues								
A74	37.4(4)	4.1(1)	5.3(1)	–	–	–	–	
A80	39.7(3)	1.4(1)	2.9(1)	–	–	–	–	–
A76	38.9(3)	–	4.3(1)	–	–	1.9(1)	–	–
Commercial Prussian blues								
C01	40.0(3)	–	0.1(1)	3.0(2)	–	–	0.5(1)	0.2(1)
C02	37.5(3)	8.3(1)	0.6(1)	0.4(1)	–	–	–	–
C03	40.2(3)	–	0.1(1)	2.3(2)	–	0.3(1)	0.4(1)	0.3(1)
C04[b]	40.6(3)	0.2(1)	–	0.7(1)	–	–	–	1.0(1)

[a]The values given in parentheses are the errors evaluated from the statistical error and the fit error given by Gupixwin. [b]The commercial ammonium containing Prussian blue is the only compound that also contains a small amount of calcium, *i.e.*, 0.14(2) weight %.

valid. In **Section 2.2.4** this model, which dates back to the 1930's is revised by using Rietveld refinement of X-ray powder diffraction patterns. The composition of insoluble commercial Prussian blue, C03, is more complex because of the presence of vacancies in the lattice. Theoretically a quarter of the $[Fe^{II}(CN)_6]^{4-}$ cationic groups is missing and their absence leads to an iron(III) to iron(II) ratio that is close to 4/3, a value that is larger than the value obtained from Mössbauer spectroscopy, see Figure 2.5. This apparent discrepancy will be revisited when the local order in Prussian blue is studied by X-ray absorption spectroscopy, see **Section 2.2.5**.

The assumption that Prussian blue contains only iron and potassium cations, cyanide anions, and water molecules is not completely valid. Some contamination arising from the starting reagents is possible. To complete the elemental characterization of the Prussian blue samples, the presence of impurities was checked by particle induced X-ray emission studies. The observed composition of the starting reagents used in the laboratory syntheses reported herein and in several Prussian blues is given in Table 2.5. For the cyanide complexes the elemental composition

takes into account the presence of cyanide anions, anions which are not detected by particle induced X-ray emission studies. The resulting values are believed to be valid because the iron weight % is close to either that measured by atomic absorption spectroscopy or to that estimated from the theoretical chemical formulae.

The contamination of the laboratory-synthesized Prussian blues necessarily results from the purity grade of the starting reagents. Some undesirable cations, such as sodium and aluminum cations, were detected in the starting reagents, but always in a concentration lower than 1.7 weight %. None of these elements were found in the laboratory-synthesized Prussian blues. In contrast, there is often contamination by chloride ions, a contamination that does not exceed two weight %. In the well-crystallized Prussian blues, the percentage of chloride ions is even higher, with up to five weight %, because the crystals were grown in concentrated hydrochloric acid. The contamination in commercial Prussian blues is distributed over several elements but the total impurity content does not exceed four weight %.

2.2.3 Color, spectral reflectance, and absorbance

Because Prussian blue is used as a pigment, its color must be evaluated. In Figure 2.11 different Prussian blues in powder mixed with gum arabic have been painted in a pure state or mixed in a 1:100 dilution ratio with titanium white, TiO_2, a modern white pigment that has been purchased from Kremer Pigmente Gmbh & Co KG, Alchstetten, Germany.

Although the commercial and laboratory-synthesized Prussian blues are all qualitatively blue in color, it is visually obvious in Figure 2.11 that the color is not identical for all Prussian blues, painted either pure or mixed with the white pigment.

The color[3] of a pigmented paint layer is defined by three parameters. First, the **hue** or **shade**, *i.e.*, *the property of a color that differentiates it from an achromatic color like grey or black* [88]. Second, the **tinting strength** which is defined as the ability of a pigment to color a white mixture [88]. Third, the **hiding power**, a parameter that refers to the ability of a pigment to scatter light to the maximum extent possible [52].

Several of the laboratory-synhthesized Prussian blues, namely A39, A43, A80, and A147 to a lesser extent, are characterized by a duller shade, a lower tinting strength, and a smaller hiding power than the C01 to C05 commercial Prussian

[3]For a general definition of color, see **Appendix D**.

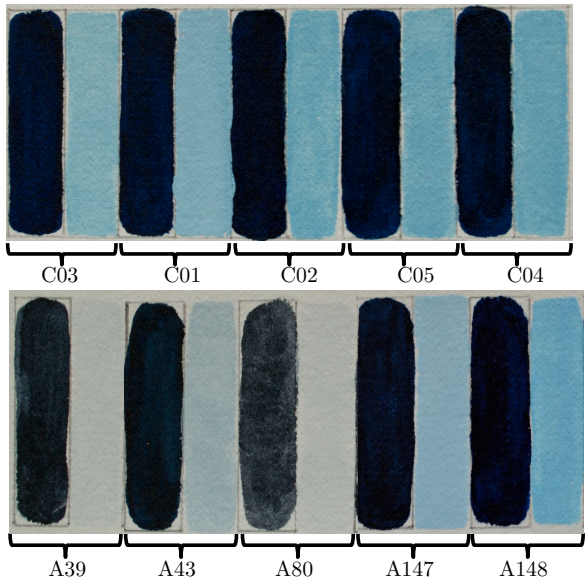

Figure 2.11 Paint layers of Prussian blue powder mixed with gum arabic, painted pure, left, and mixed with titanium white in a 1:100 dilution ratio, right. The first row corresponds to the commercial Prussian blues whereas the second one displays some of the laboratory-synthesized samples.

blues or the laboratory-synthesized A148 Prussian blue. These tinctorial properties are intimately bound to the absorption and scattering power of the pigments, the refractive indices of pigments and medium, the particle size and shape, and their distribution.

Hue

The hue of a pigment is influenced by the absorption of light by the pigment, *i.e.*, by the possible electronic transitions within the molecules. As discussed in **Section 1.1.2** the color of Prussian blue results from an intervalence charge transfer absorption band at *ca.* 700 nm that corresponds to the transfer of an electron from an iron(II) to an iron(III) ion when light is absorbed. UV-visible absorption spectroscopic studies of aqueous dispersions of Prussian blues confirm this absorption of light, see Figure 2.12. Furthermore, the strong absorbance in the near-infrared region, from 700 to 900 nm, permits an easy detection of Prussian blue by infrared photography because the pigment appears dark in infrared photographs. The position of the maximum absorbance shifts from a minimum wavelength of 682 nm for sample A180 to a maximum of 693 nm for the A148 Prussian blue.

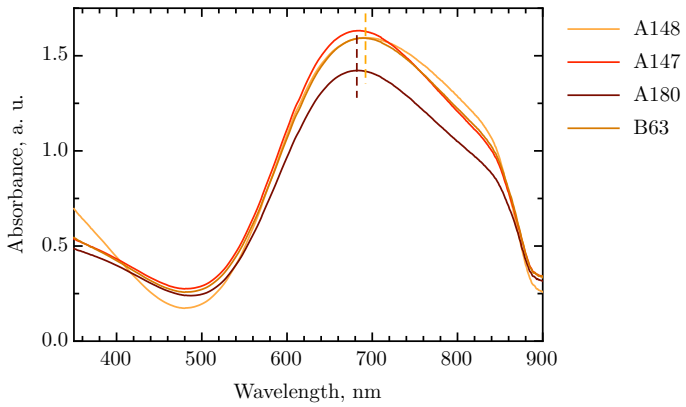

Figure 2.12 UV-visible absorption spectra of the indicated laboratory-synthesized soluble Prussian blues. The dashed vertical lines indicate the position of the maximum absorbance for the A148 and A180 Prussian blues.

The disadvantage of using UV-visible absorption spectroscopy is the necessity of dispersing the pigment in water. Attempts to characterize the pure color of Prussian blue with UV-visible reflectance spectroscopy were unsuccessful because the reflectance was too low as a result of the darkness of the pigment. In contrast, the spectral reflectance was easily measured on paint layers containing Prussian blue and titanium white, see Figure 2.13. Except for A148, the maximum in reflectance of the laboratory-synthesized A39 and A43 Prussian blues is shifted toward longer wavelengths. Such a change in shade may be caused by a smaller pigment particle size [88]. Indeed a decrease in average particle size leads to a shift of shade or absorption towards longer wavelengths. This phenomenon can be explained by the *Mie theory* [51][89]. The German physicist Gustav Mie found a solution of Maxwell's field equations that could be applied to a model in which a plane wave strikes optically isotropic spheres. Details for the Mie and other scattering theories and the absorption law are given in **Appendix C**. Although pigments are not composed of spherical particles of uniform size, as assumed by the Mie theory, the model has been shown to be valid for pigments and can be used to interpret the optical behavior of pigmented layers [90]. In summary the Mie theory states that the absorption power – as well as the scattering power of a particle – depends both on its size and on wavelength. When light strikes pigment particles, the radiation at the maximum absorption wavelength is mainly absorbed at the surface of the particles. In contrast the radiation at wavelengths other than the maximum absorption wavelength is weakly absorbed at the surface and can penetrate into the core of a particle. Small particles have a larger specific area than large particles and thus absorb more efficiently at wavelengths other

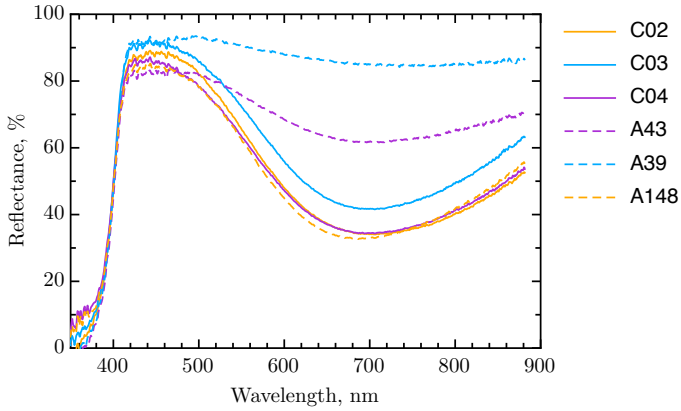

Figure 2.13 UV-visible reflectance spectra of commercial insoluble Prussian blue and soluble laboratory-synthesized Prussian blue powders painted from gum arabic with titanium white, TiO_2, in a 1:100 dilution ratio.

than the maximum absorption wavelength. This more efficient absorption causes a deviation in shade.

The particle size of powdered Prussian blues has been investigated by scanning electron microscopy and the smallest particle size was observed for the laboratory-synthesized A147 and A180 Prussian blues, see Figure 2.14. At high magnification, the primary particles of the pigment, defined as the smallest entities that can be distinguished by physical methods, can be identified, some of them are circled to guide the eye in the micrographs on the right in Figure 2.14. In the well-crystallized A80 Prussian blue the primary particles are cubic crystals of *ca.* 5 μm length. In other Prussian blues, the primary particles are most often composed of several crystallites. When the primary particles are attached together at their surfaces, they formed *aggregates*. Finally, *agglomerates* result from coalescence of primary particles and aggregates as a result of van der Waals or coulombic forces. All Prussian blues synthesized as a fine precipitate exhibit rather shapeless agglomerates, except for the commercial C03 Prussian blue, whose agglomerates are spherical. The commercial C01 and C05 Prussian blues, not shown in Figure 2.14, also consist of spherical agglomerates. The method for obtaining such uniform size, spherical, and lightly agglomerated particles is described in several patents [91]. This method requires the simultaneous and very slow introduction of the aqueous solutions of ferrocyanide and ferrous solutions into a container and an optimum mixing during the precipitation. The Berlin white precipitate is then aged at temperatures between 80 and 120°C, at a pressure of one to two atmospheres.

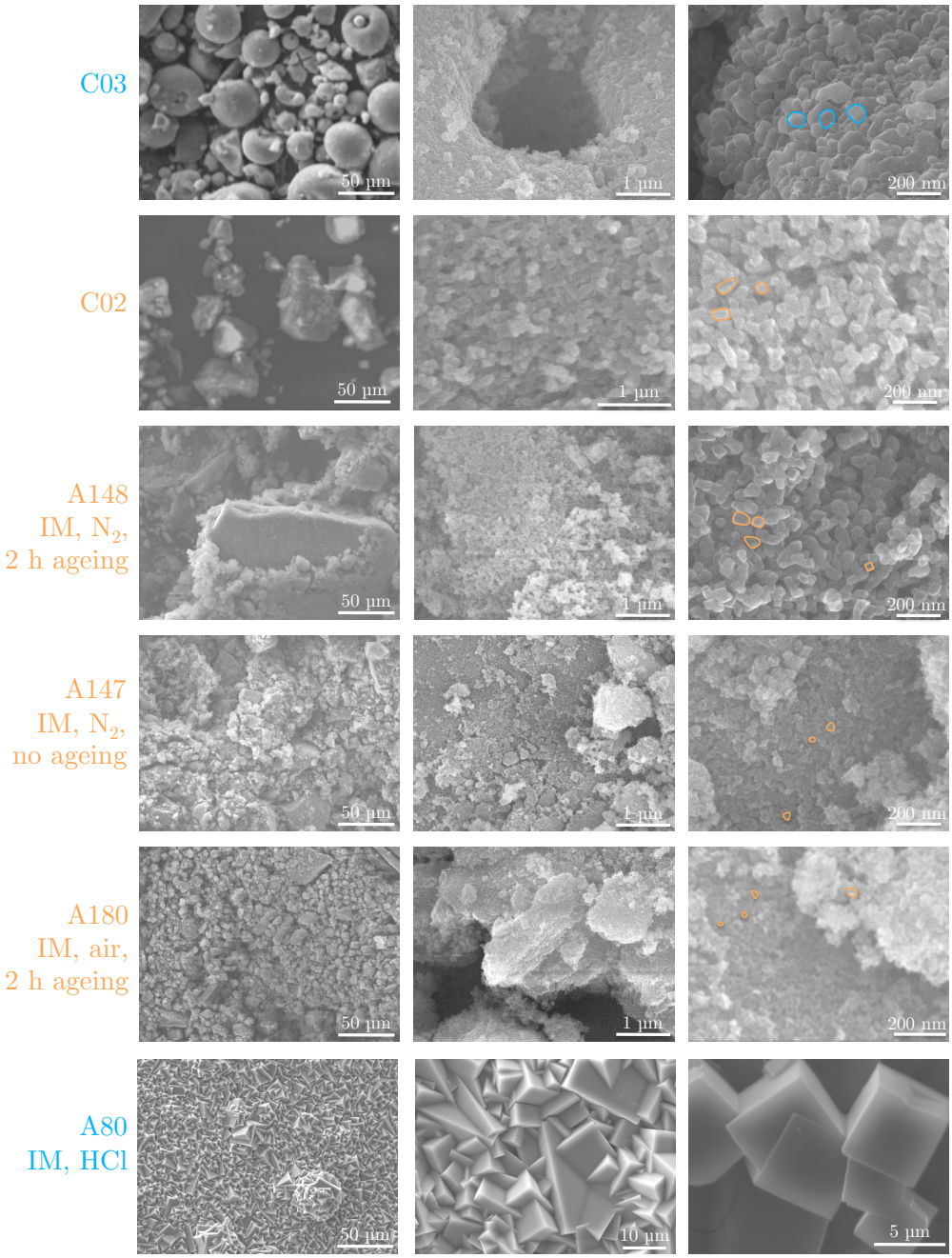

Figure 2.14 Scanning electron micrographs of several commercial and laboratory-synthesized Prussian blue samples obtained with 15 keV secondary electrons.

A quantitative analysis of the color properties as a function of particle size requires an investigation of the granulometry and the particle size distribution by techniques other than scanning electron microscopy. This has not been studied in detail in this thesis and the color properties are thus only qualitatively discussed hereafter. However, the specific surface area of the commercial C01 and C04 Prussian blues and the laboratory-synthesized A39 Prussian blue has been measured by nitrogen adsorption-desorption. The commercial C01 and C03 Prussian blues have a very similar specific surface area, of 55 and 61 m^2/g whereas the laboratory-synthesized A39 Prussian blue has a specific surface area of 201 m^2/g. Because nitrogen molecules cannot penetrate into the lattice cavities of Prussian blue, this specific surface area corresponds to the total particle surface. Thus, the specific surface area measurements confirm the smaller particle size characteristic of the laboratory-synthesized Prussian blues that have not been prepared in a nitrogen atmosphere.

In comparison with the commercial Prussian blues and the laboratory-synthesized A148 Prussian blue, which consists of spherical or amorphous agglomerates, the A147 and A180 Prussian blues are composed of finely dispersed agglomerates. The slight shift of the maximum in absorbance or reflectance observed in the UV-visible spectra can be explained by the presence of small particles that favor absorption in wavelength regions other than that of the maximum absorption observed at *ca.* 700 nm for Prussian blues.

The alkali metal ions present in the soluble Prussian blues also affect the hue of the pigment [92], *i.e.*, a sodium cation containing Prussian blue is slightly greenish whereas an ammonium cation containing Prussian blue is red-tinged. This variation in color is caused by the spectral lines of the alkali ion; a sodium ion is characterized by yellow spectral lines, a potassium ion by violet, and an ammonium cation by intense violet lines.

The shift in shade is not the most striking feature in Figure 2.11. The commercial Prussian blues and the laboratory-synthesized A148 Prussian blue, are much more efficient in coloring titanium white than the others laboratory-synthesized Prussian blues. The ability of a pigment to confer color to a light-scattering material is called the *tinting strength*.

Tinting strength

The tinting strength of a pigment depends primarily on its absorption properties. In Prussian blue the tinting strength results from the intervalence charge transfer between the iron(II) and iron(III) ions when light is absorbed at *ca.* 700 nm. In practice the determination of the tinting strength is based on the measure of

the reflectance corrected by the Kubelka-Munk theory.[4] This theory takes into account both absorption and scattering of light and is, thus, very suitable for describing the interaction of light with a heterogeneous media, such as a paint layer that strongly diffuses light. The tinting strength is measured by the K/S value, *i.e.*, the ratio between the absorption coefficient, K, and the scattering coefficient, S. In agreement with the Mie theory both coefficients depend on the particle size and the wavelength of the light. No attempt to quantify the tinting strength was made but a qualitative discussion based on theoretical considerations is proposed.

According to Mie there is an optimum particle size for the absorption of light. Commercial Prussian blues and the laboratory-synthesized A148 Prussian blue have a very high tinting strength; only one weight % of Prussian blue is sufficient to color titanium white. This high tinting strength partially explains the popularity of Prussian blue as an artist pigment. In contrast, the well-crystallized A80 Prussian blue has an extremely low tinting strength as a result of the presence of much larger primary particles, of *ca.* 5 μm length, see Figure 2.14. These larger particles are not easily penetrated by the light and their cores remain ineffective for absorption. Normally reduction in particle size is expected to increase the tinting strength because additional pigment volume is accessible for absorption. However, in case of the other laboratory-synthesized Prussian blues, the smaller particle size does not enhance the tinting strength. In Figure 2.13 the low tinting strength of the A39 and A43 Prussian blues results in a reflectance that is almost constant over the entire spectral range studied. Their UV-visible spectra are similar to that of titanium white. This low tinting strength indicates that the size of the primary particles is smaller than the optimum size such that the light passes through the particles without absorption.

Hiding power

The hiding power[5] is related to both the absorption and scattering coefficients and the refractive indices of the pigment and the medium. The refractive index, n, is defined as the ratio of the velocity, c, of light in vacuum to the velocity, v, of light in a medium or $n(\lambda) = c/v(\lambda)$. The refractive index, n, of the pigments and binders that have been used herein is given in Table 2.6. The hiding power is also influenced by the surface rouhgness and optical discontinuity in the paint layer.

In paint layers the larger the difference in refractive index between the pig-

[4] See **Appendix C** for details.

[5] Strictly speaking the hiding power of a pigment is an inappropriate term because it is the pigment coating and not the pigment itself that hides the substrate. For the sake of convenience herein, the hiding power is nevertheless assigned to the pigment itself, provided that its determination is carried out under identical conditions of coating.

Table 2.6 The refractive index, n, of Prussian blue, several white pigments, and the binders used herein

Material	n^a
Prussian blue	1.56
Titanium white (rutile), TiO_2	2.71
Lead white, $(PbCO_3)_2Pb(OH)_2$	2.04
Zinc white , ZnO	2.01
Water	1.33
Gum arabic solution 10%	1.334
Linseed oil	1.478

[a]Mean refractive index calculated for uniaxial and biaxial crystals [93].

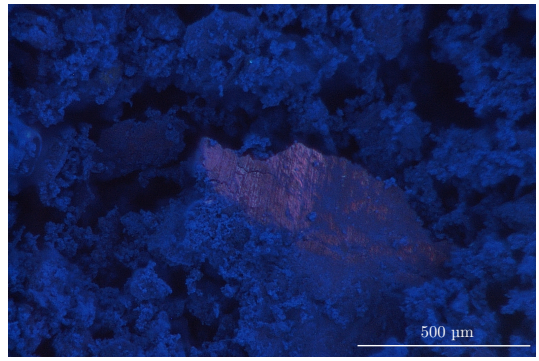

Figure 2.15 Optical photomicrograph of laboratory-synthesized A148 Prussian blue, obtained with reflected visible light, dark field illumination by using a Hirox optical microscope.

ment and the binder,[6] the higher is the hiding power because light scattering is enhanced by this large difference. The light scattering is described as the secondary radiation emitted by the oscillating dipole induced in each particle by the primary radiation. Hence, interference between this secondary radiation and the surrounding wave field occurs. When the difference in the refractive indices between the pigment and the medium is large, a substantial fraction of the light scattering is not extinguished. Pigments with a large refractive index thus have a larger hiding power than those with a small refractive index. With its very large refractive index and consequently, its large scattering coefficient, titanium white is

[6]In the case of a paint layer painted from an aqueous binder, such as gum arabic, the refractive index of the binder is taken as as 1, *i.e.*, the refactive index of air, because the water molecules are evaporated when the binder is dried.

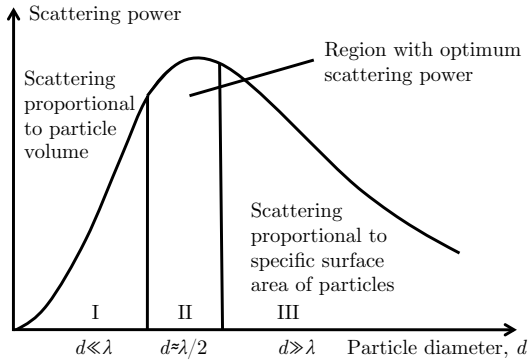

Figure 2.16 Schematic representation of the scattering power as a function of particle diameter at constant wavelength and given refractive indices of pigment and medium. Adapted from [88].

more hiding than Prussian blue, which can be considered as a transparent pigment because of its small refractive index.

It is well known that the refractive index is not constant over the entire visible spectral range because the velocity of light through matter depends on wavelength. In non-chromatic substances the refractive index continuously decreases with increasing wavelength. In coloring material, such as pigments, the refractive index is increased in the spectral range of strong absorption, whereas it follows a normal dispersion curve in the neighboring spectral regions. This phenomenon is called *anomalous dispersion*. In Prussian blue the refractive index thus has a larger value at the red end of the spectrum. This increased refractive index may cause a bronzing effect, *i.e.*, the perception of a bronze tone at near-glancing angles in Prussian blue powder and in paint layers containing Prussian blue [54]. This bronzing effect gives a metallic aspect to the pigment particles observed under an optical microscope, see Figure 2.15.

As was the case for absorption, there is an optimum particle size for scattering, see Figure 2.16. Unfortunately, for a given wavelength, the optimum particle size for scattering does not correspond to the optimum particle size for absorption. The scattering power reaches a maximum when the particle diameter is *ca.* one-half the wavelength of the incident light.

Because the commercial Prussian blues and laboratory-synthesized A148 Prussian blue are composed of particles of *ca.* 60 to 80 nm in diameter, their particle size lies below the optimum size for scattering, *i.e.*, in region I in Figure 2.16.

These pigments thus have a relatively low scattering power. The other laboratory-synthesized Prussian blues, such as A39, A43, and A147, are characterized by a particle size of *ca.* 20 to 30 nm.[7] Their scattering power is even smaller than that of the commercial Prussian blues and laboratory-synthesized A148 Prussian blue. As a pure shade they thus appear more transparent because of their small scattering power and, consequently, their poor hiding power, see Figure 2.11. The variation in particle size explains the difference in color perception of the different Prussian blues samples.

2.2.4 Crystal structure

In order to investigate the structure of Prussian blue, the commercial and laboratory-synthesized Prussian blue pigments were studied by X-ray powder diffraction, by using a PANalytical PW-3710 diffractometer. The radiation was provided by an iron anod, producing iron K_α radiation of 1.9373 Å wavelength.[8] The diffraction patterns were recorded over a 2θ angle range from 5° to 75°, with a time per step of one second. The measurements were carried out by F. Hatert, in the Geology Department at the University of Liège.

The diffraction patterns of the commercial and laboratory-synthesized Prussian blues as well as two crystallographic standards, *i.e.*, lanthanum hexaboride, LaB_6, and $Na_2Ca_3Al_2F_{14}$, NAC, are shown in Figure 2.17. The spectra were normalized to the intensity of the most intense peak to make easier a comparison between the diffraction patterns. Three features in the powder diffraction pattern are of major interest, the positions of the peaks, their intensities, and the peak profiles.

The positions of the peaks are given by Bragg's relation,[9]

$$2d_{hkl} \cdot \sin\theta_{hkl} = n \cdot \lambda, \tag{2.1}$$

where d_{hkl} is the spacing between the hkl planes[10] in the crystal lattice, θ_{hkl} is the angle of diffraction, n is the diffraction order, and λ is the wavelength of the X-ray radiation, *i.e.*, 1.9373 Å.

[7] In fact, for particles much smaller than the wavelength of incident light, the scattering power is better described by Rayleigh scattering than by Mie scattering, see **Appendix C** for details.

[8] Using the iron radiation instead of the copper radiation allows reducing the fluorescence of the sample, because iron is the main constituent of Prussian blue.

[9] For more details, see **Appendix B.2.10**.

[10] The hkl indices are the Miller indices. For a cubic system with a lattice parameter, a, d_{hkl} is defined as $d_{hkl} = \frac{a}{\sqrt{h^2+k^2+l^2}}$.

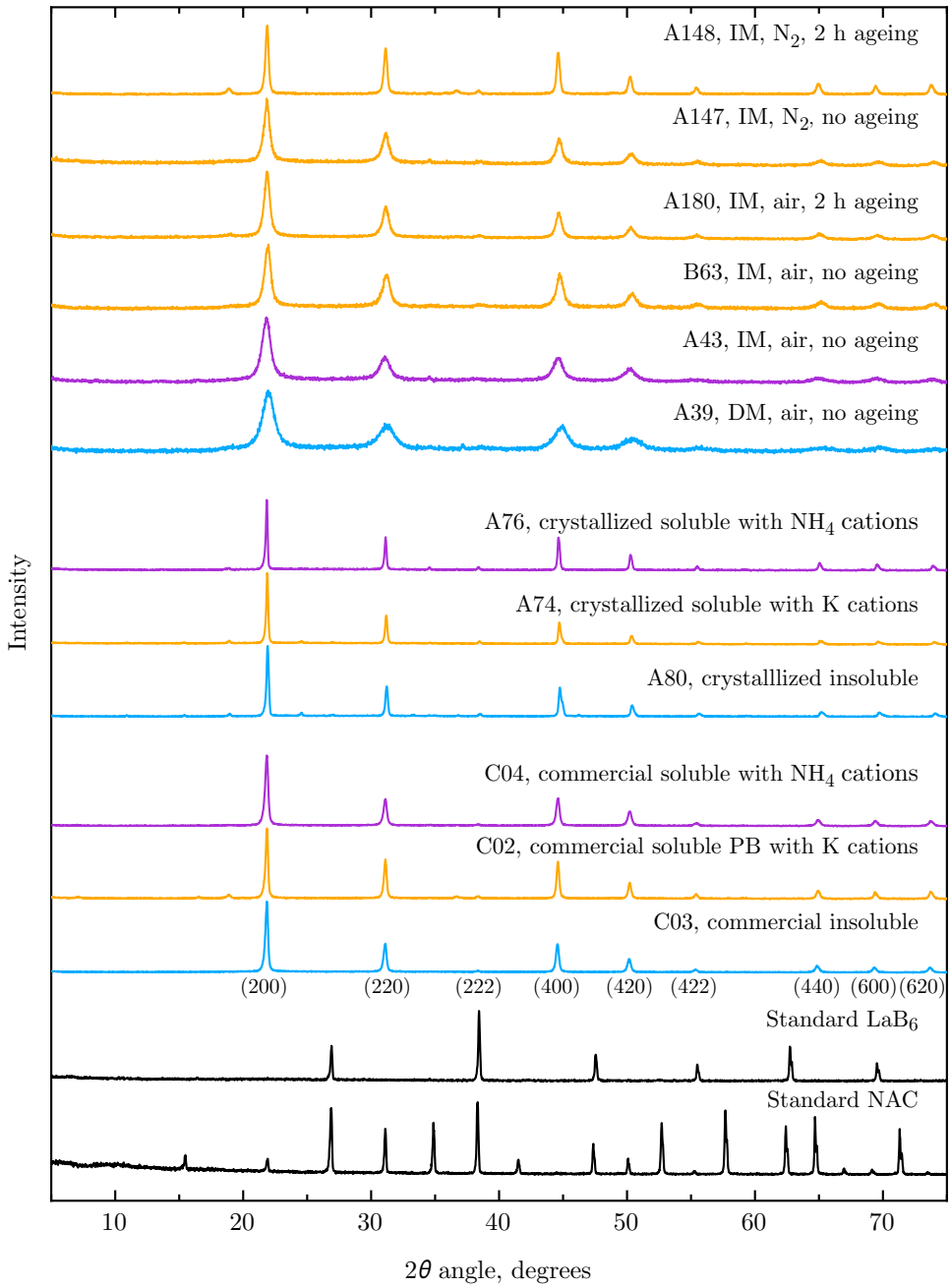

Figure 2.17 The X-ray powder diffraction patterns of laboratory-synthesized and commercial Prussian blues, obtained by using iron K_α radiation with $\lambda = 1.9373$ Å. Diffraction patterns of LaB_6 and NAC, or $Na_2Ca_3Al_2F_{14}$, standards are also shown.

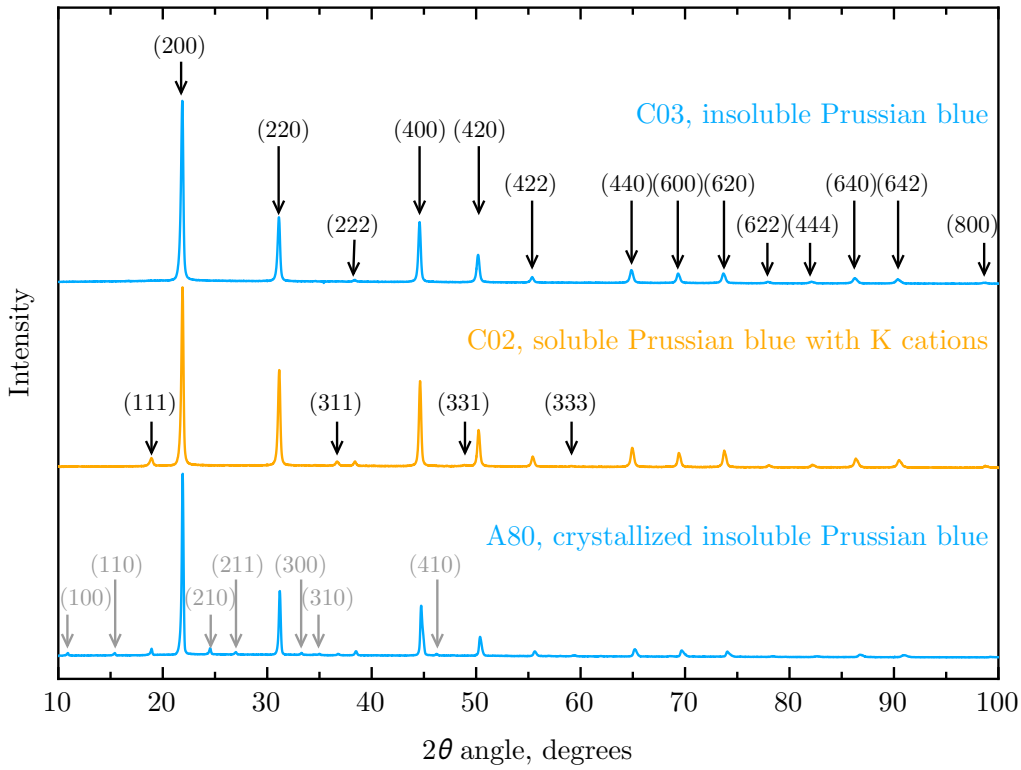

Figure 2.18 Peak assignments for commercial soluble C02 and insoluble C03 Prussian blues and well-crystallized insoluble A80 Prussian blue. The diffraction patterns have been obtained by using iron K_α radiation with $\lambda = 1.9373$ Å. Primitive reflections are visible in the well-crystallized Prussian blue and are indicated by gray arrows.

All Prussian blues crystallize in the $Fm3m$ space group, as is expected for Prussian blue in powder and powder diffraction peaks can be indexed accordingly.[11] In the well-crystallized Prussian blues additional reflections are observed. Figure 2.18 shows the diffraction patterns of commercial insoluble C03 and soluble C02 Prussian blues as well as the well-crystallized insoluble A80 Prussian blue, obtained between 10 and 100° with an increased time per step of fifteen seconds. Clearly the well-crystallized A80 Prussian blue exhibits primitive reflections, indexed in gray in Figure 2.18. The observation of these non-face-centered reflections is assigned to the partial ordering of the $[Fe^{II}(CN)_6]^{4-}$ vacancies [12]. Commercial soluble C02 Prussian blue shows some additional face-centered reflections as compared to the commercial insoluble C03 sample. Moreover the peak intensities

[11] In a face-centered cubic structure the *hkl* indices must be all even or all odd.

also differ, indicating a slightly different crystal structure. The crystal structure of both insoluble and soluble Prussian blues will be refined by *Rietveld refinement*, as is discussed below.

Besides differences in the positions and intensities of the peaks the patterns of the various samples also show large differences in peak broadening, see Figure 2.17. The laboratory-synthesized Prussian blues that were not aged, *i.e.*, A147, B63, A43, and A39, show broader peaks than the soluble A148 Prussian blue whose preparative method includes an ageing of Berlin white of two hours. The latter Prussian blues exhibit less sharp reflections than the three well-crystallized Prussian blues, A74, A76, and A80.

From the analysis of the peak broadening it is possible to obtain the average crystallite size and the strain present in each Prussian blue sample, by applying the *Scherrer formula* and the *Williamson-Hall method*.

Size effect and strain

The broadening of a diffraction line can be defined by its integral width, *i.e.*, the ratio between the line integral and its maximum intensity [94],

$$\beta = \frac{\int I(2\theta)\mathrm{d}\theta}{I_{max}(2\theta)}. \tag{2.2}$$

The integral width results from two contributions, that of the sample itself, and that of the diffractometer. The sample induces a specific broadening in the diffraction peak because of both the finite size of the crystals and the strain present in the crystals.

In the case of small[12] particles the hypothesis of an infinite diffracting crystal is no longer valid. In 1917 Scherrer [94] derived a relation between the integral width and the average size of the diffracting crystals,

$$\beta = \frac{\lambda}{L\cos\theta}, \tag{2.3}$$

where the average size, L, is defined in one particular crystallographic direction. One should note that the average size, L, is the coherence length or crystallite size and may not correspond to the primary particles, as observed at high magnification in scanning electron micrographs.

[12]For laboratory diffractometers a line broadening due to size effect typically appears for particles smaller than *ca.* 100 nm.

The strain in a crystal results from a displacement of atoms or ions from their positions in a perfect crystal. These local deformations can be relatively important but do not affect the lattice parameters. However, they induce a line broadening equal to,

$$\beta = \eta \tan\theta, \tag{2.4}$$

where η is the *strain*, as defined by Stokes and Wilson [95].

In 1953 Williamson and Hall [96] developed a method to distinguish in the peak broadening the contribution due to the particle size and that due to the strain. They assumed that both contributions could be described with a Lorentzian function. Hence the convolution product of these two functions is also a Lorentzian function. Thus, if β^S and β^D are the broadening due to the size effect and the strain effect, respectively, the total broadening is

$$\beta = \beta^S + \beta^D, \tag{2.5}$$

where

$$\beta = \frac{\lambda}{L\cos\theta} + \eta\tan\theta, \tag{2.6}$$

and

$$\frac{\beta\cos\theta}{\lambda} = \frac{1}{L} + \eta\frac{\sin\theta}{\lambda}. \tag{2.7}$$

Equation 2.7 corresponds to a linear relationship, $y = b + ax$, where y is $\beta\cos\theta/\lambda$ and x is $\sin\theta/\lambda$. The intercept of the straight line is thus the inverse of the crystal size, L, and the slope is the strain, η.

Usually the Williamson-Hall plot is found in the form,

$$\beta^* = \frac{1}{L} + \frac{\eta}{2}d^*, \tag{2.8}$$

where β^* is $\beta\cos\theta/\lambda$ and d^* is $2\sin\theta/\lambda$.

The integral width, β, in equations 2.5 to 2.7 is the *pure* integral width, *i.e.*, the integral width due to the sample itself, without any instrumental contribution. The experimental profile, $h(x)$, of a diffraction line is the convolution product of

the pure profile, $f(x)$, with the instrumental profile, $g(x)$,[13]

$$h(x) = f(x) \otimes g(x) = \int_{-\infty}^{+\infty} f(y)g(x-y)\mathrm{d}y. \tag{2.9}$$

The instrumental profile arises both from any distribution in wavelength of the incident radiation and from the intrinsic characteristics of the diffractometer. It is usually evaluated from the diffraction pattern of a standard that is considered to be a perfect crystal. The only standard that is recognized by the international community is lanthanum hexaboride, LaB_6, which is available from the National Institute of Standards and Technologies. The standard NAC, $Na_2Ca_3Al_2F_{14}$, is also appropriate for determining the instrumental line profile. The diffraction patterns of both standards are shown in Figure 2.17. The instrument resolution profile for the PANalytical diffractometer was determined from the NAC standard by Rietveld refinement.

The pure profile is extracted by deconvolution from the experimental profile, by assuming an *a priori* knowledge of the profile shape function. Herein this profile shape function was taken as a *pseudo-Voigt* profile, *i.e.*, an approximation of the normalized Voigt profile, which is the convolution product of a Lorentzian function and a Gaussian function. Details about the instrument resolution profile and the procedure used to deconvoluate the pure profile, $f(x)$, from the experimental profile, $h(x)$, are given in **Appendix B.2.10**.

The deconvolution of the X-ray powder diffraction patterns with a pseudo-Voigt profile function was carried out with the *Peakoc* software developed by Masson [97]. The adjustments were optimized with the Levenberg-Marquardt algorithm. Individual adjustment of each peak is suitable for the Prussian blues because the X-ray diffraction lines do not overlap. The Scherrer relation and the Williamson-Hall method were finally applied to extract from the line broadening the average particle size and the strain. Figure 2.19 shows the Williamson-Hall plot for the laboratory-synthesized and commercial Prussian blue powders.

No errors bars have been estimated on the absolute values reported in the Williamson-Hall plot because the method is rather more qualitative than quantitative. The main assumption of the method, *i.e.*, that the size and strain effects induce a line broadening that can be fully described by Lorentzian functions, is

[13] In this expression the noise, $\epsilon(x)$, and the *brehmsstrahlung* radiation, $b(x)$, are not taken into account. The profile of the diffraction line should be written as

$$h(x) = \left(\int_{-\infty}^{+\infty} f(y)g(x-y)\mathrm{d}y \right) + \epsilon(x) + b(x).$$

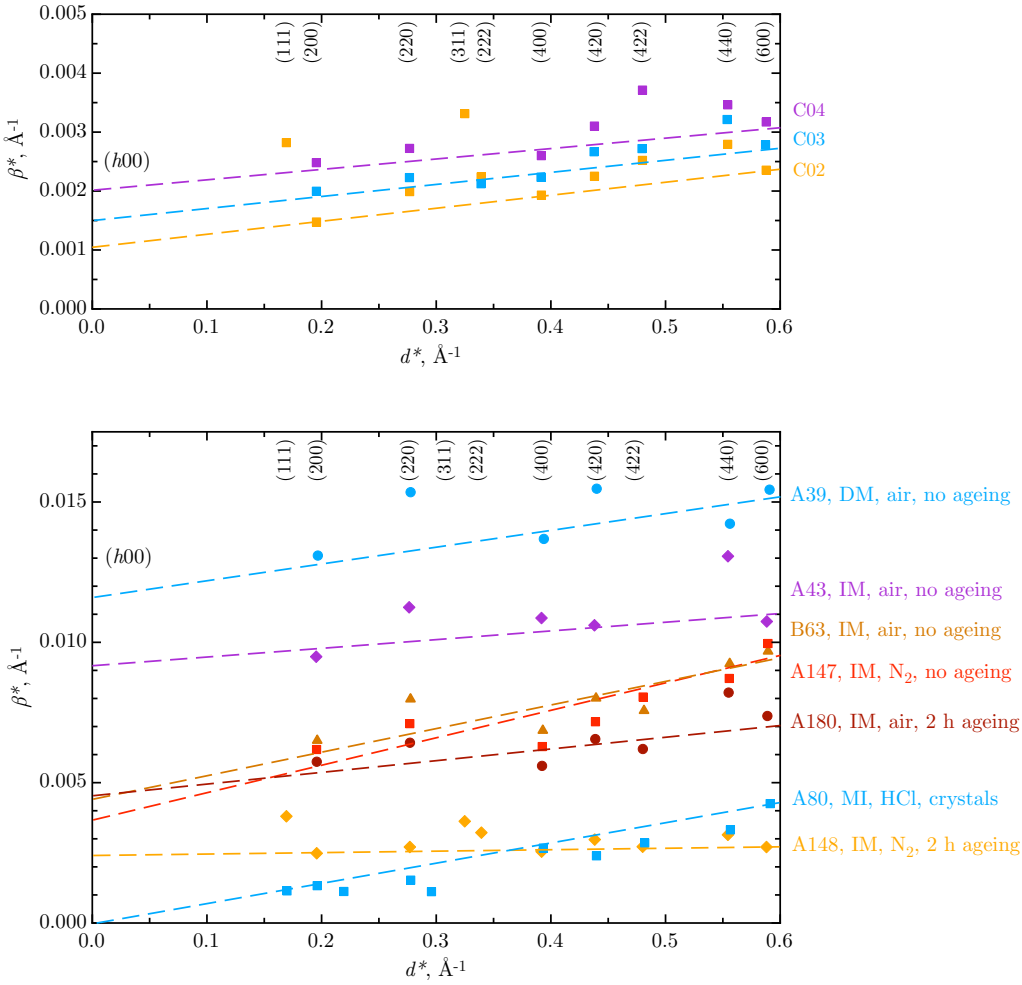

Figure 2.19 Williamson-Hall plot obtained from the X-ray diffraction patterns of the laboratory-synthesized and commercial Prussian blue powders shown in Figure 2.17. The dashed lines correspond to a linear best fit for the three (h00) reflections.

usually not realistic.[14] However, in the study of many powder diffraction patterns of the same chemical compound, but synthesized under different conditions, as is the case for the commercial and laboratory-synthesized Prussian blues, the Williamson-Hall plot might reveal trends in crystallite size and strain, trends that in turn can be related to the properties of the product.

The Williamson-Hall plot provides information about the particle size in the sample to the extent that the pure integral width, β_f^*, is larger than the instrumental contribution, β_g^*. This condition is not fulfilled for the well-crystallized laboratory-synthesized A80 sample because the intercept of the linear regression tends to zero. The crystallites in the well-crystallized A80 Prussian blue are consequently too large to induce any size-effect broadening. This is consistent with the scanning electron microscopy results, which showed micrometrical crystals of *ca.* 5 µm size, see Figure 2.14. For the other laboratory-synthesized and commercial Prussian blue samples, the particle sizes in a specific crystallographic direction can be determined either by the Williamson-Hall method or by the Scherrer relation, see Table 2.7. The number of reflections in the Williamson-Hall plots is relatively small and the values given in Table 2.7 are more qualitative than quantitative. Not surprisingly the Scherrer relation gives smaller values for particle size because the line broadening due to the strain effect is not taken into account.

The direct preparation method leads to the smallest particle size, as evidenced in the sample A39. An ageing step of two hours in an ambient atmosphere does not significantly increase the particle size as shown by the sample A180 that does not contain larger particles than samples A147 and B63. In contrast, the commercial Prussian blues and the laboratory-synthesized A148 Prussian blue are composed of larger particles. All of these samples were prepared according to methods described in patents, methods that take place under a nitrogen atmosphere and include an ageing step of the Berlin white compound prior to the oxidation to form Prussian blue. The particle sizes of the commercial C03 and C02 and laboratory-synthesized Prussian blues were determined by scanning electron microscopy to be between 60 and 80 nm, see Figure 2.14. However it is difficult to know whether the particle size measured in the scanning electron micrographs corresponds to the crystallite size, *i.e.*, the coherence length obtained from a microstructural diffraction analysis. For some Prussian blues, such as the commercial C02 and C03 or the laboratory-synthesized A147 sample, the particle size in the (hh0) crystallographic direction slightly differs from that determined from the (h00) reflexions, indicating a slight anisotropic size effect.

[14] Other methods for the microstructural analysis of diffraction line broadening exist, such as the methods based on the line profile analysis by Fourier series. These methods are not considered herein.

Table 2.7 Particle size determined from the (h00) and (hh0) reflections by the Scherrer formula and the Williamson-Hall method.

Sample	**Particle size, nm**[a]			
	Scherrer		**Williamson-Hall**	
	h00	hh0	h00	hh0
C02	54	43	96	84
C03	44	38	65	81
C04	36	33	48	50
A39	7	6	6	6
A43	9	8	11	10
B63	13	11	22	15
A180	16	13	22	21
A147	14	12	27	18
A148	39	34	43	44
	Average particle size determined by Rietveld refinement[b,c]			
C03	85(1)			
C02	84(1)			

[a]Average particle size. [b]The Rietveld refinement was performed on the diffraction patterns recorded on the CRISTAL beamline at SOLEIL, Paris, France. [c]The two values in parentheses are the standard deviations calculated by using the different reciprocal lattice directions. Hence, they indicate the degree of anisotropy, not the estimated error.

The Williamson-Hall method gives a qualitative estimate of the strain due to the presence of lattice defects in the crystallites. While the line broadening due to the size effect is independent of the reflection order, *i.e.*, independent of d^*, the line broadening due to the strain effect is dependent of this order. The larger the slope on the linear regression in a given crystallographic direction in the Williamson-Hall plot, the larger is the strain. All the commercial and laboratory-synthesized Prussian blues, as well as the well-crystallized A80 sample, exhibit strain, see Table 2.8, strain that can be related to the iron(III) quadrupole splitting previously observed by iron-57 Mössbauer spectroscopy, see Figure 2.20. A large strain is ac-

Table 2.8 Strain in the crystallographic direction (h00) obtained with the Williamson-Hall method for the laboratory-synthesized and commercial Prussian blues.

Strain, %									
C02	C03	C04	A80	A43	A39	B63	A180	A147	A148
0.45	0.40	0.35	1.48	0.64	1.19	1.62	0.83	1.91	0.11
0.309(1)[a]	0.451(1)[a]								

[a]These values correspond to the average apparent strain determined from the Rietveld refinement using the *Fullprof* software. See footnote *c* of Table 2.7 concerning the values in parentheses.

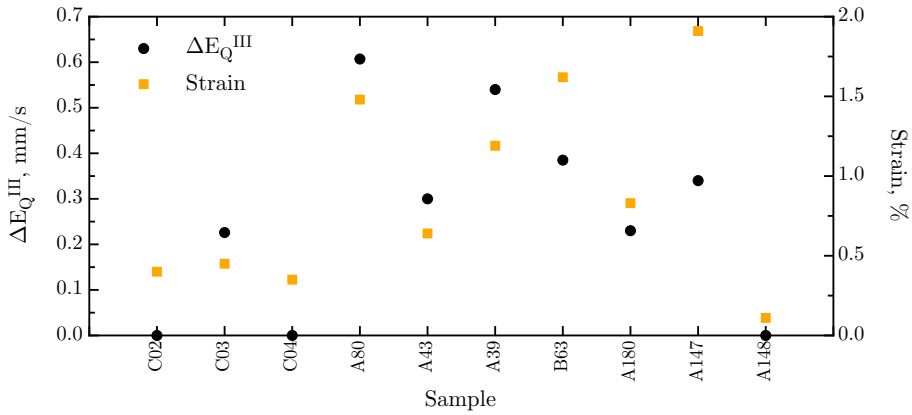

Figure 2.20 Strain determined from the Williamson-Hall plot *versus* the iron(III) quadrupole splitting, ΔE_Q^{III} of the laboratory-synthesized and commercial Prussian blue powders. The error bars on the iron(III) quadrupole splitting are smaller than the size of the data points.

companied by a large quadrupole splitting, which is a measure of the asymmetry in the iron(III) environment. The relation is well verified for all the Prussian blue samples, except for the laboratory-synthesized A147 Prussian blue that exhibits a rather large value of strain for a relatively small iron(III) quadrupole splitting. The large value of the strain may result from the inaccuracy in determining the integral width of diffraction peaks at large 2θ angle because of the weak scattering in the diffraction pattern.

The microstructural parameters, such as size and strain, can be directly extracted from a Rietveld refinement, see below for details. The *Fullprof* software automatically deconvolutes the diffraction lines by using the instrumental resolution profile that has been previously determined on a standard. The procedure of deconvolution is similar to that presented in **Appendix B.2.10**. The powder diffraction patterns of the commercial C03 and C02 Prussian blues have been measured with high-energy X-rays on the CRISTAL beamline at SOLEIL, Paris, France. The Rietveld refinement was performed on both diffraction patterns, as will be explained below. The size and strain values determined for both commercial C03 and C02 Prussian blues from the Rietveld refinement are also given in Tables 2.7 and 2.8. The average particle size is obtained from the Scherrer formula. The average strain is calculated from equation 2.4, where the parameter, η, is the apparent strain as defined by Stokes and Wilson [98].[15] The crystallite

[15]The strain value given by the *Fullprof* software corresponds to the so-called maximum strain, ϵ, which equals $\eta/4$. In order to permit a comparison with the strain values determined by the

size of the commercial C02 and C03 Prussian blues obtained with both the laboratory PANanalytical diffractomer and the instruement at the CRISTAL beamline are very similar. Similarly, the strains for the commercial C02 and C03 Prussian blues determined by the Rietveld refinement are close to those extracted from the Williamson-Hall plot. The slightly larger strain of 0.451(1) % found for the C03 sample may explain the non-zero iron(III) quadrupole splitting observed in its Mössbauer spectrum, see Figure 2.20.

The line broadening analysis of the Prussian blue X-ray diffraction patterns supports the presence of nanometer size particles in the commercial and the laboratory-synthesized Prussian blues. The particle size depends upon the type of synthesis. Furthermore the Prussian blue powders exhibit a strain that may be related to the electric field gradient at the iron(III) ions. The strain results from local distortions, such as lattice defects or vacancies. The presence of vacancies in Prussian blue is well known. However little research has been carried out on the distribution of these vacancies and the understanding of the local structure in Prussian blue powders. To overcome the lack of knowledge about the local structural arrangement and the intervalence charge transfer pathway, the Prussian blue samples were studied by pair distribution analysis and iron-K edge X-ray absorption spectroscopy. The fit and interpretation of the data obtained by both techniques are based on the known structure of Prussian blue. Although the crystal structure of insoluble Prussian blue is well known, that of soluble Prussian blue is still debated. In the next section, a new model for the structure of soluble Prussian blue, based on a difference Fourier synthesis and a Rietveld refinement of the commercial soluble C02 X-ray diffraction pattern, is presented.

Rietveld refinement

The Rietveld refinement yields a global structural refinement of the diffraction pattern. Instead of a simulation peak by peak, this method, first introduced by Rietveld in 1967 [99] for neutron diffraction, deals with the entire pattern and refines a theoretical structural model to fit the experimental data. The refined parameters are instrumental, structural – lattice parameters, atomic positional parameters, site occupancies, and thermal parameters – and microstructural – size and strain in crystallites. The Rietveld method consists of minimizing the residual, *i.e.*, the difference between the observed intensity, y_i^{obs}, and the calculated intensity, y_i^{calc}, at a point i, by a least squares approach,

$$R = \sum w_i (y_i^{\mathrm{obs}} - y_i^{\mathrm{calc}})^2, \tag{2.10}$$

Williamson-Hall method the strain reported in Table 2.8 is the apparent strain, η.

where w_i is a coefficient that depends on the count rate.

The intensity y_i^{calc} may result from the contribution of several Bragg peaks and also contains the background due to the instrument and the sample. Therefore the intensity y_i^{calc} at a point i is described by,

$$y_i^{\text{calc}} = y_i^b + \sum_{k=1}^{k=n} G_{ik} I_k, \tag{2.11}$$

where y_i^b is the intensity of the background, G_{ik} is the line profile function, and $k = 1, \ldots, n$ are the indices of the reflections that contribute to the intensity at point i.

The quality of the agreement between the observed and calculated profile is evaluated by means of several conventional agreement factors, such as the profile factor, R_p, the weighted profile factor, R_{wp}, the expected profile factor, R_{exp}, the goodness of fit, χ^2, and the Bragg factor, R_{Bragg}, defined respectively by the following expressions,

$$R_p = \frac{\sum\limits_i |y_i^{\text{obs}} - y_i^{\text{calc}}|}{\sum\limits_i y_i}, \tag{2.12}$$

$$R_{wp} = \sqrt{\frac{\sum\limits_i w_i (y_i^{\text{obs}} - y_i^{\text{calc}})^2}{\sum\limits_i w_i . y_i^2}}, \tag{2.13}$$

$$R_{exp} = \sqrt{\frac{(N - P + C)}{\sum\limits_i w_i . y_i^2}}, \tag{2.14}$$

$$\chi^2 = \frac{R_{wp}^2}{R_{exp}^2}, \tag{2.15}$$

and

$$R_{\text{Bragg}} = \frac{\sum\limits_k |I_k - y_k^{\text{calc}}|}{\sum\limits_k I_k}, \tag{2.16}$$

where N is the number of points in the pattern, P is the number of refined parameters, and C is the number of constraint functions. The sum $N - P + C$ represents the number of degrees of freedom.

If the calculated pattern is in good agreement with the observed data, the reliability factor R_{wp} tends towards R_{exp}. The weighted profile factor, R_{wp}, assigns to each point y_i a weight, w_i, that is inversely proportional to the intensity measured at that point. Therefore points with weak and strong intensities are equally considered and the R_{wp} factor gives a good indication of the refinement quality of the base of the diffraction lines. The R_{Bragg} factor is the most suitable factor to characterize the quality of the agreement between the structural model and the observed intensities. For the Rietveld refinements presented in this thesis, the agreement factors R_p, R_{wp}, χ^2, and R_{Bragg} will be reported.

Refining a diffraction pattern by the Rietveld method implies a prior knowledge of the composition and the structure of the sample. The previous analyses have revealed that the laboratory-synthesized and commercial samples were hydrated ferric ferrocyanide complexes, with a low content of impurities. The X-ray powder diffraction patterns confirmed the presence of a single crystal phase. The choice of the structural model is crucial. The crystal structure of Prussian blue is notoriously complex because of the colloidal character of the compound and the presence of vacancies in the lattice. The structure of insoluble Prussian blue is best approximated by the $Fm3m$ space group, where a quarter of the $[Fe^{II}(CN)_6]^{4-}$ sites are vacant and replaced by water molecules [13]. Additional water molecules can either occupy zeolitic positions or be bound by hydrogen bonds to coordinated water. Accordingly the chemical formula is $Fe^{III}_4[Fe^{II}(CN)_6]_3{\cdot}xH_2O$ where x is between 14 and 16, *i.e.*, 6 coordinated water molecules and 8 to 10 zeolitic or hydrogen-bond water molecules.

The $Fm3m$ space group implies a statistically random distribution of the vacancies. In contrast, in single crystals the $[Fe^{II}(CN)_6]^{4-}$ vacancies are not randomly distributed. In this particular case the structure corresponds to the lower symmetry $Pm3m$ space group [12]. In the cubic primitive model Buser *et al.* [12] introduced an occupancy parameter, p, that is the probability that the $[Fe^{II}(CN)_6]^{4-}$ site in the center of the unit cell is occupied, see Table 2.9. When p is zero the structure is completely ordered and all occupancies are integers. A p value of 3/4 means that 1/4 of the $[Fe^{II}(CN)_6]^{4-}$ sites are vacant; this situation corresponds to the cubic face-centered $Fm3m$ model previously described [12].

The structure of insoluble Prussian blue is now well established and the model developed by Buser and Herren [13] can be used as a starting model for the Rietveld refinement of the structure of the commercial insoluble C03 Prussian blue. By using the $Pm3m$ space group and an occupancy parameter p, any possible non-random distribution of vacancies is taken into account. In contrast, the structure of soluble Prussian blue remains controversial. The model developed by Keggin and Miles in 1936 is usually taken as viable [11]. It consists of a perfect cubic Fe^{II}-

Table 2.9 Atom distribution in the unit cell of Prussian blue and the occupancies in the space groups $Fm3m$ and $Pm3m$.

	$Fm3m$		$Pm3m$	
Atom	**Pos**[a]	**Occ**	**Pos**[a]	**Occ**
4 Fe^{III}	4*a*	1	1*a*	1
			3*c*	1
3 Fe^{II}	4*b*	3/4	1*b*	p
			3*d*	$1-p/3$
18 C	24*e*	3/4	6*e*	$1-p/3$
			6*f*	p
			12*h*	$1-p/3$
18 N	24*e*	3/4	6*e*	$1-p/3$
			6*f*	p
			12*h*	$1-p/3$
6 O	24*e*	1/4	6*e*	$p/3$
			6*f*	$1-p$
			12*h*	$p/3$
8 O	8*c*	1	8*g*	1
			6*f*	1

[a]Wickoff positions.

CN-Fe^{III} framework with no vacancies. The alkali cations and the water molecules are localized in the center of the lattice cavities, at zeolitic positions. Recently this model for soluble potassium cation containing Prussian blue has been revisited by Bueno *et al.* [14] who studied electrochemically synthesized potassium cation containing ferric ferrocyanide by X-ray synchrotron radiation powder diffraction. They concluded that about 25 % of the $[Fe^{II}(CN)_6]^{4-}$ sites were vacant. Moreover they claimed that the potassium cations were part of the water crystalline substructure and occupied positions comparable to those of the coordinated water in the Buser model. They proposed a new chemical formula to describe the structure as $Fe_4^{3+}[Fe^{2+}(CN)_6]_3{\cdot}[K_h^+{\cdot}OH_h^-{\cdot}mH_2O]$. The charge balance is ensured by the presence of OH^- anions, which compensate the positive charge of the potassium cations.

Rietveld refinements have been performed for commercial insoluble C03 and soluble C02 Prussian blues. Because the diffraction data previously shown in Figure 2.17 were of low quality because of low instrumental resolution and limited data, the X-ray diffraction patterns of commercial insoluble C03 and soluble C02 Prussian blues were obtained at 295 K at high-energy with 0.442930 Å synchrotron radiation on the CRISTAL beamline at Soleil, Paris, France. The measurements were carried out by Dr. Pauline Martinetto and Dr. Pierre Bordet, Department MCMF, Institut Néel, Grenoble, France.

Table 2.10 Results of the Rietveld refinement of commercial insoluble and soluble Prussian blues in the $Pm3m$ space group.[a]

		Insoluble, C03 $Fe_4^{III}Fe_{3.00(2)}^{II}(CN)_{18.0(1)}$ $\cdot 11.20(7)H_2O$			**Soluble, C02** $K_{0.83(7)}Fe_4^{III}Fe_{3.00(2)}^{II}(CN)_{18.00(3)}$ $\cdot(0.83(7)OH^- + 9.9(16)H_2O)$		
site		x	**Occ**	**U, Å^2**	x	**Occ**	**U, Å^2**
Fe(III)	$1a$	0	1	0.0096(1)	0	1	0.0113(1)
	$3c$	0	1	0.0096(1)	0	1	0.0113(1)
Fe(II)	$1b$	0.5	0.609(11)	0.0096(1)	0.5	0.724(12)	0.0113(1)
	$3d$	0.5	0.799(4)	0.0096(1)	0.5	0.759(4)	0.0113(1)
C	$6e$	0.3207(3)	0.7989(18)	0.0096(1)	0.2980(3)	0.7589(19)	0.0113(1)
	$6f$	0.3207(3)	0.6046(18)	0.0096(1)	0.2980(3)	0.7237(19)	0.0113(1)
	$12h$	0.1788(3)	0.7989(9)	0.0096(1)	0.1799(3)	0.7590(10)	0.0113(1)
N	$6e$	0.2074(2)	0.7989(18)	0.0096(1)	0.1953(3)	0.7589(19)	0.0113(1)
	$6f$	0.2074(2)	0.6046(18)	0.0096(1)	0.1953(3)	0.7237(19)	0.0113(1)
	$12h$	0.2971(2)	0.7989(9)	0.0096(1)	0.3047(3)	0.7590(10)	0.0113(1)
O	$6e$	0.2248(7)	0.2021(18)	0.225(8)	0.2202(12)	0.2412(19)	0.295(9)
	$6f$	0.2248(7)	0.3964(18)	0.225(8)	0.2202(12)	0.2764(19)	0.295(9)
	$12h$	0.2752(7)	0.2016(9)	0.225(8)	0.2991(12)	0.2412(10)	0.295(9)
	$8g$	0.2469(16)	0.649(5)	0.110(3)	0.23051	0.597(16)	0.046(3)
K	$8g$	–	–	–	0.28714	0.104(9)	0.087(4)

[a]The values given in parentheses are the estimated standard deviations. The absence of such a value indicates the parameter was constrained to the value given.

The primitive cubic model reported by Buser *et al.* [12] with an occupancy parameter, p, was used as a starting structural model for both the soluble and insoluble samples. The adjustment and the refinement of the model for both types of Prussian blue were carried out in collaboration with Dr. Pauline Martinetto and used the *Fullprof* software [100]. The structural parameters of C, N, and O on the $6e$, $6f$, and $12h$ positions were coupled by constraints. The anisotropic thermal parameter was constrained to the same value for all the atoms. The isotropic thermal parameter was constrained to zero for the iron and cyanide ions, to the same non-zero value for all the water oxygen $6e$, $6f$, and $12h$ sites, and to an independent value for the water oxygen $8g$ site. The total thermal parameter results from the sum of both the isotropic and anisotropic thermal parameter. The Rietveld refinement for commercial insoluble C03 and soluble C02 Prussian blues are shown in Figure 2.21a and 2.21b. The positional, occupancy, and thermal parameters are given in Table 2.10. The refined lattice parameters are given in Table 2.11.

The Rietveld refinement for the commercial insoluble C03 Prussian blue reveals an occupancy parameter p of 0.61(1) for the iron(II) $1b$ site, indicating that the central $[Fe^{II}(CN)_6]^{4-}$ site is vacant with a 39 % probability. The occupancy parameter is thus lower than expected in the $Fm3m$ model, which is characterized

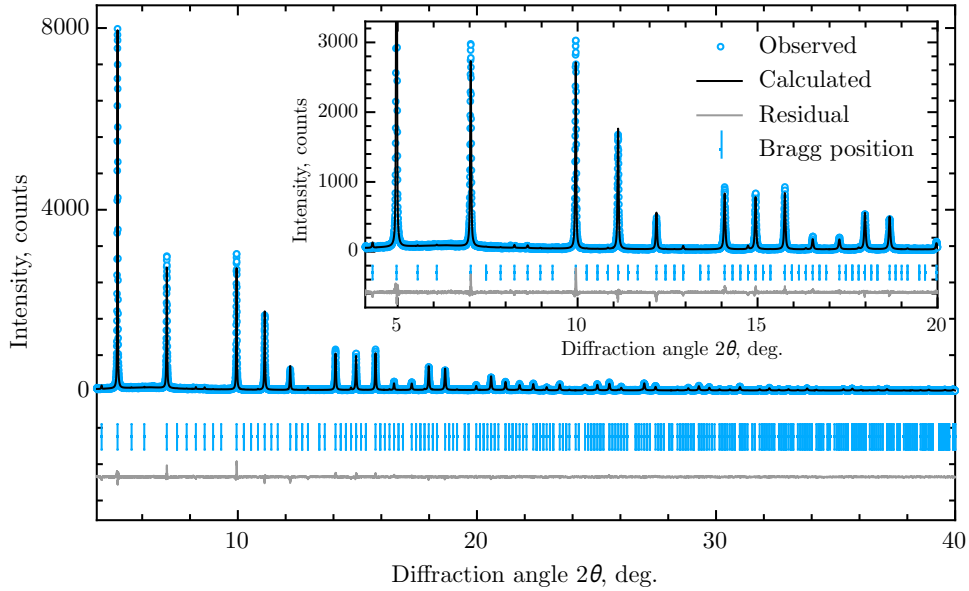

(a)

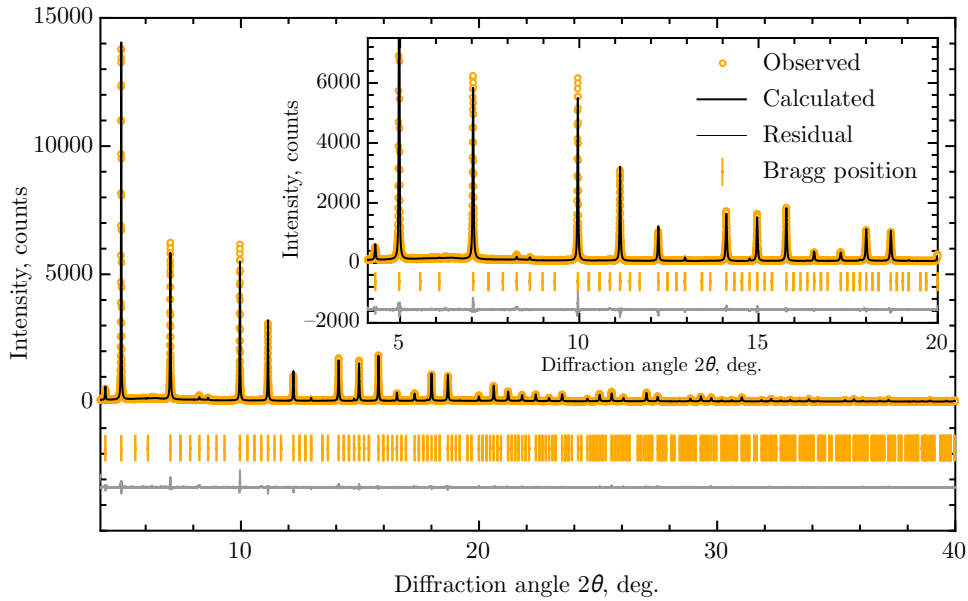

(b)

Figure 2.21 Rietveld refinement of the diffraction pattern obtained by using a wavelength of 0.442930 Å of, **a**, the insoluble commercial Prussian blue C03 with R_p = 18.3 %, R_{wp} = 19.6 %, χ^2 = 0.962, and R_{Bragg} = 5.03; and **b**, the soluble commercial Prussian blue C02 containing K cations, with R_p = 15.1 %, R_{wp} = 15.4 %, χ^2 = 1.021, and R_{Bragg} = 3.43.

Table 2.11 Lattice parameter and average interatomic distances.

Distance, Å	**This work**[a]		**Buser**	**Herren**	**Bueno**
	C03	C02	***et al.* [12]**	***et al.* [13]**[b]	***et al.* [14]**[b]
a	10.2178(1)	10.2059(1)	10.166	10.155(4)	10.1783(3)
Fe(II)-C	1.830(4)	1.949(4)	1.923(8)	1.92(1)	1.86(6)
Fe(III)-N	2.096(2)	1.993(4)	2.029(6)	2.01(1)	2.00(7)
C-N	1.183(4)	1.161(6)	1.131(6)	1.148	1.17(4)
Fe(III)-O	2.297(10)	2.149(17)	2.138(19)	1.96	2.00(7)

[a]The standard deviations in parentheses were calculated from $\sqrt{\sigma^2_{6e,6f} + \sigma^2_{12h}}$ where σ is the estimated standard deviation for a crystallographic position. [b]Refinement from the $Fm3m$ model.

by an occupancy parameter of 0.75 that indicates a random distribution of vacancies. The commercial insoluble C03 Prussian blue with a p value of less than 0.75 thus has a relatively high degree of ordering of the $[Fe^{II}(CN)_6]^{4-}$ vacancies. The resulting lattice parameter and the bond distances are compared with those previously published in the literature [12][13][14] in Table 2.11. The lattice parameter is slightly larger than expected. Lattice expansion has been reported in case of sodium ion intercalation [101] and ammonium ion insertion [64] into the Prussian blue lattice. Similarly lattice contraction has been observed in partially dehydrated Prussian blues [13]. The lattice parameter of 10.2178(1) Å determined for the commercial insoluble C03 Prussian blue can thus result from the insertion into the lattice cavities of the sodium, silicon, phosphor, and sulphur ions detected in the particle induced X-ray emission analysis, see Table 2.5. The presence of these ions may also explain the differences observed between the interatomic distances reported in this thesis and in the literature. Furthermore, a recent study [102] concerning the structure of iron(II) hexacyanometallates(III) complexes reported a Fe(III)-O interatomic distance of 2.53 Å as determined by a Rietveld refinement using the $Pm3m$ Buser model, a distance that is much larger than that reported earlier by Buser *et al.*[12].

The insoluble model yields approximately eleven water molecules, six of which are coordinated to iron(III). The water content of 7.7 weight % determined by thermogravimetric analyses, see **Section 2.2.2**, thus corresponds to the five uncoordinated water molecules that occupy the zeolitic positions. The six remaining coordinated water molecules, which are bound to iron(III), escape the lattice at a higher temperature of *ca.* 250°C. However the weight loss observed before the loss of the cyanide ions at 260°C is only 4.0 weight % instead of the approximately 10 weight % expected. Because the residual product is an iron oxide some coordinated oxygen ions may remain in the Prussian blue to form the iron oxide. In order to confirm this hypothesis, an analysis by neutron powder diffraction should

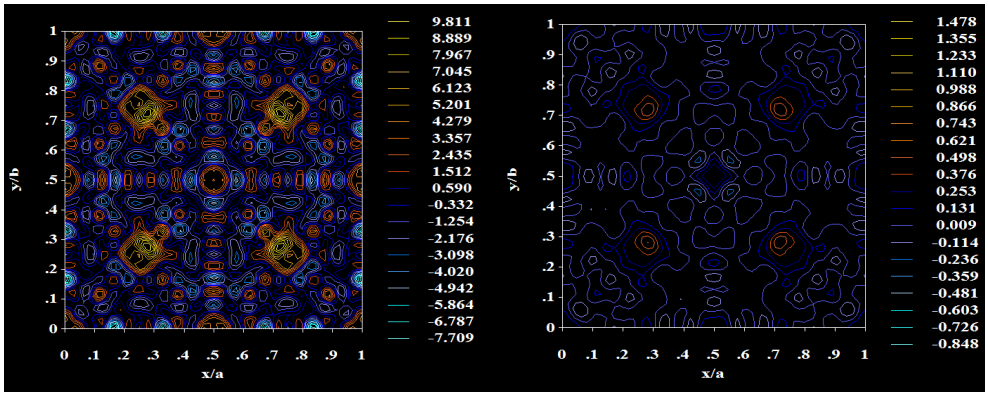

(a) (b)

Figure 2.22 The Fourier map differences obtained on the soluble structure when the potassium cations are removed, **a**, in which all the layers from $z = 0$ to 1, with an increment of 0.02, are surimposed, and **b**, at $z/a = 0.28$, with $a = 10.2056(1)$ Å, the lattice parameter. Electron density in red corresponds to an excess of electron density, whereas electron density in blue corresponds to missing electron density.

be carried out in order to refine the location and the bond distances of the water molecules in Prussian blue.

The Rietveld refinement of soluble potassium cation containing Prussian blue yields interesting results. First, it appears that the cubic primitive $Pm3m$ model used herein for refining the insoluble Prussian blue is also suitable for the soluble variety. The occupancy parameter, p, refines to a value of 0.72(1), close to the 0.75 value expected for the $Fm3m$ model, and the vacancies are rather randomly distributed in the commercial soluble Prussian blue. Furthermore, the successful refinement in the $Pm3m$ space group invalidates the previously presumed soluble $KFe^{III}Fe^{II}(CN)_6{\cdot}xH_2O$ structure, where the lattice does not contain any vacancies. The lattice parameter and average bond distances are reported in Table 2.11 and agree rather well with previously published results. The model yields 0.83(7) potassium cations, which is relatively consistent with the potassium content of 7.5 %, *i.e.*, approximately two cations per unit cell, as determined by flame emission spectroscopy. The potassium cation occupies the center of the cell octants, as is clearly evidenced by Fourier maps obtained on the structure without the potassium cations, see Figure 2.22. An excess of electron density appears in red in the zeolitic positions. The potassium cation location disagrees with the model proposed by Bueno *et al* [14], in which the potassium cations are part of the crystalline substructure, but agrees with the first model described by Keggin and Miles [11].

The $Pm3m$ model yields 5.17(3) coordinated water molecules, 0.83(7) OH^- anions, and 4.8(1) water molecules located at the 8g zeolitic positions inside the lattice cavities. The number of water molecules corresponds to 17.9 weight %, a higher water weight content than the value of 4.4 weight % determined by thermogravimetric analysis of the soluble C02 sample, see Figure 2.8. Moreover the loss of the coordinated water molecules is difficult to identify in this thermogravimetric analysis. Some coordinated oxygen ions may remain in the sample and be combined with the iron ions at high temperature to form the residual iron oxide product. However, the degree of hydration of Prussian blue is known to vary upon air exposure or humidity [83][84]. Some zeolitic water molecules may have escaped the Prussian blue lattice prior to the thermogravimetric measurement. As for the insoluble C03 sample, neutron powder diffraction studies of the soluble C02 Prussian blue may help to explain this discrepancy in water weight content.

The structure of soluble Prussian blue thus appears to be very similar to that of insoluble Prussian blue. It can be described by the formula $K_y Fe_4^{III}[Fe^{II}(CN)_6]_3 \cdot [yOH^- \cdot xH_2O]$. The presence of the OH^- anions ensures the charge balance of the potassium cations. The crystallographic position of the OH^-, either coordinated to iron(III) or inserted in the lattice cavities, is, however, not precisely known but could be resolved by neutron diffraction experiments.

In conclusion, the structural model [11] of soluble potassium cation containing Prussian blue has been revised by using high quality X-ray diffraction data obtained with synchrotron radiation. This model can now be used for interpreting the pair distribution function and X-ray absorption spectra of soluble Prussian blue. The knowledge of the soluble potassium cation containing Prussian blue structure is not only important for these interpretations, but also for the electrochromic and electroanalytical applications, which exploit the redox reactions occurring in Prussian blue.[16] The location of the water molecules and potassium cations influences the conduction mechanisms and the shape of voltammetric curves in Prussian blue films [103]. In addition, the presence of vacancies in the lattice leads to a defect structure, which is believed to influence the ionic conductivity and, hence, the electrochemistry of Prussian blue [64]. The knowledge of the soluble structure is therefore essential for understanding their redox processes and ionic exchange mechanisms.

[16] See **Section 1.1.3** for details.

2.2.5 Short-range order

In order to study the local structural configuration of the Prussian blue samples high-energy X-ray powder diffraction and iron K-edge X-ray absorption spectroscopy were carried out at the ID11 and BM26 beamlines at the European Synchrotron Research Facility, Grenoble, France.

The pair distribution function can be extracted by Fourier transform from the high-energy X-ray powder diffraction data. This function contains all the interatomic distances between nearest neighbors up to 10 nm. Iron K-edge X-ray absorption spectroscopy probes the electronic and structural environment of only iron, by measuring the X-ray absorption coefficient as a function of energy.

Pair distribution function analysis

Whereas the Bragg scattering provides average structural information, the diffuse scattering corresponds to two-body correlations and is related to the chemical short-range order and local distortions. The pair distribution function, PDF, is obtained by a Fourier transform of the total X-ray or neutron diffraction scattering pattern [104][17]

$$G(r) = 4\pi r[\rho(r) - \rho_0] = \frac{2}{\pi}\int_0^\infty Q[S(Q) - 1]\sin(Qr)\mathrm{d}Q \tag{2.17}$$

where $\rho(r)$ is the microscopic pair density, ρ_0 is the average number density, $S(Q)$ is the total structure function, *i.e.*, the normalized scattering intensity, and Q is the magnitude of the scattering vector. In case of elastic scattering, Q is defined as

$$Q = 4\pi\sin(\theta)/\lambda = 2\pi/d. \tag{2.18}$$

The Fourier transform in equation 2.17 implies recording diffraction data at an infinitely large Q. In practice, the range of Q is limited to a maximum Q value, Q_{max}. The value of Q_{max} should be as high as possible in order to maximize the window of the Fourier transform and limit truncation errors. Moreover, both good counting statistics at high Q and a low instrument background are required. These are the reasons why the PDF is best extracted from diffraction data recorded with the synchrotron radiation using high-energy X-rays.

The PDF gives the probability of finding an atom or ion at a distance r from a given atom or ion. The broadening of the peaks in the PDF depends on the distance distribution around the average value, that results from thermal vibrations or disorder. Originally the PDF analysis was used to study amorphous materials,

[17] See **Appendix B.3.2** for details.

where there is no periodicity or symmetry at long distances but where a local order exists due to atomic interactions. Since the 1990's the PDF analysis has been successfully applied to nanocrystalline compounds [105][106].

The total scattering signal of the commercial and laboratory-synthesized Prussian blues were recorded on beamline ID11 at the European Synchrotron Research Facility, Grenoble, France. The energy was 99.428 keV, with a wavelength of 0.124698 Å. A few milligrams of a Prussian blue powder were studied in glass capillaries of 0.3 mm diameter. The beam has a width of *ca.* 100 µm.

The Fit2D software [107] was used both to integrate the two-dimensional image in a linear diagram and to calibrate the sample-detector distance. Next, the PDF was extracted with the PDFgetX2 software [108]. Details about this extraction are given in **Appendix B.3.2**. Finally the PDF was fitted with the PDFGui software [109] that provides a graphical environment for PDF fitting. The PDFs of commercial insoluble, C03, and soluble, C02, Prussian blues are shown in Figure 2.23. The insoluble C03 Prussian blue exhibits slightly narrower peaks in its PDF than does the soluble C02 sample. This indicates a higher degree of ordering in the insoluble C03 Prussian blue. This is consistent with the values of the occupancy p determined by Rietveld refinement as 0.61(1) for the insoluble C03 Prussian blue, and 0.72(1) for the soluble C02 Prussian blue.

The quality of a PDF refinement is given by two agreement factors, R_w defined by equation 2.13 and a reduced χ^2, which is equivalent to the χ^2 defined in equation 2.15 divided by the number of degrees of freedom. Nevertheless the absolute value of these statistical factors are not completely relevant because most of the observed and refined parameters are not independent in the PDF profile refinement [110].

The PDFgui software used for the PDF fitting is based on an approach similar to that for Rietveld refinement. It consists of a least squares minimization in direct space of the experimental PDF with a structural periodic model. The scale factor, atomic positions, crystallite size, and thermal factors are among the parameters that can be refined to best reproduce the experimental data. The experimental resolution was determined with a LaB_6 standard. The pair distribution function was first fitted for the commercial soluble and insoluble Prussian blues, C03 and C02, respectively, and then the same model has been applied to selected laboratory-synthesized Prussian blue powders.

As evidenced by the Rietveld refinement, the insoluble C03 Prussian blue has a $Pm3m$ structure with an occupancy parameter p of 0.61(1), indicating a probability of 39% of having the central $[Fe^{II}(CN)_6]^{4-}$ site vacant. This model is believed

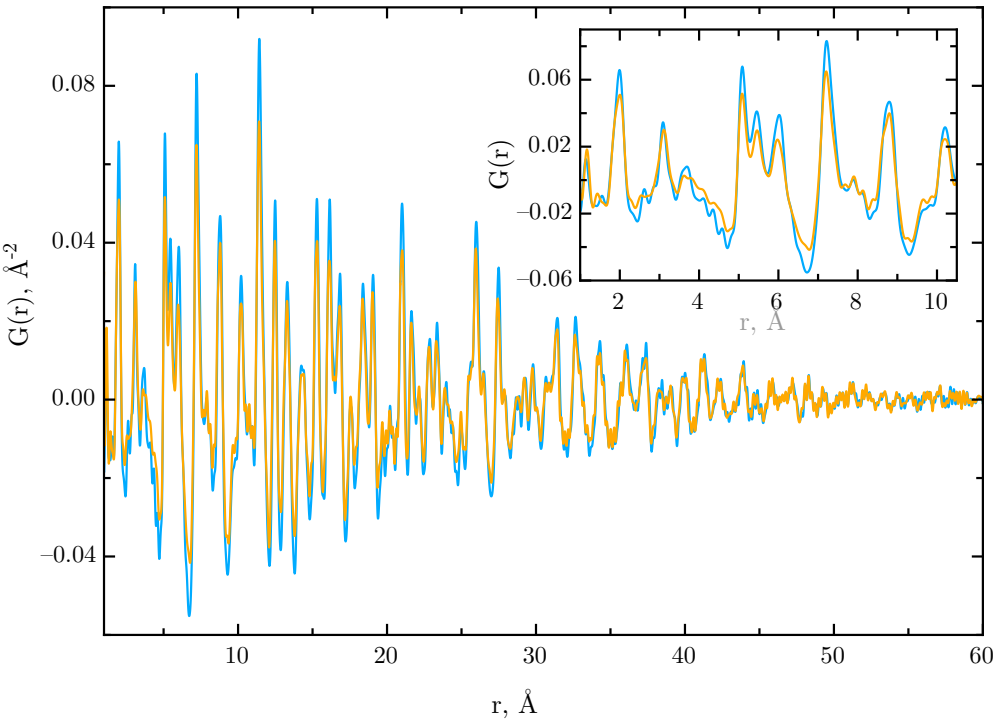

Figure 2.23 The pair distribution functions of insoluble C03 and soluble C02 commercial Prussian blues obtained with a Gaussian damping of 20 $Å^{-1}$ width and a $Q_{max} of 30$ $Å^{-1}$.

Table 2.12 Distribution of the ordered substructures for $Fe_4[Fe(CN)_6]_3{\cdot}14H_2O$ Prussian blue [13]

Substructure	No. of vacant iron(II)	Probability
A	0	0.316
B	1	0.422
C	2	0.211
D	3	0.047
E	4	0.004

to be suitable to describe the long-range ordering. In contrast, it fails to describe the local order on a length-scale shorter than or comparable to the lattice parameter, *i.e.*, up to 10.2 Å, see Figure 2.24a.

The difficulty in refining the crystal structure of Prussian blue is caused by the inherent structural disorder, due to the presence of vacancies. This is, however, characteristic of the entire class of cubic polynuclear transition metal-cyanides complexes [111]. As Herren *et al.* [13] proposed, the structure of insoluble Prussian blue can be considered as a sum of ordered substructures containing 0 to 4 $[Fe^{II}(CN)_6]^{4-}$ vacancies [13]. The distribution of these ordered substructures can be calculated by a *binomial distribution*. The probability $P_B(x;n,q)$ for observing x of the n items to be in a given state with probability q is equal to [112]

$$P_B(x;n,q) = C_n^x q^x (1-q)^{(n-x)} = \frac{n!}{x!(n-x)!} q^x (1-q)^{n-x}. \qquad (2.19)$$

In the case of Prussian blue q is the probability of having an iron(II) ion in positions 1b and/or 3d considering that four iron(III) ions occupy positions 1a and 3c, and is equal to an average of 0.75. The variable x is the number of iron(II) vacancies and can be either 0, 1, 2, 3, or 4; n is thus equal to 4. The probabilities of the substitutions are given in Table 2.12. The occupancy parameter, p, which was used in the Rietveld refinement, gives the probability of having a central iron(II) ion, *i.e.*, on position $1b$, whereas the parameter q in equation 2.19 gives an equivalent probability of having an iron(II) ion on positions $1b$ and/or $3d$. A p value of 0.61 indicates that the $[Fe^{II}(CN)_6]^{4-}$ ions are vacant on the other positions with a $p/3 \approx 20$ % probability.

The PDF data for the insoluble C03 Prussian blue was refined by combining the three substructures with the highest probability, namely substructures A, B, and C of Table 2.12. The atomic occupancies were all set to 1. The scale factor, the lattice parameter, the atomic positions, and the thermal parameters were refined for each substructure. The refinement of the PDF is much better with this

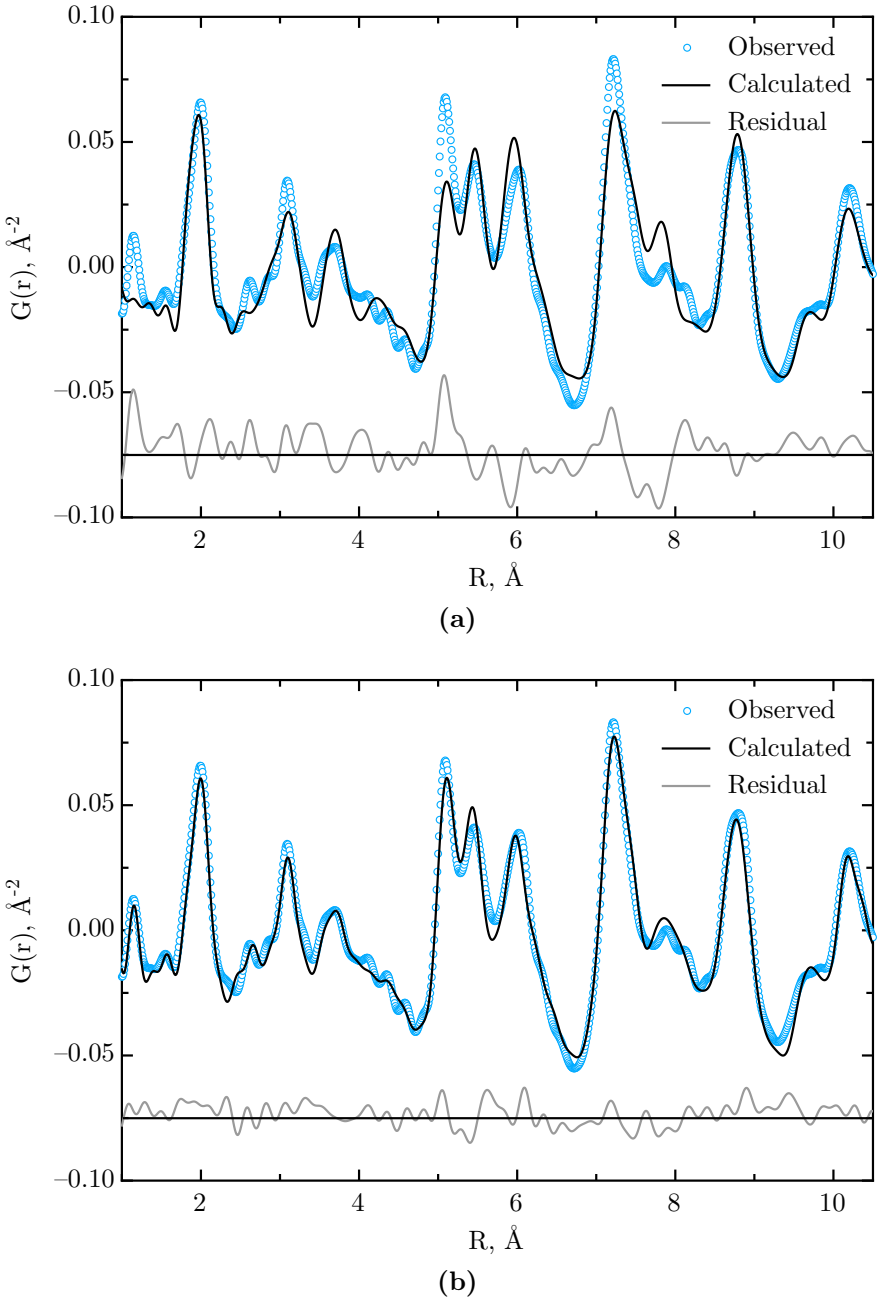

Figure 2.24 Refinement of the pair distribution function obtained for commercial insoluble Prussian blue C03 from 1 to 10.5 Å by using, **a**, the average structure $Pm3m$ with an occupancy parameter p of 0.61, R_{wp} = 33.3 %, reduced χ^2 = 0.581, and **b**, the three different substructures containing 0, 1, or 2 vacancies, R_{wp} = 17.1 %, reduced χ^2 = 0.153. The refinement is much more convincing at short distance with the modelling of the distribution of vacancies.

Table 2.13 Lattice parameter and average interatomic distances.

Label	Distance, Å				
	a	Fe(II)-C	Fe(III)-N	C-N	Fe(III)-O
C03	10.17(1)	1.92(5)	2.03(4)	1.13(6)	2.5(1)
C02	10.18(1)	1.96(9)	1.99(6)	1.18(6)	2.3(2)

[a] The values in parentheses correspond to the standard deviation of a given interatomic distance taken over the three substructures.

model, see Figure 2.24. The lattice parameter and bond distances are almost consistent within the statistical error with those presented in the previous paragraph, see Tables 2.11 and 2.13. The agreement between the observed and calculated PDF is, however, not perfect. First, only oxygen atoms and not water molecules or OH^- anions are considered in the model. This can explain the relatively high Fe(III)-O distance reported in Table 2.13. Second, impurities, such as sodium ions located in the lattice cavities of the insoluble Prussian blue, are not included in the fitting model. Finally, the oxidation state of the iron ions is not taken into account and can influence the normalization of the PDF by means of the form factor. These approximations may explain the remaining discrepancies between the experimental data and the fit shown Figure 2.24b. The model corresponds to a relative phase content in term of one unit cell of 16(3), 34(3), and 50(3) % for substructures A, B, and C, respectively. These values are different from those reported in Table 2.12, indicating that the probability, q, of having an iron(II) ions in positions 1b and/or 3d is lower than the average probability of 0.75 used in equation 2.19. This is consistent with the occupancy parameter, p, of 0.61 determined by Rietveld refinement.

A similar refinement procedure was applied to the commercial soluble, C02, Prussian blue. The resulting refinements are shown in Figure 2.25. The agreement between the calculated and observed PDF is better with the model including the three different substructures than the average $Pm3m$ model with an occupancy parameter of 0.72. The short range order clearly differs from the long range order because of non-random distribution of the $[Fe^{II}(CN)_6]^{4-}$ vacancies. The lattice parameter and interatomic bond distances are given in Table 2.13. The substructures in the commercial soluble C02 Prussian blue are distributed in terms of a unit cell with a relative phase content of 13(5), 37(5), and 50(5) % for substructure A, B, and C, respectively. This distribution confirms the presence of structural vacancies in the soluble Prussian blue that are similar to those in the insoluble Prussian blue.

The local order in Prussian blue is better described by considering several ordered substructures than with an average structure, which is only adequate for describing the long range order. Previous analyses have shown that the commer-

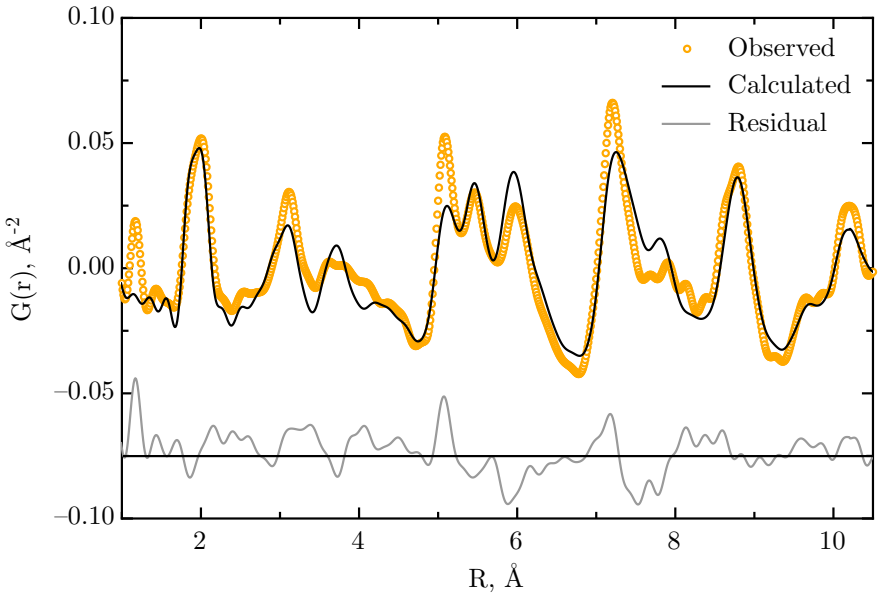

(a)

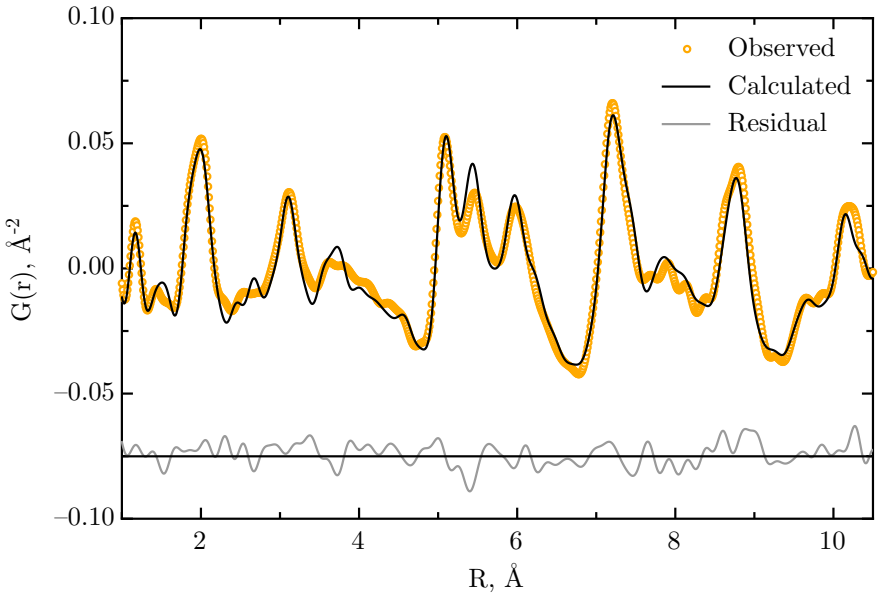

(b)

Figure 2.25 Refinement of the pair distribution function obtained for commercial soluble Prussian blue C02 from 1 to 10.5 Å using, **a**, the average structure $Pm3m$ with an occupancy parameter p of 0.72, $R_{wp} = 41.6$ %, reduced $\chi^2 = 0.351$, and **b**, three different substructures containing 0, 1, or 2 vacancies, $R_{wp} = 22.5$ %, reduced $\chi^2 = 0.103$.

cial Prussian blues and the laboratory-synthesized Prussian blues, whose synthesis included an ageing step of two hours under nitrogen atmosphere, were comparable in the sense that they exhibit similar Mössbauer spectra and X-ray powder diffraction patterns. In contrast, all the other laboratory-synthesized Prussian blues, except the well-crystallized Prussian blues, are characterized by a larger iron(III) quadrupole splitting and broader diffraction lines. Are these features related to the inherent disorder at local order? In other words, does the distribution of the ordered substructures containing zero, one, or two vacancies, significantly change with the type of synthesis?

The PDF refinement was therefore performed on three laboratory-synthesized potassium containing Prussian blues in order to determine the relative substructure distribution for each sample. The PDF of the laboratory-synthesized soluble A65, A147, and A148 Prussian blues are shown in Figure 2.26. The broadening of the PDF peaks, which is related to the disorder, clearly differs in these samples. The laboratory-synthesized A65 Prussian blue was prepared according to the direct method, without any ageing step, and is expected to be highly disordered. The degree of disorder can be related to the substructure distribution, see Table 2.14. Whereas the laboratory-synthesized soluble A148 Prussian blue has a substructure distribution similar to that of commercial Prussian blues, the A147 and A65 samples are characterized by a large relative percentage of the substructure C, corresponding to two vacancies. Attempts to fit the observed PDF for A65 with the three substructures lead to a negative relative content of substructure A. The A147 and A65 samples thus contain more iron(II) site vacancies than the A148 sample. The presence of numerous lattice defects can explain the higher strain evidenced by the Williamson-Hall method and the larger iron(III) quadrupole splitting observed for these samples. However, the number of vacancies present in the Prussian blue can not be directly calculated from the substructure distribution because the nearby unit cells share lattice edges. The final number of vacancies depends on the unit cell repartition and their tendency to group. The structural refinement of a well crystallized Prussian blue, such as the A80 sample, may help to better understand the lattice vacancy distribution in Prussian blue.

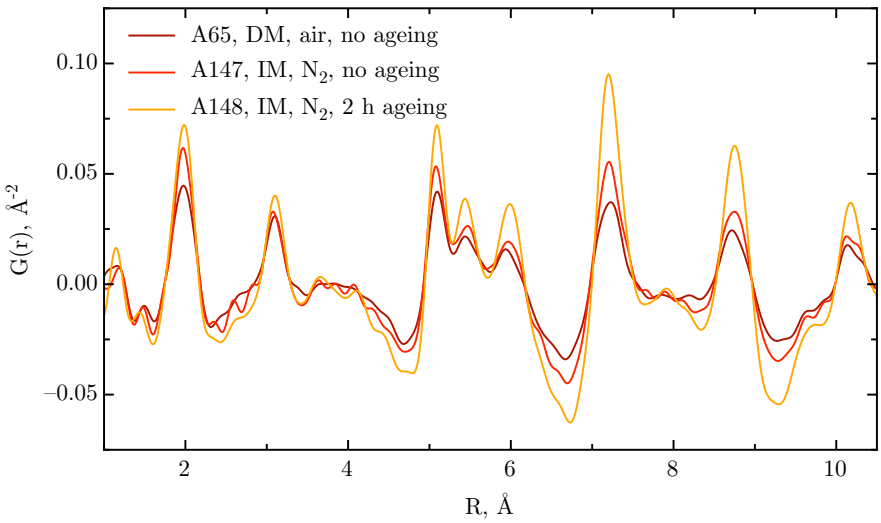

Figure 2.26 The observed pair distribution function of laboratory synthesized soluble A65, A147, and A148 Prussian blues from 1 to 10.5 Å obtained with a similar Gaussian damping width of 15 $Å^{-1}$ and a Q_{max} of 30 $Å^{-1}$.

Table 2.14 Distribution of ordered substructures for commercial Prussian blues and laboratory-synthesized potassium containing Prussian blues.

Label	**Substructures**[a]			R_w, %
	A, no vacancy	B, 1 vacancy	C, 2 vacancies	
Commercial Prussian blues				
C02	13(5)	37(5)	50(5)	22.5
C03	16(3)	34(3)	50(3)	17.1
Soluble Prussian blues containing potassium cations				
A65	0	39(1)	61(1)	29.7
A147	4(3)	37(3)	59(3)	26.0
A148	10(2)	41(2)	49(2)	24.4

[a]Relative phase content in terms of a unit cell.

X-ray absorption spectroscopy

X-ray absorption spectroscopy is based on the measurement of the absorption coefficient, $\mu(E)$, as a function of X-ray energy, E, near the absorption edge of a given element, or ion, herein iron(II) and iron(III). This technique probes the local structure around iron ions on the atomic and molecular scale. An X-ray absorption spectrum is typically divided in two parts, which are treated separately, first, the X-ray near edge absorption spectrum, XANES, which provides information up to 50 eV above the absorption edge and second, the extended X-ray absorption fine structure, EXAFS, which deals with the oscillations of the X-ray absorption coefficient, $\mu(E)$, that occur at higher energies. Basic principles, experimental details, and data reduction are detailed in **Appendix B.3.3**.

The XANES spectra of several Prussian blues obtained in transmission mode are shown in Figure 2.27. Two major features are worthy of comment, the main edge and the pre-edge.

Physically the main K-edge position corresponds to the energy threshold, E_0, *i.e.*, the lowest energy required for electrons to leave their binding site and for their associated wave to travel and be scattered in the material. The edge jump is used to normalize the full X-ray absorption spectrum and is often taken as the first inflection point on the edge. For all Prussian blues, the iron K-edge absorption edge occurs at the same energy, 7129.30 eV. The accuracy on this position is approximately 0.26 eV, half the energy step of 0.52 eV per data point used herein. The edge position can be correlated to the formal charge state, *i.e.*, to the oxidation state of the ion. This can be easily understood by considering the following. For two ions, the ion with the larger positive charge, *i.e.*, the higher oxidation state, will more strongly interact with all electrons present, increasing their binding energy. Thus a higher X-ray photon energy is required to remove additional electrons from the ion and the X-ray absorption edge shifts to higher energy. An illustration of the correlation between oxidation state and edge position may be seen in hexacyanoferrate(II) and (III) complexes, see Figure 2.27. In ammonium ferrocyanide, $(NH_4)_4Fe^{II}(CN)_6{\cdot}3H_2O$, the iron(II) K-edge position is shifted towards lower energy, at 7128.79 eV, whereas the contrary occurs for the iron(III) K-edge in potassium ferricyanide, $K_3Fe^{III}(CN)_6$, whose edge position is at 7129.82 eV. However, the correlation between the oxidation state and the edge shift is not always linear because other parameters influence this shift such as the symmetry, the neighboring atoms, or the metallic character of the sample. For example, $K_4Fe^{II}(CN)_6{\cdot}3H_2O$ has an edge position of 7129.30 eV and does not exhibit any shift in comparison with Prussian blue. The intensity of its mean edge peak, the *principal maximum*, is shifted toward lower energy. The sharpness

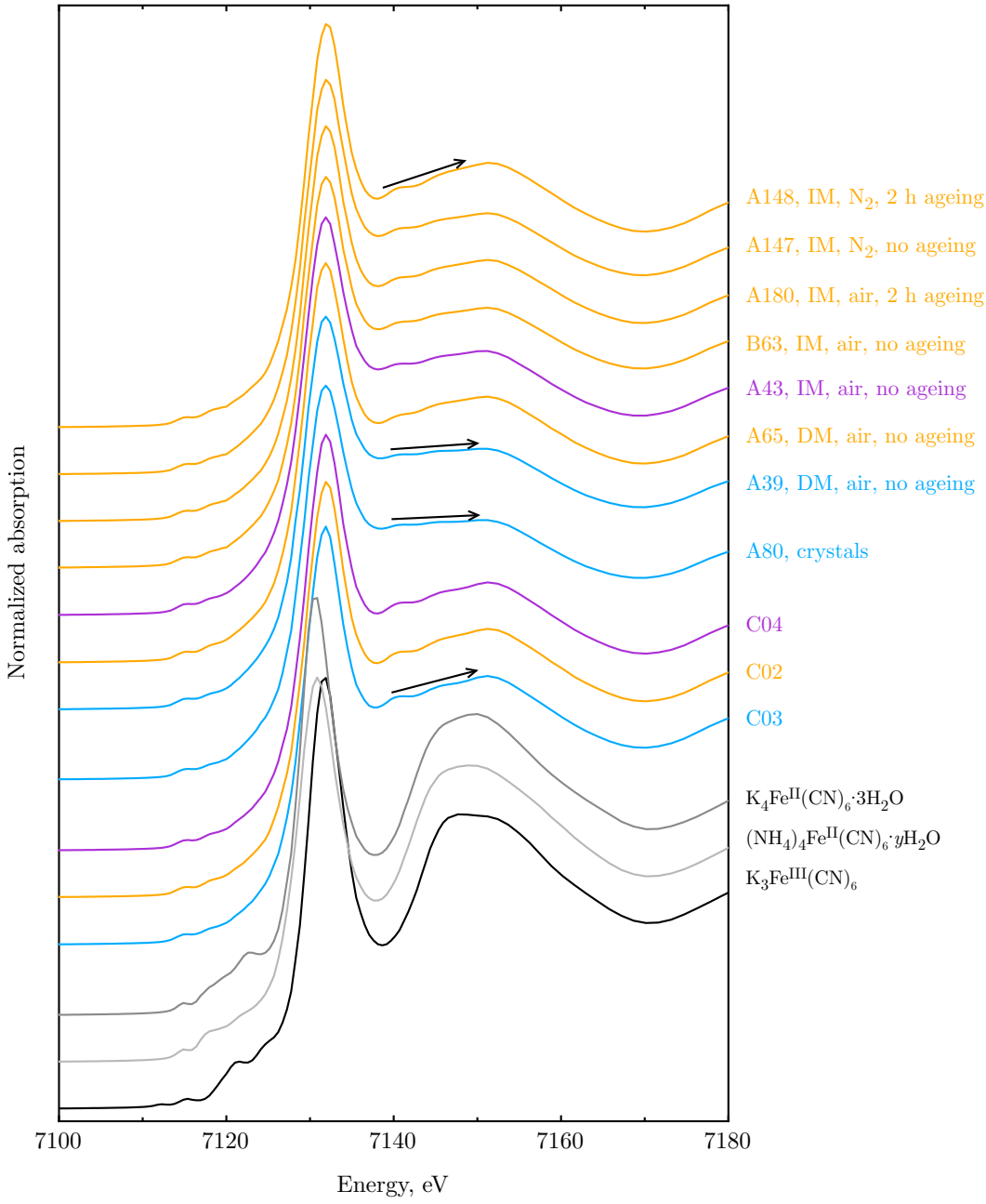

Figure 2.27 Iron K-edge XANES spectra of commercial and laboratory-synthesized Prussian blues as well as the reference compounds, $K_4Fe^{II}(CN)_6{\cdot}3H_2O$, $(NH_4)_4Fe^{II}(CN)_6{\cdot}3H_2O$, and $K_3Fe^{III}(CN)_6$. The arrows indicate the different trends in the absorption just above the K-edge absorption.

of the band is related to the confinement of the final states and core-hole lifetime.[18]

The pre-edge is the feature located just below the energy of the K-edge. These transitions are related to the local site symmetry and orbital occupancy [113] and involve linear combinations of molecular orbitals with specific symmetry properties. Strong pre-edge transitions are associated with a breaking of the inversion symmetry. In the case of centrosymmetric molecules, such as Prussian blue, the pre-edge transition strength is very weak and results rather from quadrupole transitions.

Let us now compare the XANES spectra of Prussian blues and note that they all look rather similar, there is no significant difference between the soluble and insoluble Prussian blues. The feature that can be pointed out is the slope of $\mu(E)$ above the main absorption K-edge band, as indicated by the arrows in Figure 2.27. For some samples, such as A39, A43, and A80, the slope is almost zero. This feature could be related to a specific vacancy distribution, as evidenced by the pair distribution function analysis. Some authors have explained this feature in terms of a distorted $Fe^{II}-C-N-Fe^{III}-N-C-Fe^{II}$ arrangement and its deviation from linearity [101].

The EXAFS spectra of commercial insoluble, C03, and soluble, C02, Prussian blues both in k-space and in R-space are shown in Figure 2.28. The general expression for EXAFS oscillations gives the contribution of each coordination shell, j, *i.e.*, the atoms or ions of the same type situated at approximately the same relative distance, R_j, from the absorbing atom or ion,[19]

$$\chi(k) = \sum_{j=1}^{shells} A_j(k) \sin[2kR_j + \phi_j(k)], \tag{2.20}$$

where $\phi_j(k)$ is the phase function and $A_j(k)$ is the scattering amplitude, an amplitude that takes into account a damping factor, the scattering power, and any disorder.

In Figure 2.28, the $\chi(k)$ function is weighted by k^2 in order to balance the damping of $\chi(k)$ at high k due to the decrease in the scattering amplitude. Both soluble and insoluble Prussian blues exhibit similar EXAFS spectra. This suggests that the incorporation of alkali cations does not seem to alter significantly the coordination environment of the iron ions and supports the new structural model for

[18] Due to the Heisenberg uncertainty principle the finite lifetime produces a broadening of the energy. The K core-hole full width at half maximum for the iron ion is *ca.* 1 eV [113].

[19] see **Appendix B.3.3** for details

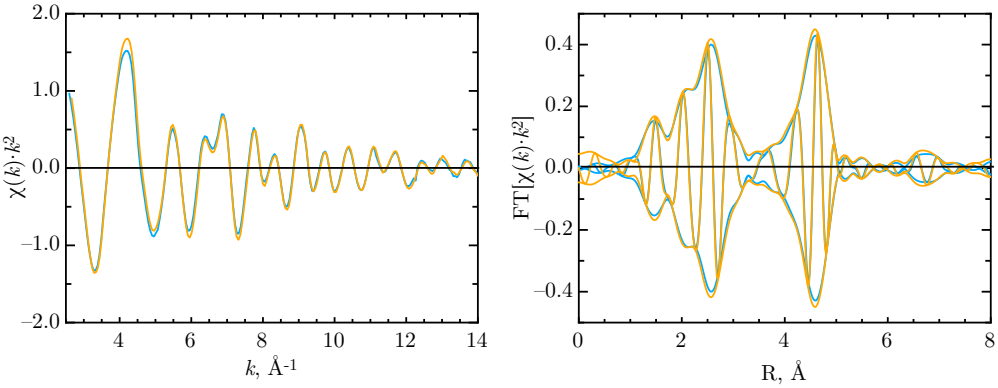

Figure 2.28 Iron K-edge $\chi(k)\cdot k^2$ and FT$[\chi(k)\cdot k^2]$ spectra with $\Delta k \sim 5.3 - 13.9$ Å^{-1} for insoluble C03 and soluble C02 commercial Prussian blues.

soluble Prussian blue determined by Rietveld refinement in **Section 2.2.5**.

Structural parameters, such as coordination number, average bond distance, and structural disorder can be obtained by fitting the EXAFS data. The starting fit model that was applied to all the Prussian blues has been elaborated by Dr. Geert Silversmit, from the Ghent University [114]. There was no significant difference in the EXAFS spectra between insoluble and soluble Prussian blues, therefore all the Prussian blues, whatever their source or preparation, were fit with the same starting coordination environment. Details concerning this fitting model are given in **Appendix B.3.3**. The experimental data and the fit of the EXAFS spectrum for soluble commercial C02 Prussian blue agree perfectly, see Figure 2.29.

According to equation 2.20, the small R_j distances contribute to oscillations with a long period in k-space, whereas the long R_k distances or path lengths contribute to oscillations with a short period in k-space. The separate contribution of each shell in k-space are evident in Figure 2.30. Further, it can be shown that the scattering amplitude for low Z elements decreases faster with k than that for high Z elements.

The commercial and laboratory-synthesized Prussian blues were fit with the same model in the k-range of *ca.* 5.3 to 13.9 Å^{-1}. Bond distances, coordination numbers, Debye-Waller factors, and inner potential corrections are reported in Table 2.15. The errors on the fit parameters were estimated from the standard deviations of the fit values obtained on six Prussian blue reference samples.[20]

[20]See **Appendix B.3.3** for details.

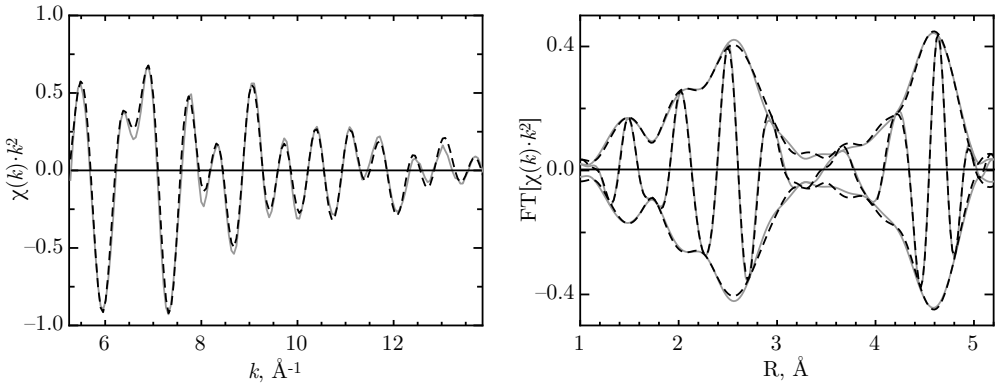

Figure 2.29 $\chi(k)\cdot k^2$ and FT$[\chi(k)\cdot k^2]$ spectra with $\Delta k \sim 5.3$ to 13.9 Å^{-1} and $\Delta R = 1.0$ to 5.2 Å for soluble C02 commercial Prussian blue. The experimental data, solid line, and fit, dotted line, agree well.

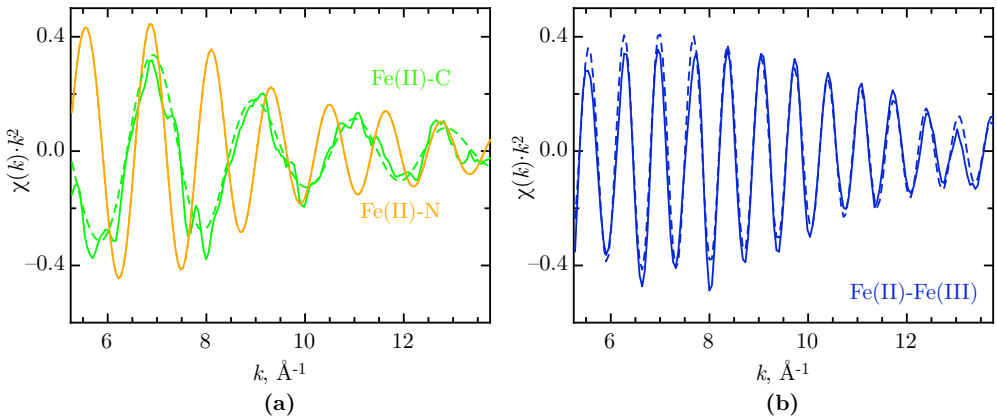

Figure 2.30 $\chi(k)\cdot k^2$ spectra of **a**, the first Fe(II)-C shell, green solid line, and the second Fe(II)-N, orange solid line, and, **b**, the third shell, Fe(II)-Fe(III). The third shell, which has the longer path length, contributes to the short period oscillations in k-space. All spectra and fits are obtained with $\Delta k \sim 5.3 - 13.9$ Å^{-1} for soluble C02 commercial Prussian blue. Experimental data and fit are in solid and dotted lines, respectively.

These quantities are indeed representative of the fit accuracy, if one considers the data quality, the fit routine, and the systematic errors due to differences in background subtraction and data reduction. The errors determined from the EXAFS spectra of Prussian blue reference samples are thus applicable to the other transmission EXAFS spectra of similar data quality. The Debye-Waller factor, σ^2, as well as the inner potential, E_0, are relative to the $K_4Fe(CN)_6$ structure, used as a reference compound, and are therefore referred as $\Delta\sigma^2$ and ΔE_0, respectively.

All commercial and laboratory-synthesized Prussian blues, independent of their method of preparation, exhibit very similar bond distances. In contrast the samples differ quite significantly in their coordination numbers, N, and especially in the iron(II)-iron(III) coordination number, see Figure 2.31. Commercial Prussian blues and laboratory-synthesized soluble A148 Prussian blue have an iron(II)-iron(III) coordination number of approximately 6, as theoretically expected. The preparation method of sample A148 was based on the synthesis of Prussian blue described in patents and includes an ageing time of Berlin white under nitrogen. The laboratory-synthesized A148 Prussian blue is thus supposed to be comparable with commercial pigments as is observed. The other laboratory-synthesized Prussian blues were either synthesized at ambient atmosphere or without any ageing. They are characterized by a smaller iron(II)-iron(III) coordination number. This is undoubtedly correlated with the presence of vacancies in the lattice with some local order, as previously observed in the pair distribution function analysis. This point is further developed in the discussion, in **Section 2.2.7**. The characterization of the modern Prussian blue samples was completed by a vibrational analysis with Raman spectroscopy.

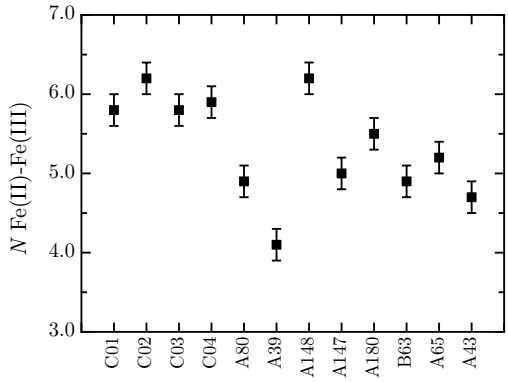

Figure 2.31 Iron(II)-iron(III) coordination number, N.

Table 2.15 Bond distances, R, coordination numbers, N, Debye-Waller factors, $\Delta\sigma^2$, and inner potential corrections, ΔE_0, for the EXAFS fit of the Prussian blues

.

Sample	Absorber-scatterer	R, Å	N	$\Delta\sigma^2$, Å^2	ΔE_0, eV
C01	Fe(II)-C	1.90(1)	2.9(1)	0.0008(2)	-4.4(3)
	Fe(III)-N	2.07(1)	3.1(1)	0.0008(2)	-0.3(5)
	Fe(II)-N	3.05(1)	2.7(1)	0.0008(2)	1.3(5)
	Fe(III)-C	3.15(1)	2.7(2)	0.0008(2)	5.2(6)
	Fe(II)-Fe(III)	5.11(1)	5.8(2)	-0.0004(2)	-4.9(3)
C02	Fe(II)-C	1.90(1)	2.9(1)	0.0000(2)	-3.9(3)
	Fe(III)-N	2.06(1)	3.0(1)	0.0000(2)	2.6(5)
	Fe(II)-N	3.04(1)	2.9(1)	0.0000(2)	2.1(5)
	Fe(III)-C	3.14(1)	3.0(2)	0.0000(2)	5.1(6)
	Fe(II)-Fe(III)	5.10(1)	6.2(2)	-0.0006(2)	-4.5(3)
C03	Fe(II)-C	1.90(1)	2.9(1)	0.0005(2)	3.6(3)
	Fe(III)-N	2.07(1)	3.0(1)	0.0005(2)	0.8(5)
	Fe(II)-N	3.04(1)	2.8(1)	0.0005(2)	1.2(5)
	Fe(III)-C	3.15(1)	2.9(2)	0.0005(2)	5.1(6)
	Fe(II)-Fe(III)	5.10(1)	5.8(2)	-0.0005(2)	-4.5(3)
C04	Fe(II)-C	1.89(1)	2.8(1)	0.0006(2)	1.9(3)
	Fe(III)-N	2.06(1)	3.1(1)	0.0006(2)	2.6(5)
	Fe(II)-N	3.04(1)	2.8(1)	0.0006(2)	2.4(5)
	Fe(III)-C	3.14(1)	2.9(2)	0.0006(2)	5.7(6)
	Fe(II)-Fe(III)	5.10(1)	5.9(2)	-0.0007(2)	-4.8(3)
A80	Fe(II)-C	1.90(1)	3.0(1)	0.0005(2)	-1.9(3)
Crystals	Fe(III)-N	2.07(1)	3.5(1)	0.0005(2)	5.2(5)
IM, HCl	Fe(II)-N	3.06(1)	3.0(1)	0.0005(2)	-2.9(5)
	Fe(III)-C	3.14(1)	3.1(2)	0.0005(2)	6.9(6)
	Fe(II)-Fe(III)	5.08(1)	4.9(2)	0.0007(2)	-4.7(3)
A39	Fe(II)-C	1.90(1)	2.8(1)	0.0009(2)	0.2(3)
DM, air	Fe(III)-N	2.07(1)	3.1(1)	0.0009(2)	3.5(5)
No ageing	Fe(II)-N	3.04(1)	2.1(1)	0.0009(2)	0.9(5)
	Fe(III)-C	3.12(1)	2.2(2)	0.0009(2)	5.9(6)
	Fe(II)-Fe(III)	5.08(1)	4.1(2)	-0.0004(2)	-4.5(3)
A148	Fe(II)-C	1.90(1)	2.8(1)	0.0000(2)	-3.8(3)
IM, N_2	Fe(III)-N	2.06(1)	3.1(1)	0.0000(2)	2.1(5)
2 h ageing	Fe(II)-N	3.04(1)	3.0(1)	0.0000(2)	1.2(5)
	Fe(III)-C	3.14(1)	3.1(2)	0.0000(2)	5.8(6)

continued on next page

Sample	Absorber-scatterer	R, Å	N	$\Delta\sigma^2$, Å^2	ΔE_0, eV
	Fe(II)-Fe(III)	5.10(1)	6.2(2)	-0.0008(2)	-5.0(3)
A147	Fe(II)-C	1.90(1)	2.7(1)	0.0007(2)	-3.9(3)
IM, N_2	Fe(III)-N	2.06(1)	3.2(1)	0.0007(2)	1.9(5)
No ageing	Fe(II)-N	3.06(1)	3.0(1)	0.0007(2)	-1.5(5)
	Fe(III)-C	3.14(1)	3.1(2)	0.0007(2)	6.3(6)
	Fe(II)-Fe(III)	5.09(1)	5.0(2)	-0.0004(2)	-4.6(3)
A180	Fe(II)-C	1.91(1)	2.9(1)	0.0000(2)	0.7(3)
IM, air	Fe(III)-N	2.08(1)	3.1(1)	0.0000(2)	0.7(5)
2 h ageing	Fe(II)-N	3.05(1)	2.9(1)	0.0000(2)	-1.2(5)
	Fe(III)-C	3.14(1)	3.0(2)	0.0000(2)	5.6(6)
	Fe(II)-Fe(III)	5.09(1)	5.5(2)	-0.0004(2)	-4.8(3)
B63	Fe(II)-C	2.13(1)	2.6(1)	0.0010(2)	-3.1(3)
IM, air	Fe(III)-N	2.13(1)	3.0(1)	0.0010(2)	1.6(5)
No ageing	Fe(II)-N	3.04(1)	3.0(1)	0.0010(2)	-0.9(5)
	Fe(III)-C	3.13(1)	3.1(2)	0.0010(2)	6.5(6)
	Fe(II)-Fe(III)	5.09(1)	4.9(2)	-0.0003(2)	-4.8(3)
A65	Fe(II)-C	1.89(1)	2.8(1)	0.0010(2)	-1.2(3)
DM, air	Fe(III)-N	2.08(1)	2.8(1)	0.0010(2)	-0.1(5)
No ageing	Fe(II)-N	3.04(1)	2.5(1)	0.0010(2)	2.2(5)
	Fe(III)-C	3.12(1)	2.6(2)	0.0010(2)	5.6(6)
	Fe(II)-Fe(III)	5.09(1)	5.2(2)	0.0001(2)	-4.6(3)
A43	Fe(II)-C	1.90(1)	2.9(1)	0.0008(2)	-0.9(3)
IM, air	Fe(III)-N	2.08(1)	3.0(1)	0.0008(2)	-0.9(5)
No ageing	Fe(II)-N	3.03(1)	2.4(1)	0.0008(2)	2.0(5)
	Fe(III)-C	3.13(1)	2.5(2)	0.0008(2)	7.4(6)
	Fe(II)-Fe(III)	5.09(1)	4.7(2)	-0.0002(2)	-4.5(3)

2.2.6 Vibrational analysis

The vibrational analysis of modern Prussian blue samples was carried out with the help of Pr. B. Gilbert and the measurements were performed in the Chemistry Department at the University of Liège.

The Raman spectra of selected commercial and laboratory-synthesized Prussian blues, as well as potassium ferrocyanide, $K_4Fe^{III}(CN)_6{\cdot}3H_2O$, and potassium ferricyanide, $K_3Fe^{III}(CN)_6$, are shown in Figure 2.32.

As cyanide complexes, Prussian blue, potassium ferrocyanide and ferricyanide exhibit sharp CN^- stretching bands, ν(CN), in the 2000 to 2200 cm^{-1} region of the spectrum [115]. In aqueous solution the stretching mode for free CN^- occurs at 2080 cm^{-1}, whereas the ν(CN) frequency increases upon coordination to a metal ion. Indeed, the CN^- ligand acts both as a σ-donor and a π acceptor,[21] removing electrons from the ligand's weakly antibonding σ-orbital tends to increase the ν(CN) whereas the π-back-bonding leads to a decrease in ν(CN) because electrons from the π-bonding metal ion are delocalized to the antibonding $2p\pi^*$ ligand orbital. As CN^- is a better σ-donor than a π-acceptor, the energy of the ν(CN) band in complexes is slightly increased in comparison with the free CN^-. Thus, the position of the ν(CN) bands depends on the strength of the bond with the central metal cation, which itself is influenced by the electronegativity, the oxidation state, and the coordination number of the metal ion. For example, the ν(CN) bands are higher in $K_3Fe^{III}(CN)_6$, at 2135 and 2130 cm^{-1}, than in $K_4Fe^{II}(CN)_6{\cdot}3H_2O$, where they are at 2082 and 2066 cm^{-1}. This results because the higher is the oxidation state, the stronger is the σ-bonding.

Prussian blue, potassium ferrocyanide and ferricyanide crystallize with O_h symmetry and thus have a center of symmetry. Selection rules require that only vibrations that are symmetric with respect to the center of symmetry, *i.e.*, g vibrations, are active in a Raman spectrum [115][116]. Therefore the two CN^- stretching bands are assigned to the A_{1g} and E_g modes; only the F_{1u} mode is infrared active, as is stated by the *mutual exclusion rule*, see **Appendix B.2** for more details. According to recent studies on the vibrational spectra of the cyanide ligand in Prussian blue analogs, the totally symmetric A_{1g} Raman mode often has both the larger energy and the higher intensity [117][118].

The Prussian blue bands in the low-frequency spectral region correspond to the stretching and bending modes, ν(FeC) at 600 to 350 cm^{-1}, δ(FeCN) at 500 to 350 cm^{-1}, and δ(CFeC) at 130 to 60 cm^{-1} [115][119]. However, the assignement of each specific low-frequency band has not been reported in the literature.

[21] For details about the ligand-metal bonding in complexes, see **Section 1.1.2**.

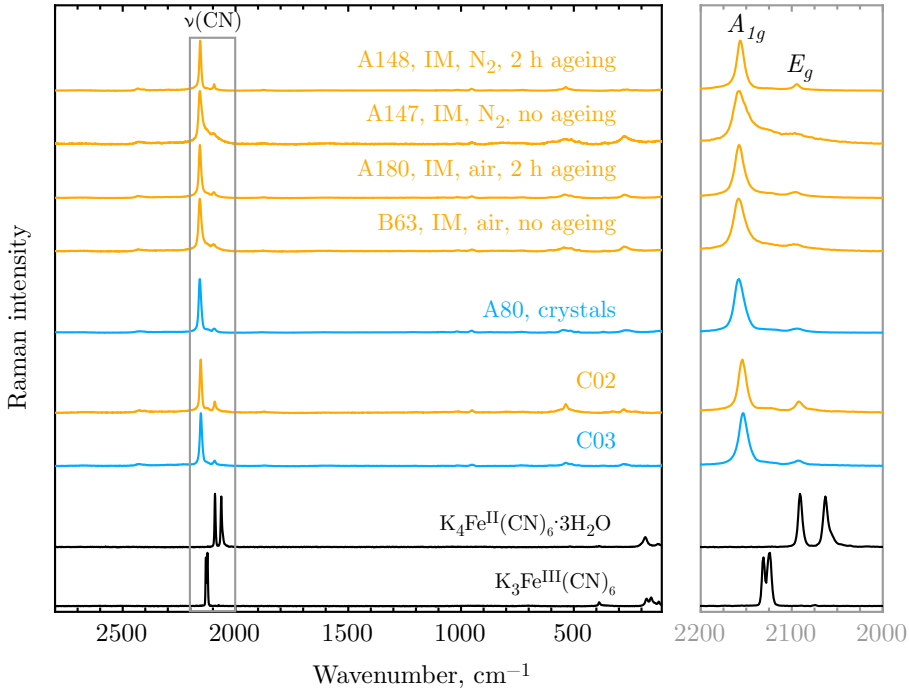

Figure 2.32 Raman spectra of Prussian blues. Each spectrum is normalized to the intensity of its most intense absorption band.

Is there any characteristic feature observed in the Raman spectra shown in Figure 2.32 that is correlated with the Prussian blue preparation method? Visually all the Raman spectra look very similar, see Figure 2.32. Taking into account the experimental error on the wavenumber estimated to ± 2 cm^{-1}, the position of the A_{1g} mode at 2154 cm^{-1} and the E_g mode at 2090 cm^{-1} are identical in all Prussian blues and agree with the data previously published in the literature. It is noteworthy that the ν(CN) bands are broader than the two sharp bands in potassium ferrocyanide and ferricyanide. This sharpness probably arises form their excellent crystallinity. The peak broadening varies slightly among the Prussian blues. For example, the laboratory-synthesized soluble B63 and A147 Prussian blues, which were prepared without any ageing of Berlin white, exhibit broader peaks and a less well resolved E_g mode. This could be due to poor crystallinity and local disorder, as is evidenced by the previous studies. This could also suggest the presence of some $[Fe^{III}(CN)_6]^{3-}$ ions [62], because the characteristic ν(CN) bands of $K_3Fe^{III}(CN)_6$ are at 2135 and 2130 cm^{-1}.

2.2.7 Discussion

The objective of this section has been the identification of the various spectral and physical properties that vary with the type of synthesis and that could, thus, influence the fading of a Prussian blue pigment in paint layers. From the thorough characterization of the modern Prussian blue samples two major features appear to be strongly dependent on the preparative methods, the particle size and the local disorder.

Commercial Prussian blues and laboratory-synthesized Prussian blues that were prepared according to the indirect method under a nitrogen atmosphere, with an ageing of the Berlin white, exhibit larger pigment particles of *ca.* 50 to 80 nm diameter, than do the other laboratory-synthesized Prussian blues, which consist of particles smaller than 15 nm. The particle size in the Prussian blue samples has been directly determined by scanning electron microscopy and the crystallite size, *i.e.*, the coherence length, has been indirectly derived from the peak broadening of X-ray powder diffraction data. Although the primary particle size does not necessarily correspond to the crystallite size, both crystallites and particles seem to have similar dimensions in the Prussian blues.

The ageing step and the atmosphere were identified as the parameters that affect the particle size. It is well known that an ageing step can help a system to tend toward or to reach stability. Thermodynamic stability implies a minimization of the surface area of the precipitate. Therefore an ageing of colloidal suspension usually tends to increase the particle size [120]. As is evidenced by X-ray powder diffraction, Prussian blues that have been aged during synthesis are indeed more crystalline and exhibit sharper diffraction lines. Crystal growth and ageing time are thus intimately correlated. However, the crystal growth is less significant when the ageing step occurs in the ambient atmosphere, as was the case for the laboratory-synthesized A180 Prussian blue. Oxygen from the air rapidly oxidizes the Berlin white precipitate into Prussian blue and no further growth then seems to occur.

Results obtained by iron K-edge X-ray absorption spectroscopy, pair distribution function analysis, and iron-57 Mössbauer spectroscopy indicate a local disorder in all Prussian blue samples. This inherent structural disorder, which is representative of the entire class of cubic polynuclear transition-metal cyanide complexes, is well known [111]. This is the reason why the structure of Prussian blue and other transition-metal cyanides is usually approximated by the $Fm3m$ space group. However, the Rietveld refinement of X-ray powder diffraction data using a cubic primitive $Pm3m$ model permits an evaluation of the degree of ordering by means of the occupancy parameter, p. The soluble potassium cation

containing Prussian blue structure has been revisited. It can be described with the $Pm3m$ space group where approximately one quarter of the $[Fe^{II}(CN)_6]^{4-}$ sites are vacant. The structural similarity between the insoluble and soluble Prussian blues may explain why the iron-57 Mössbauer spectra and the iron K-edge absorption spectra of both varieties of Prussian blue are not significantly different.

The local short range disorder studied in Prussian blue by pair distribution function analysis can be quantified by considering three different ordered substructures. The probability of having a unit cell containing more than one vacancy increases for the poorly crystallized Prussian blue samples. As a result, the iron-iron coordination number, which has been determined by iron K-edge EXAFS analysis, is smaller for these samples. The well-crystallized A80 Prussian blue is also characterized by a small iron-iron coordination number, but, in this particular case, this small number results from a high degree of ordering in the crystals. A higher vacancy content and a small particle size are thus correlated. Because the small particle size results from a rapid crystallization, the presence of additional defects in the lattice is also expected.

Particle size and local disorder are certainly among the parameters that can influence the fading of Prussian blue. It has been shown that the particle size directly affects the color of the pigment [51]. Moreover, small pigment particles tend to fade more rapidly upon light exposure than larger particles because of their increased surface area. The presence of additional $[Fe^{II}(CN)_6]^{4-}$ vacancies reduces the probability of intervalence charge transfer. However the smallest particle size and the largest extent of disorder were observed for the laboratory-synthesized Prussian blues that were not prepared according to methods recommended by the pigment industry. The latter methods are expected to be optimized in order to ensure the highest pigment stability. Therefore, the particle size and the local disorder in the commercial Prussian blues or the laboratory-synthesized Prussian blues that are prepared according to syntheses described in patents, such as the soluble A148 sample, may not be that critical for the fading of Prussian blue.

2.3 Ancient syntheses

The composition and quality of Prussian blue pigments synthesized according to the ancient methods were much more variable because of the rather empirical character of the process. Ingredients and their proportions used in the ancient recipes have been studied and indexed in details by Kirby *et al.* [58] and Asai [121]. However, the underlying chemical reactions have not been clearly identified nor have the factors that, in the eighteenth century syntheses, influenced the light fastness of Prussian blue. In the following subsections the ancient syntheses and their preparation are presented. Next, the so-obtained pigments are analyzed with the techniques previously used for the characterization of modern Prussian blues. Finally, the results are discussed and compared with those obtained on modern Prussian blue samples.

2.3.1 Eighteenth century recipes

Only two reagents are essential to produce Prussian blue by precipitation, an iron salt and an alkali hexacyanoferrate. However, the latter product was unknown in the eighteenth century. At that time potassium hexacyanoferrate was indirectly obtained from the calcination of animal matter and an alkali. The residue of this calcination was thrown in boiling water and a pale-yellow solution resulted that presumably contained potassium hexacyanoferrate. This solution was then mixed with a solution of an iron(II) salt and alum, leading to the formation of a pale greenish precipitate. This was filtered and, finally, treated with hydrochloric acid to yield Prussian blue.

For a long time color pigment makers believed Prussian blue to be a lake as it was prepared from organic material. The term *lake* referred to an organic pigment obtained from the precipitation of a soluble organic dye which is absorbed onto a mineral support, such as alumina hydrate, *i.e.*, aluminum hydroxide [122]. This erroneous belief explains why alum was used as a starting reagent, although Macquer had already observed in 1752 that alum was not required for the precipitation of Prussian blue [15].

Reproduction of two eighteenth century syntheses

Two eighteenth century syntheses were reproduced herein, one preparative method based on the recipe developed by R. Dossie in 1758 [123] and a second synthesis based on the preparation described by M. Le Pileur d'Apligny in 1779 [124]. The original text of both recipes is reproduced in **Appendix D**. The major difference

Table 2.16 Reagent proportions for the two selected eighteenth century recipes

Synthesis	**Reagent proportions in parts**				
	Dried blood	Alkali K_2CO_3	Iron salt $FeSO_4{\cdot}7H_2O$	Alum $KAl(SO_4)_2{\cdot}12H_2O$	Acid HCl
Dossie	3	1	1	2	4
Le Pileur d'Apligny	8	8	3	4	4

between the two methods is the proportion of the ingredients, see Table 2.16.

Most of the designations for the ingredients cited in both recipes are no longer in use. For example, *green vitriol/vitriol de Mars* or *copperas* refers to iron(II) sulfate, $FeSO_4$. The terms *spirit of salt* or *acide marin* correspond to hydrochloric acid. By *pearl-ashes* one should understand potassium carbonate, K_2CO_3. The term *potasse* used in Le Pileur d'Apligny's recipe is confusing and could be either potassium hydroxide, KOH, or potassium carbonate; the latter was finally chosen as the starting reagent, as has been suggested by Kirby and Saunders [58].

Dried blood used as garden fertilizer was taken as the organic matter. All other reagents used herein for the syntheses of ancient Prussian blue were of reagent grade quality and obtained form Sigma-Aldrich, Steinheim, Germany. Appropriate amounts of dried blood and potassium carbonate, K_2CO_3, were mixed in a crucible and progressively heated in a Nabertherm furnace. The temperature was allowed to increase from room temperature to 650°C in two hours. The mixture initially burned with an orange flame. At 450°C the contents were remove from the furnace and stirred. At a temperature of 650°C, no combustion was taking place and the contents of the crucible were reddish. The crucible was then removed from the furnace and the contents were dropped into approximately 300 mL of boiling deionized water and the mixture was boiled for 45 minutes. After filtration, a pale yellow filtrate was collected and mixed with an aqueous solution of iron sulfate, $FeSO_4{\cdot}7H_2O$ and alum, $KAl(SO_4)_2{\cdot}12H_2O$ previously dissolved in deionized water. A pale-greenish precipitate immediately formed and was collected by filtration. A prolonged delay of several hours between the formation and the filtration of the greenish precipitate leads to the formation of an orange compound at the surface of the sediment.

Because two shades of Prussian blue were reported in the eighteenth century, a pale one and a dark one, the collected precipitate was divided in two fractions. The first part was treated with hydrochloric acid in order to eliminate the aluminum

Figure 2.33 Important steps in the eighteenth century recipe for producing Prussian blue. 1. Calcination of a mixture of dried blood and alkali; 2. Extraction of a yellow filtrate from the calcined residue dropped into boiling water; 3. Mixture of iron(II) sulfate and alum; 4. Precipitation of both solutions; 5. Filtration and washing with water; Optional 6. Addition of hydrochloric acid.

compound presumably hydroxide, and then thoroughly washed with deionized water. The product was finally air-dried and ground into a dark blue powder. The second part was only washed with deionised water so that the aluminum compound remains in the pigment as an extender. After air-drying and grinding a pale green-blue powder was obtained. The important steps of the eighteenth century recipes are illustrated in Figure 2.33.

Both syntheses were reproduced several times, first to determine the missing parameters in the recipes, such as the maximum calcination temperature and duration of the calcination and, second, to evaluate the reproducibility of the syntheses. A calcination temperature of at least 600°C was necessary to obtain a complete combustion of the dried blood. The duration seems to be less critical but must be long enough to combust all of the animal matter between room temperature and 600°C. The liquor that is collected after filtration of the aqueous solution containing the residue of the calcination, presumably contains potassium ferrocyanide. The yield of the synthesis is extremely small; although 30 g of dried blood was used for Dossie's synthesis, less than 1g of Prussian blue was col-

lected. The same occurs for Le Pileur d'Apligny's recipe. The limiting reagent is most likely the hexacyanoferrate(II) complex, presumably formed by calcination of blood and potassium carbonate.

Although the synthesis is expected to be better controlled due to modern laboratory conditions in comparison with the situation in the eighteenth century, the reproducibility of the eighteenth century recipes is problematic and the attempts were not always successful. The critical step appears to be the filtration of the greenish precipitate followed by its washing with water. Before treatment with hydrochloric acid the precipitate should be light blue, presumably containing Prussian blue and aluminum hydroxide. However it was often rather light-green. Moreover, when the precipitate is not treated with acid in order to preserve the aluminum compound as an extender, the precipitate could turn completely brown, spoiling the pigment. It was already mentioned in eighteenth and nineteenth century books that the washing of the pigment was critical in order to obtain an intense blue color.

Five samples from successful syntheses, as well as one sample from an unsuccessful synthesis, which led to the production of a brown powder, were selected for further analyses, see Table 2.17. The color of each powder, which was mixed with gum arabic and painted in a pure state on watercolor paper, was evaluated by UV-visible reflectance, see Figure 2.34. The final pigments obtained were of variable color quality after treatment with hydrochloric acid, ranging from intense blue for B64 and B61b to blue-gray for B42a. B46b and B61a were not treated with hydrochloric acid and contain an aluminum compound, presumably aluminum hydroxide, as an extender. Consequently, they show a higher reflectance due to their paler shade. B61a has a greenish tint; the position of its reflectance extents from a shoulder at 450 nm to a maximum at 514 nm, see Figure 2.34. B42b was also not treated with hydrochloric acid and contain an aluminum compound, but, in contrast to B46b and B61a, which are light blue, B42b turns completely brown. The UV-visible reflectance spectrum of B42b is not shown in Figure 2.34.

The following subsections concern the characterization of these laboratory-synthesized eighteenth century samples, *i.e.*, their analytical composition and vibrational and structural configurations, in order to identify the parameters that could play a role in their fading.

Table 2.17 Description and labels of the eighteenth century laboratory-synthesized Prussian blues

Synthesis		Labels	Color appreciation
Dossie	Treated with acid	B61b	Dark blue
	No acid treatment, + Al compound	B61a	Light blue-green
		B46b	Light blue
Le Pileur d'Apligny	Treated with acid	B42a	Dark blue-gray
		B64	Intense dark blue
	No acid treatment, + Al compound	B42b	Brown

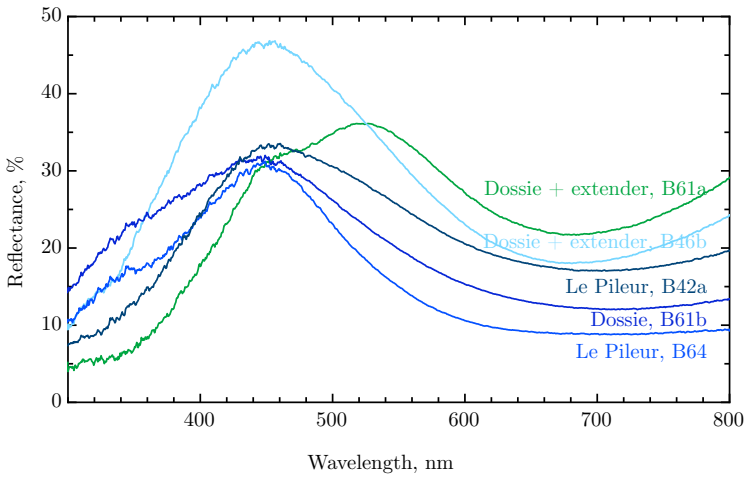

Figure 2.34 UV-visible spectra of laboratory-synthesized Prussian blues prepared according to the eighteenth century recipes, mixed with gum arabic, and painted onto watercolor paper.

2.3.2 Elemental composition

Identification

As previously reported for the modern Prussian blue samples, iron-57 Mössbauer spectroscopy was used to confirm the formation of ferric ferrocyanide. The Mössbauer spectra at 295 K of the laboratory-synthesized eighteenth century samples are shown in Figure 2.35. The spectra of B61b and B64 were fit similarly to the spectra of modern Prussian blues, *i.e.*, with two Lorentzian components, one iron(II) singlet and one iron(III) doublet, see Table 2.18. In contrast samples B42a and the samples containing an extender, B42b, B61a, and B46b, exhibit rather different Mössbauer spectra.

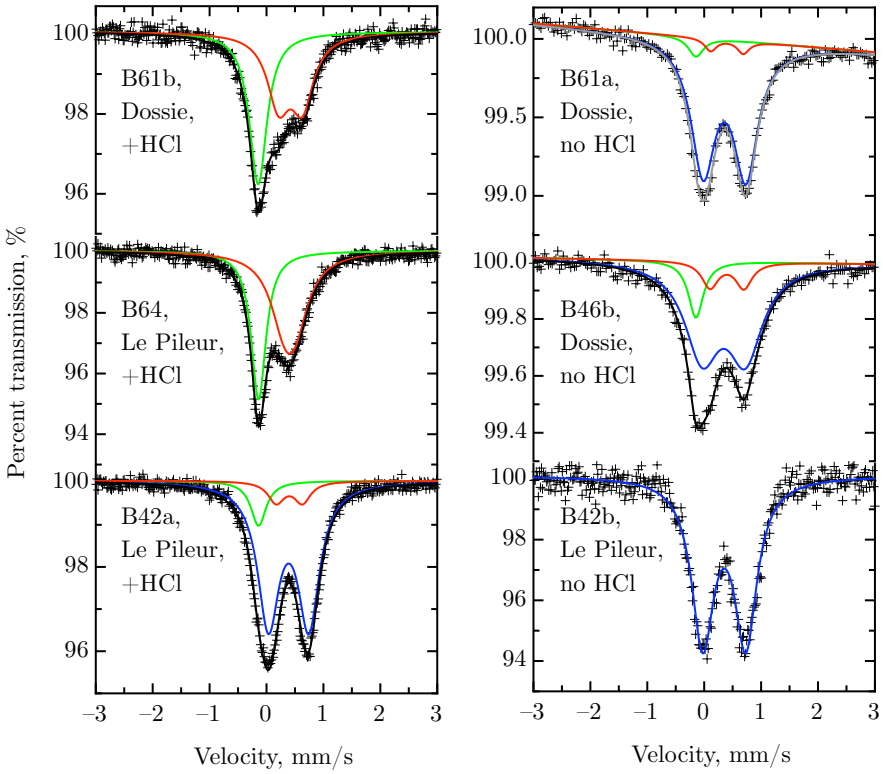

Figure 2.35 The 295 K Mössbauer spectra of laboratory-synthesized eighteenth century Prussian blues. The green and red solid lines represent the iron(II) and iron(III) components of Prussian blue, respectively. The blue solid line corresponds to a ferrihydrite quadrupole doublet.

Table 2.18 The 295 K Mössbauer spectral parameters of laboratory-synthesized eighteenth century Prussian blues

Labels	Synthesis	δ^{II} mm/s[a]	Γ^{II} mm/s[b]	A^{II} %[c]	δ^{III} mm/s[a]	Γ^{III} mm/s[b]	$\Delta E_Q^{\mathrm{III}}$ mm/s
B61b	Dossie, +HCl	-0.146(3)	0.37(1)	47(2)	0.42(1)	0.48(2)	0.42(1)
B64	Le Pileur, +HCl	-0.139(2)	0.32(1)	41(1)	0.407(5)	0.59(2)	–

[a]The isomer shift, δ, is referred to α-iron at 295 K. [b]Γ is the full line width at half-maximum. [c]$A^{\mathrm{III}} = 100 - A^{\mathrm{II}}$.

The Mössbauer spectrum of the brown powder, B42b, resembles that of *ferrihydrite*, *Fh*. Ferrihydrite is a poorly-ordered hydrous iron(III) oxide, composed of spherical particles of 2 to 7 nm diameter and described by the chemical formula $Fe_5HO_8{\cdot}4H_2O$ [125]. However, because of the nanocrystallinity of ferrihydrite, the determination of an accurate stoichiometry and structure is difficult and is still questioned [126]. The iron-57 Mössbauer spectrum of ferrihydrite consists of a doublet with an isomer shift of *ca.* 0.35 mm/s and an average quadrupole splitting of 0.70 mm/s [125][127]. The value of the quadrupole splitting is correlated with the crystallinity of the ferrihydrite; the poorer the crystallinity, the higher is the quadrupole splitting, which can increase up to 0.8 mm/s. Ferrihydrite is formed by the rapid oxidation of iron-containing solutions [125]. The possibility that ferrihydrite could be produced during the ancient synthesis of Prussian blue is reasonable. B42a, B61a, and B46b, which exhibit a blue shade, are thus believed to contain ferrihydrite as well as a small amount of Prussian blue.

The Mössbauer spectra of B42a, B61a and B46b were fit with three components, the iron(II) singlet and the iron(III) doublet characteristic of Prussian blue and a third doublet with the spectral parameters of ferrihydrite. The isomer shifts of the iron(II) singlet and the iron(III) quadrupole doublet were fixed to an average value of -0.145 mm/s and 0.400 mm/s, respectively. The line width Γ^{III} was set to 0.350 mm/s. The percent areas of both Prussian blue components were constrained to be equal, *i.e.*, $A^{\mathrm{II}} = A^{\mathrm{III}}$. The isomer shift, δ^{Fh}, the quadrupole splitting, ΔE_Q^{Fh}, the full line widths at half-maximum, Γ^{Fh} and Γ^{II}, the quadrupole splitting, $\Delta E_Q^{\mathrm{III}}$, and the percent area of Prussian blue, A^{II}, were adjusted, and the results are given in Table 2.19.

Table 2.19 The 295 K Mössbauer spectral parameters of laboratory-synthesized eighteenth century Prussian blues containing an extender

Labels	Synthesis	Comp.	δ, mm/s[a]	Γ, mm/s[b]	ΔE_Q, mm/s	A, %[c]
B42b	Dossie no HCl	Fh	0.352(3)	0.48(1)	0.76(1)	100
B42a	Le Pileur, no HCl	Fe(II)	-0.145[d]	0.33(2)	–	9.3(5)
		Fe(III)	0.400[d]	0.350[d]	0.46(3)	9.3(5)
		Fh	0.388(2)	0.46(1)	0.709(4)	81(1)
B61a	Dossie no HCl	Fe(II)	-0.145[d]	0.3(1)	–	5(1)
		Fe(III)	0.400[d]	0.350[d]	0.5(2)	5(1)
		Fh	0.359(5)	0.50(1)	0.75(2)	91(2)
B46b	Dossie, no HCl	Fe(II)	-0.145[d]	0.32(3)	–	11(1)
		Fe(III)	0.400[d]	0.350[d]	0.56(6)	11(1)
		Fh	0.34(1)	0.75(3)	0,76(2)	78(3)

[a]The isomer shift, δ, is referred to α-iron at 295 K. [b]Γ is the full line width at half-maximum. [c]$A^{\mathrm{III}} = A^{\mathrm{II}}$ and $100 = A^{Fh} + A^{\mathrm{II}} + A^{\mathrm{III}}$. [d]Constrained parameter; *cf.* text.

Among the iron ions in B42a and B46b, only *ca.* 20 % are found in Prussian blue. For the powder B61a this proportion decreases to 10 %. The large amount of ferrihydrite, which is orange-colored, as are other iron oxides, could explain the color shift from blue to dark blue-gray for B42a, and from light blue to light green, for B61a. B46b contains somewhat more Prussian blue than B61a, and appears bluer, see Figure 2.34. Particles of ferrihydrite can be easily identified in optical micrographs, see Figure 2.36. The dominant blue in these three powders highlights the very high tinting strength of Prussian blue. The relatively high ferrihydrite quadrupole splitting suggests a poor crystallinity of ferrihydrite in the powders.

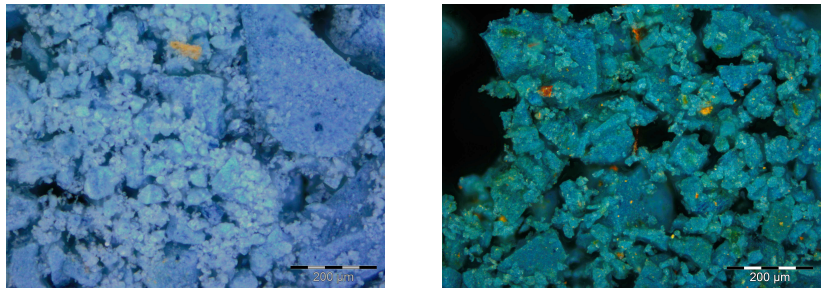

(a) **(b)**

Figure 2.36 Optical micrographs of laboratory-synthesized eighteenth century Prussian blues containing an extender, **a**, B46b and **b**, B61a. The micrographs have been obtained with reflected visible light and dark field illumination. The orange particles are ferrihydrite.

Elemental analysis

The powders were analyzed by proton induced X-ray emission studies in order to determine their elemental composition. The results are reported in Table 2.20. The elemental composition was calculated by taking into account the undetectable elements present in the sample, such as the H, C, N, and O found in the CN^- and OH^- present; the water was not considered in the elemental composition. As expected, the samples that were not treated with hydrochloric acid contains a relatively large aluminum content. The iron content in the B64 and B61b pigments is in agreement with the previous analytical results obtained on modern Prussian blues, see **Section 2.2.2**. B64 contains potassium cations whereas B61b does not. One should note the relatively high phosphorus and sulphur content present in all samples; it most likely comes from the dried blood used as a starting reagent.

Table 2.20 Composition of laboratory-synthesized eighteenth century Prussian blues and the dried blood used as starting reagent determined by PIXE

	Element, wt %[a]								
Label	**Na**	**Al**	**Si**	**P**	**S**	**Cl**	**K**	**Ca**	**Fe**
B64[b]	–	0.2(1)	0.2(1)	1.1(1)	0.9(1)	0.1(1)	7.4(1)	–	37.2(2)
B61b[b]	–	–	0.4(1)	0.2(1)	0.7(1)	0.5(1)	0.7(1)	0.1(1)	40.0(3)
B42a[c]	–	3.6(2)	0.6(1)	14.6(2)	1.5(1)	–	0.7(1)	–	49.2(4)
B61a[d]	–	24.0(3)	–	1.3(1)	8.5(2)	–	0.2(1)	–	13.5(2)
B46b[d]	–	28.9(5)	0.3(1)	1.0(1)	8.0(2)	–	0.1(1)	–	19.6(7)
B42b[d]	0.3(1)	12.7(2)	0.5(1)	0.6(1)	2.0(1)	–	0.7(1)	–	30.7(2)
Compound	**Na**	**Mg**	**Si**	**P**	**S**	**Cl**	**K**	**Ca**	**Fe**
Dried blood	7.4(7)	3.4(4)	–	7.8(3)	12.8(4)	13.8(4)	29.7(6)	16.2(6)	3.1(3)

[a]The values given in parentheses are the errors evaluated from the statistical error and the fit error given by Gupixwin. The elemental concentration is calculated by taking into account the undetectable elements, H, C, N, and O elements, as [b]$Fe(CN)_6$, [c]FeOOH, and [d]FeOOH and $Al(OH)_3$.

2.3.3 Structural configurations and short-range order

The structural configurations in the laboratory-synthesized eighteenth century Prussian blues were studied by X-ray powder diffraction, high-energy X-ray powder diffraction in order to obtain the pair distribution function, and, finally, by iron K-edge X-ray absorption spectroscopy.

Crystal structure

X-ray laboratory powder diffraction patterns are shown in Figure 2.37. The Prussian blue B64 and B61b samples exhibit a diffraction pattern that is similar to that of commercial Prussian blue. The diffraction lines are however broadened, indicating the presence of nanoparticles and strain. Particle size and strain were estimated by the Williamson-Hall method, see Figure 2.38. B64 contains particles

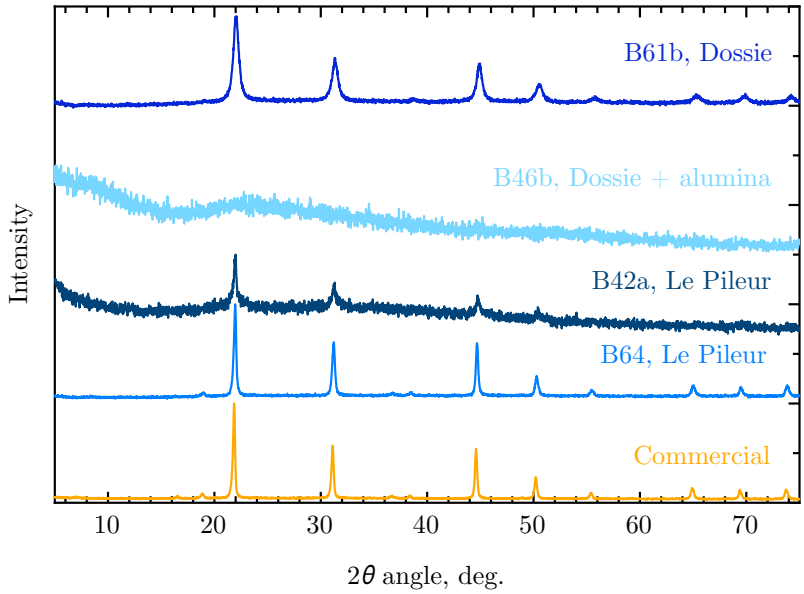

Figure 2.37 X-ray powder diffraction patterns of laboratory-synthesized eighteenth century Prussian blues obtained by using iron-K_α radiation with $\lambda = 1.9373$ Å.

of approximately 60 nm diameter whereas B61b is characterized by particles of 18 nm diameter, in the (h00) crystallographic direction. The strain in both samples is evaluated from the slope of the linear regression and is equal to 0.37 and 0.89 % in B64 and B61b, respectively. Not surprisingly B61b, which exhibits an iron(III) quadrupole splitting of 0.42(1) mm/s whereas B64 does not, is characterized by a higher amount of strain.

B42a which contains a large amount of ferrihydrite, exhibits highly broadened diffraction peaks and a high amorphous background. Similarly, powders that were not treated with acid, B46b, B61a, and the brown powder B42b, show an amorphous diffraction pattern. X-ray powder diffraction does not provide suitable data for structural investigations of the latter samples because all the Bragg peaks are strongly broadened or inexistent.

Therefore the ancient Prussian blue samples were analyzed by high-energy X-ray diffraction at beamline ID11 at the European Synchrotron Research Facility, Grenoble, France. The measurements were carried out under the same conditions as used for the modern Prussian blues, see **Section 2.2.5** and **Appendix B.3.2**.

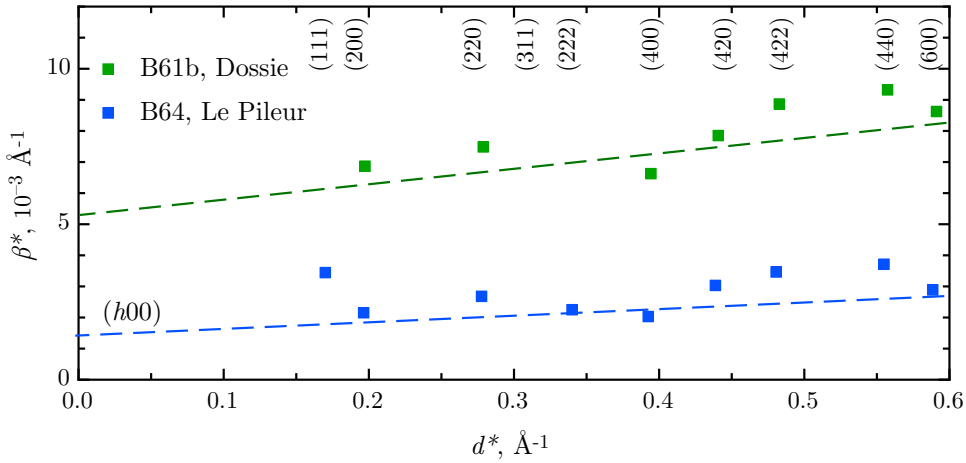

Figure 2.38 The Williamson-Hall plot of laboratory-synthesized eighteenth-century Prussian blue powders. The dashed lines correspond to a linear best fit for the three (h00) reflections.

Pair distribution function analysis

The pair distribution function of the laboratory-synthesized eighteenth century powders are shown in Figure 2.39. The PDF of soluble commercial C02 Prussian blue is added as a reference.

The PDF of the B42a, B42b, and B61a ancient Prussian blues are dramatically different from the PDF of the modern Prussian blues. The strong signal attenuation above 10 Å, suggests nanocrystalline powders. The structure of the brown powder B42b can be fully described by using the model of nanocrystalline alumina hydrate, *tohdite*, $Al_{10}O_{14}(OH)_2$, see Figure 2.40a. The name *tohdite* refers to the synthetic alumina hydrate phase, whereas *akdalaite* is the natural form of alumina hydrate [128]. Both compounds were eventually shown to have the same structure and composition and are described by the hexagonal $P63mc$ space group with $a = 5.58(1)$ and $c = 8.86(2)$ Å [129]. In 2007 Michel *et al.* determined through PDF analysis a similar structure and composition for nanocrystalline ferrihydrite, $Fe_{10}O_{14}(OH)_2$, with lattice parameters $a \approx 5.95$ and $c \approx 9.06$ Å [126]. Ferrihydrite and alumina hydrate exhibit a very similar PDF because they are isostructural.

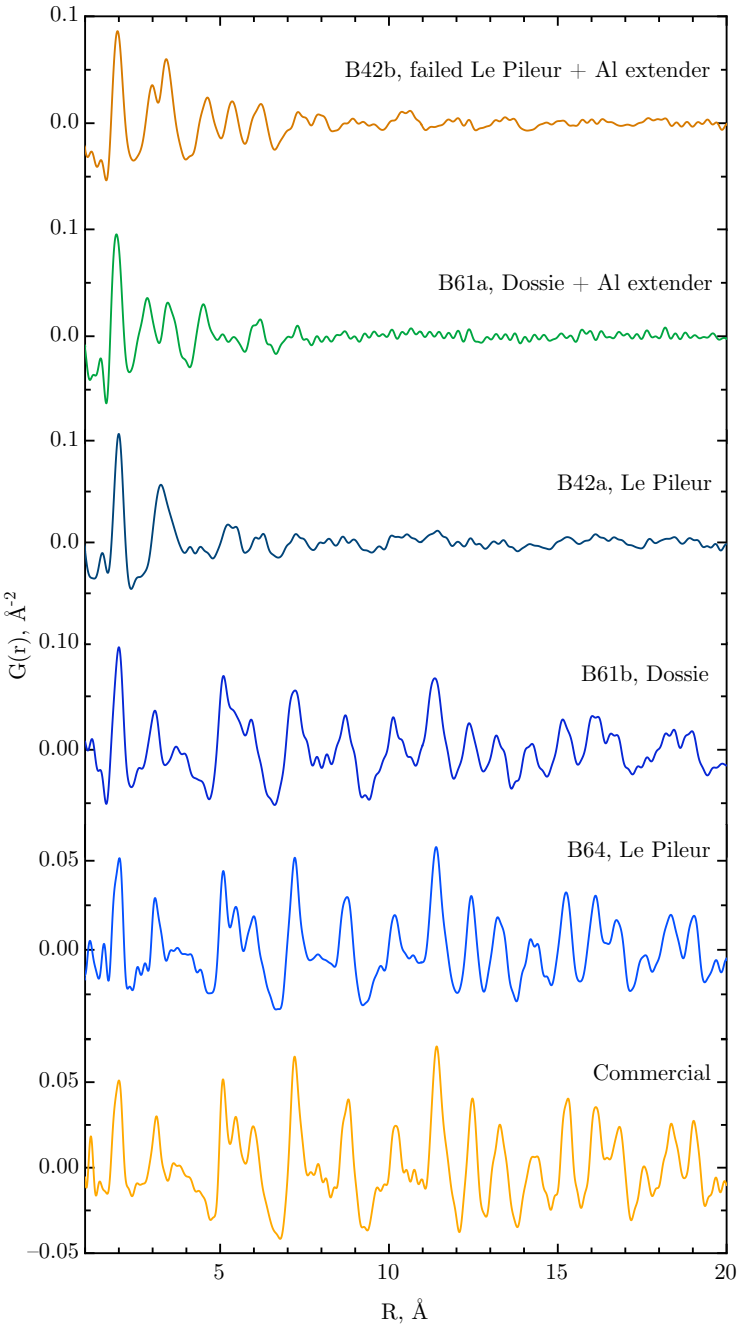

Figure 2.39 The pair distribution function for the laboratory-synthesized eighteenth century powders and commercial soluble Prussian blue.

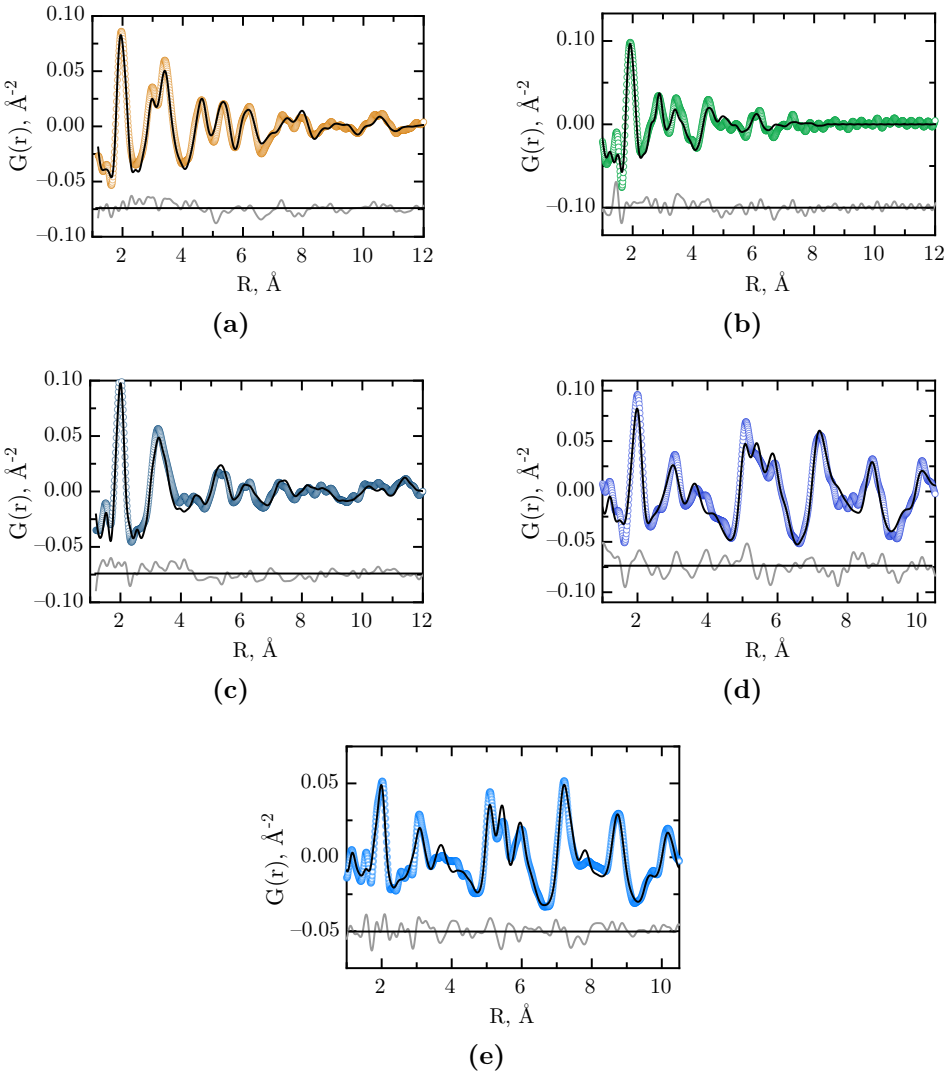

Figure 2.40 Refinement of the PDF obtained on laboratory-synthesized eighteenth century powder samples, **a**, B42b, R_w= 21.8 %; reduced $\chi^2 = 0.090$; **b**, B61a, R_{wp}= 31.8 % ; reduced $\chi^2 = 0.061$; **c**, B42a, R_{wp}= 25.7 %; reduced $\chi^2 = 0.102$; **d**, B61b, R_{wp}= 29.6; reduced $\chi^2 = 0.196$; **e**, B64, R_{wp}= 24.8 %; reduced $\chi^2 = 0.100$. Experimental data and fit are shown in open colored circles and a solid line, respectively.

The average crystallite size[22] in B42b is 15 Å and the unit cell dimensions are $a = 5.96(2)$ and $c = 8.64(3)$ Å. On the basis of Mössbauer spectroscopy and PIXE analysis, one can conclude that B42b contains nanocrystalline alumina hydrate as well as nanocrystalline ferrihydrite. The brown hue of B42b is additional proof of the presence of an orange iron oxide, as white alumina hydrate would not color the powder.

As is indicated by the PIXE analysis B61a is expected to contain a large amount of alumina hydrate, ferrihydrite, and a small amount of Prussian blue. On the basis of the structural composition of B42b, the PDF of B61a was refined by using the structural phase of nanocrystalline alumina hydrate, see Figure 2.40b. Attempts to fit the PDF with additional phases in order to take into account the presence of ferrihydrite and Prussian blue in B61a result either in negative relative phase contents or unlikely lattice parameters. The discrepancy between the observed data and the calculated PDF can be attributed to the particularly large amount of impurity in B61a, *i.e.*, phosphorus and sulphur contents of 1.3 and 8.5 weight %, respectively.

The B42a, B61b, and B64 samples were treated with hydrochloric acid in order to eliminate the extender, *i.e.*, alumina hydrate. According to Mössbauer spectral results, the B42a sample is mainly composed of ferrihydrite whereas the samples B61b and B64 are rather pure Prussian blues. Therefore the PDF of B42a was fit by combining the structural models of ferrihydrite and Prussian blue. Because of the restricted data range and, in order to avoid overfitting the PDF, the structural model for Prussian blue was restricted to the most probable ordered substructure, *i.e.*, the substructure containing one vacancy. The model with the three ordered substructures of soluble Prussian blue was used to fit the PDF of B61b and B64. The refinements are shown in Figures 2.40c, 2.40d, and 2.40e.

The PDF refinement parameters for B42a revealed a relative phase content in terms of one unit cell of 92(1) and 8(1) % for ferrihydrite and Prussian blue, respectively. These values agree with the Mössbauer spectral results. The refinement quality is in general poorer for the B64 and B61b Prussian blues than for the modern Prussian blues. Because of the empirical character of the recipes for their preparation, these samples contain more impurities, as is evidenced by the PIXE analysis. These impurities are probably localized in the lattice cavities of the pigment but they were not taken into account in the structural model. Be-

[22] In order to determine the crystallite size from the PDF, the resolution damping factor, Q_{damp}, must be taken into account. This factor evaluates how the experimental resolution affects the PDF and was determined as a value of 0.05 from the LaB_6 standard PDF analysis. This value was used in the remaining PDF fits as the data were recorded under similar experimental conditions.

cause the peaks are broader[23] in the B61b PDF than in the B64 PDF, the latter is expected to be more ordered. Effectively, B64 is characterized by a relative phase content in terms of one unit cell of 15(4), 40(4), and 45(4) % for substructures with zero, one, and two vacancies, respectively. In B61b, the one unit cell content of the substructure A, with zero vacancies, is virtually zero whereas the one unit cell % content of the substructures B and C, with one and two vacancies, are 50(3) and 49(3) %, respectively. Thus, B61b is more disordered than B64 because more vacancies are present. This higher disorder also increases its thermal factors.

X-ray absorption spectroscopy

The ancient Prussian blues were analyzed by iron K-edge X-ray absorption spectroscopy on beamline BM26 at the European Synchrotron Research Facility, Grenoble, France. The XANES spectra are shown in Figure 2.41. B64 and B61b visually exhibit the typical XANES spectrum of Prussian blue. In contrast, the XANES spectra of the samples containing ferrihydrite, as evidenced by Mössbauer spectroscopy, are close to that of goethite, α-FeOOH, which is the most common of the ferric oxyhydroxides. Like ferrihydrite, the goethite structure can be considered as a hexagonal close-packed array of oxygens and hydroxyls with the iron(III) ions occupying the octahedral positions. In goethite these octahedral positions are arranged in double rows along [001]. In ferrihydrite some of the iron positions are vacant [130]. According to Wilke *et al.* the XANES spectra at the iron K-edge of goethite and ferrihydrite are very similar [131].

The B64 and B61b Prussian blue samples, as well as commercial C02 Prussian blue, are characterized by comparable iron ionic environments, as is evidenced by the EXAFS spectra shown in Figure 2.42. The two laboratory synthesized eighteenth century Prussian blues were fit similarly to modern Prussian blues. Bond distances, coordination numbers, Debye-Waller factors, and inner potential corrections for the B61b and B64 laboratory-synthesized eighteenth century Prussian blues are given in Table 2.21. The procedure for fitting and for the estimation of errors are explained in **Section 2.2.5** and **Appendix B.3**.

The EXAFS spectra of B42a and goethite are shown in Figure 2.43. At very short range, both compounds exhibit a similar iron ion environment. According to Mikutta *et al.* the FT$[\chi(k)\cdot k^2]$ spectrum of goethite results from the contribution of three shells: one corresponding to the Fe-O coordination, with a bond distance

[23]The broadening of the peaks can also be caused by the damping of $F(Q)$. For B61b, the damping width is 10 Å^{-1} whereas a damping of 20 Å^{-1} width was applied to the PDF of B64. The damping consists of multiplying $F(Q)$ by a Gaussian function of adjustable width, centered about zero. It reduceds the statistical noise at high-Q on the PDF obtained from the Fourier transform of $F(Q)$.

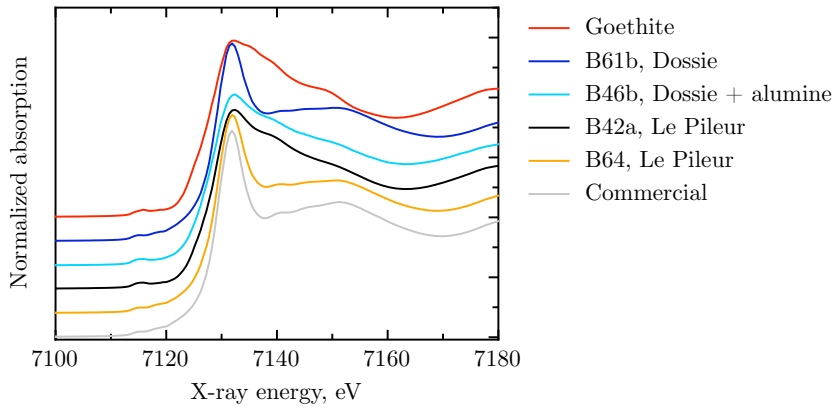

Figure 2.41 Iron K-edge XANES spectra of laboratory-synthesized eighteenth century Prussian blues, modern commercial C02 Prussian blue and goethite, α-FeOOH. XANES spectra of samples B42a and B46b are very similar to that of goethite, FeOOH.

of 1.97(1) Å , and two Fe-Fe shells, at 3.04(4) and 3.44(4) Å [127]. Mössbauer spectral results have shown that B42a is mainly composed of ferrihydrite and that only 19(1)% of the iron ions were part of the Prussian blue. The FT[$\chi(k)\cdot k^2$] spectrum of B42a is mostly dominated by the Fe-O coordination shell, at *ca.* 2 Å. The strong attenuation of the EXAFS oscillations of the B42a sample above 4 Å probably masks the coordination shells characteristic of a Prussian blue. The damping of the signal indicates an extremely small particle size, as is also observed in the PDF analysis.

Table 2.21 Bond distances, R, coordination numbers, N, Debye-Waller factors, $\Delta\sigma^2$, and inner potential corrections, ΔE_0, for the EXAFS fits obtained for two laboratory-synthesized eighteenth century Prussian blues.

Sample	Absorber-scatterer	R, Å	N	$\Delta\sigma^2$, Å^2	ΔE_0, eV
B64	Fe(II)-C	1.90(1)	2.7(1)	0.0030(2)	3.6(3)
	Fe(III)-N	2.10(1)	3.0(1)	0.0030(2)	-0.9(5)
	Fe(II)-N	3.06(1)	2.0(1)	0.0030(2)	2.5(5)
	Fe(III)-C	3.11(1)	2.0(2)	0.0030(2)	5.8(6)
	Fe(II)-Fe(III)	5.10(1)	5.0(2)	-0.0002(2)	-5.1(3)
B61b	Fe(II)-C	1.91(1)	3.3(1)	0.0020(2)	3.2(3)
	Fe(III)-N	2.11(1)	2.9(1)	0.0020(2)	-3.8(5)
	Fe(II)-N	3.06(1)	2.1(1)	0.0020(2)	-0.3(5)
	Fe(III)-C	3.12(1)	2.2(2)	0.0020(2)	3.5(6)
	Fe(II)-Fe(III)	5.08(1)	4.1(2)	-0.0003(2)	-4.3(3)

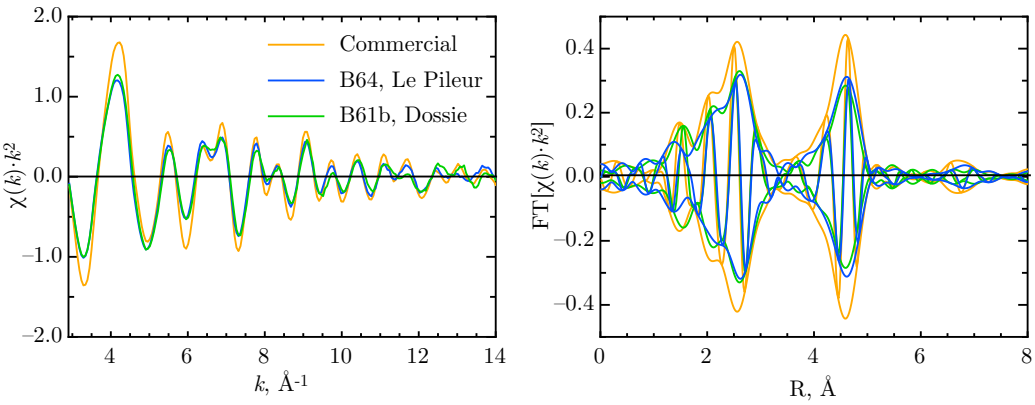

Figure 2.42 $\chi(k)\cdot k^2$ and FT$[\chi(k)\cdot k^2]$ spectra with $\Delta k \sim 5.3$ to 13.9 Å^{-1} for laboratory-synthesized Prussian blues prepared according to an eighteenth century recipe and a commercial soluble reference Prussian blue.

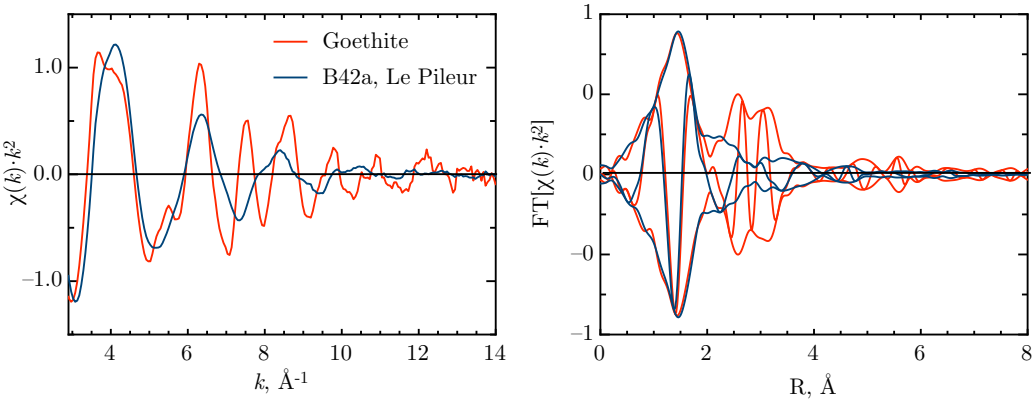

Figure 2.43 $\chi(k)\cdot k^2$ and FT$[\chi(k)\cdot k^2]$ spectra with $\Delta k \sim 5.3$ to 13.9 Å^{-1} for laboratory-synthesized Prussian blues prepared according to an eighteenth century recipe that also yields ferrihydrite. The spectra for goethite, α-FeOOH, are shown for comparison.

Vibrational analysis

Finally the ancient Prussian blues were analyzed by Raman spectroscopy. The Raman spectra of selected laboratory-synthesized powders are shown in Figure 2.44. The spectra do not significantly differ from those of modern Prussian blues presented in Figure 2.32 in **Section 2.2.6**. The two strong vibrational bands at *ca.* 2150 and 2088 cm^{-1}, visible in all samples, correspond to the stretching vibration of CN^- and confirm the presence of Prussian blue. The shoulder peak at 2120 cm^{-1} may indicate the presence of a coprecipitated ferricyanide ion [62][132]. Lower-frequency bands arise from iron to ligand vibrations, such as ν(Fe-C), δ(Fe-CN), and δ(C-Fe-C)[115][119]. B64 and the commercial soluble C02 Prussian blue show a very similar Raman spectrum, with sharp vibration bands, whereas broader peaks characterize B42a and B46b, broadening that is most likely caused by the presence of nanoparticles in the pigment. The very broad peaks in the 600 to 1800 cm^{-1} region in B42a and B46b can be attributed to either nanocrystalline ferrihydrite or alumina hydrate.

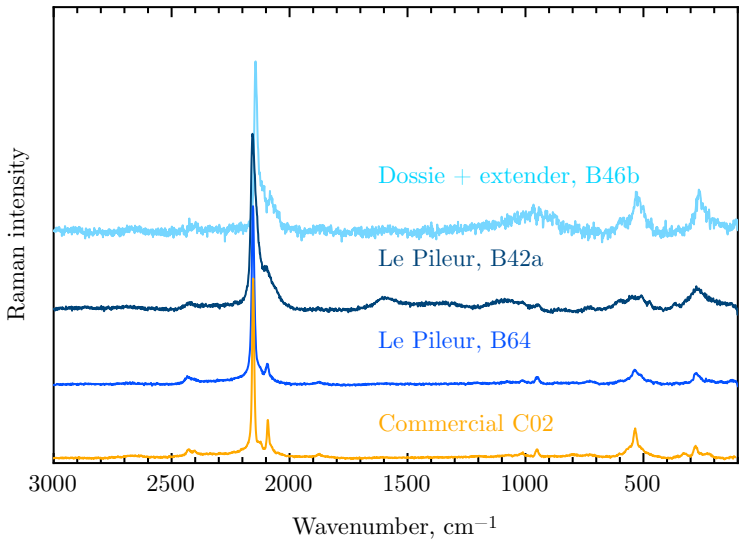

Figure 2.44 Raman spectra of Prussian blues synthesized according to eighteenth century recipes and commercial C02 Prussian blue. All spectra are normalized according to the intensity of their most intense absorption band. All pigments exhibit a ν(CN) band at 2150 cm^{-1}, a band that is characteristic of ferrocyanide complexes.

2.3.4 Discussion

The Le Pileur d'Apligny and Dossie recipes lead to the formation of a Prussian blue that may be of similar quality to the modern commercial pigments. Samples B64 and B61b support this assertion. However, these recipes can also result in the production of blue-colored pigments that cannot be considered to be Prussian blue, as is evidenced by the blue-gray color of B42a, which mainly consists of nanocrystalline ferrihydrite. Similarly, B46 and B61a, which correspond to a pale variety of Prussian blue because they were not treated with hydrochloric acid, are largely composed of poorly ordered hydrous iron oxide.

The formation of the undesirable hydrous iron oxide, identified as nanocrystalline ferrihydrite, occurs during the synthesis and, most likely, forms before the filtration of the pale blue-green precipitate. This precipitate results from the reaction between the potassium hexacyanoferrate and iron(II) sulfate. The chemical compound that is immediately formed is ferrous ferrocyanide, also known as Berlin white or Everitt's salt, $[Fe^{II}Fe^{II}(CN)_6]^{2-}$, formed by the reaction,

$$Fe^{II}\ (aq) + [Fe^{II}(CN)_6]^{4-}(aq) \rightarrow [Fe^{II}Fe^{II}(CN)_6]^{2-}(s).$$

Ferrous ferrocyanide is rapidly oxidized in air to yield Prussian blue. The precipitate retains a pale color because of the presence of a large amount of a white aluminum compound. The latter product has been identified as alumina hydrate, $Al_{10}O_{14}(OH)_2$ by the PDF analysis and is formed by the hydrolysis of the trivalent Al^{3+} cation arising from alum, $KAl(SO_4)_2{\cdot}12H_2$, used as a starting reagent.

According to the above chemical reaction, the formation of ferrous ferrocyanide requires a stoichiometric amount of iron(II) and $[Fe^{II}(CN)_6]^{4-}$. The iron(II) ions are provided by the iron(II) sulfate solution, used as a starting reagent whereas the $[Fe^{II}(CN)_6]^{4-}$ ions are derived from the blood calcination with potassium carbonate; the hexacyanoferrate(II) anion is most likely the limiting reagent. Consequently, iron(II) ions from iron(II) sulfate remain in excess in the aqueous solution after precipitation of ferrous ferrocyanide. However iron(II) ions are easily oxidized to iron(III) ions; the latter can then hydrolyze to produce an iron oxide, such as ferrihydrite, which is known to be formed by rapid oxidation of iron-containing solutions. A rapid filtration that immediately follows the precipitation, as was the case for B64 and B61b, avoids the formation of the orange hydrous iron oxide on the surface of the blue-green precipitate and, thus, preserves the color and nature of Prussian blue.

The presence of a certain amount of iron oxide in the ancient Prussian blue pigments is expected to play a role in the fading of Prussian blue containing paint

layers. Because this undesirable iron oxide is orange, it could explain why numerous authors of eighteenth and nineteenth century books[24] warned artists about the tendency of Prussian blue to turn green in light. In order to confirm this hypothesis, the light fastness of modern and ancient Prussian blue pigments was evaluated by accelerated ageing experiments in order to induce degradations in the paint layers upon exposure to light. This work will be discussed in the following chapter.

[24]See **Section 1.2.2** and **Appendix A**.

Chapter 3

A Study of the Degradation of Prussian Blue in Paint Layers

Summary. *The fading of laboratory-synthesized and commercial Prussian blues in paint layers during exposure to light has been investigated. The Prussian blue pigments were painted with linseed oil, gum arabic, or casein, as either a pure pigment or mixed with lead white, $(PbCO_3)_2Pb(OH)_2$, zinc white, ZnO, or titanium white, TiO_2, pigment. The samples were subjected to accelerated ageing of up to 800 hours. Pure Prussian blue painted in dark shade is extremely light fast whereas it fades in pale shade and when mixed with a white pigment, especially with lead white and zinc white. The painted samples were studied by UV-visible, iron K-edge X-ray absorption, iron-57 transmission Mössbauer, attenuated total reflectance infrared, and Raman spectroscopy. The results revealed an iron ion partial oxidation, with an increased amount of $[Fe^{III}(CN)_6]^{3-}$ ions, prior to the ageing in the entire bulk layer. Upon exposure to light, iron(III) ions at the surface of the paint layer of Prussian blue are reduced.*

Contents

The permanence of Prussian blue had already been questioned by the mid-eighteenth century. The preparative methods were recognized as contributory factors in the impermanence of Prussian blue and have, therefore, been reproduced in order to identify the parameters that could play a role in the fading, as has been thoroughly detailed in **Chapter 2**. The next step in this research is to evaluate the light fastness of the so-obtained pigments and identify the changes in local electronic and structural configurations of the iron(II) and iron(III) ions in aged paint layers, in order to understand the degradation mechanisms of Prussian blue.

3.1 Sample preparation

Paint layers were prepared with commercial pigments and laboratory-synthesized Prussian blues, whose synthesis was described in **Chapter 2**. Because of the large number of laboratory-synthesized pigments, a selection was necessary. The most representative pigments are listed in Table 3.1. The laboratory synthesized A147 and A148 Prussian blues differ by their crystallite size, which is approximately two times smaller for A147, and by their inherent disorder, which is higher for A147 because of a larger $[Fe^{II}(CN)_6]^{4-}$ vacancy content. Most of the samples synthesized according to eighteenth century recipes were selected because they are expected to have a poorer light fastness than modern Prussian blues. The light fastness of soluble sodium ion containing modern Prussian blues was not studied because this cation is much less frequently used in the preparative methods of Prussian blue than are the potassium and ammonium cations. The commercial Prussian blues, such as the C01 sample, are still used as artist pigment and have already been rated for their permanence by artist suppliers. Their permanence rating will be compared with those determined by the accelerated ageing experiments that are carried out in this thesis.

For clarity in the description of sample preparation, the paint layers for accelerated ageing were classified according to the type of support, *i.e.*, canvas, paper, or glass slides. Supports, binders, diluents, and pencils were purchased at the artist materials supplier Schleiper SA, Liège, Belgium.

3.1.1 Paint layers on canvas

Canvas, as a painting support, has been widely used since Antiquity; fragments of painted linen canvas have been found in Egypt and have been dated from the twelfth dynasty, 2000 to 1785 BC [55]. The canvas consists of a cotton or linen fabric stretched over a wooden frame to ensure stability. The canvas is usually prepared with an application of *size*. Size is a diluted glue, typically made from animal skins, that prevents the absorption and penetration of the binder and vehicles present in the paint layers into the support. The sized canvas is next covered

Table 3.1 Selected Prussian blues for the preparation of paint layers

Label	Description	Composition
Modern laboratory-synthesized Prussian blues		
A148	Indirect method under N_2, 2 hours ageing	Potassium containing Prussian blue
A147	Indirect method under N_2, no ageing	Potassium containing Prussian blue
Prussian blues synthesized according to eighteenth century recipes		
B64	Recipe of Le Pileur d'Apligny, 1779	Potassium containing Prussian blue
B42a	Recipe of Le Pileur d'Apligny, 1779	Insoluble Prussian blue + ferrihydrite
B46a	Recipe of Le Pileur d'Apligny, 1779 No HCl treatment	Insoluble Prussian blue + ferrihydrite + alumina hydrate
B61b	Recipe of R. Dossie, 1758	Insoluble Prussian blue
B61a	Recipe of R. Dossie, 1758 No HCl treatment	Insoluble Prussian blue + ferrihydrite + alumina hydrate
Commercial Prussian blues		
C01	Winsor & Newton provenance	Insoluble Prussian blue
C02	Winsor & Newton provenance IRPA archives	Potassium containing Prussian blue
C03	Sigma-Aldrich product	Insoluble Prussian blue
C04	Degussa product Provided by Blockx	Ammonium containing Prussian blue

by a coating or *ground layer* for an optimum isolation between the support and the paint layers. To date, the ground layer is a white preparation layer containing a binder of acrylic polymer [93]. For the preparation of Prussian blue containing paint layers, a universally primed 100% linen canvas was used.

The preparation of the paint layers on canvas for the accelerated ageing is detailed below. The powders were mixed with boiled linseed oil and painted in thin layers onto a 2 cm^2 universally primed 100 % linen canvas. Linseed oil was chosen as a binder because it is the most common oil binder and is widely used in oil paint. The boiling treatment ensures a more rapid drying process. Turpentine was used as a vehicle.[1] Because pure Prussian blue has such a deep color it was rarely used by artists in the pure form. Thus the samples were also diluted with white pigments obtained from Kremer Pigmente GmbH & Co KG, Alchstetten, Germany. The specific white pigments used were, first, *lead white* or basic lead carbonate, the most popular white pigment, used in the eighteenth and nineteenth centuries, which can have a somewhat variable composition but is typically close to $(PbCO_3)_2Pb(OH)_2$; second, *zinc oxide*, ZnO, introduced as a pigment in the mid-nineteenth century and still in use; third, *titanium dioxide*, TiO_2, in the ru-

[1] A *vehicle* or *diluent* is a substance that is compatible with the binder and that allows the paint to be spread more easily [93].

tile[2] form, the most popular white pigment since 1945.

Samples containing weight to weight dilution ratio of Prussian blue pigment to white pigment of 1:1, 1:10, and 1:100 were prepared. The amount of linseed oil needed for each mixture was determined by considering the oil absorption indices of Prussian blue, lead white, zinc white, and titanium white, which are 100, 8 to 12, 13 to 22, and 15 to 20 wt %, respectively [133]. The density of Prussian blue painted with lead white in 1:1, 1:10, and 1:100 dilution ratios are approximately 1.6, 0.7, and 0.04 mg cm^{-2}, respectively. Paint layers prepared with zinc white and titanium white in a 1:10 dilution ratio contain a density of Prussian blue of *ca.* 0.7 mg cm^{-2}. In order to evaluate the light fastness of the white pigments used, paint layers containing only white pigments have also been prepared.

Laboratory-synthesized Prussian blues prepared according to eighteenth century recipes were only studied in dilution with lead white because the other white pigments, zinc white and titanium white, were not used during that period.

Paint layers from commercial Prussian blue and lead white ready-to-use oil colors were also prepared. The Prussian blue oil color was purchased from the artist materials supplier Winsor & Newton, Harrow, Middlesex, England. The lead white oil color, which is no longer commercially produced because of its toxicity, was part of a private collection of artist's materials and was manufactured by the artist materials supplier Blockx SA., Nandrin, Belgium. Prussian blue was diluted with lead white, in eight different blue pigment to white weight to weight dilution ratios, namely 1:1, 1:5, 1:10, 1:20, 1:50, 1:100, 1:200, and 1:400. Layers containing pure Prussian blue and pure lead white were also prepared. Figure 3.1 gives a schematic overview of the prepared samples on canvas.

3.1.2 Paint layers on paper

Besides oil painting, Prussian blue was widely used in watercolor painting. The pigment powder is mixed with a plant gum, the most commonly used is gum arabic, which is produced by a particular variety of the *acacia* shrublike tree [93]. The watercolor technique has probably been known since antiquity but became really popular and widely used only from the eighteenth century [55]. Watercolor paints are usually used on paper. The powders from Table 3.1 were mixed with a

[2]Titanium(IV) dioxide, TiO_2, exists in three different crystallographic forms, *rutile*, the high temperature tetragonal polymorph, *anatase*, the low temperature tegragonal polymorph, and *brookite*, the orthorhombic polymorph. The industrial production of synthetic titanium(IV) dioxide in the rutile type since the early twentieth century has largely contributed to the massive use of titanium dioxide as a white pigment [87][133].

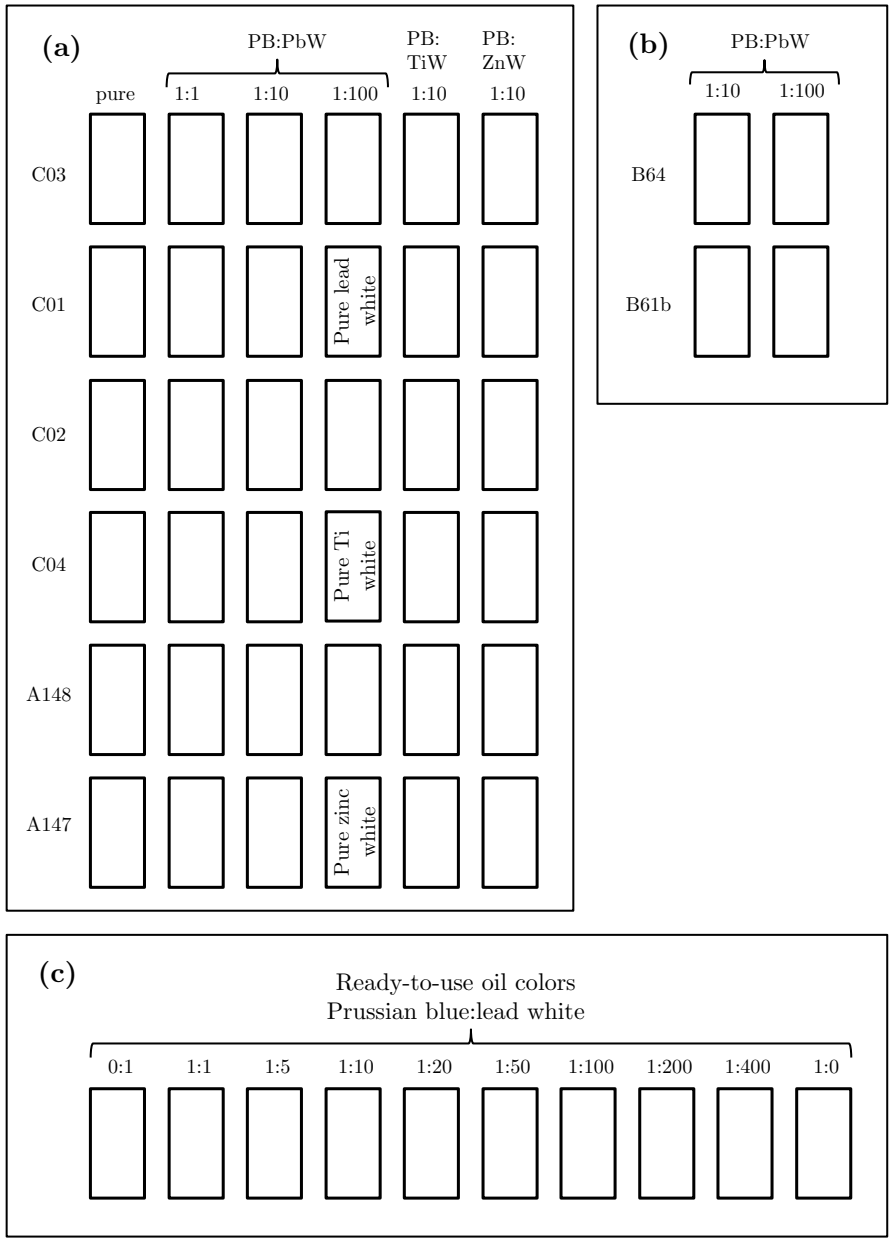

Figure 3.1 Schematic overview of the prepared paint layers on canvas, **a**, pure and diluted modern commercial and laboratory-synthesized Prussian blues and white pigments, **b**, eighteenth-century laboratory-synthesized Prussian blues diluted with lead white, and **c**, pure and diluted Prussian blue and lead white ready-to-use oil colors. PB is Prussian blue, PbW is lead white, $(PbCO_3)_2Pb(OH)_2$, TiW is titanium white, TiO_2, and ZnW is zinc white, ZnO.

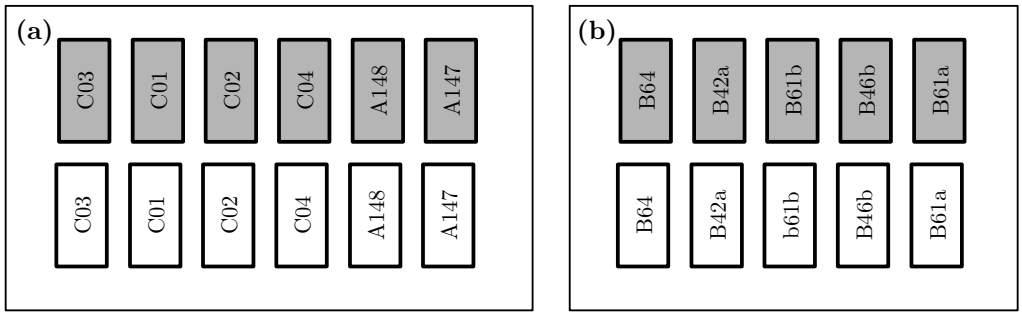

Figure 3.2 Schematic overview of the prepared paint layers on watercolor paper. Dark shade, in gray, and light shade, in white, of watercolor paint layers of **a**, pure modern commercial and laboratory-synthesized Prussian blues and, **b**, eighteenth-century laboratory-synthesized Prussian blues.

10 % gum arabic containing aqueous solution in a pigment to binder 1:2 weight-to-weight ratio. The mixtures were painted onto a 2 cm^2 100 % cotton watercolor paper. In watercolor painting white pigments are rarely employed because the white of the paper is usually used in transparency to lighten the color. Therefore the samples were not diluted with a white pigment but were rather painted in a light shade, by decreasing the pigment concentration. Water was used as a vehicle. Figure 3.2 shows a schematic overview of the prepared watercolor paint layers.

3.1.3 Paint layers on glass slides

Glass has the advantage of being relatively inert and, hence, any contribution from the support can be eliminated. The paint layers on 75×25 mm microscope glass slides were prepared to systematically study the effect of the binder and the admixture of a white pigment upon the Prussian blue fading. Three types of binders were used, boiled linseed oil, gum arabic in a 10 % water dilution, and casein in a 10 % water dilution. Casein refers to a mixture of proteins that can be separated from milk and, when diluted in water, produces a brilliant, opaque paint film. This organic binder is related to *tempera* paint and is slightly basic, in contrast to linseed oil or gum arabic. The commercial insoluble C03 Prussian blue was mixed with each binder, pure or diluted, with one of the above mentioned white pigments in a weight to weight ratio of Prussian blue pigment to white pigment of 1:1, 1:10, and 1:100.

In order to clearly identify the contribution of Prussian blue in the fading, paint layers containing, weight to weight ratio of phtalocyanine blue to each of the above mentioned white pigments 1:100 dilution, were prepared in both a boiled linseed oil and a gum arabic medium. Two glass slides were prepared for each type

of paint layers shown in Figure 3.3, one to be aged, and the second one to serve as a reference.

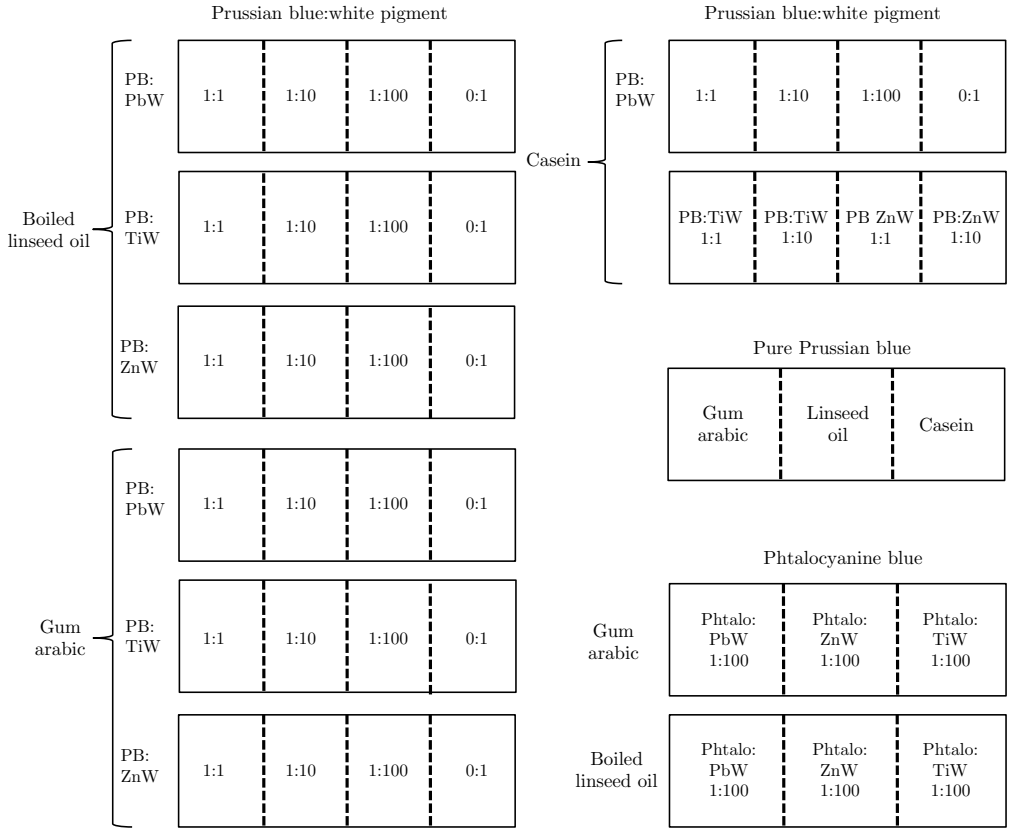

Figure 3.3 Schematic overview of the prepared paint layers on microscope glass slides. PB is Prussian blue, Phtalo is phtalocyanine blue, PbW is lead white, $(PbCO_3)_2Pb(OH)_2$, TiW is titanium white, TiO_2, and ZnW is zinc white, ZnO.

3.2 Accelerated ageing

The light stability of pigmented systems is defined as *the resistance of coatings towards changes caused by the action of global radiation, possibly in the presence of moisture* [52]. The International Organization for Standardization has set standards to test the resistance to light of pigments and extenders. It recommends the exposure of the samples under glass to either natural light or to direct artificial light [134]. For the latter, the ageing tests are carried out in a weathering instrument which simulates exposure to daylight. Radiation from a xenon arc lamp is usually used because it satisfactorily simulates solar spectral irradiance according

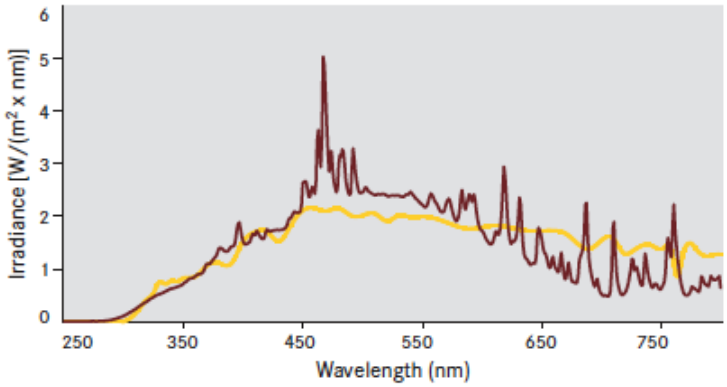

Figure 3.4 Comparison between the solar spectral irradiance according to CIE 85:1989, in yellow solid line, and the irradiance of a xenon lamp used in SUNTEST weathering instruments, in dark red solid line [136].

to the CIE 85:1989 recommendations for solar spectral irradiance,[3] see Figure 3.4.

The samples were subjected to accelerated ageing of up to 800 hours, or almost five weeks, by using a SUNTEST CPS+ weathering chamber equipped with a xenon lamp; a window glass filter that removed UV radiation below 320 nm was used to simulate indoor ageing, as is recommended in the ISO 787-15 standard. The reflectance spectrum of the xenon lamp equipped with the window glass filter was measured by UV/visible spectroscopy at the level of the sample tray, see Figure 3.5. The shape of the reflectance curve is comparable to that shown in Figure 3.4. A ventilation system was used to cool the ageing chamber to a constant black standard temperature of *ca.* 35°C. The luminance at the surface of the sample was *ca.* 90 000 lux. Because of the limited 560 cm^2 surface area of the sample tray, the ageing experiments were carried out in three steps. During the ageing process half of the painted canvas or paper surface area was covered with aluminum to serve as a reference after ageing. The glass slides used as references were placed under the plate exposed to light, where the temperature is approximately the same as in the chamber. In order to quantify the permanence of the pigments, the samples were aged together with blue wool light fastness reference standards as specified in ISO 105-B04, standards that are used by the pigment industry for determining the resistance of color to the action of artificial light.

The modern Prussian blue samples, see Figure 3.1a and 3.2a were subjected to accelerated ageing of up to 800 hours. During the first 400 hours of weathering

[3]Irradiance at a point of a surface is defined as *the ratio of the radiant power or flux emitted by an infinitesimal surface element containing the point, to the area of that surface element* [135].

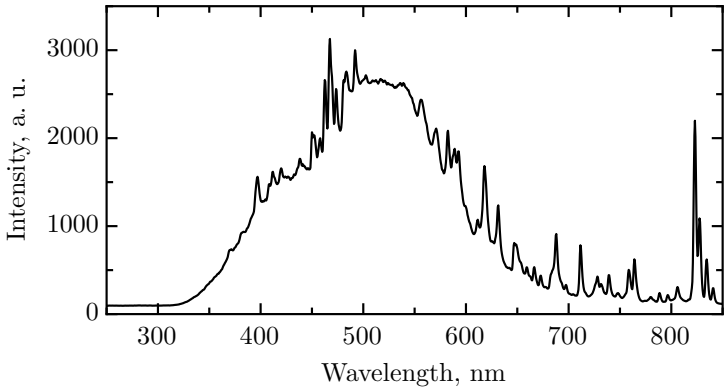

Figure 3.5 The UV/visible spectrum of the xenon lamp equipped with the window glass filter used in the SUNTEST CPS+ weathering chamber.

the samples were removed from the weathering chamber every 50 hours for *ca.* 1 hour in order to perform colorimetric measurements which could not be carried out in the chamber. After 400 hours of light exposure, the samples were removed from the chamber and kept in the dark for one week in order to determine whether there was a return of the original color of the samples after dark storage, a phenomenon that has been reported earlier [57]. After one week in the dark, the ageing experiment was continued under the same conditions as described above with colorimetric measurements every 100 to 150 hours. The other samples were subjected to accelerated ageing over 400 hours, without any interruption, except to perform periodic colorimetric measurements.

3.3 Color change

Figures 3.6 and 3.7 show pictures of the paint layers prepared on canvas and watercolor paper, respectively, after the accelerated ageing experiment. The half of the painted surface area that was covered with aluminum during the ageing indicates the degree of fading. On the basis of Figures 3.6 and 3.7, the color change of Prussian blue can be qualitatively discussed.

Pure modern Prussian blue pigments are light fast because no significative discoloration appeared after 800 hours of light exposure, see Figure 3.6a. This is consistent with the permanence rating determined for modern commercial Prussian blue by pigment suppliers. According to the Winsor & Newton rating, which scales the pigment light fastness between extremely permanent, permanent, moderately durable, or fugitive, Prussian blue is considered as a permanent pigment [137]. In the American Society for Testing and Materials, ASTM, system, the

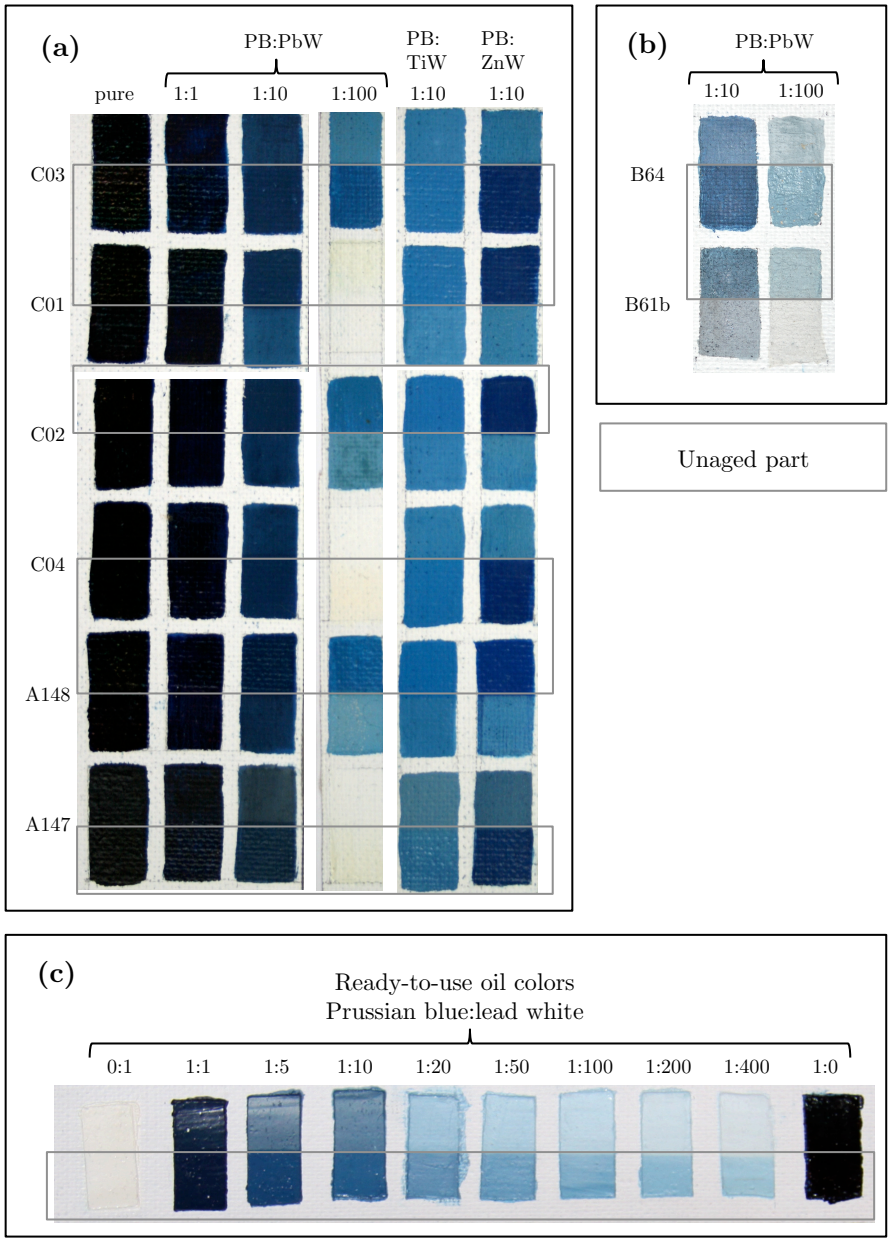

Figure 3.6 Pictures of the prepared paint layers that were subjected to accelerated ageing, **a**, pure and diluted modern commercial and laboratory-synthesized Prussian blues and white pigments, **b**, eighteenth-century laboratory-synthesized Prussian blues diluted with lead white, and **c**, pure and diluted Prussian blue and lead white ready-to-use oil colors. PbW is lead white, $(PbCO_3)_2Pb(OH)_2$, TiW is titanium white, TiO_2, and ZnW is zinc white, ZnO.

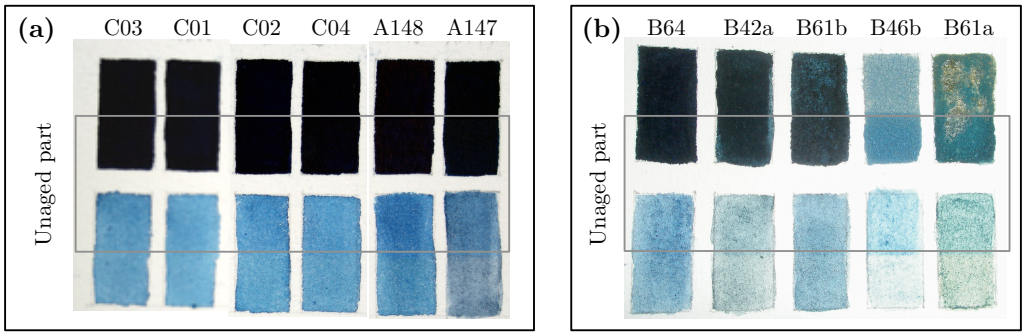

Figure 3.7 Pictures of the prepared paint layers on watercolor paper. Dark shade and light shade of watercolor paint layers of **a**, pure modern commercial and laboratory-synthesized Prussian blues and **b**, eighteenth-century laboratory-synthesized Prussian blues.

Prussian blue light fastness is rated I on a scale from I to IV, I being the highest light fastness available.[4] In contrast, Prussian blues mixed with lead white, zinc white, and titanium white, to a lesser extent, are faded upon light exposure, see Figure 3.6. A color change is also noticeable in the pure white pigment containing paint layers, the covered unfaded part of these paint layers has a yellowish tint in comparison with the exposed portion. This phenomenon is well known and results from the yellowing of the linseed oil when it is kept in the dark [55]. The light fastness of the white pigments will be further discussed below on basis of colorimetric measurements. The degree of fading seems to increase with the white pigment dilution, see Figures 3.6b and 3.6c, for example.

The presence of potassium or ammonium cations does not seem to influence the fading because the potassium cation containing C02, the ammonium cations containing C04, and the insoluble commercial C03 Prussian blues all exhibit a similar fading behavior. The soluble laboratory-synthesized A147 sample differs in hue from the other modern Prussian blues. It has a grayish tint, which is more noticeable when mixed with a white pigment. This difference in color was previously discussed in **Section 2.2.3** and can be attributed to a smaller particle size. This duller grayish hue is also characteristic of the laboratory-synthesized ancient Prussian blue B61b and, to a lesser extent, B64. These Prussian blues, synthesized according to the eighteenth century recipes, also exhibit a fading when mixed with lead white, see Figure 3.6b.

UV-visible spectroscopy has been performed on commercial soluble Prussian

[4] In the ASTM system, the light fastness of a pigment is determined on paint layers containing the pigment and titanium white, in order to reduce the reflectance to a level of 40 %. The light fastness is tested under both sunlight and artificially accelerated conditions [137].

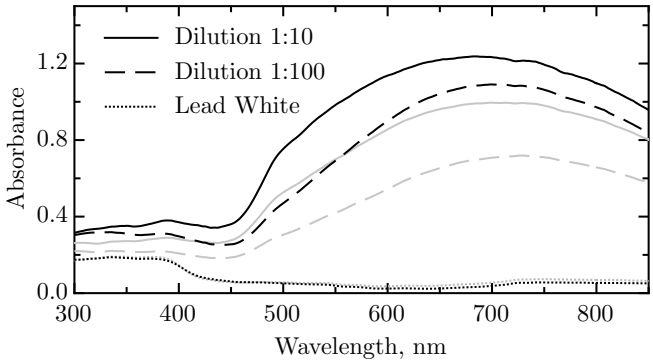

Figure 3.8 UV-visible spectra of a commercial soluble Prussian blue mixed with lead white, $(PbCO_3)_2Pb(OH)_2$, at 1:10 and 1:100 dilution ratios and of pure lead white, painted from linseed oil. The lighter curves correspond to the faded portion of the sample.

blue diluted with lead white and a loss of absorbance is clearly observed upon ageing, see Figure 3.8. There is also a small shift in absorbance of *ca.* 50 nm towards lower energy, *i.e.*, longer wavelength, upon increasing the dilution ratio from 1:10 to 1:100 in both the unaged and aged samples. The UV-visible spectrum of pure lead white painted from linseed oil exhibits virtually no change upon ageing; as expected, above 400 nm the absorbance of lead white is very small.

Another characteristic feature of the aged oil paint layers is the loss of gloss. Gloss is related to the fraction of the incident radiation that is reflected by the surface of the paint layer. In the case of a perfectly smooth surface, specular reflection occurs and the paint layer is highly glossy. In contrast, if the surface is rough, the light is scattered or diffused and a matt or semi-glossy surface appearance results [88]. Surface gloss is best achieved by a homogeneous dispersion of pigment particles in the binder. The loss of gloss that appears upon light exposure in pigmented layers is quite common and results from a breakdown of the binder, that leads to a rougher paint layer surface [52].

Pure modern Prussian blues mixed with gum arabic and painted in dark shade do not exhibit any discoloration upon light exposure. In contrast, a very slight fading can be observed for the lighter shades, *i.e.*, for lower concentration of Prussian blue pigment, especially for the laboratory-synthesized A147 Prussian blue, see Figure 3.7a. It is well known that the concentration of the pigments influences the degree of fading [122][138]. Watercolor paint layers containing Prussian blues synthesized according to the eighteenth century methods do not exhibit a similar fading behavior upon light exposure. The samples that contain a fraction of ferrihydrite, such as B42a, or an extender, such as B61a and B46b, fade more

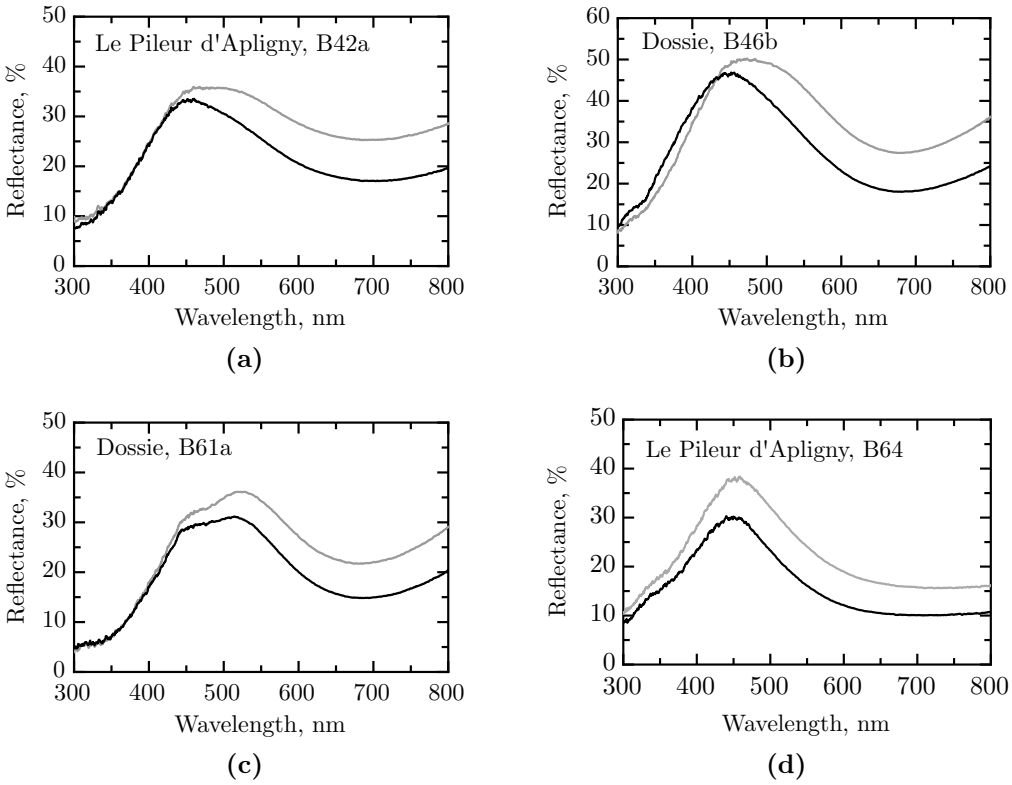

Figure 3.9 Reflectance UV-visible spectra of eighteenth century synthesized Prussian blues mixed with gum arabic and painted in light shade on watercolor paper. The gray curves correspond to the faded portion of the paint layer.

strongly than B64 and B61b. Furthermore, they show a tendency to turn green, as is evidenced by the reflectance spectra obtained by UV-visible spectroscopy, see Figure 3.9.[5] The maximum in the reflectance for the B42a, B46b, and B61a samples is clearly shifted upon ageing towards longer wavelengths, a shift that results in a greenish appearance of the aged paint layers. In contrast, B64 does not exhibit such a shift but, rather exhibits a slightly higher reflectance after ageing, see Figure 3.9d. The tendency of Prussian blue to turn green and the importance of the preparative method have already been reported in eighteenth and nineteenth centuries books, see **Appendix A**.

The evolution of the fading of Prussian blue was quantitatively evaluated by colorimetric measurements. The light fastness of the Prussian blue samples ranges

[5]The UV-visible spectra of the unaged laboratory-synthesized Prussian blues prepared according to eighteenth century recipes were previously discussed in **Section 2.3.1**.

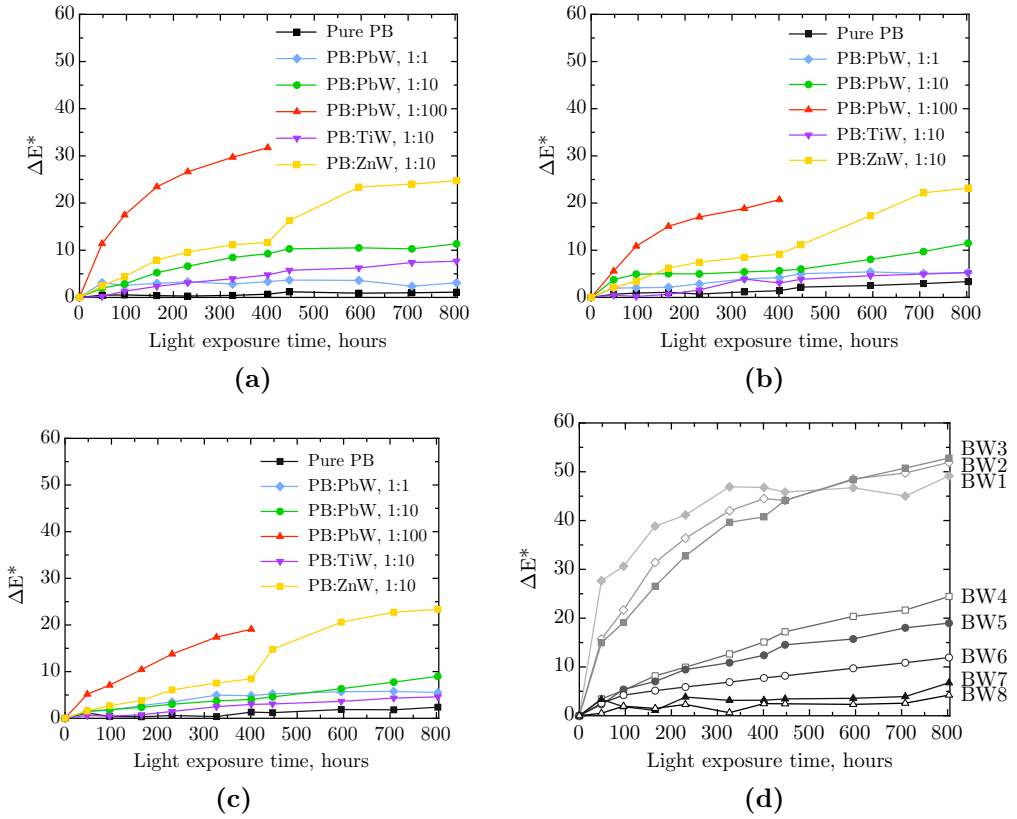

Figure 3.10 Color changes with light exposure time in the laboratory-synthesized, **a**, the commercial soluble, **b**, the commercial insoluble, **c**, Prussian blues painted on canvas in linseed oil medium, and **d**, the blue wool, BW1 to 8, standard samples. PbW is lead white, $(PbCO_3)_2Pb(OH)_2$, TiW is titanium white, TiO_2, and ZnW is zinc white, ZnO.

from zero, for very poor or fugitive, to eight for extremely good light fastness as determined by a comparison with the light fastness of the blue wool standards. The evolution of the color change with light exposure for the modern laboratory-synthesized soluble A148 Prussian blue and the commercial soluble C02 and insoluble C03 Prussian blues, painted from linseed oil in different white pigment dilutions, as shown in Figure 3.6a; and the blue wool standards are shown in Figure 3.10.

After 800 hours, or almost 5 weeks, of light exposure no discoloration or fading was observed for the pure soluble Prussian blue samples and, thus, one can conclude that pure Prussian blue is as light fast as the blue wool standards 7 and 8. In contrast, soluble Prussian blue mixed with white pigments exhibited extensive fading. In mixtures with lead white, $(PbCO_3)_2Pb(OH)_2$, it is noteworthy

that discoloration increased with dilution. In this case, the paint layer containing Prussian blue and lead white in a 1:100 ratio was so extensively faded that the ageing experiments were discontinued after 400 hours. The rating of light fastness of Prussian blue mixed with lead white progressively decreases as the proportion of white pigment increases. The paint layer prepared in a 1:1 dilution ratio is as light fast as the blue wool standard 6 whereas the light fastness of the 1:100 dilution ratio is comparable with blue wool standards 3 or 4. However, it should be noted that the Prussian blue concentration also decreased with higher dilution ratio. Among the samples with a 1:10 dilution ratio, all of which contained the same amount of Prussian blue for the three white pigments used, the 1:10 Prussian blue zinc white mixture exhibits the strongest sensitivity to irradiation, with a fair light fastness that is comparable with blue wool standard 4. In contrast, the 1:10 dilution with titanium white shows a very good light fastness that is comparable with blue wool standard 6.

No significant regain of color was observed in the samples placed in dark storage after 400 hours of light exposure. Thus the color loss appears irreversible in all the samples painted from linseed oil. Evidence of reversible fading has been reported in films exposed for relatively short periods before dark storage [56][57][58]. The sensitivity of the samples to irradiation is more pronounced at the beginning of the exposure, as is clearly observed for the zinc white mixtures. This may explain why the discoloration increases abruptly when these samples are again subjected to the accelerated ageing after one week of dark storage.

The color change for Prussian blue mixed with lead white in a 1:100 dilution ratio is smaller for the commercial soluble C02 Prussian blue with $\Delta E^* = 21(1)$ than for the laboratory-synthesized A148 pigment with $\Delta E^* = 32(1)$. This slightly improved light fastness of the commercial pigment is presumably related to the industrial manufacturing process which may better control the uniformity of the Prussian blue particle size. However, commercial and laboratory-synthesized A148 Prussian blues generally exhibit similar light fastness behavior. Moreover, the apparent solubility is not expected to play a role in the fading because both soluble and insoluble commercial Prussian blues exhibit a similar color change evolution, see Figures 3.10b and 3.10c.

The light fastness of Prussian blue mixed with white pigments was further investigated for paint layers prepared on glass slides. The evolution of the color change with light exposure for the commercial insoluble C03 Prussian blue painted from linseed oil with a white pigment at a 1:100 dilution ratio is compared to that of phtalocyanine prepared under identical conditions, see Figure 3.11a. Phtalocyanine blue is a synthetic blue pigment that has supplanted Prussian blue because of its higher stability. It indeed exhibits less color change than Prussian blue in sim-

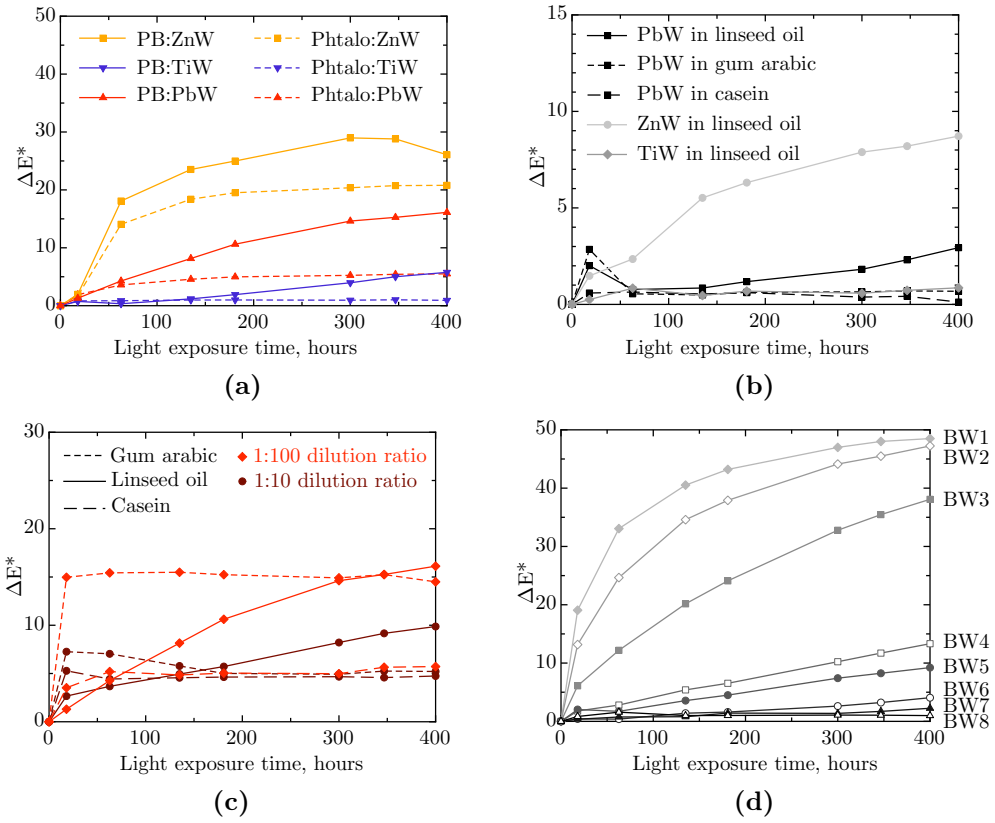

Figure 3.11 Color changes with light exposure time for **a**, the commercial insoluble Prussian blue and phtalocyanine blue painted from linseed oil and mixed with a white pigment in a 1:100 dilution ratio, **b**, the commercial insoluble Prussian blue painted from various binders, **c**, the white pigments, and **d**, the blue wool, BW1 to 8, standard samples. PbW is lead white, $(PbCO_3)_2Pb(OH)_2$, TiW is titanium white, TiO_2, and ZnW is zinc white, ZnO.

ilar white pigment dilutions, although phtalocyanine blue mixed with zinc white noticeably fades upon light exposure. The very strong color change with light exposure observed for paint layers containing Prussian blue and zinc white is not only due to the fading of Prussian blue but also to that of zinc white. The discoloration of zinc white upon light exposure is shown in Figure 3.11b. In contrast to lead white and titanium white, zinc white in linseed oil is less light fast, with a light fastness comparable with blue wool standard 5, see Figure 3.11d. These color difference values result from an increased lightness, ΔL^*, upon light exposure for Prussian blue mixed with zinc white. This increased fading can be attributed to the photochemical activity of zinc white. This point will be discussed below.

Among the 1:100 dilutions with a white pigment, the dilutions with titanium white, TiO_2, show the best light fastness. This can be partially related to the higher relative hiding power of titanium white in linseed oil, resulting in a more opaque paint layer. The relative hiding power is evaluated by the difference between the indices of refraction of the pigment and the medium [93]. Linseed oil has a refractive index of 1.48 whereas zinc white, lead white, and titanium white have refractive indices of 2.01, 2.04, and 2.71, respectively. Consequently, the difference, Δn, beween the refractive indexes of the white pigment and linseed oil is 0.53 for zinc white, 0.56 for lead white, and 1.23 for titanium white, respectively. Thus, light propagates more easily in lead white and zinc white dilutions as these pigments produce a less opaque paint layer than titanium white. The Prussian blue particles embedded in such paint layers are thus more susceptible to light exposure. However, this difference in refractive index between the white pigments does not completely explain the variation in Prussian blue fading. Other properties of the white pigments, such as their photochemical activity, must be considered in the degradation mechanisms of Prussian blue. These mechanisms will be further discussed in **Section 3.5**.

The influence of the binder was also examined, see Figure 3.11c. Whereas the color change with light exposure continuously increases in samples painted from linseed oil, it abruptly increases at the beginning of the light exposure for samples painted from gum arabic. The discoloration very rapidly reaches a maximum; the paint layers prepared with casein do not exhibit a strong sensitivity to irradiation whatever the dilution ratio. In contrast, with linseed oil and gum arabic, which are rather neutral or slightly acidic with a pH between 5 and 7, casein is a basic binder with a pH between 8 and 9. Prussian blue is known to be degraded in a basic medium into iron hydroxide and, therefore, can not be used in fresco. However the slightly acidic or basic character of the binder does not seem to play a significant role in the discoloration process of Prussian blue.

For completeness, the evolution with light exposure of the lightness difference, ΔL^*, the red-greeness difference, Δa^*, and the yellow-blueness difference, Δb^*, was separately evaluated for the laboratory-synthesized soluble A148 Prussian blue and compared to the evolution of the color difference, ΔE^*. The results are shown in Figure 3.12. Both the lightness and the yellow-blueness are significantly increased upon ageing, yielding a paler and less blue final color. The increase for both parameters is gradual and comparable to the evolution of ΔE^*. In contrast, the red-greeness difference, Δa^*, remains relatively unchanged upon ageing, see Figure 3.12c, except for Prussian blue mixed with zinc white. This particular sample shows a decrease in Δa^*, *i.e.*, an increase in greenness.

Finally, the final color change in the six modern and five ancient samples

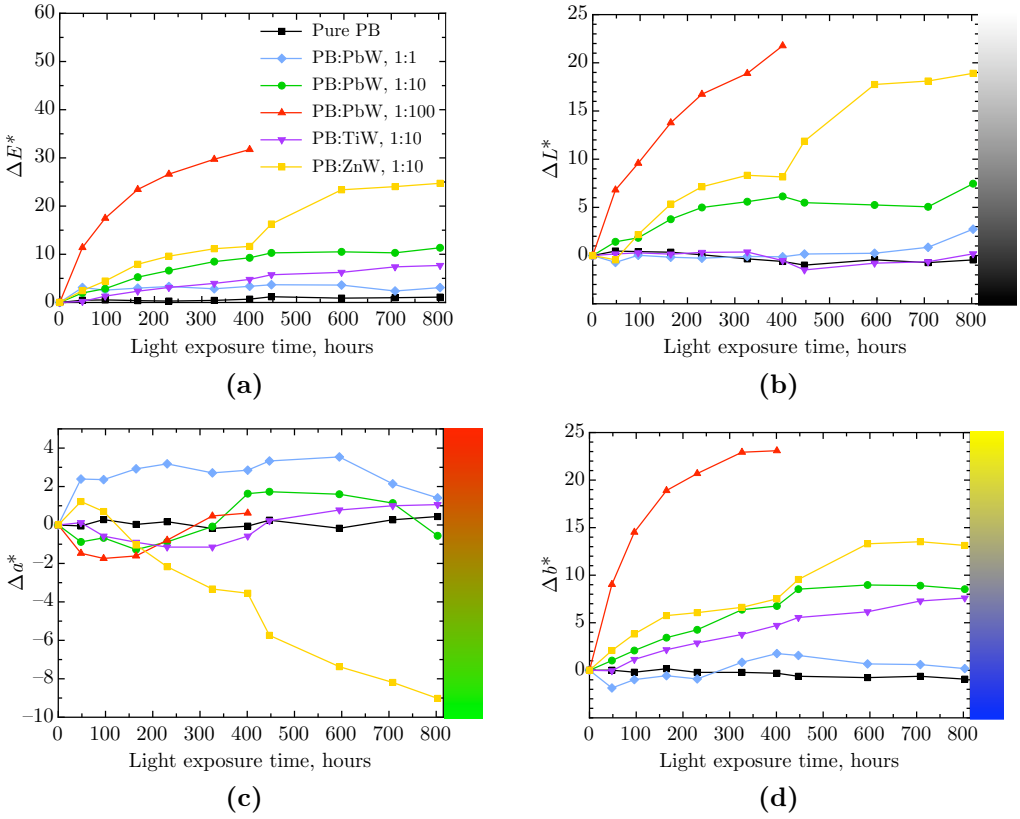

Figure 3.12 Evolution with light exposure time of **a**, the color, ΔE^*, **b**, the lightness, ΔL^*, **c**, the red-greeness, Δa^*, and **d**, the yellow-blueness, Δb^*, differences in the laboratory-synthesized soluble A148 Prussian blue. PbW is lead white, $(PbCO_3)_2Pb(OH)_2$, TiW is titanium white, TiO_2, and ZnW is zinc white, ZnO.

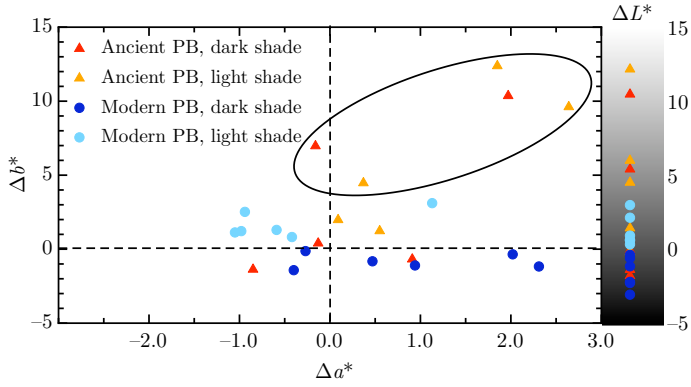

Figure 3.13 Final color change in modern and ancient Prussian blues painted from gum arabic in dark and light shades. The values inside the oval are for B42a, B46b, and B61a, all of which contain ferrihydrite.

painted from gum arabic, shown in Figure 3.7, was investigated. The lightness, red-greenness, and yellow-blueness differences for these samples after 400 hours of light exposure are shown in Figure 3.13. The ancient samples differ significantly from the modern samples by an increase in Δb^*, *i.e.*, a loss of blue leading to a yellower tint. The samples that exhibit the highest increase in Δb^*, *i.e.*, the samples that are circled by an oval in Figure 3.13, are the B42a, B46b, and B61a samples that all contain a large amount of ferrihydrite which is precipitated during the synthesis. These samples also show an increase in Δa^*, *i.e.*, in redness, an increase that can be attributed to the presence of the orange ferrihydrite that becomes more visible as the paint layer fades. The B64 and B61b samples, which contain only Prussian blue and no extender or iron oxide, have a similar fading behavior as the modern Prussian blues.

From these ageing experiments, several conclusions can be drawn. First, pure modern Prussian blue in a dark shade is extremely light fast. Second, pure ancient Prussian blue is light fast if well prepared. Third, the discoloration of ancient and modern Prussian blues is dramatically increased when diluted in mixtures with a white pigment or an extender. Fourth, the discoloration behavior of Prussian blue mixed with a white pigment seems to partially depend on the properties and light stability of the white pigment present. Fifth, the faded Prussian blue containing paint layers have an increased lightness and yellowness and the tendency to turn green is enhanced in ancient Prussian blues that contain ferrihydrite. These conclusions agree with the reports of degradation found in eighteenth and nineteenth century books, see **Appendix A**. The discoloration mechanisms of Prussian blue are, however, not yet explained and their understanding requires the study of the local electronic and structural configurations of the iron ions in aged Prussian blue containing paint layers.

3.4 Characterization of degradation in Prussian blue

The intense color of Prussian blue arises from an intervalence charge transfer between the iron(II) and iron(III) oxidation states when light is absorbed at *ca.* 700 nm. Thus, any color fading or change corresponds to a disruption in the electron transfer pathway in Prussian blue, *i.e.*, in the $Fe^{III}-N-C-Fe^{II}$ bonding pathway. As explained in **Section 1.2.3**, several hypotheses for explaining the fading of Prussian blue have been proposed in the literature: (1) the reduction of Prussian blue, (2) the oxidation of Prussian blue, (3) ion exchange within the Prussian blue, and (4) substitution reactions within the Prussian blue.

In order to identify which mechanisms are involved in the fading of Prussian blue, the iron ion electronic and structural configurations were investigated by

iron-57 transmission Mössbauer, iron K-edge X-ray absorption, attenuated total reflection Fourier transform infrared, and Raman spectroscopy. It should be noted that all these techniques, except transmission Mössbauer spectroscopy, and, to a lesser extent, X-ray absorption in the fluorescence mode, are surface sensitive and provide little or no information about the bulk of the paint layers. This difference in probing depth is crucial for interpreting the data because paint layers are heterogeneous and can exhibit a fading gradient with layer thickness.

Changes in the local electronic and structural configurations of the iron(II) and iron(III) ions of Prussian blue are expected upon ageing, see **Section 1.2.3**. These changes will be related to the formation of a fading product, such as iron(III) ferricyanide, iron(II) ferrocyanide, iron(III) aquapentacyanoferrate, and Prussian blue analogs. The last two are expected to show very different X-ray absorption, Mössbauer, and vibrational spectra. The reduced and oxidized forms of electrochemically synthesized Prussian blue have been almost exclusively investigated by electrochemical studies. The next section deals with the bulk synthesized reduced and oxidized forms of Prussian blue.

3.4.1 Oxidized and reduced forms of Prussian blue

Berlin green, the partially oxidized form of Prussian blue, and Berlin white, the reduced form of Prussian blue, are among the possible fading products. In order to interpret the spectral variations observed upon ageing, both compounds were synthesized and characterized. The various results found in the literature are also summarized in order to complete the characterization.

Synthesis

Berlin green was synthesized according to the method developed by Kumar *et al.* [139]. Equimolar aqueous solutions of $FeCl_3{\cdot}6H_2O$ and $K_3Fe(CN)_6$ were mixed together and heated to 50°C for one hour. After cooling, the precipitate was washed with deionized water and collected by centrifugation. After air drying and grinding, a dark green powder was obtained. The synthesis was twice reproduced in the ambient atmosphere and once in a nitrogen atmosphere. Because the resulting powders were green rather than yellow, the composition of the compounds was expected to vary between the potassium cation containing Prussian blue and the fully oxidized form of Prussian blue. The products can be best described as $\{KFe^{III}Fe^{II}(CN)_6\}_x\{Fe^{III}Fe^{III}(CN)_6\}_{1-x}$, where the water molecules have been omitted and the value of x has not been determined. The fraction, x, of hexacyanoferrate(II) is highly variable, even for different samples similarly prepared [140][141].

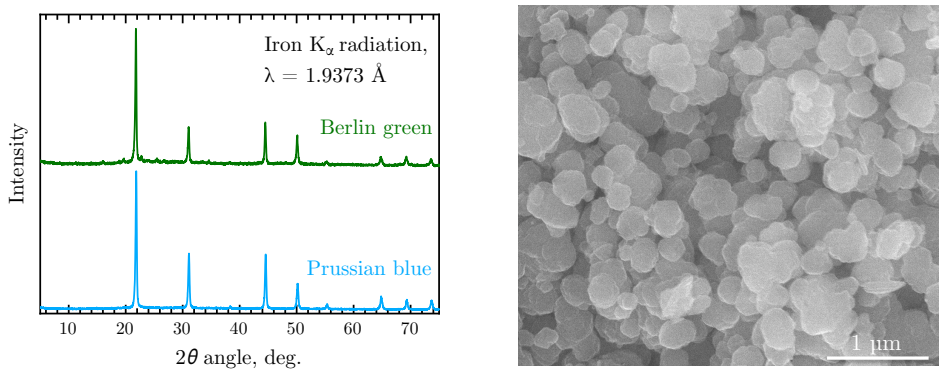

(a) **(b)**

Figure 3.14 a, X-ray powder diffraction patterns of Berlin green and Prussian blue, and **b**, a scanning electron micrograph of Berlin green synthesized in the ambient atmosphere and obtained with 15 keV secondary electrons.

Berlin white, ferrous ferrocyanide, $[Fe^{II}(Fe^{II}(CN)_6)]^{2-}$, was synthesized under an argon atmosphere in order to avoid oxidation by air. Equimolar aqueous solutions of iron(II) sulfate, $Fe(SO)_4{\cdot}7H_2O$, and potassium ferrocyanide, $K_4Fe(CN)_6{\cdot}3H_2O$, were prepared with triply distilled water and mixed together with magnetic stirring. A pale blue-green precipitate immediately formed. The surface of the solution turns completely dark blue, due to oxidation by the remaining oxygen in the argon atmosphere. The precipitate was extremely fine and attempts to filter it under the argon atmosphere were unsuccessful. The solution was then poured in a hermetic glass cell. Because the precipitate is partially light blue, it is suspected to have an intermediate composition between ferrous ferrocyanide, $Fe^{II}[Fe^{II}(CN)_6]^{2-}$, and ferric ferrocyanide $[Fe^{III}Fe^{II}(CN)_6]^{-}$. Although the synthesized product may not be, strictly speaking, Berlin white because of its intermediate composition, we will continue to use this name herein. Because of its air-sensitivity, it was impossible to obtain and further manipulate Berlin white powder under normal conditions. The analysis performed on this sample was restricted to Raman spectroscopy.

Crystal structure

The X-ray powder diffraction pattern of Berlin green reveals a structure similar to that of Prussian blue, with the $Fm3m$ space group and a lattice parameter of *ca.* 10.2 Å, see Figure 3.14a. This is in agreement with a previous investigation of ferric ferricyanide by neutron diffraction [139]. Some additional weak diffraction peaks are visible in the Berlin green diffraction pattern. They are likely to

result from primitive reflections but have not been studied in detail herein. The narrow diffraction peaks indicate the presence of large crystallites. Berlin green was studied by scanning electron microscopy and was found to consist of rounded flat particles of *ca.* 200 to 300 nm diameter, see Figure 3.14b.

Berlin white also exhibits a similar crystal structure, with a lattice parameter of *ca.* 10.2 Å. In $K_2Fe^{II}[Fe^{II}(CN)_6]$, the potassium cations occupy the lattice cavities, at interstitial positions [17].

Iron ion electronic and structural configurations

The electronic and structural configurations of the iron ions in Berlin green and Berlin white were studied by iron K-edge X-ray absorption, iron-57 transmission Mössbauer, Fourier transform infrared, and Raman spectroscopy, the same techniques that were used for the characterization of the unaged and aged Prussian blue containing paint layers.

Iron K-Edge X-ray Absorption Spectroscopy. Figure 3.15 shows the iron K-edge X-ray absorption near edge spectra of Berlin green, the soluble commercial C02 Prussian blue, and the insoluble commercial C03 Prussian blue. The spectra were obtained in transmission mode on powder samples. The main K-edge absorption edge of Berlin green is shifted by 1.0 eV towards higher energy in comparison with the absorption edge of the commercial and laboratory-synthesized Prussian blues. In contrast, the pre-edge peak position of the three compounds is virtually identical, although a shift towards higher energy was expected because of the higher oxidation state of the iron ions in Berlin green. The similar shape of the XANES spectra for Prussian blue and Berlin green suggests an octahedral environment of the iron ions in both compounds.

The EXAFS spectrum of Berlin green and Prussian blue are compared in Figure 3.16. The EXAFS fit for Berlin green is shown in Figure 3.17. The average fit parameters obtained on the two Berlin green samples synthesized in air are given in Table 3.2; the bond distances are identical to those in Prussian blue. Only the iron-iron coordination number is reduced to 4.1(8). This reduction can be attributed to a larger vacancy content. Because of the green color, Berlin green must contain some fraction of iron(II) ions. Some authors attribute the autoreduction of iron(III) ferricyanide to the reaction [140]

$$Fe^{3+} + [Fe^{III}(CN)_6]^{3-} + 2H_2O \rightarrow Fe^{2+} + [Fe^{III}(CN)_5]^{3-} + NH_4^+ + CO_2.$$

During the precipitation reaction, the hexacyanoferrate(III) ions are readily reduced by water molecules present in the solution. In the solid state, the electrons required for the reduction of iron(III) are provided by the water molecules inserted

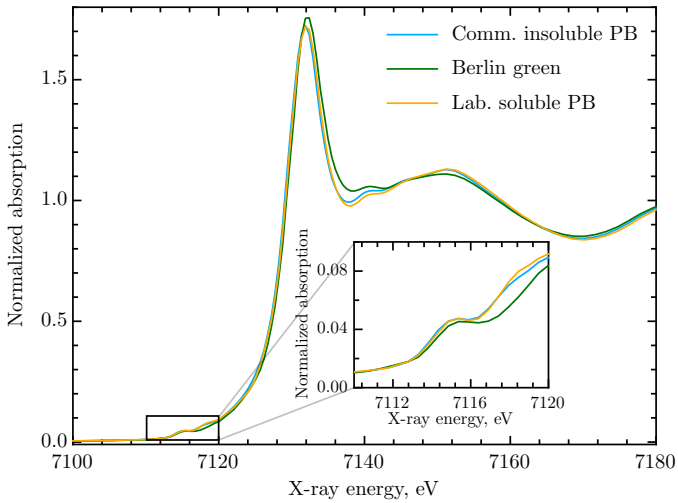

Figure 3.15 Iron K-edge X-ray absorption near edge spectra of commercial insoluble C03 Prussian blue, commercial soluble C02 Prussian blue, and Berlin green. Inset: an expanded view of the pre-edge peak spectral region.

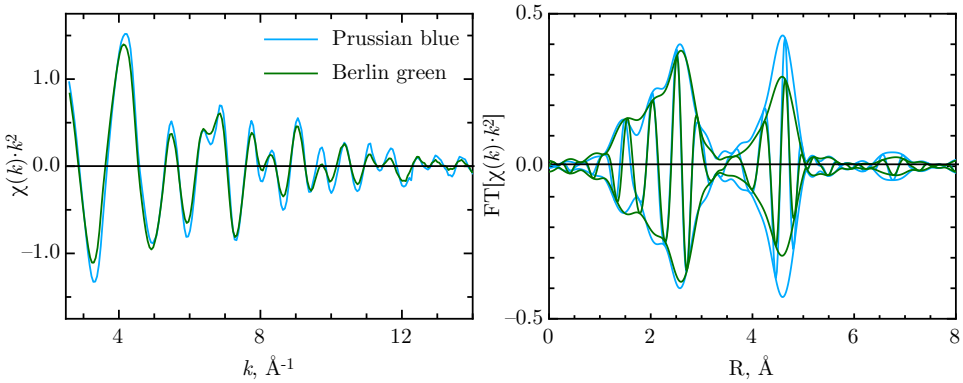

Figure 3.16 Iron K-edge $\chi(k)\cdot k^2$ and FT$[\chi(k)\cdot k^2]$ spectra with $\Delta k \sim 5.3 - 13.9$ Å^{-1} for insoluble commercial Prussian blue and Berlin green.

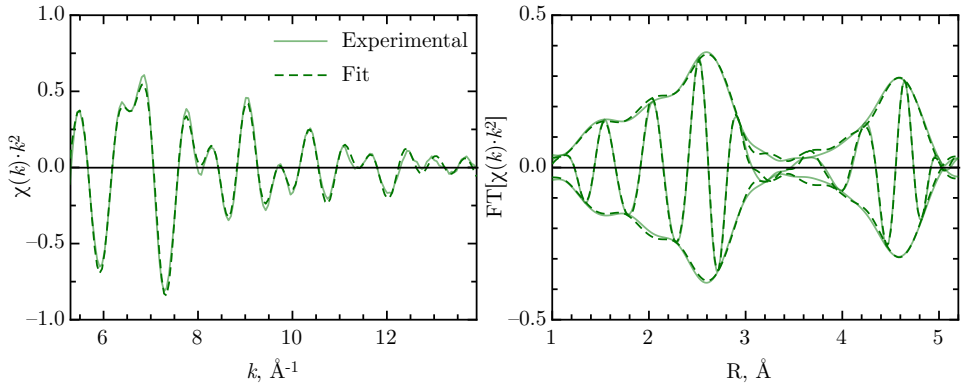

Figure 3.17 $\chi(k)\cdot k^2$ and FT$[\chi(k)\cdot k^2]$ spectra with $\Delta k \sim 5.3 - 13.9$ Å^{-1} for Berlin green with k^2 variances: 0.48 (imaginary part) and 0.23 (absolute part). Experimental data, solid line, and fit, dotted line, agree.

Table 3.2 Average bond distances, R, coordination numbers, N, relative Debye-Waller factors $\Delta\sigma^2$, and inner potential corrections, ΔE_0, for the EXAFS fit of two Berlin green samples synthesized in air.

		EXAFS fit values[a]			
Compound	Absorber-scatterer	R, Å	N	$\Delta\sigma^2$, Å^2	ΔE_0, eV
Berlin green	Fe(II)-C	1.92(1)	3.0(4)	-0.0002(4)	-4(1)
	Fe(III)-N	2.06(1)	3.0(4)	-0.0002(4)	4(2)
	Fe(II)-N	3.06(1)	2.2(1)	-0.0002(4)	0.2(6)
	Fe(III)-C	3.14(1)	2.3(1)	-0.0002(4)	4.9(3)
	Fe(II)-Fe(III)	5.10(1)	4.1(8)	0.0006(4)	-3(1)

[a]The values in parentheses are the standard deviations.

in the lattice cavities of Berlin green. The presence of pentacyanoferrate(III) could then explain the lower iron-iron coordination number. Berlin white was not studied by iron K-edge X-ray absorption spectroscopy because of its air-sensitivity and unfortunately, no X-ray absorption spectroscopy data could be found in the literature.

Iron-57 Mössbauer Spectroscopy. The Mössbauer spectra of two Berlin green samples are shown in Figure 3.18. The spectra were fitted with two Lorentzian components, one singlet and one doublet. The resulting spectral parameters for both the high-spin and low-spin iron ions, *i.e.*, the isomer shift, δ, the full line width at half-maximum, Γ, the quadrupole splitting, ΔE_Q, and the percent area, A, are given in Table 3.3.

Mössbauer spectral studies [27][142][143] on the fully oxidized form of Prussian

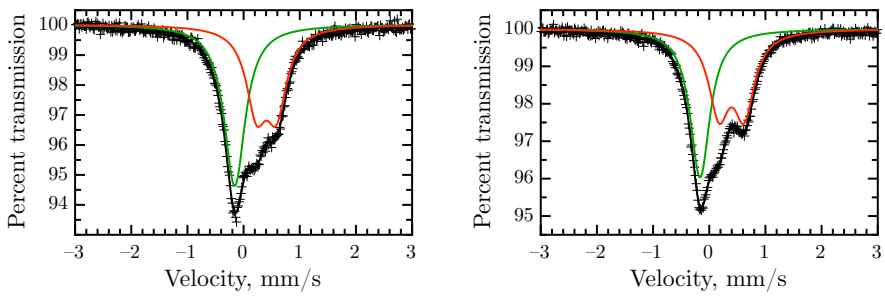

Figure 3.18 The Mössbauer spectra of two Berlin green samples obtained at 295 K. **a**, Berlin green synthesized under nitrogen and **b**, Berlin green synthesized in the ambient atmosphere.

Table 3.3 The Mössbauer spectral parameters of reduced and oxidized Prussian blue.

Compounds[a]	Ions	δ mm/s[b]	Γ mm/s[c]	A %	ΔE_Q mm/s	Ref.
Berlin green, N_2 synthesized $\{KFe^{III}Fe^{II}(CN)_6\}_x\{Fe^{III}Fe^{III}(CN)_6\}_{1-x}$	LS iron HS iron(III)	-0.158(2) 0.407(4)	0.45(1) 0.44(1)	51(1) 49(1)	0 0.35(4)	This work
Berlin green, air synthesized $\{KFe^{III}Fe^{II}(CN)_6\}_x\{Fe^{III}Fe^{III}(CN)_6\}_{1-x}$	LS iron HS iron(III)	-0.164(2) 0.397(3)	0.43(1) 0.44(1)	47(1) 53(1)	0 0.45(1)	This work
Prussian yellow $Fe^{III}[Fe^{III}(CN)_6]$	HS iron(III)	0.37(2)			0.41(2)	[142]
Prussian yellow $Fe^{III}[Fe^{III}(CN)_6]$	LS iron(III) HS iron(III)	-0.06 0.50			0.43 0.52	[27][d]
Prussian yellow $Fe^{III}[Fe^{III}(CN)_6]$	LS iron(III) HS iron(III)	-0.17 0.38	0.44 0.36		0.13 0.44	[143]
Berlin white $K_2Fe^{II}[Fe^{II}(CN)_6]$	HS iron(II)	1.14(2)			1.13(2)	[142]
Berlin white $K_2Fe^{II}[Fe^{II}(CN)_6]$	LS iron(II) HS iron(II)	-0.09 1.42			0 3.02	[27][d]

[a]The water molecules have been omitted in the chemical formulae. [b]The isomer shift, δ, is referred to α-iron at 295 K. [c]Γ is the full line width at half-maximum. [d]The data were obtained at 77K.

blue, *i.e.*, Prussian yellow, $Fe^{III}[Fe^{III}(CN)_6]$, indicate that Prussian yellow contains low-spin and high-spin iron(III) ions. The Mössbauer spectrum of Prussian yellow, $Fe^{III}[Fe^{III}(CN)_6]$, consists of a doublet assigned to the high-spin iron(III) ion and a singlet assigned to the low-spin iron(III) ion in $[Fe^{III}(CN)_6]^{3-}$. The isomer shift and quadrupole splitting parameters found in the literature [27][142][143] are given in Table 3.3. Because Berlin green also contain low-spin iron(II) ions, the singlet shown in Figure 3.18 must contain the contributions of both the low-spin iron(II) and iron(III) ions. A distinction between the low-spin iron(II) and iron(III) ions was not possible because of their very similar isomer shifts, see **Section 2.2.2**. In contrast, Berlin white, $K_2Fe^{II}[Fe^{II}(CN)_6]$, contains high-spin iron(II) ions, which are easily distinguished from the other iron ions present by its isomer shift of 0.8 and 1.2 mm/s. Mössbauer spectral parameters on electrochemically synthesized Berlin white found in the literature [27] are also given in Table 3.3.

Vibrational Analysis. Vibrational spectroscopy is very suitable for studying the fading products of Prussian blue because the position of the ν(CN) band depends upon the oxidation state of the metal ion to which the cyanide ions are coordinated. In aqueous solution, the stretching mode for the free CN^- ion occurs at 2060 cm^{-1}, whereas the ν(CN) frequency increases upon coordination to a metal ion. The position of this band also depends on the electronegativity and the coordination number of the metal ion [115]. Lower frequency bands can be assigned to a ν(CN) mode associated with iron(II) whereas the higher frequency bands at *ca.* 2155 cm^{-1} can be assigned to a ν(CN) mode associated with iron(III) [144][145]. Therefore, oxidized and reduced forms of Prussian blue should be easily distinguishable in their infrared and Raman spectra.

Attenuated total reflectance Fourier transform spectroscopy was performed on the Berlin green samples and the spectra are shown in Figure 3.19. Upon oxidation, an additional absorption band appears at 2169(2) cm^{-1}. This band is assigned as the CN^- stretching band of the hexacyanoferrate(III) ions. The intense ν(CN) band at 2075(2) cm^{-1} corresponds to the CN^- stretching vibration of hexacyanoferrate(II) ions. As expected, the ν(CN) frequency of hexacyanoferrate(III) ions is increased in comparison with the ν(CN) frequency of hexacyanoferrate(II) ions. These results agree with those previously reported in the literature for bulk Berlin green [140] and electrochemically synthesized Berlin green [34][62]. A loss of absorbance and a broadening are also observed for the ν(CN) band at 2075(2) cm^{-1} in Berlin green. The relative intensity of the two ν(CN) bands in both Berlin greens are almost identical, however the intensity has been found to vary strongly with the type of synthesis used [140]. A ν(CN) frequency of 2089 cm^{-1} was also reported for Berlin green [132]. Furthermore, a shoulder peak at *ca.* 2120 cm^{-1}

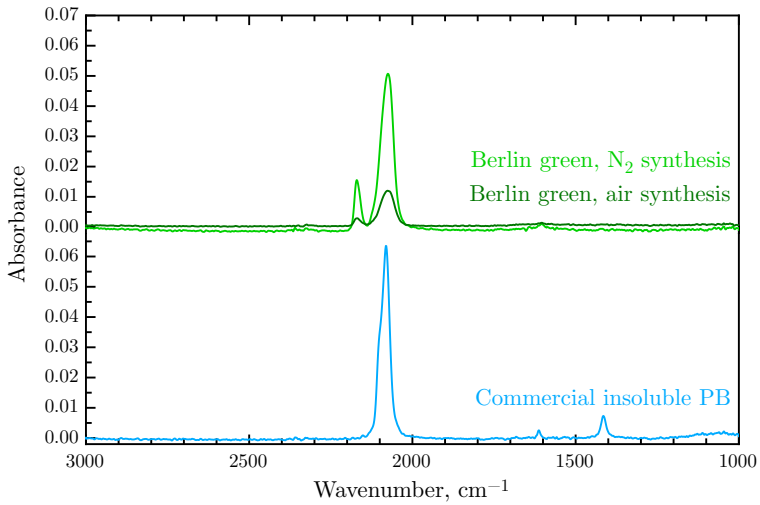

Figure 3.19 The attenuated total reflectance infrared spectra of two laboratory-synthesized Berlin greens and a commercial insoluble Prussian blue.

was attributed to the presence of hexacyanoferrate(III) ions [62].

The infrared spectrum of electrochemically synthesized Berlin white in the stretching region is reported to be very similar to that of Prussian blue [62]. It also exhibits a unique strong ν(CN) stretching band between 2075 and 2085 cm^{-1} [146]. Hamnet *et al.* [147] reported the evolution of the ν(CN) bands upon reduction of an electrochemically synthesized Prussian blue film. Initially Prussian blue exhibits a broad band in the CN^- stretching region at *ca.* 2075 cm^{-1}. Upon reduction, the band narrows and shifts to 2080 cm^{-1}. A shoulder also appears at about 2106 cm^{-1}. In contrast, other authors reported upon electrochemically induced reduction [34] the presence of a single ν(CN) band at 2060 to 2070 cm^{-1} of lower absorbance in comparison with Prussian blue.

Finally, Berlin green and Berlin white samples were analyzed by Raman spectroscopy, see Figure 3.20. The Raman spectra of potassium ferricyanide, $K_3[Fe^{III}(CN)_6]$, potassium ferrocyanide, $K_4[Fe^{II}(CN)_6]$, and insoluble Prussian blue, $Fe_4^{III}[Fe^{II}(CN)_6]_3$, are also shown for comparison in this figure.

Berlin green exhibits a broad band at 2149 cm^{-1} as well as a broad shoulder at lower wavenumbers. No significant shift toward higher wavenumbers in comparison with the A_{1g} mode in Prussian blue was observed within the experimental resolution, as would be expected in view of the higher oxidation state of the iron ions in Berlin green. A ν(CN) band at 2152 cm^{-1} was previously reported for

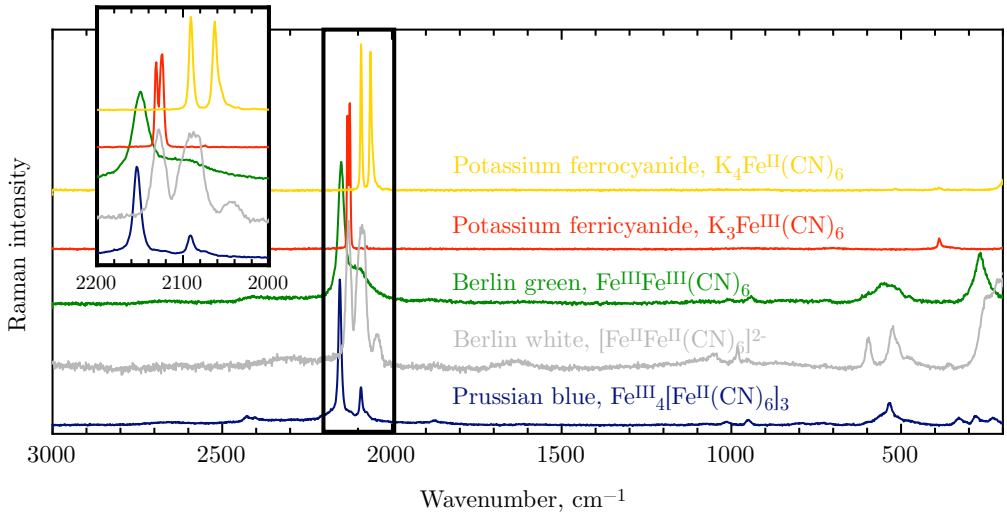

Figure 3.20 The Raman spectra of potassium ferrocyanide, potassium ferricyanide, Berlin green, Berlin white, and laboratory-synthesized Prussian blue. Raman spectrum of Berlin white was obtained on the unwashed precipitate in aqueous solution. Inset: an expanded view of the ν(CN) stretching band.

Prussian blue [132]. The shoulder in Figure 3.20 seems to arise from two contributions first, from the antisymmetric stretching vibration mode of Prussian blue at 2091 cm^{-1} and, second, from the stretching vibration of the ferricyanide ion, $[Fe^{III}(CN)_6]^{3-}$, at 2124 to 2131 cm^{-1}. The relatively strong band at 266 cm^{-1} in Berlin green corresponds to an iron-ligand bending vibration but has not been assigned.

Berlin white, the reduced form of Prussian blue, exhibits a totally different Raman spectrum, with three CN^- stretching vibration bands. It should be noted that the spectrum was obtained directly from the unwashed wet precipitate, hermetically stored in an analysis cell. The two bands at 591 and 520 cm^{-1} result from the presence of sulfate ions. Similar Raman results were obtained on the electrochemically reduced Prussian blue deposited as a thin film on a silicon substrate [148]. On the basis of its vibrational spectrum, Berlin white is thus easily identified by Raman spectroscopy, whereas Berlin green can be identified by Fourier transform infrared spectroscopy.

3.4.2 Characterization of the unaged and aged paint layers

Because the diluted paint layers exhibit a stronger discoloration than pure Prussian blue paint layers, the diluted paint layers have been characterized in order to identify the degradation mechanisms. However, the dilution with a white pigment is problematic because it implies a rather low concentration of Prussian blue and, furthermore, the signal arising from the white pigment will partially mask the signal characteristic of Prussian blue. In the case of dilution with lead white, this masking interference is even more critical because lead white, $(PbCO_3)_2Pb(OH)_2$, strongly absorbs X-rays.

Another difficulty is the non-homogeneous character of the paint layer itself. Any discoloration is expected to take place initially at the surface before spreading into the paint layer. In order to determine the discolored paint layer thickness, cross-sections of millimeter size fragments of the aged and unaged paint layers that were embedded in resin and carefully polished were studied with an Olympus BX51 optical microscope. For the samples painted from linseed oil, see Figure 3.6a, the paint layer is about 20 µm thick and appears to have a homogenous color indicating a discoloration or fading throughout the entire paint layer, see Figure 3.21. The paint layers shown in Figure 3.6c are *ca.* 300 µm thick and the discolored upper layer thickness does not exceed 20 µm, see Figure 3.22. These samples clearly exhibit a discoloration at the surface layer whereas the bulk remains unaged. Due to the inhomogeneity in depth of the paint layer, the probing depth of the various techniques must be taken into account for interpreting the results.

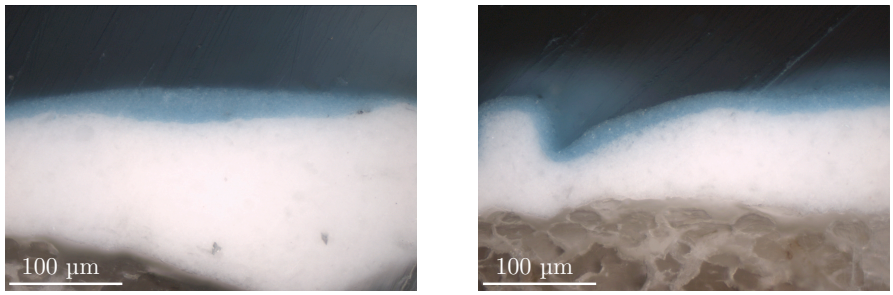

(a) **(b)**

Figure 3.21 Optical micrographs of a cross-section of laboratory-synthesized soluble Prussian blue powder painted from linseed oil with lead white in a 1:100 dilution ratio. Cross-sections of **a**, the unfaded portion, and, **b**, the faded portion. The white layer corresponds to the preparation layer sized on the canvas. Results obtained with reflected visible light and dark field illumination.

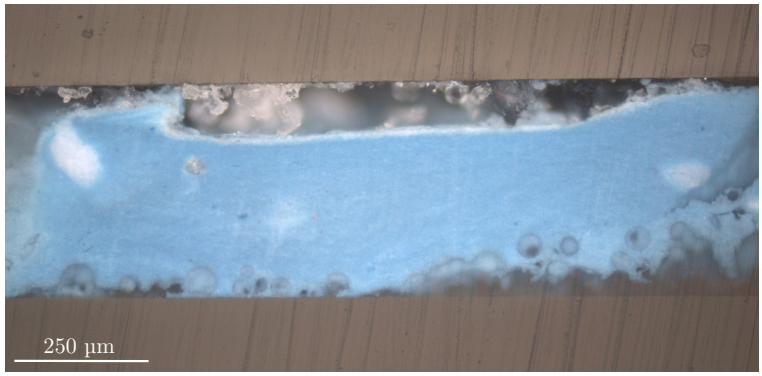

Figure 3.22 Optical micrograph of a cross-section of faded ready-to-use oil Prussian blue color mixed with ready-to-use oil lead white at a 1:50 dilution ratio. Results obtained with reflected visible light and dark field illumination.

We first focused on the characterization of the thin paint layers prepared with modern commercial and laboratory-synthesized Prussian blues in a linseed oil medium, see Figure 3.6a. Because they appear homogeneous in depth, with no optical difference between the bulk and the surface, both bulk and surface-sensitive techniques are expected to provide relevant information about the discoloration processes.

Iron ion electronic and structural configurations

X-ray Absorption Near Edge Spectroscopy. The iron K-edge X-ray absorption near edge spectra of pure, unaged and aged laboratory-synthesized A148 Prussian blue mixed with lead white, $(PbCO_3)_2Pb(OH)_2$, in 1:10 and 1:100 dilution ratios are shown in Figure 3.23. The black curve represents the spectrum obtained in transmission mode on the pure soluble laboratory-synthesized Prussian blue. The other spectra have been obtained in fluorescence mode and differences in absorption intensity compared with the transmission spectrum result from self-absorption effects.

The weak intensity of the pre-edge peak is characteristic of the centrosymmetric iron(II) and iron(III) sites in soluble Prussian blue [12][131]. The main K-edge and pre-edge positions have been determined from the maxima in the first derivative that has an accuracy of about one-half the energy step of 0.52 eV. A shift in the absorption edge by approximately 0.2(2) and 2.5(2) eV for the 1:10 and 1:100 dilution ratios, respectively, towards lower energy is observed upon ageing in the presence of lead white. This shift corresponds either to a change in the density of states or to a decrease in the average iron oxidation state in the Prussian blue, *i.e.*, an increase in the amount of low-spin iron(II) as compared to

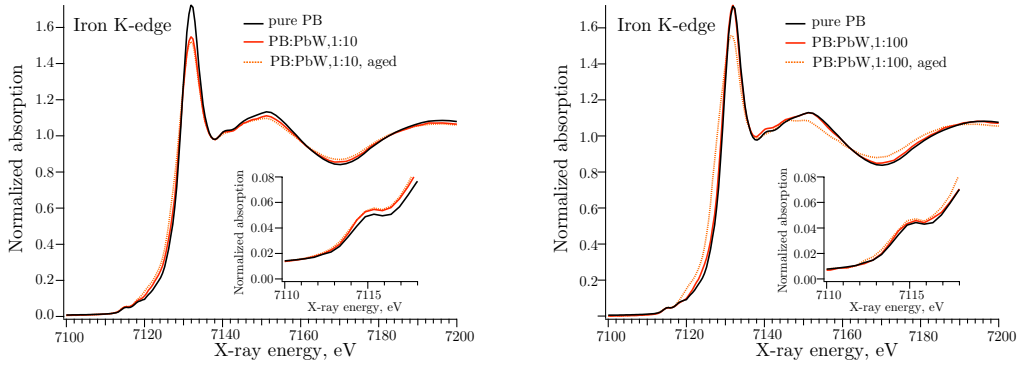

Figure 3.23 Iron K-edge X-ray absorption near edge spectra of pure laboratory-synthesized soluble A148 Prussian blue painted from linseed oil with PbW, lead white, $(PbCO_3)_2Pb(OH)_2$, in a 1:10 dilution ratio, **a**, and in a 1:100 dilution ratio, **b**. Inset: An expanded view of the pre-edge peak.

high-spin iron(III).

The shift of the absorption edge towards lower energy may suggest a partial reduction of Prussian blue, leading to a partial formation of Berlin white, *i.e.*, some iron(II) ferrocyanide, perhaps on the particle surfaces. In contrast, the centroid of the pre-edge peaks does not show a significant shift towards lower energy, see the insets to Figure 3.23, and the absence of a shift does not support the hypothesis of a reduction. However, the centroid of the pre-edge peak may not be very sensitive to the iron oxidation state. Indeed, the centroid of the pre-edge peak in the XANES spectrum obtained on Berlin green was not shifted towards higher energy, even though Berlin green contains iron ions with a higher average oxidation state.

The iron K-edge X-ray absorption near edge spectra were also obtained on unaged and aged insoluble commercial C03 Prussian blue mixed with lead white, zinc white, or titanium white in a 1:10 dilution ratio. The spectra shown in Figure 3.24 are the differences between the unaged and the aged XANES spectra. The importance of the difference in absorbance, $\Delta\mu$, can be directly correlated with the extent of the color change, ΔE^*, observed for these samples and given in the legend in Figure 3.24.

Extended X-ray absorption Fine Structure Spectroscopy. The EXAFS spectra of the painted Prussian blue samples have been recorded in fluorescence mode, which resulted in lower quality data as compared to the transmission mode used for the reference samples. As an example, the k^2 weighted EXAFS spectra

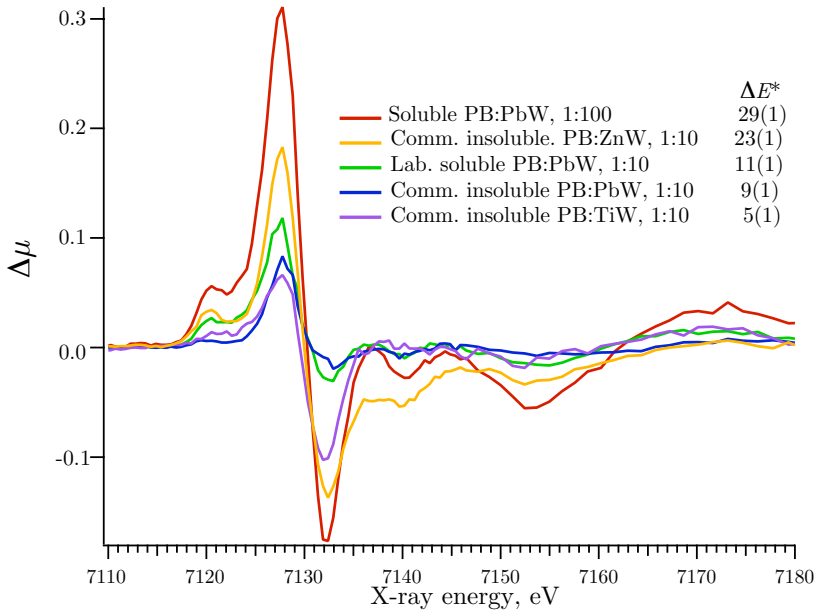

Figure 3.24 Iron K-edge difference XANES spectra of aged and unaged laboratory-synthesized soluble A148 Prussian blue painted from linseed oil with PbW, lead white, $(PbCO_3)_2Pb(OH)_2$, in 1:10 and 1:100 dilution ratios and of insoluble commercial Prussian blue, $Fe_4^{III}[Fe^{II}(CN)_6]_3$, painted from linseed oil with lead white, zinc white, ZnO, and titanium white, TiO_2, in a 1:10 dilution ratio. The color change, ΔE^*, for each sample is given in the legend.

for the pure laboratory-synthesized soluble Prussian blue measured in transmission mode is compared in Figure 3.25 with the fluorescence mode spectra for the unaged and aged pigment mixed with lead white in a 1:100 dilution ratio. The spectra for the pure powder and the unaged painted layer are identical. The EXAFS spectra of laboratory-synthesized and commercial non-aged Prussian blue painted layers mixed with lead white, zinc white, and titanium white in different dilution ratios were analyzed and showed no significant differences. Bond distances and coordination numbers close to the X-ray crystal structure values were obtained by fixing the Debye-Waller factor to the average value obtained from the transmission EXAFS spectra, see Table B.1 in **Appendix B.3.3**. The average fit values for the five unaged painted samples are given in Table 3.4. The standard deviations are representative for the fit accuracy taking into account the data quality, the fit routine, and the systematic errors due to differences in background subtraction and data reduction. These standard deviations represent our best estimates of the errors in the EXAFS fits on the aged samples.

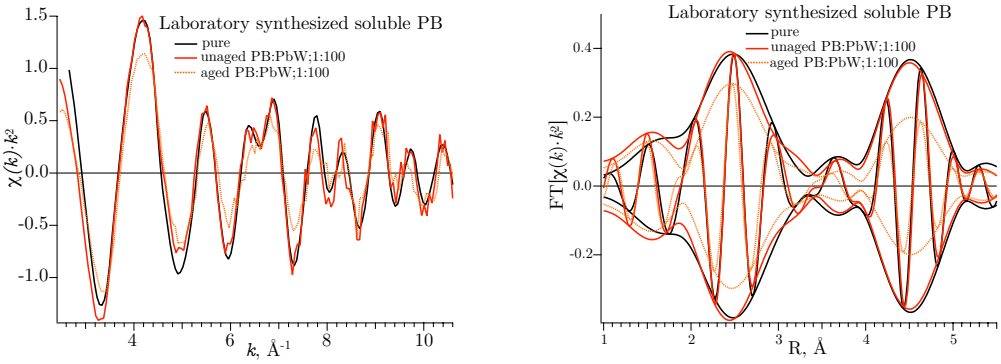

Figure 3.25 $\chi(k)\cdot k^2$ and FT$[\chi(k)\cdot k^2]$ spectra with $\Delta k \sim 5.3 - 10.5$ Å^{-1} for laboratory-synthesized soluble Prussian blue, in pure form and as unaged and aged painted layers mixed with lead white in a 1:100 dilution ratio.

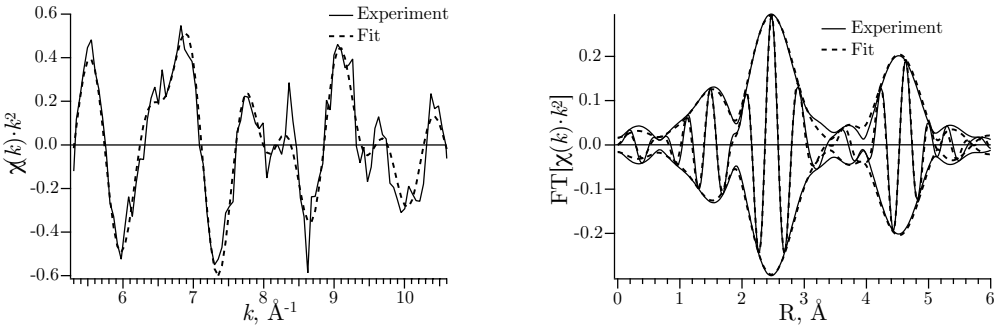

Figure 3.26 $\chi(k)\cdot k^2$ and FT$[\chi(k)\cdot k^2]$ of the experimental and fit spectra of aged laboratory synthesized soluble Prussian blue painted with lead white in a 1:100 dilution ratio with $\Delta k \sim 5.3 - 10.5$ Å^{-1}, $\Delta R = 1.0 - 5.2$ Å^{-1}, with k^2 variances: 1.51 (imaginary part) and 0.51 (absolute part).

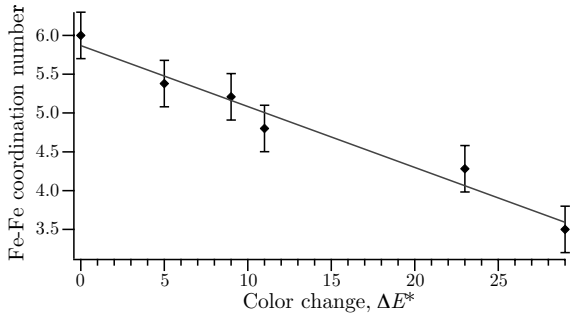

Figure 3.27 The linear correlation between the iron-iron ion coordination number in aged painted Prussian blue pigments mixed with different white pigments as a function of color change, ΔE^*.

Table 3.4 EXAFS fit parameters for the five unaged Prussian blue paint layers and the aged laboratory synthesized Prussian blue pigment mixed with lead white in a 1:100 dilution ratio

	Crystal structure		Fit values[a] for the unaged layers				Fit values for the aged layers			
Absorber-scatterer	R, Å	N	R, Å	N	$\Delta\sigma^2$, Å^{2b}	ΔE_0, eV	R, Å	N	$\Delta\sigma^2$, Å^{2b}	ΔE_0, eV
Fe(II)-C	1.92(1)	3	1.90(1)	3.0(2)	0.0002	1.0(3)	1.91(1)	3.2(2)	0.0002	2(1)
Fe(III)-N	2.04(1)	3	2.11(1)	3.0(1)	0.0002	-0.5(8)	2.13(1)	3.2(1)	0.0002	0.7(8)
Fe(II)-N	3.04(1)	3	3.05(1)	3.0(1)	0.0002	0.2(3)	3.04(1)	2.4(1)	0.0002	-0.2(3)
Fe(III)-C	3.16(1)	3	3.15(1)	2.9(1)	0.0002	5.3(5)	3.13(1)	2.3(1)	0.0002	4.5(5)
Fe(II)-Fe(III)	5.08(1)	6	5.10(1)	5.9(3)	-0.0005	-4.0(7)	5.1(1)	3.5(3)	-0.0005	-4.6(7)

[a]Average values on the five unaged Prussian blue paint layers. [b]The Debye-Waller factors, $\Delta\sigma^2$, are fixed to the average value obtained from the transmission EXAFS spectra of the reference samples, see Table B.1 in **Appendix B.3.3**.

Table 3.5 Mössbauer spectral parameters of Prussian blue and its mixtures

Samples		T, K	δ^{II}, mm/s[a]	Γ^{II}, mm/s[b]	A^{II}, %[c]	δ^{III}, mm/s[a]	Γ^{III}, mm/s[b]
A148	unaged	295	-0.14(1)	0.255(1)	49(1)	0.40(1)	0.356(2)
		225	-0.11(1)	0.25(1)	49(1)	0.440(5)	0.362(3)
		155	-0.08(1)	0.25(1)	48(1)	0.478(5)	0.375(1)
		85	-0.06(1)	0.25(1)	48(1)	0.504(5)	0.381(2)
A148:$(PbCO_3)_2Pb(OH)_2$	unaged	295	-0.17(1)	0.25(3)	53(3)	0.43(2)	0.40(8)
1:100	aged	295	-0.17(1)	0.27(3)	52(6)	0.41(3)	0.46(9)
A148:ZnO	unaged	295	-0.15(1)	0.23(3)	53(5)	0.41(2)	0.34(6)
1:10	aged	295	-0.13(1)	0.25(3)	56(5)	0.41(2)	0.30(5)

[a]The isomer shift, δ, is referred to α-iron at 295 K. [b]Γ is the full line width at half-maximum. [c]$A^{III} = 100 - A^{II}$.

For the EXAFS fit on the aged painted layers, the fitting model used for the corresponding non-aged paint layer was used as a starting model and the bond distances, inner potential corrections, and coordination numbers were optimized. The EXAFS fit on the aged laboratory synthesized soluble Prussian blue painted with lead white in a 1:100 dilution ratio is shown in Figure 3.26. In general, there is no change in bond distances, but there is a decrease in the iron-iron coordination number with increasing color change, ΔE^*, see Figure 3.27. A decrease in coordination number for the second $Fe^{II}-N$ and $Fe^{III}-C$ shells was also observed for the aged laboratory-synthesized soluble Prussian blue paint layer mixed with lead white in a 1:100 ratio, see Table 3.4. Such a decrease in the iron-iron coordination number was also observed for Berlin green, the partially oxidized form of Prussian blue, see Figure 3.16 and Table 3.2.

Iron-57 Mössbauer Spectroscopy. The 85 and 295 K Mössbauer spectra of pure soluble laboratory-synthesized A148 Prussian blue are shown in Figure 3.28; the spectra obtained at 155 and 225 K are very similar. The Mössbauer spectral parameters resulting from a fit with two Lorentzian single lines are given in Table 3.5. The spectra and the resulting fit parameters agree very well with those previously published for Prussian blue [27][149]. The absorption lines with negative and positive isomer shifts are assigned to low-spin iron(II) and high-spin iron(III), respectively. As the temperature decreases from 295 to 85 K, both isomer shifts, as expected, become more positive as a result of the second-order Doppler shift [150]. The relative areas of the iron(II) and iron(III) absorptions are temperature independent and, if the recoil-free fractions of iron(II) and iron(III) are assumed equal, a reasonable assumption at 85 K [26], the $A^{II}/A^{III} = 48.5/51.5 = 0.94(4)$, a ratio that is in fair agreement with the ratio of close to one obtained for the laboratory-synthesized soluble A148 Prussian blue in **Section 2.2.2**.

Because the relative areas were found to be independent of temperature in the pure A148 soluble Prussian blue, the Mössbauer spectra of the mixtures of Prussian blue with lead white, $(PbCO_3)_2Pb(OH)_2$, and zinc white, ZnO, were only measured at 295 K; the resulting spectra are shown in Figures 3.28b and 3.28c, respectively. Because these Mössbauer spectra were obtained on material containing only a small amount of iron, the percent absorption is much smaller than in Figure 3.28a. The Mössbauer spectral parameters resulting from a fit with two Lorentzian single lines are given in Table 3.5. It is immediately obvious that there is no change within the error limits in the isomer shifts of the iron(II) and iron(III) absorption lines, either upon mixing the pure Prussian blue with lead white, or with zinc white, or upon ageing. The only barely significant change in the Mössbauer spectral parameters is the A^{II}/A^{III} ratio that increases to *ca.* $53/47 = 1.1(2)$ upon mixing with the white pigments and remains unchanged

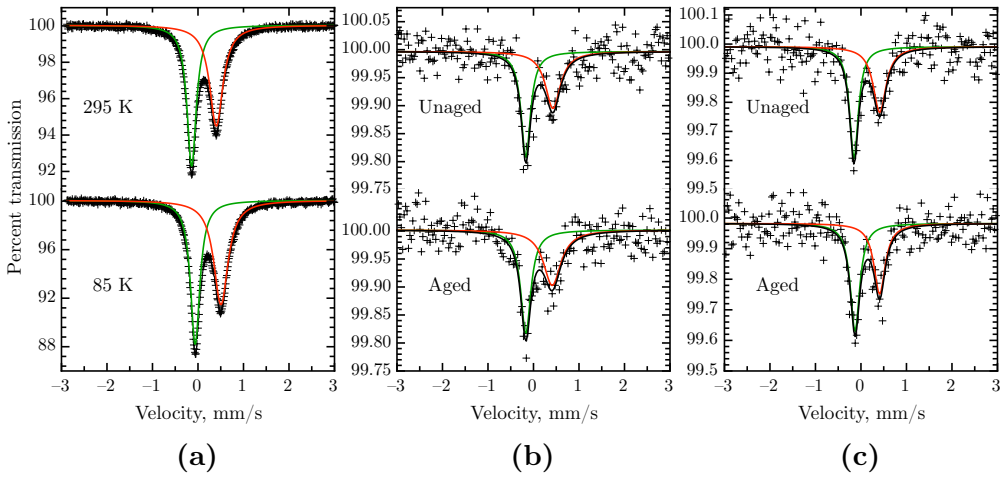

Figure 3.28 The Mössbauer spectra of laboratory-synthesized soluble A148 Prussian blue obtained at 85 and 295 K, **a**, a 1:100 mixture of Prussian blue and lead white, $(PbCO_3)_2.Pb(OH)_2$, unaged and aged, **b**, and a 1:10 mixture of laboratory-synthesized soluble A148 Prussian blue and zinc white, ZnO, unaged and aged, **c**. The green and red solid lines represent the iron(II) and iron(III) spectral components, respectively.

upon ageing. This increase may indicate a reduction of iron(III) to iron(II) upon mixing with lead white or zinc white. However, this straightforward conclusion may be too simple. Indeed, if some high-spin iron(III), located on the 1*a* and 3*c* sites of the Prussian blue $Pm3m$ structure in the weak crystal field of the nitrogen neighbors, is reduced, it is expected to be reduced to high-spin iron(II). Within the limits of the statistics of the spectra shown in Figures 3.28b and c, there is no obvious contribution from high-spin iron(II) ions with their characteristic *ca.* 1.1 mm/s isomer shift. Hence, the increase in A^{II} does not result from this reduction process. In contrast, if some of the low-spin iron(II), located on the 1*b* and 3*d* sites of the Prussian blue $Pm3m$ structure in the strong crystal field of the carbon neighbors, is oxidized, it is expected to yield low-spin iron(III). Unfortunately, low-spin iron(III) and low-spin iron(II) in the same crystallographic environment yield very similar and perhaps identical isomer shifts within the error limits and also in view of the narrow observed line width, Γ^{II}. Hence, the oxidation is observed, rather unexpectedly as an increase in A^{II} upon mixing with lead or zinc white. This conclusion is supported by the observation of low-spin iron(III) with an isomer shift of –0.164(2) mm/s in the Mössbauer spectrum of Berlin green, see Figure 3.18 and Table 3.3.

Discussion. At this point, the iron K-edge extended X-ray absorption fine structure and the iron-57 Mössbauer spectra results do not support the hypothesis of a partial reduction usually proposed for explaining the discoloration of Prussian blue. The unchanged iron(II) and iron(III) isomer shift and the increase in absorption area at *ca.* 0.0 mm/s, upon ageing, and the decrease of the iron-iron coordination number observed in the X-ray absorption spectra suggest rather a partial oxidation of Prussian blue and the formation of iron(III) hexacyanoferrate(III). The lower iron-iron coordination number observed in Berlin green and aged paint layers could be indicative of the creation of defects in the Prussian blue crystals. The pure iron(III) hexacyanoferrate(III) is auto-reduced into Berlin green because of the presence of water molecules inside the structure [140]. The loss of coordinated water may in part lead to these defects and to the observed decrease in the iron-iron coordination number.

The possibility of ion exchange between the weakly bond nitrogen-coordinated iron(III) ions and other metal ions, as suggested by electrochemical studies [151], does not seem to be a realistic hypothesis for understanding the color loss in Prussian blue mixtures with white pigments. The very unlikely substitution reaction between the Prussian blue iron(III) ions and the lead(II) and zinc(II) ions of the white pigments would have led to a far larger variation in the X-ray absorption spectra than has been observed.

Although optical photomicrographs reveal a homogenous colored layer after ageing, see Figure 3.21, it is reasonable to consider that the chemical change upon light illumination first takes place in the Prussian blue at the surface before appearing in the deeper layers. In the case of a thicker paint layer, fading is observed at the surface of the layer, whereas the bulk remains unfaded, as is evidenced in Figure 3.22 and in the previous report by Kirby *et al.* [57]. One can thus assume that surface discoloration in Prussian blue paint layers occurs prior to any bulk color change. However, iron-57 transmission Mössbauer spectroscopy is a bulk technique and X-ray absorption spectroscopy has reduced surface sensitivity. The X-ray penetration depth, L, which is the inverse of the X-ray absorption coefficient of the sample, $\mu_(E)$, is strongly energy dependent, approximately as E^3 [113]. For an X-ray energy of 7.1 keV, the penetration depth at an angle of 90° in pure Prussian blue is approximately 200 µm whereas it decreases to 9 µm for pure lead white, $(PbCO_3)_2Pb(OH)_2$ [152][153]. Under such conditions, a reduction or an oxidation occurring in the uppermost nanometer layer of the surface is thus close to undetectable.

In contrast to iron-57 transmission Mössbauer spectroscopy, iron-57 conversion electron Mössbauer spectroscopy is surface-sensitive. This technique is based on the detection of the conversion electrons that are emitted by the resonantly ex-

cited nuclei in the absorber. Because the emission probability of electrons is higher than the re-emission probability of a γ-ray, the number of Mössbauer active nuclei in the sample can be quite low for conversion electron Mössbauer spectroscopy measurements. The emitted electrons are strongly attenuated by the sample and only electrons coming from the uppermost few hundred nanometers can escape the surface and be detected [154]. Iron-57 conversion electron Mössbauer spectroscopy experiments have been attempted but have been unsuccessful. A typical conversion electron Mössbauer spectrum was obtained on the iron-57 foil standard but the signal-to-noise ratio was relatively low because of the weak cobalt-57 source activity. Consequently, it was impossible to obtain in a reasonable time a spectrum of even a pure Prussian blue paint layer.

Nuclear forward scattering experiments were also carried out on aged Prussian blue paint layers by Drs. Benedikt Klobes and Raphaël Hermann from the Forschungszcentrum Jülich GmbH, at beamline P01, at the synchrotron PETRAIII, Hamburg. Nuclear forward scattering is the time-resolved analog of Mössbauer spectroscopy. The measurements were performed in grazing incidence in order to analyze only the surface regions of the paint layer. Unfortunately, because of poor statistics, the results can hardly be quantitatively interpreted. Nevertheless, it clearly appeared that the surface region differs from the bulk as measured by transmission Mössbauer spectroscopy.

Confocal iron K-edge μ-XANES experiments have been carried out by Drs. Geert Silversmit and Bart Vekemans on Beamline L at DORIS III at the HASYLAB, DESY, Hamburg, Germany. The confocal iron K-edge μ-XANES spectra were recorded on the cross section prepared from a millimiter size fragment of ready-to-use Prussian blue oil color mixed with lead white in a 1:50 dilution ratio. The optical photomicrograph of the cross-section clearly reveals the discolored layer, see Figure 3.22. Because of the small beam size, it was possible to position the beam precisely on the discolored part. Several spectra, with a total irradiation time of almost three hours for each spectrum, were recorded in the bulk and in the discolored area. The comparison between the XANES spectra from the aged and unaged parts reveals a slight shift of the absorption edge towards a smaller X-ray energy for the aged part. This suggests a reduction of Prussian blue upon ageing. However, after the data collection, beam spot damage on the sample could be observed in optical photomicrographs. Moreover, a shift towards lower X-ray energy was also observed between the scans recorded on the aged area. It is therefore difficult to determine whether the shift of the absorption edge is due to radiation damage or to a change in the average oxidation states of the iron ions in Prussian blue. The characterization of the aged and unaged paint layers was completed by using two other surface-sensitive techniques, namely, attenuated total reflectance Fourier transform infrared and Raman spectroscopy.

Vibrational analysis

As discussed above, the position of the CN^- stretching band depends on the coordination and will be used to distinguish the fading products formed upon ageing in Prussian blue containing paint layers. The probing depth in attenuated total reflectance Fourier transform infrared spectroscopy depends on the incident wavelength, the refractive indexes of the crystal and the sample, and the angle of incidence. The probing depth has been estimated to be between 0.2 and 1 μm [34][116]. In Raman spectroscopy, the probing depth depends on the incident wavelength, *i.e.*, on the laser wavelength, λ, on the focal distance, f, and on the lens diameter, d, and can be approximated by $L = 16\lambda f^2/(\pi d^2)$ [155]. In case of a 50× objective and a 514 nm laser, the penetration depth is found to be *ca.* 2 μm when the focus point is at the surface of the sample.

Attenuated Total Reflectance Infrared Spectroscopy. The attenuated total reflectance Fourier transform infrared spectra, obtained between 2200 and 1000 cm^{-1}, on the laboratory-synthesized soluble A148 Prussian blue, mixed with lead white, $(PbCO_3)_2Pb(OH)_2$), in 1:10 and 1:100 dilution ratios, are shown in Figure 3.29. The gray curve corresponds to the aged portion of the sample. Soluble Prussian blue is characterized by a single peak at 2088 cm^{-1} that corresponds to the CN^- stretching vibration [115]. The other peaks in the infrared spectrum correspond either to the binder or to the white pigment.

The band at 1735 cm^{-1} is assigned to the ester carbonyl vibrational absorption arising from the linseed oil used as binder. The spectral features at 1238w,[6] 1162m, and 1095m cm^{-1} are assigned to CO stretching modes and are also characteristic of the triglyceride ester linkages found in linseed oil. The narrow peak at 1042w cm^{-1} is assigned to the symmetric CO_3-stretching vibration of lead white, whereas the broad intense peak at 1390 cm^{-1} is assigned to the antisymmetric CO_3-stretching vibration.

Lead white is known to accelerate the drying and ageing of linseed oil and to produce a hard and resistant film with durable and stable properties [156]. This film is commonly believed to result from the formation of metal carboxylates, induced by the saponification of esters and the deprotonation of carboxylic acids. The presence of lead white thus influences the ageing of linseed oil by causing the hydrolysis of its triglycerides. This is indicated by a loss of absorbance for the ester linkages at 1735, 1238, 1162, and 1095 cm^{-1} in the spectra obtained after ageing [157][158]. The areas of the carbonate absorptions at 1042w and 1390s,br cm^{-1} decrease slightly with ageing. This decrease can be attributed to the displacement of the carbonate ligands from the lead ions by the carboxylate anions

[6] The abbreviations w, m, s, and br stand for weak, medium, strong, and broad, respectively.

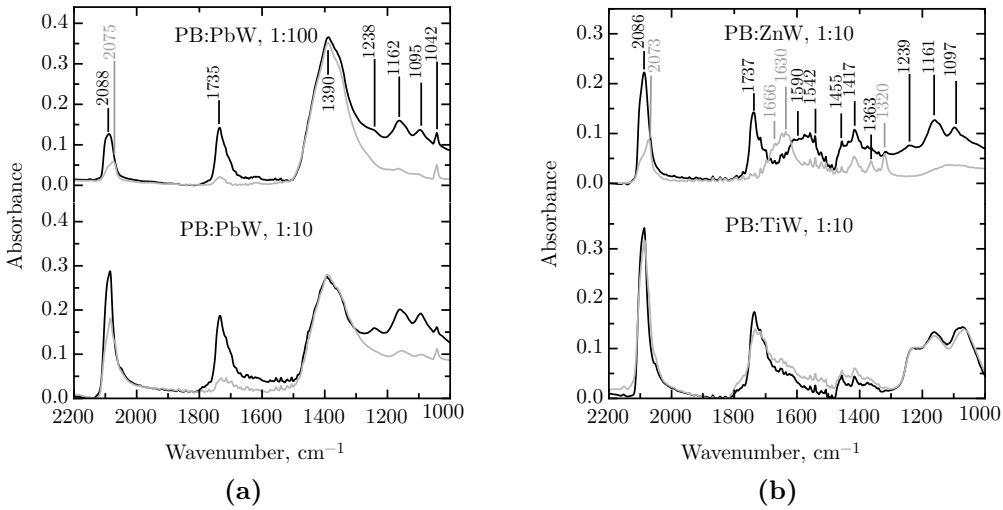

Figure 3.29 The attenuated total reflectance infrared spectra of laboratory-synthesized A148 Prussian blue, PB, mixed with PbW, lead white, $(PbCO_3)_2Pb(OH)_2$, in 1:10 and 1:100 dilution ratios, **a**, and commercial Prussian blue mixed with ZnW, zinc white, ZnO, and TiW, titanium white, TiO_2, in a 1:10 dilution ratio, **b**. The gray curve corresponds to the aged part of the sample.

derived from the esters and acids. However, the rate of decrease in area of the carbonate absorption depends on the concentration of lead white and is almost negligible when the proportion of lead white is important in comparison with the amount of linseed oil. In this study, the paint layers have been prepared with consideration of the oil absorption indices of Prussian blue and lead white, *i.e.*, *ca.* 100 and 9 to 13 wt %, respectively. The quantity of oil in mixtures of the Prussian blue and lead white in a 1:10 and 1:100 dilution ratio is thus *ca.* 20 and 13 wt % of the total weight of the pigments, respectively. Because of the small amount of oil in the samples, the intensity of the carbonate absorption remains unaffected through ageing. This band can be considered as an indirect calibration that permits a comparison between the aged and unaged spectra and any other loss of absorbance is thus of quantitative significance.

It is noteworthy that the intensity of the CN^- vibrational band at 2088 cm^{-1} dramatically decreases upon ageing, whatever the dilution. Because the molar concentration of the Prussian blue has not varied during ageing, this loss of absorbance indicates an electronic change in the Prussian blue, a change which leads to a slightly different intervalence charge transfer pathway and, as a consequence, a reduced extinction coefficient. Aside from the loss of absorbance, it is worth noting that the shape of the CN^- stretching band changes after ageing, see Figure

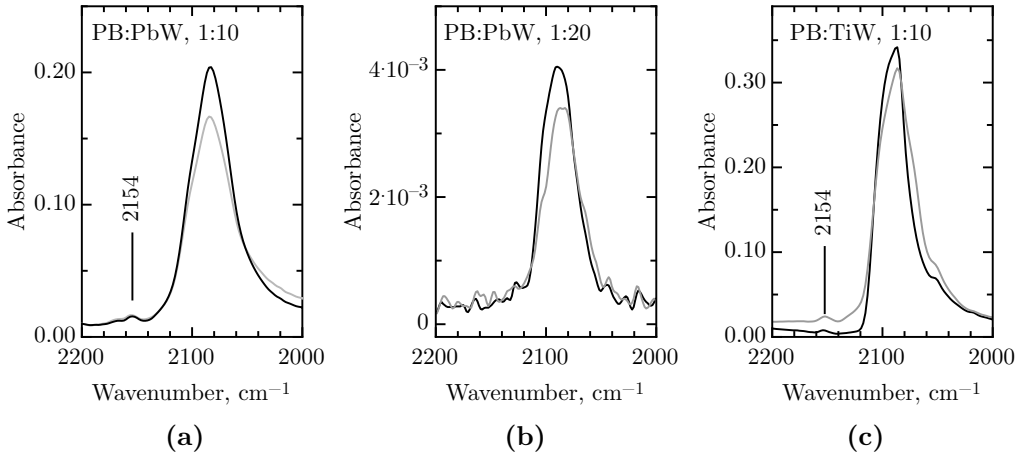

Figure 3.30 The attenuated total reflectance infrared spectra of, **a**, ancient laboratory-synthesized B64 Prussian blue mixed with PbW, lead white, $(PbCO_3)_2Pb(OH)_2$, in a 1:10 dilution ratio, **b**, ready-to-use Prussian blue and lead white oil colors mixed in a 1:20 dilution ratio, and **c**, commercial Prussian blue mixed with TiW, titanium white, TiO_2, in a 1:10 dilution ratio. The gray curve corresponds to the aged portion of the sample.

3.29. For the dilution of Prussian blue with lead white in a 1:10 ratio, a shoulder appears at a lower energy of 2072 cm^{-1}. For the dilution in a 1:100 ratio, two absorptions at 2088 and 2075 cm^{-1} are observed for the CN^- stretching band with the maximum in the absorbance shifted towards lower energy. A shift towards lower energies of the ν(CN) band can result from, (1) a change in electronegativity, (2) a change in the oxidation state, or (3) a decrease in the coordination of the iron ions. In this case, the shift towards lower energies observed in the infrared spectra after ageing may indicate the formation of increased amounts of iron(II) ferrocyanide. However, the shift in the maximum of absorbance was not observed in all aged paint layers, whereas the loss of absorbance was a more systematic feature, see Figure 3.30. In thin paint layers, a very weak peak in both the unaged and aged infrared spectra appears at 2154 cm^{-1}, see Figure 3.30.a and 3.30.c. This feature was however not observed in lower quality spectra obtained with thicker paint layers, see Figure 3.30b. This weak peak suggests the formation of $[Fe^{III}(CN)_6]^{3-}$, as is shown by the infrared spectrum of Berlin green, see Figure 3.19.

The formation upon ageing of iron(III) aquapentacyanoferrate, $Fe^{III}[Fe^{II}(CN)_5(H_2O)]$, as a result of the substitution of a CN^- ion by a water molecule, would have led to a larger shift towards smaller energy because the $[Fe^{II}(CN)_5(H_2O)]^{3-}$ ion is characterized by a CN^- stretching frequency of

2043 cm^{-1} [159][160]. The formation of iron(III) aquapentacyanoferrate as a fading product can thus be rejected on the basis of the infrared spectra.

The infrared spectra of commercial insoluble Prussian blue, $Fe_4^{III}[Fe^{II}(CN)_6]_3$, mixed with zinc white, ZnO, and titanium white, TiO_2, between 2200 and 1000 cm^{-1} are shown in Figure 3.29b. The absorption bands that characterize titanium white and zinc white occur below 700 cm^{-1} and therefore have not been observed in this study. The spectrum of Prussian blue mixed with zinc white dramatically changes upon ageing. Similar features, such as the loss of absorbance and a shift towards lower energy has been observed for the ν(CN) mode in Figure 3.29a. Upon ageing the intensity of the carbonyl band at 1737 cm^{-1} decreases substantially as is also the case for the broad carboxylate absorptions at 1590 and 1542 cm^{-1} and for the CH bending vibrations at 1455, 1417, and 1363 cm^{-1}. Moreover, two new bands at 1320 and 1630 cm^{-1} appear, bands which can be assigned to the antisymmetric COO-stretching mode and may be attributed to the formation of oxalates. The band at 1666 cm^{-1} indicates the formation of zinc carboxylates [161]. These new features are a consequence of the tendency of zinc oxide to form a soap with the free acids found in oils [162]. In contrast, in the titanium white mixture there is no significant modification in the infrared spectrum upon ageing. This is consistent with the very good light fastness observed for this mixture, see Figure 3.10. Rutile, titanium dioxide, is chemically inert and does not react either with the linseed oil medium or with the other pigments [163].

Raman Spectroscopy. Raman spectra obtained on unaged samples painted with an oil binder in different blue to white pigment dilution ratios are shown in Figures 3.31 and 3.32. In order to permit a comparison, the Raman spectra were normalized to the intensity of the band at 2150 cm^{-1} of Prussian blue. An additional vibrational band appeared at *ca.* 2130 cm^{-1} in the Prussian blue painted from linseed oil, as highlighted by the black arrow in both Figures 3.31 and 3.32. This additional band is rather a shoulder peak in the pure Prussian blue oil paint layer but becomes progressively better resolved as the blue to white pigment dilution ratio increases, see Figure 3.31. The strong band at 1033 cm^{-1} corresponds to the CO stretching vibration of lead white, $(PbCO_3)_2Pb(OH)_2$. The intensity of the ν(CO) band gradually increases as the dilution with the white pigment increases.

The band at 2130 cm^{-1} coincides with the CN^- stretching vibration observed in potassium ferricyanide, $K_3[Fe(CN)_6]$, [115] and therefore suggests the partial formation of $[Fe^{III}(CN)_6]^{3-}$ anions, see Figure 3.20, or, in other words, the partial oxidation of Prussian blue. This feature could be related to the presence of the oil used as binder because it does not appear in Prussian blue powders. During the

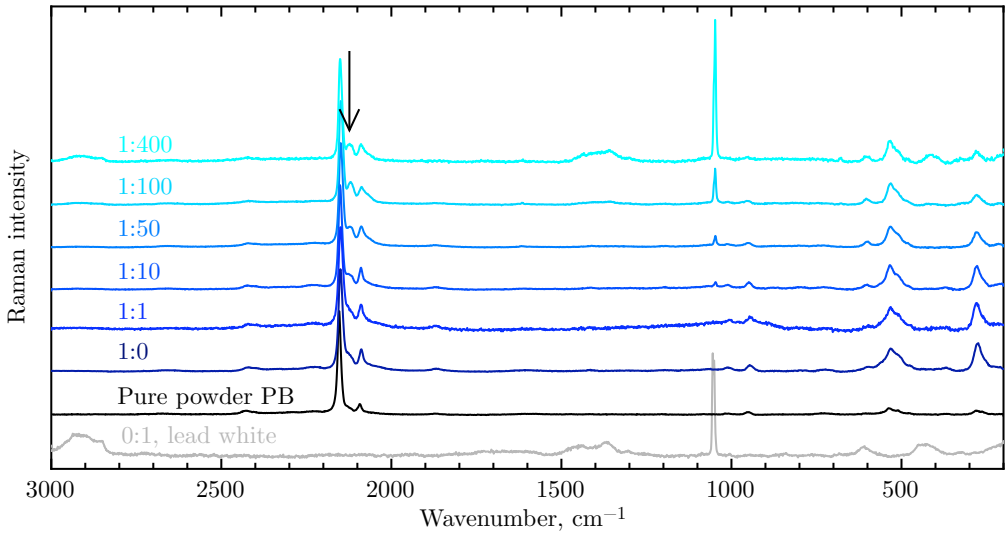

Figure 3.31 Raman spectra of commercial C03 Prussian blue in powder and non-aged ready-to-use Prussian blue oil color mixed with lead white, $(PbCO_3)2Pb(OH)_2$, in various dilution ratios.

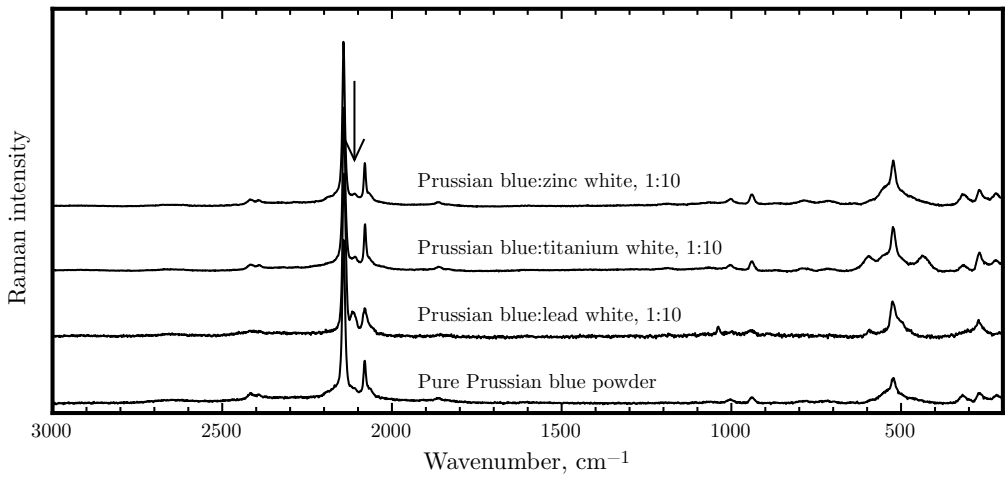

Figure 3.32 Raman spectra of non-aged laboratory-synthesized soluble A148 Prussian blue in powder and mixed with different white pigments in a 1:10 dilution ratio.

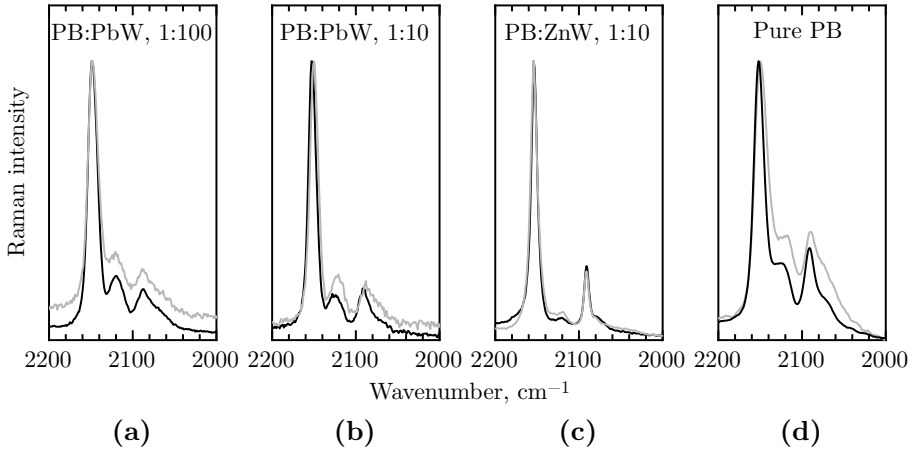

Figure 3.33 Raman spectra obtained before and after ageing normalized to the intensity of the ν(CN) streching band at 2150 cm^{-1}. The gray curves correspond to the aged samples.

drying process, the oil is partially polymerized by oxidation reactions, implying electron exchange that could, in turn, induce the oxidation of Prussian blue. In order to verify this hypothesis, Prussian blue samples that were freshly painted from linseed oil were analyzed by Raman spectroscopy. The additional band at 2130 cm^{-1} was observed even before the oil begins to dry and invalidates the above suggestion. Moreover, a shoulder peak at 2130 cm^{-1} also appeared in unaged and aged pure Prussian blue painted from gum arabic, see Figure 3.33. The appearance of the band at 2130 cm^{-1} does not seem to be influenced by the nature of the binder.

Another characteristic feature in the Raman spectra of Prussian blue in paint layers is the increase in intensity of the lower frequency bands at *ca.* 520 and 270 cm^{-1}, see Figures 3.31 and 3.32. The band at 520 cm^{-1} actually consists of two contributions, at 510 and at 530 cm^{-1}, which are assigned to the Fe-N and Fe-C stretching vibrational bands, respectively [119]. The band at 270 cm^{-1} is not easily assigned but may correspond to a ligand-iron ion bending band. An increase in intensity of this band was observed in Berlin green and thus supports a partial oxidation prior to the ageing.

Finally, unaged and aged paint layers containing Prussian blue were also studied by Raman spectroscopy. Because the color loss must be related to the configuration that causes the blue color, *i.e.*, the intervalence charge transfer Fe^{II}–C–N–Fe^{III} pathway, a change upon ageing is expected in the characteristic bands

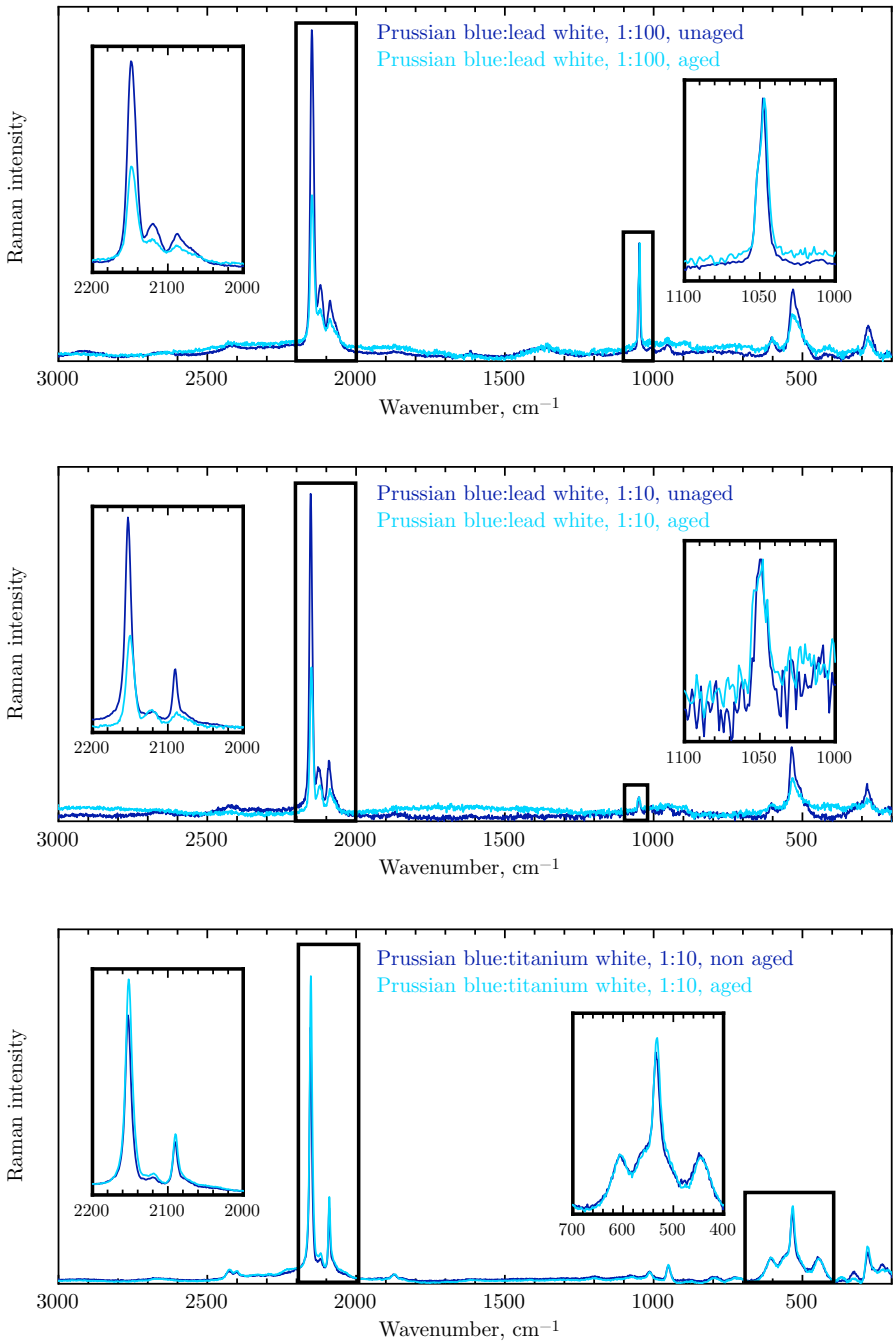

Figure 3.34 Comparison between Raman spectra before and after ageing for three different paint layers of Prussian blue oil color mixed with lead white or titanium white. Left inset:an expanded view of the ν(CN) streching band; right inset:an expanded view of the characteristic peaks of the mixed white pigment, used as an internal calibration with ageing.

of Prussian blue rather than in those characteristic of the white pigment used in the mixture. The specific bands of the white pigment in dilution were used as an internal standard in order to compare the Raman spectra before and after ageing, as was already the case for the Fourier transform infrared spectra. The spectra of ready-to-use Prussian blue oil color mixed with lead white were calibrated by using the vibrational band of 1033 cm^{-1}, whereas the bands at 600 and 435 cm^{-1} were used as an internal reference in the titanium white dilutions. Zinc white dilutions, however, were problematic because this white pigment does not exhibit any strong specific band.

After ageing the CN^- stretching band at 2153 cm^{-1} dramatically decreases in intensity in Prussian blue with lead white dilutions, see Figure 3.34. However, it does not show any shift towards lower or higher energy. In contrast, Prussian blue mixed with titanium white in 1:10 dilution ratio exhibits an increase of *ca.* 17 % in intensity upon ageing. This increase in intensity for the aged portion reflects the limitation of using an internal standard in heterogeneous systems such as paint layers. The Prussian blue concentration can vary from one local analysis spot to another, introducing artefacts in the spectrum. Nevertheless the loss of intensity observed in Prussian blue mixed with lead white upon ageing is considered as qualitatively significant, because a loss of *ca.* 50 % intensity can hardly be attributed only to the sample inhomogeneity. Furthermore, the relative intensity of the characteristic stretching bands of Prussian blue changes slightly upon ageing, see Figure 3.33. The intensity of the bands at 2130 and 2090 cm^{-1} increases upon ageing in comparison with the intensity of the strong band at 2150 cm^{-1}. The CN^- stretching vibrational frequencies at 2124 to 2131 cm^{-1} correspond to the CN^- stretching vibration of $[Fe^{III}(CN)_6]^{3-}$, whereas the bands at 2063 to 2091 cm^{-1} are assigned to the stretching vibration of $[Fe^{II}(CN)_6]^{4-}$. Consequently, an increase in intensity of these CN^- stretching vibrational bands suggests the formation of an increased amount of $[Fe^{III}(CN)_6]^{3-}$ and $[Fe^{II}(CN)_6]^{4-}$, or, in other words, a combination of partial oxidation and reduction in Prussian blue paint layers. The formation of some $[Fe^{III}(CN)_5H_2O]^{2-}$ ion is also possible in view of the CN^- stretching vibration frequency in this compound [115]. The loss of intensity observed for the strong peak at 2150 cm^{-1} indicates a decreased number of Fe^{II}–C–N–Fe^{III} pathways.

On the basis of the numerous analyses carried out on the pure Prussian blue pigments, the unaged and aged paint layers, and the partially oxidized and reduced forms of Prussian blue, conclusions about the degradation of Prussian blue can now be drawn from the ensemble of results. A model for the degradation mechanisms of Prussian blue is then proposed.

3.5 Degradation mechanisms of Prussian blue in paint layers

The accelerated ageing experiments and the colorimetric measurements carried out in this thesis indicate that pure Prussian blue painted in dark shade is extremely light fast. The light fastness of Prussian blue slightly decreases in pale shade paint layers and decreases even more in the presence of a white pigment. It is well established that a pale shade is much less light fast than a deep shade. This phenomenon has been mainly studied in case of dyes [138]. Intuitively this behavior can be understood by considering that well dispersed pigment particles in a matrix in which light easily propagates are more vulnerable to light exposure than close-packed pigment particles. The nature of the white pigment present affects the degree of fading because Prussian blue mixed with zinc white or lead white is much less light fast than when mixed with titanium white. In contrast, neither the nature of the binder nor its acidic or basic character seem to play a role in the discoloration of the paint layer.

As explained in **Section 1.2.3**, several hypotheses have been proposed in the literature for explaining the fading of Prussian blue, (1) the reduction of Prussian blue, (2) the oxidation of Prussian blue, (3) ion exchange within the Prussian blue, and (4) substitution reactions within the Prussian blue. Based on the results presented in **Section 3.4.2**, one can both determine which one or more of the hypotheses are the most probable for the discoloration of Prussian blue and identify the degradation mechanisms. Table 3.6 summarizes the main results presented in **Chapter 3** for the different spectroscopic techniques used herein.

From Table 3.6 it is immediately obvious that changes in the local electronic and structural configurations of the iron ions in Prussian blue occur even prior to any accelerated ageing. However, the ageing of the paint layers could have already begun as the paint layers were drying in daylight. The results suggest a partial oxidation in Prussian blue containing paint layers. Because a variation in the low-spin iron to high-spin iron ratio has been detected by Mössbauer spectroscopy, a bulk technique, the oxidation must occur in the entire paint layer. Moreover, the oxidation is probably related to the presence of the binder because the phenomenon is observed in pure Prussian blue painted with gum arabic.

Upon ageing the results indicate both oxidation and reduction processes. The hypothesis of a partial reduction of Prussian blue is supported by the XANES and infrared spectral results, whereas the EXAFS and Mössbauer spectral results rather suggest an oxidation of the iron ions in Prussian blue. Because the reduction of high-spin iron(III) to high-spin iron(II) is not observed in the Mössbauer spectra

Table 3.6 Summary of the results presented in **Chapter 3**

Spectroscopy	**Observed variations in paint layers**	
	before ageing[a]	upon ageing
XANES	–	Shift of the absorption edge towards lower energy; no significant shift of the pre-edge peak.
EXAFS	–	Decrease in the iron-iron coordination number.
Iron-57 Mössbauer	Slightly increased low-spin iron to high-spin iron ratio	Unchanged spectral parameters.
FTIR	Appearance of an additional weak band at higher energy	Loss of absorbance in the CN^- vibration band; shift of the maximum towards lower energy.
Raman	Appearance of an intermediate CN^- band at 2130 cm^{-1}	Loss of intensity of the strongest ν(CN) band at 2150 cm^{-1}; increase in intensity for the weaker bands at lower energy.

[a]Variations in comparison with the results obtained on pure Prussian blue powder samples.

as a drastic change in the iron(II) isomer shift, it must occur at the surface of the pain layer, a surface that contributes a very small absorption that is dominated by the bulk absorption in the Mössbauer spectra. It is reasonable to consider that the chemical change upon illumination takes place first in the Prussian blue at the surface before spreading to the deeper layers. Surface discoloration in Prussian blue paint layers occurs prior to any bulk color change. This phenomenon could explain why the attenuated total reflectance infrared and Raman spectra, with a probing depth of up to 2 µm, exhibit the most noticeable differences upon ageing. Similarly, the X-ray absorption near-edge spectrum of Prussian blue mixed with lead white in a 1:100 dilution ratio exhibits the highest shift of the absorption edge towards lower energy because only the first few microns are probed. In contrast, X-rays penetrate more deeply into paint layers containing Prussian blue and zinc white or titanium white and both bulk and surface are thus analyzed.

The third and fourth hypotheses, ion exchange and substitution reaction, can be excluded as being responsible for the fading of Prussian blue and its mixtures. The possibility of ion exchange between the weakly bonded, nitrogen-coordinated, iron(III) ions and other metal ions, as suggested in electrochemical studies [151], does not seem to be a realistic hypothesis for understanding the color loss in Prus-

sian blue and white pigment mixtures. The very unlikely substitution reaction between the Prussian blue iron(III) ions and the lead(II) and zinc(II) ions of the white pigments would have led to a far larger change in both the X-ray absorption spectra and their corresponding Fourier transforms than has been observed. Further, no ligand substitution reactions have been clearly identified. The formation of ferric aquapentacyanoferrate(II) is unlikely in view of infrared results. However, the formation of some $[Fe^{III}(CN)_5H_2O]^{2-}$ ions upon ageing can not be excluded in view of the Raman spectral results.

The fading of Prussian blue pigments in paint layers thus results from both a partial oxidation and reduction of the iron ions in Prussian blue. Both the oxidation and the reduction lead to a loss of color because the intervalence charge transfer between iron(II) and iron(III) ions is hindered. The reduction takes place at the upper surface of the paint layers whereas the oxidation occurs in the entire paint layer. The quantification of the proportion of iron(III) ions being reduced to iron(II) ions at the surface layer and the amount of $[Fe^{III}(CN)_6]^{3-}$ ions formed in the bulk, has not been established. The proportion of $[Fe^{III}(CN)_6]^{3-}$ ions formed in the bulk is expected to be quite low because no significant difference in color was observed in the bulk. The following paragraphs provide some suggestions for explaining the occurrence of both oxidation and reduction processes in Prussian blue pigments in paint layers.

In the nineteenth century, Chevreul [61] had already noted the discoloration of pure Prussian blue on dyed fabrics exposed to light in a vacuum and in an anoxic or low-oxygen content atmosphere. The fabrics tend to regain their color upon contact with oxygen. In 2004, the experiments of Chevreul were reproduced and his observations confirmed [164]. However, attempts to discolor pure powder Prussian blue upon light exposure in an ambient atmosphere were unsuccessful. In an ambient atmosphere, Prussian blue pigment is thus stable because it has access to oxygen to maintain an equilibrium between the amount of iron(II) and iron(III) ions required for the intervalence charge transfer. In contrast, Prussian blue pigment in a paint layer system is not as stable as in a powder in an ambient atmosphere. Lightly colored paint layers containing Prussian blue show a tendency to discolor upon light exposure. Oxidation in the entire paint layer and reduction at the surface upon light exposure occur. The presence of a binder and/or a white pigment is necessarily involved in the degradation mechanisms of Prussian blue.

Because Prussian blue seems to be oxidized even without the addition of a white pigment, the binder necessarily plays a role in the oxidation. The oxidation process is most likely linked to the ability of Prussian blue to incorporate water molecules in its defect structure. The OH^- anions provided by the oil binder or by the aqueous diluent can then oxidize the iron(II) ions, which can then form the

pentacoordinated iron(III) $[Fe^{III}(CN)_5OH]^{3-}$ ion. The role of structural water molecules has recently been observed in studies of the electrochromic process in electrochemically synthesized Prussian blue [31][165].

The reduction takes place at the surface of the paint layer upon light exposure. Both photoinduced reduction or oxidation in Prussian blue are made possible when Prussian blue is coupled with a material that generates electrons upon UV or visible light irradiation [63]. Reduction in a Prussian blue paint layer may thus occur in the presence of a species that can provide electrons upon irradiation. Zinc white and titanium white are both known for their photochemical activity and strongly absorb near ultraviolet radiation, below 366 nm and 415 nm, respectively [52]. Both are semiconductors with a band gap of *ca.* 3 to 3.3 eV, *i.e.*, in the ultraviolet spectral region. Consequently, when the zinc white or titanium white absorb ultraviolet light, an electron-hole pair is created in the crystal lattice and migrates to the surface of the pigment. The electron can then reduce the iron(III) ion of Prussian blue. The remaining hole can oxidize an OH^- adsorbed in the structure of the Prussian blue or at the surface of the white pigment to an $OH^{\cdot}$ radical. This radical can cause oxidative break down of the binder. This photodegradation process of the binder is known as chalking. The paint medium is physically removed, causing a loss of gloss and mass, and leaving the pigment as a loose powder on the surface. In the aged paint layers containing Prussian blue, a loss of gloss was observed and supports the hypothesis of a reduction of the iron(III) ions coupled with an oxidation of the binder. The photochemical activity of rutile, titanium dioxide, used as an artist's pigment is reduced as much as possible by adding stabilizing elements such as zinc or aluminum metals [52]. The use of coatings acting as a physical barrier to limit the diffusion of the oxidizing species out from the pigment surface can inhibit the break down of the binder [163]. This reduced photochemical activity of titanium white can thus explain why Prussian blue mixed with titanium white does not discolor strongly.

Lead white is not particularly photochemically active. It is remarkably permanent and unaffected by light. Because of their basic character, lead white and zinc white tend to form a soap by interacting with the linseed oil esters of fatty acids [166]. The presence of these basic pigments in linseed oil may favor the production of electrons that will initiate the reduction of Prussian blue. However, discoloration of Prussian blue painted from gum arabic, in a pure state or mixed with lead white, was also observed, suggesting that a reduction of the iron(III) ions in Prussian blue is possible upon light exposure without being initiated by an admixed pigment. Although the reduction mechanisms are not completely identified, the structural and interstitial water molecules in the Prussian blue lattice and the formation of hydroxyl ions and $OH^{\cdot}$ radicals are expected to play an important role in the redox processes, as has been evidenced in Prussian blue electrochromic

mechanisms. Electron paramagnetic resonance spectral measurements may help to understand the discoloration mechanisms through the detection of free radicals induced by light irradiation in the paint layers.

Chapter 4

Case Study of Prussian Blues in Genuine Historical Samples

Summary. *The thorough analysis of the laboratory-synthesized samples leads to the hypothesis of partial bulk oxidation and surface reduction in Prussian blue containing paint layers upon light exposure. This hypothesis must be verified on genuine Prussian blues found in our cultural heritage. Various types of works of art from the eighteenth to twentieth centuries are analyzed, i.e., a polychrome sculpture, wallpapers, an oil painting, watercolors, and a wall decoration. Millimeter-sized fragments from these objects were studied by Raman spectroscopy. Fourier transform infrared spectroscopic analysis was carried out in situ on the oil and watercolor paintings. The results confirm the previous conclusions drawn from laboratory-prepared paint layers: Prussian blue in paint layers undergoes redox reactions, which are enhanced in a diluted Prussian blue matrix.*

Contents

In the previous chapter, aged laboratory-prepared paint layers have been extensively studied. Among the various experimental techniques, Raman and Fourier transform infrared spectroscopy were the most suitable techniques to detect the degradation at the surface of Prussian blue containing paint layers. Infrared spectra revealed a loss of absorbance upon ageing whereas Raman spectra revealed a loss of intensity in the CN^- stretching vibration bands in conjunction with a change in relative intensity of the various different bands. Because of these changes in relative intensity, Raman spectroscopy should permit the detection of degraded Prussian blue pigments without requiring any comparison with an unaged Prussian blue containing paint layer.

The works of art containing Prussian blue studied herein differ in their type, provenance, and period. This variety illustrates the wide use of Prussian blue since the eighteenth century. Although Prussian blue has also been used in books, as ink, or mixed with gum arabic in watercolors, the inner pages of books are supposed to be protected from light and, hence, no degradation induced by light exposure is expected. For that reason books have been excluded from this work.

4.1 Analyses of paint fragments

The analyzed paint fragments are part of the archives of the Royal Institute for Cultural Heritage, Brussels. The art objects have been previously sampled and studied by the pictorial laboratory of the institute. Three types of objects were selected for the study of Prussian blue degradation, a polychrome sculpture, wallpapers, and a mural decoration. In these art objects, the presence of Prussian blue has already been detected by X-ray dispersive, Fourier transform infrared, or Raman spectroscopic analyses. The goal herein is to detect any degradation in the Prussian blue by Raman spectroscopy in order to compare the results obtained from genuine art samples with those obtained from laboratory prepared paint samples presented in the previous chapters. Samples that were of interest for this work were thus selected on the basis of these previous investigations. They were studied as either embedded in synthetic resin and transformed into cross-sections, or as non-embedded fragments. The cross-sections were carefully repolished and studied by optical microscopy, scanning electron microscopy coupled with X-ray dispersive, and Raman spectroscopy, with a particular emphasis on the Prussian blue and its possible degradation. These additional analyses were carried out under the supervision of Dr. Jana Sanyova, with the help of Cecile Glaude, for optical and electronic microscopy, and with Dr. Steven Savewyns for Raman spectroscopy.

4.1.1 A polychrome sculpture, the guardian angel of La Gleize

The guardian angel shown in Figure 4.1 is located in the Assumption's Church of La Gleize, in the Belgian Ardennes. This large linden wood sculpture with dimensions of 133×110 cm, dates from the beginning of the eighteenth century. At that time, the representation of guardian angels was quite popular and many examples of such sculptures can be found in Liège and the surrounding areas. However, the guardian angel of La Gleize differs in style from other seventeenth and eighteenth century barocco sculptures of angels. The guardian angel of La Gleize is remarkable for its polychrome character, which is unusual for the Belgian Ardennes [167]. The polychromy was studied in 1994-1995 during the restoration of the sculpture at the Royal Institute for Cultural Heritage in Brussels. The wood of the sculpture had been sized with several diluted glue layers. The last one contained a white calcium sulfate extender and a small amount of a zinc salt. The sculpture was then covered by several thin layers of white preparation layer, containing an animal glue and chalk. Finally, the chalk ground layer was isolated by applying an animal glue with a small amount of gypsum and a zinc salt. The pigment analysis revealed the presence of Prussian blue mixed with alumina hydrate in the interior of the angel's dress and on its sandals. The presence of Prussian blue in the original paint layers of the guardian angel provides a *terminus ante quem non* because the sculpture can not be dated before the discovery of Prussian blue in 1704. The binder in the blue paint fragments has been identified by gas chromatography-mass spectrometry as linseed oil [167].

In order to update the results obtained in 1994, the cross-section prepared from a millimeter-size fragment from the angel's right sandal was again studied by optical microscopy and by scanning electron microscopy coupled with energy-dispersive X-ray spectroscopy. The analyses were carried out by Cécile Glaude. Raman spectroscopy was then performed in order to detect any degradation in the blue original paint layers.

Photomicrographs of the cross-section prepared from a paint fragment from the angel's right sandal are shown in Figure 4.2. Four different layers can be identified, as indicated by the numbers in the optical micrograph of the cross-section shown in Figure 4.3. The elemental composition of each paint layer was determined by scanning electron microscope coupled with energy-dispersive X-ray spectrometry, see the mapping shown in Figure 4.3. The first thick white layer corresponds to the chalk ground layer and mainly contains calcium ions. The second gray layer is the proteinic isolation layer, which strongly reflects UV light, see Figure 4.2d. The third layer is composed of Prussian blue, alumina hydrate, and lead white. A few small orange grains can be seen in this layer but their composition could not been determined. The upper layer is a retouching layer that was not originally

Figure 4.1 Guardian angel, a polychrome 133×110 cm linden wood sculpture from the early eighteenth century located at the Assumption's church in La Gleize, Belgium.

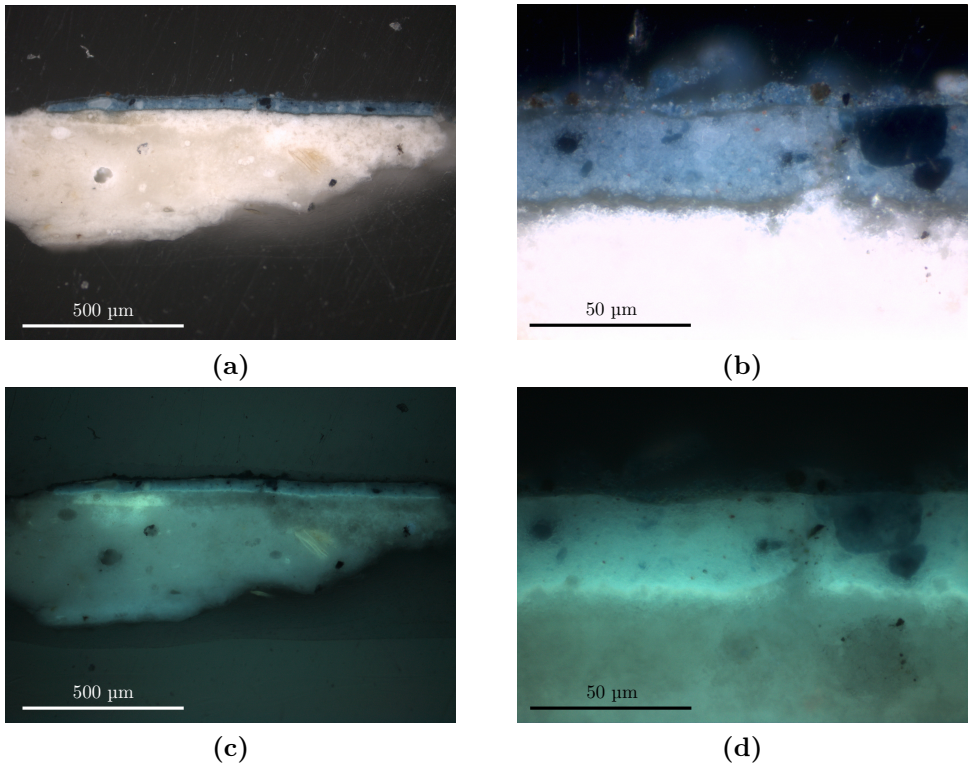

Figure 4.2 Optical photomicrographs of a cross-section at two different magnifications, obtained with a dark field illumination from the guardian angel of La Gleize, with **a** and **b**, visible reflected light, and **c** and **d**, UV reflected light.

present on the sculpture. It presumably contains cerulean blue, a cobalt(II) stannate, mixed with calcite and magnesia extenders.

The large dark blue particles observed in the optical photomicrographs contain both Prussian blue and alumina hydroxide, as evidenced by the mapping in Figure 4.3. Hence, Prussian blue was synthesized according to the ancient preparative method, in which alum was used as a starting reagent. After precipitation of Prussian blue, the alumina hydrate could remain as an extender to lighten the dark color of Prussian blue. The cross-section was then analyzed by Raman spectroscopy; the resulting spectra are shown in Figure 4.4. The spectrum obtained from the light blue area differs from that obtained on the dark blue area because of the presence of lead white, as is indicated by the peak at 1050 cm^{-1}. The characteristic band for alumina hydrate could not been found in the Raman spectra. For both analysis spots, the Prussian blue exhibits similar CN^- stretching vibrational bands. The intermediate band at 2130 cm^{-1} and the relatively large

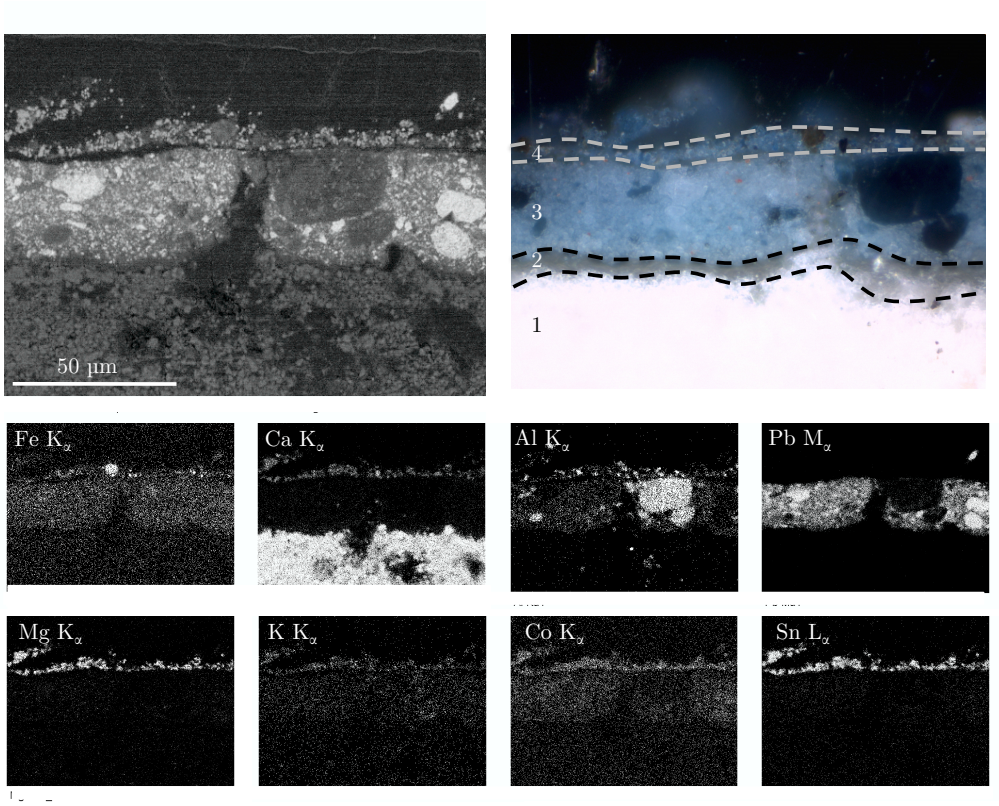

Figure 4.3 Scanning electron micrograph obtained with an energy of 15 keV and backscattered electrons, optical photomicrograph obtained in reflected visible light and a dark field illumination, and the elemental composition mapping performed by energy-dispersive X-ray spectroscopy, of the cross-section of a blue fragment from the guardian angel of La Gleize.

intensity of the band at 2090 cm^{-1} suggest the presence of degraded Prussian blue, *i.e.*, partially oxidized and reduced Prussian blue. Although it is difficult to detect a visual fading on the basis of the cross-section, the original Prussian blue paint layers on the polychrome sculpture were probably discolored.

The Raman spectrum obtained on a small orange grain revealed a molecular composition close to that of raw Sienna, see Figure 4.4. Raw Sienna is a yellow-brown pigment which consists of clay and a mixture of iron(ÌII) oxyhydroxides and iron(III) oxides [87]. In **Chapter 2**, the formation of ferrihydrite, an orange hydrous iron(III) oxide compound, was observed in ancient laboratory-synthesized Prussian blues. Thus, the presence of some orange particles of an iron(III) oxide

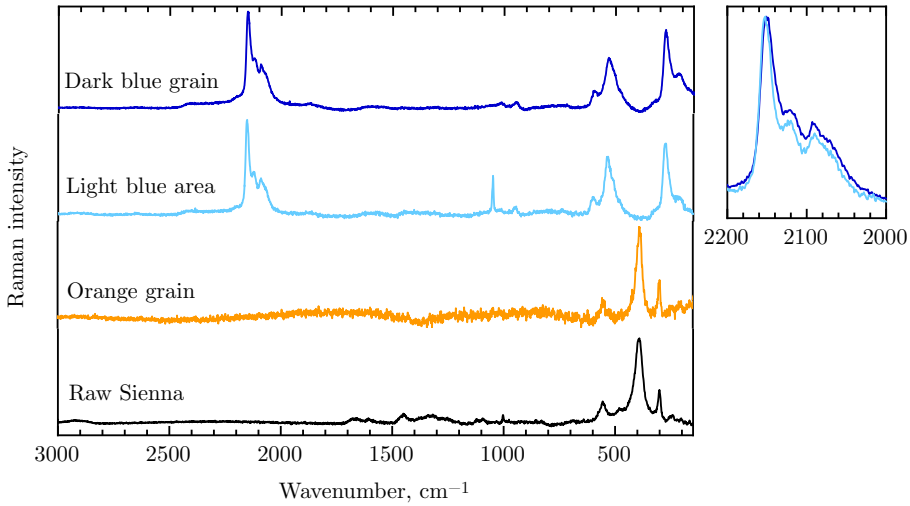

Figure 4.4 Raman spectra obtained on a cross-section from a blue fragment from the guardian angel of La Gleize by using a 785 nm laser and a reference spectrum of raw Sienna, from the database of the Royal Institute for Cultural Heritage. Right: an expanded view of the CN^- stretching vibration.

compound most likely results from the ancient preparative method of Prussian blue, in agreement with the experimental results reported in **Chapter 2**.

4.1.2 Wallpapers from the Dewez house

The study of wallpapers presented herein is part of a project about wallpapers and decorations directed by Wivine Waillez of the Service for Research on finishings of historic buildings at the Royal Institute for Cultural Heritage, Brussels.

The use of wallpapers as wall decoration began shortly after the invention of printing during the Renaissance [168]. Wallpapers rapidly became a common element of a home's interior and evolved over the centuries, from the first printing of papers of the early sixteenth century, to the eighteenth-century handpainted papers imported from China, and to the nineteenth-century washable machine-printed wallpapers [169]. Because of its low cost, Prussian blue was widely used as pigment in wallpapers [4].

The wallpapers analyzed herein came from the Dewez house, situated at 73 and 75 Laeken street, Brussels, see Figure 4.5. This building was the private residence of the Belgian architect, Laurent-Benoît Dewez (1731-1812), who is considered as

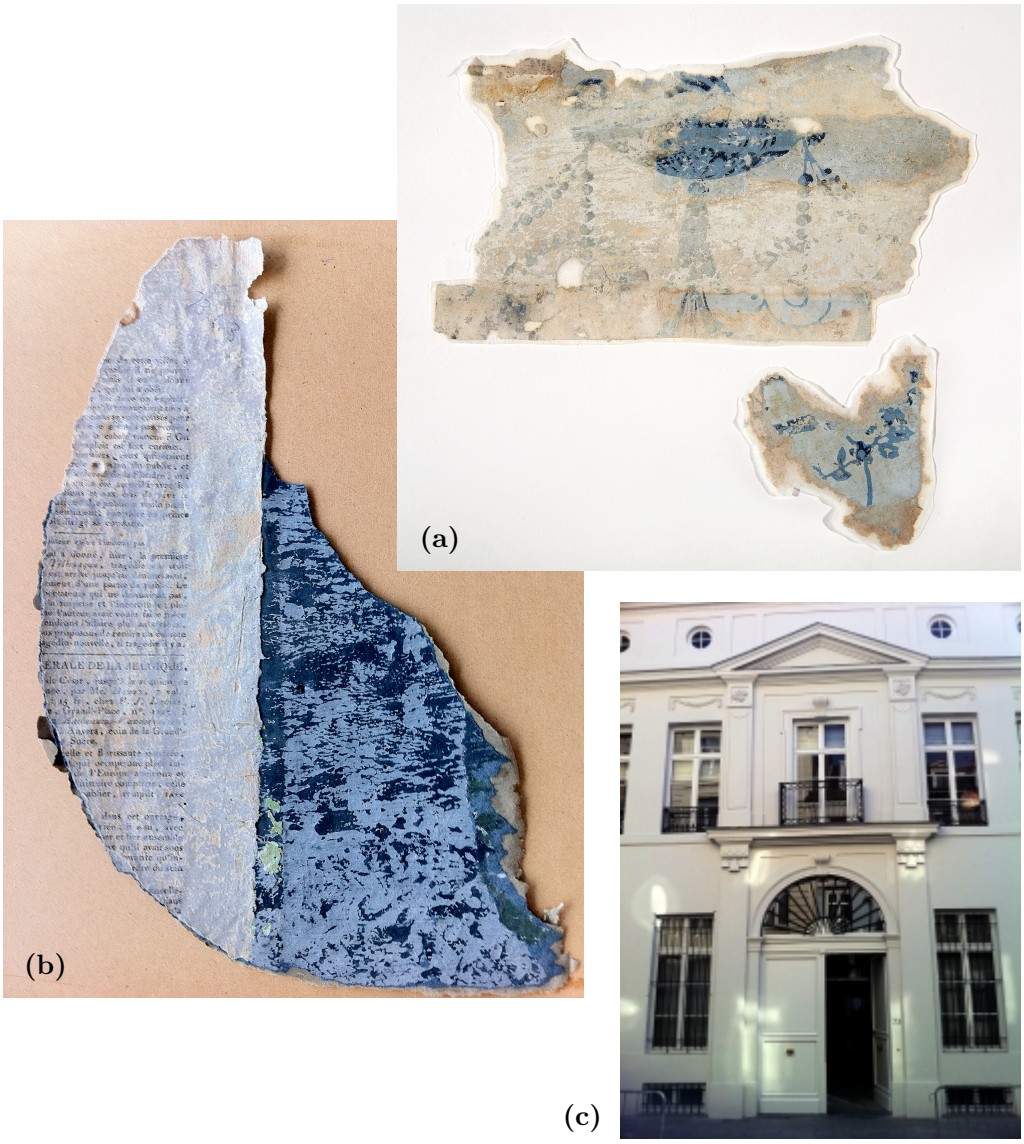

Figure 4.5 Fragments of eighteenth century wallpapers from the Dewez house, **a**, arabesque wallpaper and, **b**, lining paper; **c**, façade of the Dewez house, Brussels.

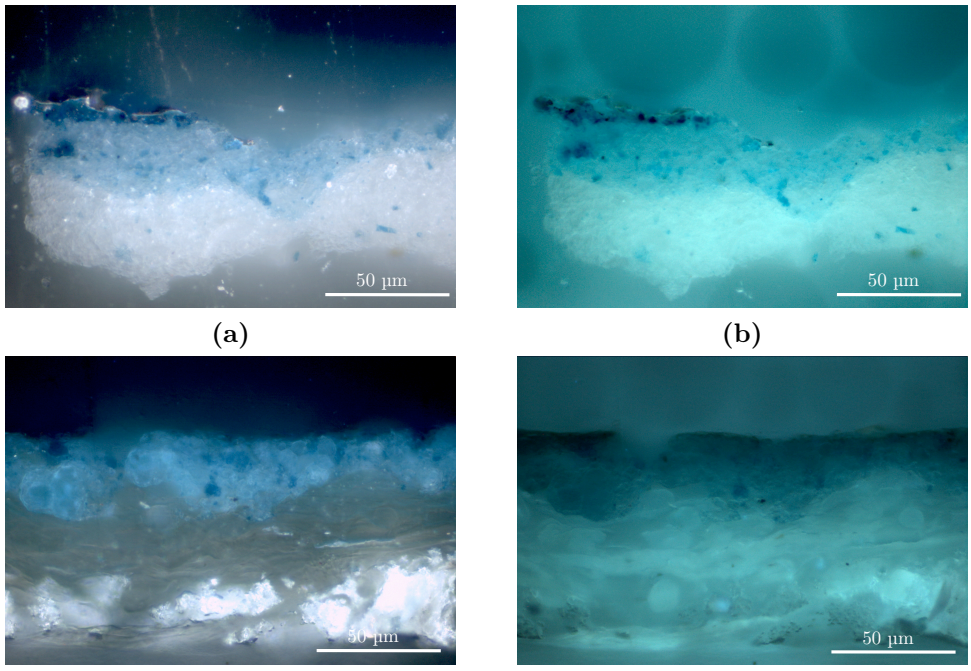

Figure 4.6 Dark field illumination, optical photomicrographs of a cross-section from wallpapers of the Dewez house. Left, visible reflected light, right, UV reflected light.

a promoter of neoclassicism in architecture. The Dewez house consists of several units dating back to the fifteenth century, units which were combined into a single building around 1775 to 1785 by Dewez [170]. The architect also designed the interior and decorated the rooms of the house with stuccoed ceilings, wood paneling, and wallpapers. Since 1992 the entire Dewez house has been classified as a listed building. In 1999 a project of renovation and change in the use of the building began. Simultaneously, archival studies, surveys, and archaeological research were undertaken. Stratigraphic studies on the wooden elements and wallpaper were performed by the Service for Research on finishings of historic buildings with collaboration of the wall painting unit from the Laboratory Department at the Royal Institute for Cultural Heritage, Brussels [170]. The analyzed fragments are part of the collection of wallpapers of the Dewez house.

Pictures of two wallpaper fragments are shown in Figures 4.5a and 4.5b. The wallpaper fragment in Figure 4.5a is an *arabesque* wallpaper, with a pattern of baskets, flowers, and garlands. It may be dated from the end of the eighteenth century, *ca.* 1785 [171]. The fragment in Figure 4.5b was part of a *lining* or *mac-*

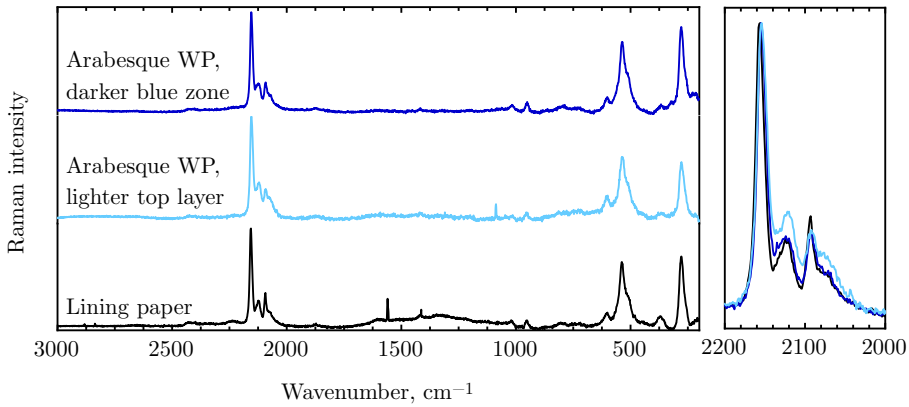

Figure 4.7 Raman spectra of eighteenth-century wallpapers of the Dewez house obtained by using a 785 nm laser. Right: An expanded view of the CN^- stretching vibration.

ulature paper, *i.e.*, a paper which was placed under the final wallpaper to serve as an isolation and preparation layer. Newspapers were commonly used for the lining and provide a *terminus post quem* for the installation of the mural decoration. The fragment in Figure 4.5b could be dated from the end of the eighteenth century [171].

The cross-sections studied herein have been prepared from embedded millimeter-size fragments by Marina Van Bos and observed with an optical microscope with visible and UV light, see Figure 4.6. The cross-section from the arabesque wallpaper exhibits a very light blue paint ground layer with a darker blue zone at the top of the layer. The cross-section shown in Figures 4.6c and 4.6d was prepared with a fragment from the dark blue portion of the lining paper of Figure 4.5b and consists of a relatively homogeneous blue paint layer. The Raman spectra obtained on both cross-sections are shown in Figure 4.7. Although the cross-sections have already been studied by Raman spectroscopy, the goal herein is to detect any degradation in the paint layers. The Raman spectra of the paint layer from the arabesque wallpaper was measured at both dark blue and light blue areas on the top of the surface layer. The three Raman spectra exhibit the characteristic vibrational bands of Prussian blue. The peak at *ca.* 1090 cm^{-1} observed in the light blue zone can be assigned to the carbonate absorption in chalk, calcium carbonate, $CaCO_3$. The two narrow peaks at *ca.* 1550 and 1410 cm^{-1} observed in the Raman spectrum of the lining paper could not be assigned.

The Prussian blue present in the lining wallpaper exhibits similar CN^- stretching bands as the Prussian blue in the darker blue area of the arabesque wallpaper.

In contrast, the intensity of the vibrational band at 2120 cm^{-1} is slightly increased for the Prussian blue in the light blue area. This increase suggests the formation of $[Fe^{III}(CN)_6]^{3-}$ ions. The shoulder peak at lower energy, at *ca.* 2070 cm^{-1}, suggests an increased amount of $[Fe^{II}(CN)_6]^{4-}$ ions in the light blue region. The Prussian blue pigment is thus more strongly degraded in the diluted Prussian blue containing paint layers. This observation is consistent with the experimental results reported in **Chapter 3**, results which indicated a good light fastness for Prussian blue painted in a dark shade.

4.1.3 Wall decorations of the *Villa Germaine*

The analyzed paint fragment comes from the front-wall of a house, *Villa Germaine*, located at Avenue Richard Neybergh 23 in Laeken, Belgium, see Figure 4.8. The house was decorated in 1910 by the Belgian architect Paul Cauchie (1875-1952). The front-wall is presumably decorated with *sgraffiti* [172], which are wall decorations produced by engraving a drawing in plaster layers when the layers are still soft [173]. This technique has been used in Europe since the classical period and regained its popularity in Belgium during the Art Nouveau movement at the end of the nineteenth century and the beginning of the twentieth century; Cauchie is particularly famous for this type of stylistic wall decoration. Cauchie's work has recently been studied in the master's thesis by Arijs [172].

The *Villa Germaine* exhibits several wall decorations colored in pale green and orange, as is shown in Figure 4.8. Details of these decorations were found in the preparative studies of the artist [172]. Surprisingly, the green areas in the wall decorations were colored in blue in the architect's plans. It is thus not clear whether the green areas of the sgraffiti were initially green or whether the color results from a fading of the pigments.

The optical micrographs shown in Figure 4.9 reveal a heterogeneous composition, with blue and yellow grains in a light green matrix. The analysis by energy-dispersive X-ray spectrometry was performed by Louise Decq [174] and indicates the presence of calcium, barium, zinc, sulfur, magnesium, silicon, and aluminum ions, suggesting the presence of clay components, lithopone, which is a mixture of barium sulfate, $BaSO_4$ and zinc sulfide, ZnS, and gypsum, a calcium sulfate dihydrate, $CaSO_4{\cdot}2H_2O$, or chalk, $CaCO_3$. Iron, potassium, and chromium ions were also detected. The first two ions could indicate the use of Prussian blue. The detection of chromium ions suggests the presence of a chrome pigment, such as the green chromium oxide pigment, Cr_2O_3, or viridian, $Cr_2O_3{\cdot}2H_2O$. The use of chrome yellow, $PbCrO_4$, is unlikely because lead was not detected by energy-dispersive X-ray spectroscopy.

Figure 4.8 Front-wall of the *Villa Germaine* located at Avenue Richard Neybergh 23 in Laeken, Belgium.

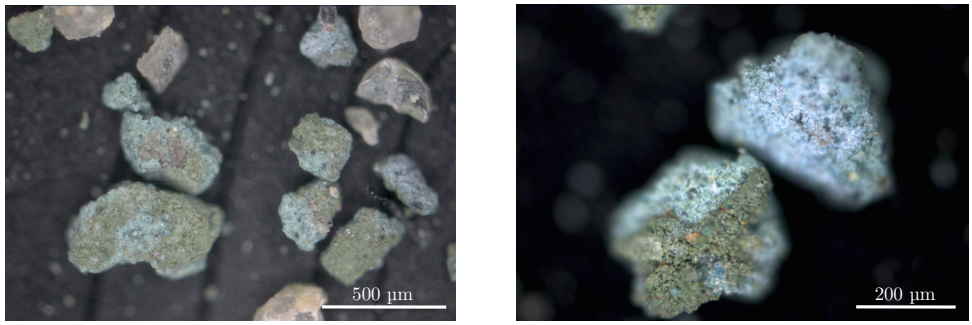

(a) **(b)**

Figure 4.9 Reflected light, dark field illumination optical photomicrographs of the powder fragment obtained from a sgraffito of the *Villa Germaine*.

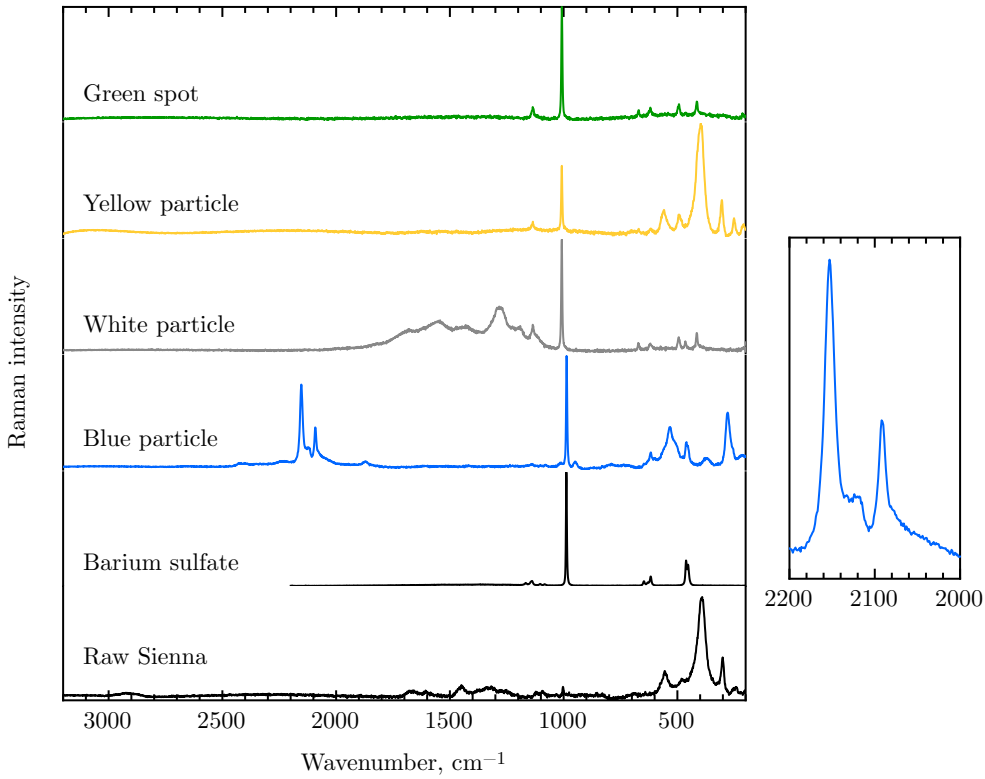

Figure 4.10 Raman spectra of the mural sample from the sgraffito of a house built by the architect Cauchie and a reference spectra of barium sulfate and raw Sienna, from the database of the Royal Institute for Cultural Heritage. Right: An expanded view of the CN^- stretching vibration.

The powder fragment was then analyzed by Raman spectroscopy, by using a 785 nm laser, see Figure 4.10. Raman spectroscopy clearly confirms the use of Prussian blue and barium sulfate. The yellow color seems to be associated with the presence of mixtures of iron(III) oxyhydroxide and barium sulfate. Indeed the Raman spectrum obtained on the yellow particle is partially similar to that of raw sienna, which is a yellow-brown pigment composed of limonite clay, containing iron(III) oxyhydroxide and iron(III) oxide. The Raman spectrum obtained on a green particle does not undoubtedly indicate the presence of a green chromium(III) oxide pigment. Indeed, it does not show the characteristic strong bands at 552 or 487 cm^{-1} for chromium(III) oxide, Cr_2O_3, or viridian, $Cr_2O_3 \cdot 2H_2O$, respectively [175]. On the basis of the Raman spectral results, one can ask whether raw Sienna has been deliberately used for the realization of the sgraffito or whether it results from a degradation process of Prussian blue.

The presence of particles of an iron(III) oxyhydroxide was also detected in a paint layer of the guardian angel of La Gleize and was attributed to the preparative method of Prussian blue. This explanation is however not convincing in the case of the sgrafitto because, in the early twentieth century, Prussian blue was synthesized according to modern preparative methods and the formation of the undesirable iron(III) oxyhydroxide during the synthesis is unlikely.

Three distinct bands are observed in the CN^- vibrational stretching region of the Prussian blue spectrum. The relative intensity of the three bands differs from the previous observations in the polychrome sculpture and in the wallpapers because the band at 2090 cm^{-1}, corresponding to the CN^- vibration in $[Fe^{II}(CN)_6]^{4-}$, is much more intense than the band at 2120 cm^{-1}, which is assigned to the CN^- vibration in $[Fe^{III}(CN)_6]^{3-}$. Prussian blue is known to be sensitive to alkali and cannot be used in fresco paintings because it degrades through the reaction [9]

$$[Fe^{III}Fe^{II}(CN)_6]^- + 3\ OH^- \rightarrow Fe(OH)_3 + [Fe^{II}(CN)_6]^{4-}.$$

The technique of sgraffito requires the use of lime plaster, which is a mixture of calcium hydroxide and sand. Prussian blue is thus expected to be degraded into iron hydroxide in such a basic medium. However, the sensitivity of Prussian blue to alkali is well known and the use of the pigment for sgrafitti is thus surprising, especially in the early twentieth century. A historical and technological study of Cauchie's wall decoration technique will be necessary to finally decide whether or not the green color of the sgraffiti of the *Villa Germaine* was intended or results from the degradation of Prussian blue in a basic medium. Further, the environmental conditions, such as rain, dust, and atmospheric pollution, can also strongly affect the degradation of the wall decoration.

4.2 Analyses *in situ*

Because of their value and their fragility many works of art cannot be moved or sampled for analysis and must be studied *in situ*. Mobile non-invasive analytical systems are thus particularly important in the study cultural heritage objects and have been increasingly developed in the past few years.

A collection of Vietnamese works of art that belongs to the Artistic Collections of the University of Liège has been analyzed by mobile Fourier transform infrared spectroscopy. The collection initially belonged to M. Joseph Poncin, an alumnus of the University of Liège. In 2008 he gave his entire collection to the Artistic Collections of the University. The Poncin donation consists of more than 140 works of art, such as drawings, watercolors, oil paintings, photographs, and prints, that were gathered in Hanoi from the end 1970's to the early 1980's [176]. Some of these paintings are attributed to known Vietnamese painters, others are the works of anonymous artists.

A few examples of the Poncin collection are shown in Figure 4.11. The pictorial technique varies from oil painting, watercolor on paper or silk, gouache on journal paper, to print on wood. The objective of the analyses carried out on these Vietnamese paintings was the identification of Prussian blue and the detection of any possible alteration of the blue pigment. Because of the large number of works of art, a first selection was made on the basis of a visual, and therefore subjective, detection criterion for Prussian blue. Fifteen paintings and prints were selected and analyzed by Fourier transform infrared spectroscopy. The measurements were carried out *in situ* in the Wittert Gallery, where the Artistic Collections of the University of Liège are kept, by using a Bruker ALPHA mobile Fourier transform infrared spectrometer. The infrared spectra were recorded in external reflection mode because this mode does not require any physical contact with the paint surface. An integrated video camera controls the positioning of the instrument. The absorbance spectra were calculated with the OPUS software. The Bruker ALPHA mobile Fourier transform infrared spectrometer and the OPUS software were kindly loaned to the author by Antwerp University.

Prussian blue is easily identified by Fourier transform infrared spectroscopy because of its characteristic CN^- stretching band at *ca.* 2080 cm^{-1}. Prussian blue was undoubtedly detected in five art works among the fifteen studied, see Figure 4.12. However, the Fourier transform infrared spectroscopic measurements were not always successful. In some cases, the pigment was present in such a low concentration that measurements on the unpainted support and on the painting itself resulted in identical spectra. In other cases, it was impossible to obtain any spectrum in the very dark areas because each measurement attempt was rejected

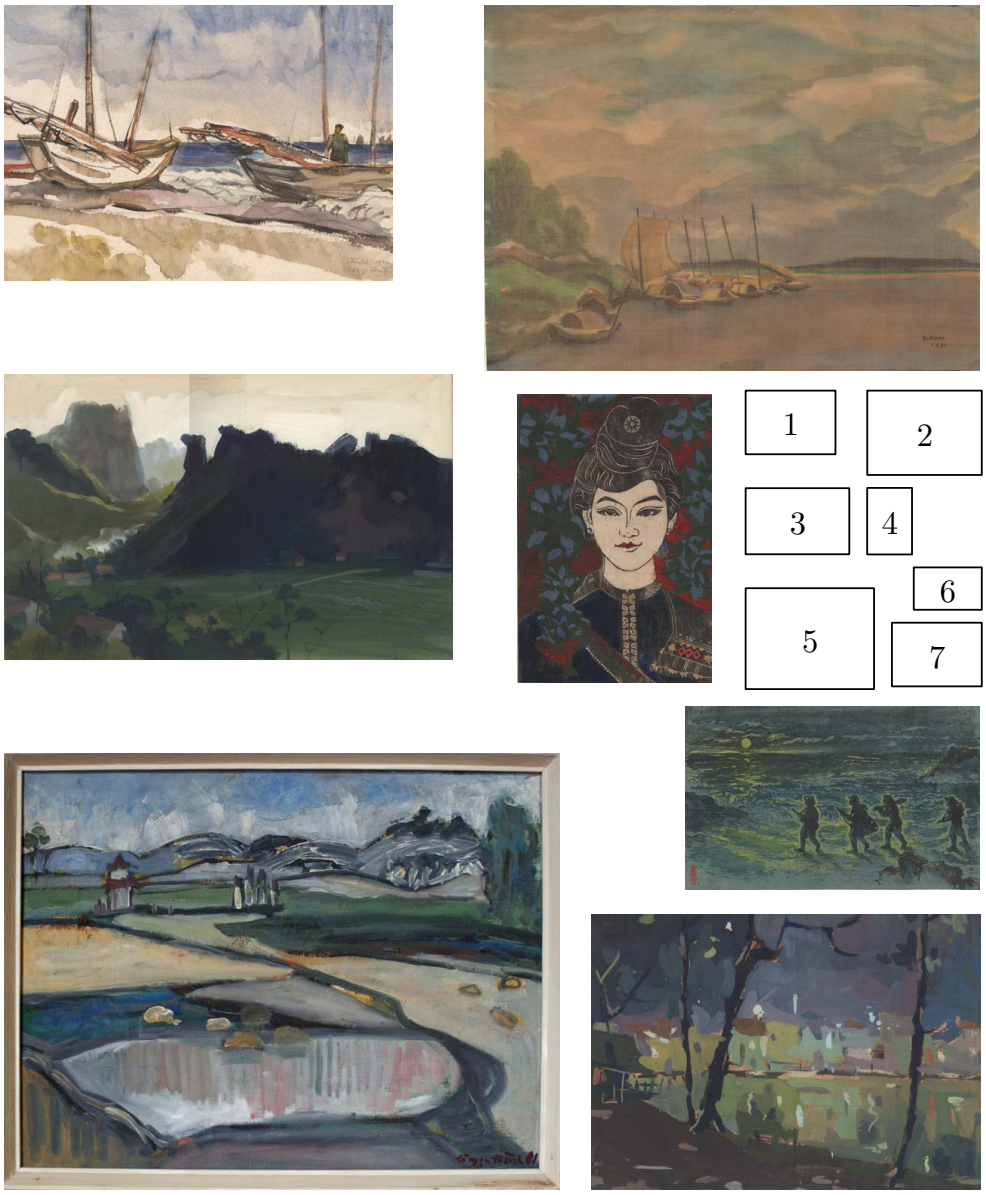

Figure 4.11 Prints and paintings from the Poncin collection. 1. *Sam Son Beach*, **To Ngoc Danh**, 1977, watercolor. 2. *Red river*, **D. Nam**, 1981, watercolor on silk. 3. *Mountains*, **Anonymous**, 1978, watercolor and gouache. 4. *Young woman from a minority living in the mountains*, **Anonymous**, undated, print on colored wood. 5. *Temple in countryside*, **To Ngoc Thanh**, 1981, oil on canvas. 6. *Patrol*, **Pham Van Don**, 1972, print on colored wood. 7. *The small lake of Hanoï at night*, **Viet Dung**, undated, gouache on newspaper.

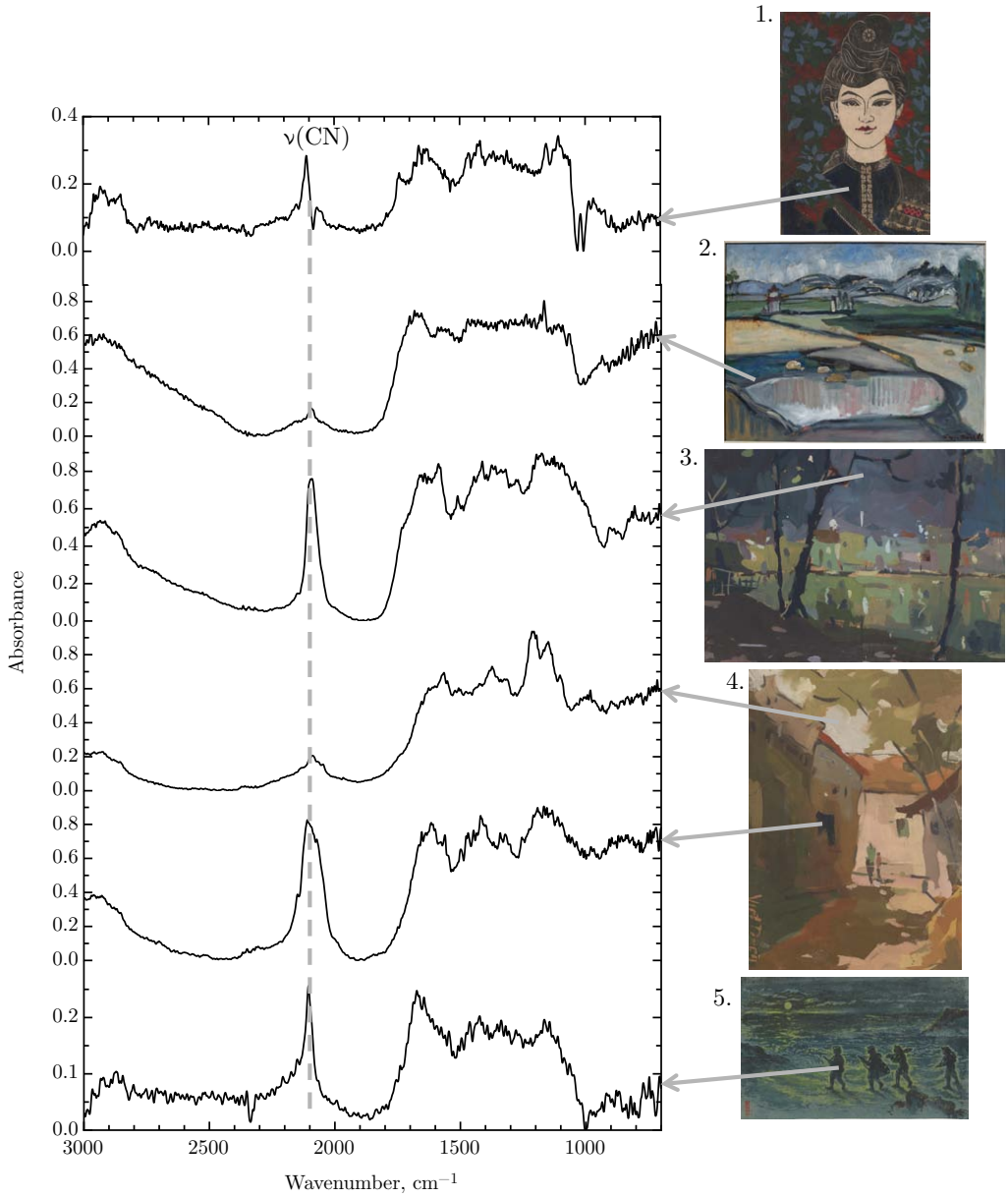

Figure 4.12 The Fourier transform infrared spectra recorded in external reflection mode on five Vietnamese works of art from the Poncin collection. 1. *Young woman from a minority living in the mountains*, **Anonymous**, undated, print on colored wood. 2. *Temple in countryside*, **To Ngoc Thanh**, 1981, oil on canvas. 3. *The small lake of Hanoï, at night*, **Viet Dung**, undated, gouache on newspaper. 4. *A street in the sunligh* **Viet Dung**, undated, gouache. 5. *Patrol*, **Pham Van Don**, 1972, print on colored wood.

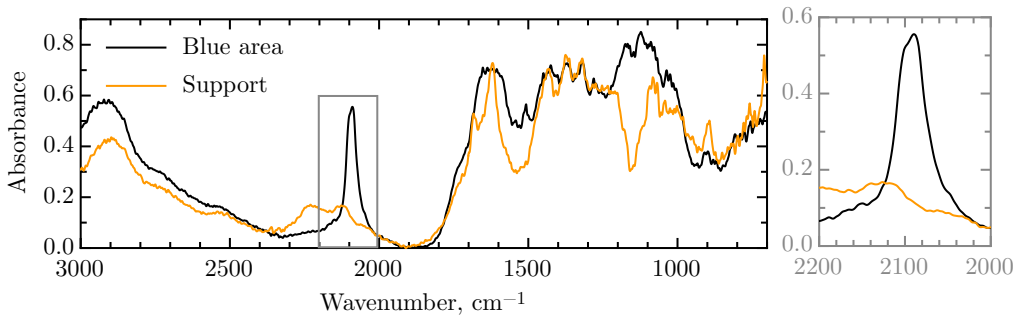

Figure 4.13 The Fourier transform infrared spectra recorded in external reflection mode on the painting by Viet Dung, *The small lake of Hanoï, at night*. Right: an expanded view of the CN^- vibration.

by the OPUS software. This rejection probably results from an extremely large absorption of the infrared radiation by the paint layer. Consequently, the reflected signal was too weak to produce a suitable interferogram. For example, the Fourier transform infrared spectrum shown at the top of Figure 4.12 exhibits a relatively weak and distorted ν(CN) band, although the analyzed blue area seems to be painted with an almost pure blue pigment. This problem probably results from the mathematical Fourier transform of the interferogram.

Visually the works of art containing Prussian blue do not exhibit any noticeable discoloration. An expanded view of the CN^- stretching vibration band reveals, for one painting by Viet Dung entitled *The small lake of Hanoï at night*, a slight deformation in shape of the CN^- band, see Figure 4.13. Instead of a strong single band, two contributions can be distinguished, with the maximum in absorbance shifted towards lower energy. This may suggest a partial reduction of Prussian blue. The detection of other pigments was complex because of the strong signal coming from the support, namely paper, and the binder, see Figure 4.13. The strong absorbance between *ca.* 1700 and 900 cm^{-1} in the Fourier transform infrared spectra obtained on the blue area results from the presence of the paper. The broad band between 1000 and 1200 cm^{-1} can be assigned to the binder, most likely gum arabic.

In conclusion, Vietnamese artists used Prussian blue as a pigment for watercolor, gouache, and oil paintings. No alteration of the pigment was firmly confirmed by Fourier transform infrared spectroscopy. In the twentieth century Prussian blue was prepared according to the modern methods and had a good light fastness in the pure state. In watercolor painting, white pigments are rarely

employed and Prussian blue is expected to be used pure and thus, to be light fast. In gouache and oil paintings, white pigments are often used and may affect the permanence of Prussian blue. An investigation by Raman spectroscopy may be considered in order to detect a possible degradation of Prussian blue in paint layers painted from gouache or an oil binder.

Final Conclusions

The main objective of this thesis has been the identification and understanding of the degradation mechanisms of Prussian blue in paint layers. At the end of this research, the goal can be considered as reached, although some unresolved questions remain, questions that may open new research perspectives.

The preparative methods of Prussian blue were thoroughly investigated because, since the mid-eighteenth century, they have been recognized as contributory factors in the fading of Prussian blue. From this study, it appears that both the crystallite size and the inherent disorder in Prussian blue strongly vary with the type of modern synthesis. Moreover, the soluble variety of Prussian blue, *i.e.*, the variety that contains alkali cations, was shown to have a structure that is similar to the structure of insoluble Prussian blue, a structure which is described by the chemical formula, $Fe_4^{III}[Fe^{II}(CN)_6]_3 \cdot xH_2O$, where x is *ca.* 11. Although beyond the scope of this thesis, the structural determination of the potassium cation containing Prussian blue and the characterization of the vacancy distribution are also of great interest for understanding the electrochromic processes occurring in Prussian blue and the magnetic properties of Prussian blue nanoparticles of controlled size.

The reproduction of several ancient preparative methods indicated the possible formation of an undesirable iron(III) reaction product, identified as ferrihydrite. The ancient methods are based on the calcination of dried blood to produce a potassium hexacyanoferrate complex, which is, with an iron salt, the essential reactants for synthesizing Prussian blue. This organic process yields only a small amount of potassium hexacyanoferrate complex, an amount that is stoichiometrically much smaller than the iron salt. The excess iron ions remaining from the iron salt in the aqueous solution form an hydrous iron(III) oxide, which gives a greenish tint to the Prussian blue pigment. The presence of particles of hydrous iron(III) oxides was also apparent in an eighteenth century genuine Prussian blue sample obtained from a polychrome sculpture, the guardian angel of La Gleize.

The light fastness of Prussian blue containing paint layers upon light exposure

was then investigated. The accelerated ageing experiments revealed an excellent light fastness for pure Prussian blue pigments painted in a dark shade, a light fastness that was independent of the binder. In contrast, Prussian blue with a pale shade, such as in a light watercolor shade and mixed with a white pigment or an extender, fades. Both oxidation and reduction reactions occur in the Prussian blue containing paint layers. A partial oxidation of the iron(II) ions, resulting in the formation of $[Fe^{III}(CN)_6]^{3-}$, was evidenced prior to the accelerated ageing. This oxidation could result from an exchange of hydroxyl groups between Prussian blue and the binder. Upon ageing a reduction of the iron(III) ions occurs at the surface of the paint layer. This partial reduction of Prussian blue coincides with an oxidative break down of the binder, leading to a loss of gloss. The degree of fading depends on the white pigment present and its specific properties, such as its photochemical activity or its basic character. An investigation of the local electronic and structural changes occurring in the white pigment may help to better understand its role in the fading of Prussian blue.

In this thesis, the degradation of Prussian blue was only studied upon light exposure. However, moisture and temperature also affect the fading of pigments [177]. Preliminary studies of the influence of the relative humidity and moisture on the degradation of Prussian blue have been reported in the master's thesis of Lauricella [178]. Accelerated ageing experiments were carried out on pure and diluted laboratory-synthesized ancient and modern Prussian blues painted onto watercolor paper, first, in a high relative humidity of 75 % at 35°C and, second, in a relative humidity of 35 %, at 75°C. At a high relative humidity both the ancient and modern Prussian blues did not visually discolor. In contrast, a fading was observed at high temperature. The larger changes in color were observed for the ancient Prussian blues that contained an extender or that were mixed with a white pigment. At 75 °C, zeolitic water molecules can escape the lattice cavities of Prussian blue. Thus, the loss of water molecules as well as the presence of an extender and/or a white pigment effectively affect the degree of fading.

Further, the influence of the varnish has not been considered in this research. The varnish is expected to protect the paint layers from the light and environmental exposure and can reduce or slow the fading of the underlying Prussian blue paint layer. In addition varnishes often absorb ultraviolet radiation and can hinder the photochemical activity of the pigments. Accelerated ageing experiments of varnished and unvarnished Prussian blue containing paint layers upon light exposure may bring answers to this question of the importance of the varnish.

Finally, the experimental results obtained on laboratory-prepared paint layers were confirmed by studying works of art containing Prussian blue. Analyses of cross-sections prepared from genuine paint fragments indicated both an oxidation

and a reduction of Prussian blue, especially when painted in a light shade. Thus, Prussian blue used for painting light blue areas in works of art is probably discolored. Does it mean that a retouching intervention is justified? The discoloration of Prussian blue is not striking because it is relatively homogeneous. The loss of color affects our perception of the art object but does not hinder its global appreciation. Moreover, the current conservation ethics recommends reversible and objective restoration interventions to preserve the historical coherence of the art objects. Retouching entire blue zones containing presumably discolored Prussian blue is thus not conceivable. Although this research did not lead to a reconsideration of the restoration of works of art containing Prussian blue, it surely may help in better understanding the degradation and alteration processes in a painting's material.

Appendix A

Reports of Degradation in Eighteenth and Nineteenth Century Books

Soon after the discovery of Prussian blue in the beginning of the eighteenth century artists, colormakers, and scientists warned against the impermanence of Prussian blue used as a pigment. Prussian blue was said to fade and to turn green upon light exposure. Despite these disadvantages, Prussian blue remained widely used because of its high tinting strength and its low cost until the 1970's. Some citations, that deal with the durability of Prussian blue and were found in eighteenth and nineteenth books, are given below, usually in their original language.

> *With respect to standing, Prussian blue can neither be esteemed the most perfect, nor the most faulty, colour. When it is very dark,* [...], *it will sometimes stand extremely well* [...]; *on the other hand, when it is light, or with a small proportion of tinting part, it is more frequently bright, and cool, as it is called* [...]; *but extremely subject to fly, or to turn to a greyish green.*

In Dossie R., *The Handmaid for the Arts*, Nourse, J., London (1757).

> *Du bleu de Prusse, qui devient un peu vert dans la fuite du tems* [sic]

In Pernety, A.-J., *Dictionnaire portatif de peinture, sculpture et gravure avec un traité pratique des différentes manières de peindre*, **4**, Bauche, Paris (1757).

> *Theophrastus, Pliny, and others, have enumerated the colours, employed in the various methods of antique painting. These colours include almost all the pigments, which are employed by the moderns.*

> *Prussian blue, which, with a few others, has been added, was discovered by an accidental mixture of the ingredients, which enter into the composition of it. Nor is it so durable as the blue paints, which were in use before its introduction.*

In Delaval E., *An enquiry into the cause of the permanent colours of opake bodies*, Eyres, W., Warrington (1785).

> *The iron in this colour always tends to regenerate and turn black* [...]. *From the same cause, greens composed with this colour, blacken by time.*

In de Massoul C., *A Treatise on the Art of Painting, and the Composition of Colours*, Baylis, London (1797).

> *Ce bleu est bien exempt de la plupart des défauts que présente l'azur; il est vraiment céleste et si intense qu'il paraît noir; il se réduit facilement en poudre; il se mêle aussi bien avec l'huile qu'avec la gomme; il réunit enfin toutes les qualités, si on en excepte une seule, la solidité; mais ce défaut est le plus à craindre parce qu'il est sans remède. Qu'on jette les yeux sur un tableau moderne; le ciel qui en est d'abord admirable, perd bientôt de son éclat; il s'altère, il devient promptement, et dès lors on n'y reconnaît plus celui de la nature.*

In Thénard, L.-J., *Considérations générales sur les couleurs, suivies d'un procédé pour préparer une couleur bleue aussi belle que l'outremer*, Journal des Mines, **15**, 86, 128-136, (an XII [1803-1804]).

> *Le bleu de Prusse, quoiqu'inférieur aux couleurs d'outremer et de cobalt, sous le rapport de la fixité, ne laisse pas d'avoir sur elles, à volume égal, l'avantage d'une bien plus grande quantité de principes colorans* [sic]*; quantité que nous avons trouvée, par l'expérience, être dans le rapport de dix à un environ. Malheureusement tous les alcalis attaquent le bleu de Prusse; c'est pourquoi, lorsqu'on le combine avec des couleurs qui en contiennent, l'on expose ce bleu à disparaître ou à changer en peu de temps.*

In Watin, M. and Bourgeois, Ch., *L'art du peintre, doreur et vernisseur*, ninth edition, Belin-Leprieur, Paris (1823).

> *Le bleu de Prusse exposé à l'air, à la température ordinaire, s'altère peu à peu et passe au vert.*

In Thénard, L.-J., *Traité de chimie élémentaire, théorique et pratique*, **4**, Clochard, Paris (1824).

> *On doit choisir le bleu de Prusse foncé en couleur, brillant, et sans aucune teinte pourprée. Lorsque sa couleur est pâle ou verdâtre, c'est un signe d'impureté. Ce n'est guère que lorsqu'il est mêlé avec du blanc que l'on peut en connaître parfaitement le caractère chromatique.*

In de Montabert, P., *Traité complet de la peinture*, **9**, Bossange Père, Paris (1829).

> *Prussian blue does very well; but for skies it wants breaking with a quantity of lake, as thus, which brings it very near ultramarine. For other uses, such as mixing greens and neutral tint, it may be introduced as you find it: It will not stand very long in the sun.*

In Ibbetson, J. C., *An accidence, or gamurt, of painting in oil*, second edition, Harvey and Darton, London (1828).

> *Cette couleur serait des plus précieuses, si elle avait de la solidité: elle a beaucoup d'intensité, elle se peint facilement, elle sèche promptement; mais elle perd de son éclat, devient verdâtre et grise lorsqu'elle est exposée à une lumière vive: ainsi elle ne pourrait pas être employée pour faire des verts brillans* [sic] *durables.*

In Mérimée, J.-F.-L., *De la peinture à l'huile: ou des procédés matériels employés dans ce genre de peinture depuis Hubert et Jean Van Eyck jusqu'à nos jours*, Huzard, Paris (1830).

> *Le bleu de Prusse est employé pour peindre soit à la gouache, soit à l'huile; il se distingue par l'intensité et la stabilité de sa couleur.*

In Berzelius, J. J. *Traité de Chimie*, traduit par Me. Esslinger, **4**, Firmin Didot Frères, Paris (1831).

> [...] *toutes ces couleurs* [dont le bleu de Prusse] *ne sont malheureusement pas très solides, plusieurs passent un peu, tandis que d'autres gagnent de ton en vieillissant, surtout lorsqu'on laisse les dessins exposés à l'air, mais faute de mieux, il faut s'en contenter.*

In Douhaire, P., *Cours théorique et pratique de peinture à l'aquarelle*, Roret, Paris (1848).

> *It* [Prussian blue] *is a deep and powerful blue colour, of vast body and considerable transparency, and forms tints of much beauty with white lead, though they are by no means equal in purity and brilliancy to those of cobalt and ultramarine, nor have they the perfect durability of the latter. Notwithstanding Prussian blue lasts a long time under favourable circumstances, its tints fade by the action of strong light, and it is purpled or darkened by damp or impure air.* [...] *time has a neutralizing tendency upon its colour.*

In Field G., *Rudiments of the painters' art; or a grammar of colouring applicable to operative painting, decorative architecture, and the arts*, John Weale, London (1850).

> *C'est un très beau sel qui s'altère à l'air et donne avec le temps une couleur verte* [...] *le bleu de Prusse est très intense et a une belle couleur mais il devient verdâtre mélangé à du blanc de plomb.*

In Riffault, J., *Nouveau manuel complet du fabricant de couleurs et de vernis*, Roret, Paris (1850).

> *Le bleu de Prusse, s'altérant facilement sous l'influence de la radiation solaire, doit, autant que possible, n'être appliqué que sur des objets placés à l'ombre.*

In Pelouze, J. and Fremy, E., *Traité de Chimie générale, analytique, industrielle et agricole*, **6**, Victor Masson et Fils, Paris (1864).

> *Le bleu de Prusse sur tissus se décolore à la lumière, sans doute sous l'influence d'une réduction. Il reprend sa couleur dans l'obscurité. Il est rare que les produits commerciaux soient purs. Tantôt ils renferment du peroxyde de fer hydraté, s'ils ont été préparés par oxydation du précipité blanc. D'autres fois ils sont mélangés à plus ou moins d'alumine précipitée, en même temps que le bleu, par l'action du cyanure jaune sur un mélange de sels ferreux et aluminique (1 partie de vitriol vert et 2-4 parties d'alun). On y incorpore aussi souvent des substances blanches, telles qu'albâtre gypseux, ou de l'amidon coloré en bleu par l'iode. Toutes ces fraudes sont de nature à altérer la pureté de la nuance.*

In Schützenberger, M. P., *Traité des matières colorantes contenant leurs applications à la teinture et à l'impression et des notices sur les fibres textiles, les épaississants et les mordants*, Victor Masson et Fils, Paris (1867).

Appendix B

Description of Techniques

Basic principles and experimental instrumentation for all the techniques used in this thesis are detailed in this section. Laboratory techniques and synchrotron radiation-based techniques are presented separately in **Section B.2** and **B.3**. For easy reference, laboratory techniques are presented in alphabetic order in **Section B.2**.

Contents

B.1 General considerations

Most of the techniques used in this study are based on the interaction between electromagnetic radiation and matter. Quantum mechanics indicates that the energy of a system can not be seen as a continuum but, in contrast, is quantized. When a molecule experiences an electromagnetic field, any energy exchange between the molecule and the field satisfies the relation,

$$\Delta E = h\nu, \tag{B.1}$$

where ΔE is the difference in energy between two quantized states of the molecule, h is Planck's constant, and ν the frequency of the radiation. The total energy of a free molecule is the sum of four quantized energy components, the translational energy, E_{trans}, the energy associated with the motions of the electrons in the molecule, E_{el}, the energy associated with the vibrations of the constituent atoms, E_{vib}, and the energy resulting from the rotation of the molecule as a whole, E_{rot},

$$E_{tot} = E_{trans} + E_{el} + E_{vib} + E_{rot}. \tag{B.2}$$

In the following discussion the translational energy of the molecule, E_{trans} will be ignored. Because the energy variations, ΔE_{el}, ΔE_{vib}, and ΔE_{rot} have very different magnitude, as shown in Figure B.1, they are easily separated and each one can be probed by an appropriate spectroscopic technique, depending on the spectral range.

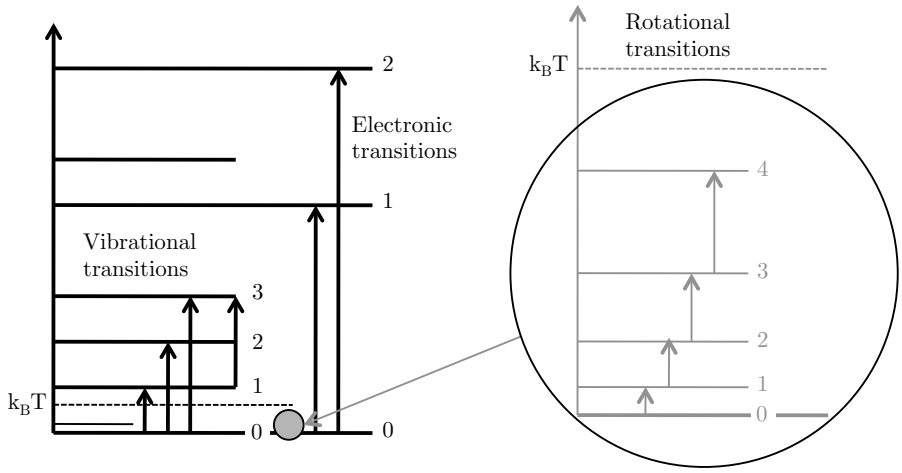

Figure B.1 Quantized states of electronic, vibrational, and rotational energy and transitions between corresponding states. k_BT is the thermal energy. Reproduced from [116].

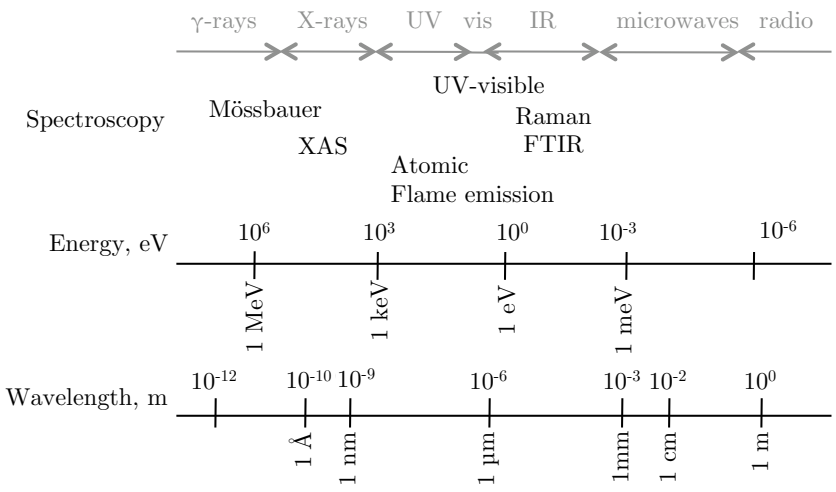

Figure B.2 Electromagnetic spectrum and the spectral ranges of spectroscopic techniques.

Figure B.2 shows the electromagnetic spectrum and the spectral range in which each of the different spectroscopic techniques is applicable. Iron-57 Mössbauer spectroscopy uses a transition of 14.4 keV between nuclear states to study hyperfine interactions between the nucleus and its environment. X-ray absorption spectroscopy uses X-rays at energies close to an atomic absorption edge to obtain information on the absorbing atom or ion and its environment, whereas UV-visible spectroscopy studies the electronic transitions within a molecule. Atomic absorption and flame emission spectroscopy are quantitative analytical techniques based on the measurement of light emitted or absorbed by thermally excited atoms or ions. Raman and infrared spectroscopies use transitions in the range between 10^2 cm^{-1} (10^2 µm) to 10^3 cm^{-1} (10 µm) to gain information on the vibrations within a molecule.

Particle-induced X-ray emission can not be considered as a spectroscopic technique because the perturbation is induced by particles, *e.g.*, protons, and not by radiation. Similarly to X-ray fluorescence spectroscopy it provides information on the electronic binding energy. X-ray diffraction is not a spectroscopic technique because it does not provide information in the form of a spectrum, *i.e.*, a plot of the response of the material as a function of energy of the electromagnetic radiation. It is a structural technique, based on the constructive interference between the incident X-rays and the X-rays diffracted by the crystal at a given angle. Finally, thermogravimetric analyses record the loss of mass of a sample as a function of temperature.

B.2 Laboratory techniques

B.2.1 Atomic absorption and flame emission spectroscopy

Both atomic absorption and flame emission spectroscopy are used to quantify the elemental compositions of compounds. The basic principle relies on the measurement of the emission or absorption spectrum of an atomic species. The sample is heated at a sufficiently high temperature to reach atomization, *i.e.*, the breaking of molecular bonds. A fraction of the atoms are thermally excited and emit radiation at specific wavelength as electrons return from excited states to their ground-state. The intensity of the emission lines is directly related to the number of excited atoms, and consequently, to the concentration of an element in the sample. This is the basic principle of flame emission spectroscopy. Similarly, in atomic absorption spectroscopy, the atoms in the ground-state can absorb a radiation at the same energy that is emitted by the excited atoms. When a monochromatic radiation at this resonant energy passes through the flame containing free atoms, a fraction of the photons is absorbed proportionally to the number of atoms in their ground-state in the flame.

Flame emission spectroscopy is mainly used for the analysis of alkali and alkaline earth metals because these elements are atomized at a relatively low temperature of less than 2500°C and have their emission lines in the visible spectrum. Atomic absorption spectroscopy is more commonly used than flame emission spectroscopy because of the availability of easy-to-use and unexpensive instruments [179] and because it can be employed for more than 70 elements, metals and non-metals [180]. Further, absorption spectra are simpler than emission spectra, beause there is only one initial state, the ground state.

The measurements have been carried out by M. B. Belot and J. Otten, from the Department of Geology, at the University of Liège. The Prussian blue powder samples were dissolved in concentrated sulfuric acid and then treated with hydrochloric acid to dissolve the iron sulfate formed. The concentration of iron and potassium are given in weight percent and are averaged on three successive measurements. The accuracy of the measurement is estimated to be 0.01 weight %.

B.2.2 Fourier transform infrared spectroscopy

The Fourier transform infrared spectroscopy measurements were performed at the Royal Institute for Cultural Heritage, Brussels, under the supervision of Dr. J. Sanyova. Basic information on Fourier transform infrared spectroscopy can be found in the books of Poilblanc [116] and Nakamoto [115].

Basic principles

Infrared spectra result from the transitions between two vibrational levels of the molecule in the electronic ground state. The energy of infrared radiation corresponds to the energy required to induce vibrations in a molecule, *i.e.*, individual atoms within the molecule can change position relative to one another without moving or rotating the molecule. All vibrational transitions are not allowed and selection rules derived from quantum mechanics exist.

According to the selection rule of the harmonic oscillator, only transitions that correspond to $\Delta n = \pm 1$ transitions are allowed. Because the number of molecules in the electronic ground state is much larger compared with that in the excited states, only the fundamental transition, *i.e.*, only the transition from $n = 0$ to 1, in the electronic ground state, is usually observed in infrared spectra.[1] In addition another restriction results from the symmetry in the molecule. Infrared spectroscopy is based on the interaction between the oscillating electric field of the electromagnetic radiation and the electric charges of the molecules, *i.e.*, the electric *oscillating dipole moment*. The electric dipole moment μ is a vector that can be resolved into three components in the x, y, and z directions,

$$\begin{aligned} \mu_x &= \sum_i e_i x_i \\ \mu_y &= \sum_i e_i y_i \\ \mu_z &= \sum_i e_i z_i \end{aligned} \tag{B.3}$$

where e_i is a charge and x_i, y_i, and z_i are the coordinates of the i^{th} particle, nucleus or electron of the molecule. The dipole moment operator, $\hat{\mu}$, can be written as

$$\hat{\mu} = \hat{\mu}_x + \hat{\mu}_y + \hat{\mu}_z. \tag{B.4}$$

From a quantum mechanical point of view, the electric dipole moment resulting from a transition from the initial state m, described by the wavefunction ψ_m, to the excited state n, described by the wavefunction ψ_n, is given in the Dirac notation by

$$\mu_{mn} = \langle \psi_n | \hat{\mu} | \psi_m \rangle. \tag{B.5}$$

[1] This selection rule can be partially removed because of the anharmonicity of the vibration and *overtone bands*, *i.e.*, bands that are multiples of the fundamentals, and *combination bands*, *i.e.*, bands resulting from the sum or difference of two different fundamentals, may be weakly observed.

The electric dipole transition is allowed if $\mu_{mn} \neq 0$ and forbidden if $\mu_{mn} = 0$. In other words, a vibration is active in the infrared spectrum *if the dipole moment of the molecule is changed during the vibration.* In centrosymmetric molecules, such as Prussian blue, only the vibrations that belong to the *ungerade*, u, type are infrared active.

Experimental instrumentation

Modern infrared spectrometers usually consist of a Fourier transform interferometer, such as the Michelson interferometer with a moving mirror. The intensity of the infrared radiation that passes through the interferometer is recorded as a function of time delay or optical light path length difference that is introduced by the moving mirror. The resulting signal is an interferogram that contains all the beam frequencies. The interferogram, $I(\delta)$, of a spectrum that is represented by the function $B(\nu)$, is described by the expression

$$I(\delta) = B(\nu) \cos\left(\frac{2\pi\delta}{\lambda}\right), \tag{B.6}$$

where δ is the optical light path length difference, ν is the frequency, and λ is the monochromatic radiation of the source. The interferogram is then converted in an infrared spectrum by the Fourier transform,

$$B(\tilde{\nu}) = \int_{-\infty}^{+\infty} I(\delta) cos(2\pi\delta\tilde{\nu}) \mathrm{d}\delta, \tag{B.7}$$

where $\tilde{\nu}$ is the wavenumber defined as $\tilde{\nu} = 1/\lambda$.[2] The Fourier transform of a typical interferogram is shown in Figure B.3.

Prior to sample measurements, a background scan is usually recorded with no sample in the infrared beam path. The sample is then analyzed and the resulting spectrum is ratioed to the background spectrum. The infrared spectrum is plotted either in percent transmittance, % T, or in absorbance, A, which is obtained by taking the base 10 log of the reciprocal of transmittance, *versus* infrared frequency, in wavenumber, in cm^{-1}. In this thesis, the Fourier transform infrared measurements are presented as absorbance spectra.

[2] In practice, the integral in equation B.7 is limited to a finite interval because the interferogram is only recorded on a finite δ interval. This results in the truncation of the interferogram on the interval $[-\Delta, +\Delta]$, obtained by the convolution product of the interferogram $I(\delta)$ with a rectangle function, referred as to *window*, that equals 1 on the interval $[-\Delta, +\Delta]$ and zero on the intervals $]-\infty, -\Delta[$ and $]+\Delta, +\infty[$. The convolution theorem states that the Fourier transform of the convolution of two functions is the product of their Fourier transform.

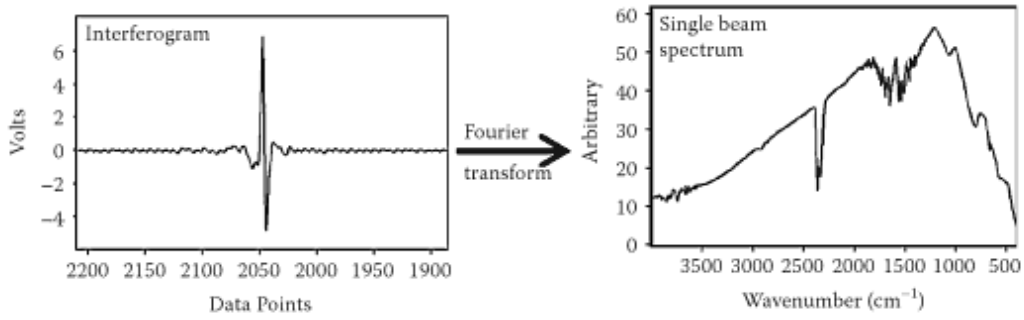

Figure B.3 The Fourier transform of an interferogram produces a single beam spectrum [181].

Painted Prussian blue samples were studied by attenuated total reflectance Fourier transform infrared spectroscopy by using a VERTEX spectrometer coupled with a Bruker Hyperion 3000 FT-IR microscope, located at the Royal Institute for Cultural Heritage in Brussels, Belgium. The attenuated total reflectance objective is equipped with a germanium crystal. Attenuated total reflection, or internal reflection, occurs when the incident beam is internally reflected in a high-refractive-index material placed in contact with the sample. By knowing the wavelength, the refractive indices of germanium and Prussian blue, and the incidence angle, the depth of penetration was found to be approximately 1 μm [34]. The contact area between the germanium crystal and the sample is approximately 100 μm^2. All spectra result from the sum of 64 scans at a resolution of 4 cm^{-1} between 4000 and 600 cm^{-1}. The spectra were baseline-corrected and no further ATR corrections were applied. The samples were analyzed at several spots in order to both ensure reproducibility and to evaluate the homogeneity of the paint layer.

Measurements on genuine paintings were carried out by using a Bruker ALPHA FT-IR spectrometer because this portable instrument allows *in-situ* measurements in museums. The infrared spectra were recorded in external reflection mode in order to avoid any contact with the paint surface. The sampling area and positioning of the instrument were controlled by an integrated video camera.

B.2.3 Mössbauer spectroscopy

Mössbauer spectroscopy is based on the Mössbauer effect, which consists of the recoil-free emission and resonant absorption of γ-radiation in solids. The Mössbauer results presented in this thesis were obtained in the laboratory of Prof. Fer-

nande Grandjean and analyzed with the help of Prof. Gary J. Long, Dr. Moulay T. Sougrati, and Dr. Raphaël Hermann.

Basic information on Mössbauer spectroscopy can be found in the books of Long [130], of Janot [182], and in the course notes of Grandjean [183].

Physical concept

By definition resonant absorption occurs when the emission energy is identical to the absorption energy. When a γ photon is emitted by a free atom the nucleus recoils because of conservation of momentum, and hence, the energy of the γ photon is reduced by the recoil energy.

$$E_\gamma^{em} = E_0 - \left(\frac{(E_\gamma^{em})^2}{2Mc^2} \right) = E_0 - E_R, \tag{B.8}$$

where E_R is the recoil energy, M the mass of the nucleus and c the speed of light in vacuum. Similarly, the absorption energy will be increased by the recoil energy

$$E_\gamma^{abs} = E_0 + E_R. \tag{B.9}$$

Hence, depending on the line width of the absorption and emission lines, resonant absorption may or may not be possible, as is shown in Figure B.4.

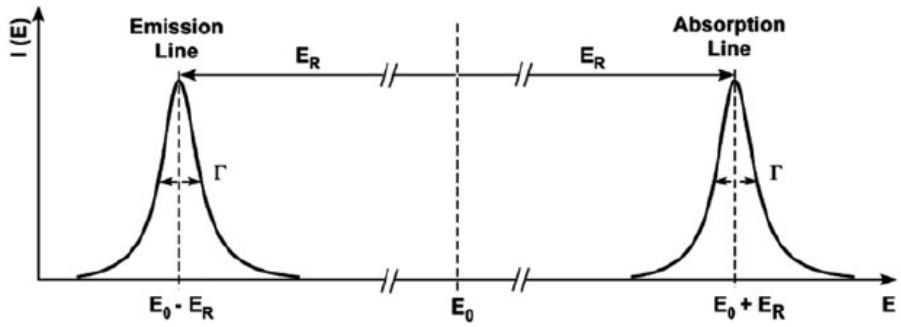

Figure B.4 Energy separation of γ-emission and absorption lines caused by the recoil of resting free nuclei, with $2E_R \approx 10^6\Gamma$. The two Lorentzian lines are centered on $E_0 - E_R$ and $E_0 + E_R$. Resonant absorption is not possible because there is virtually no overlap between the emission and absorption lines [184].

If the line width of the nuclear transtion is greater than E_R resonant absorption is possible. Because the recoil energy remains small compared to the X-ray energy,

E_R can be approximated by

$$E_R = \frac{(E_\gamma^{em})^2}{2Mc^2} \approx \frac{(E_0)^2}{2Mc^2}. \tag{B.10}$$

For a nuclear mass of 100 and a γ-ray energy of 10 keV, E_R is approximately 0.001 eV. The line width of the nuclear transition is given by Heisenberg's uncertainty principle,

$$\Gamma \geq \frac{h \ln 2}{2\pi t_{1/2}}, \tag{B.11}$$

where $t_{1/2}$ is the half-life of the excited state. At this point, we will limit our discussion to the case of iron-57 and its 14.4 keV nuclear transition, the case of interest for the Mössbauer spectral study of Prussian blue.

For iron-57, the half-life $t_{1/2}$ of the excited state I = 3/2 is 141 ns. Hence,

$$\Gamma \geq 4.6 \times 10^{-9} \text{ eV}. \tag{B.12}$$

The line width, Γ, of the nuclear transition is thus much smaller than the recoil energy and no resonant absorption may thus occur between free iron-57 nuclei, see Figure B.4.

In solids, atoms are bonded together with a binding energy of typically a few eV. Three types of events may then occur. First, if the recoil energy is larger than the atomic binding energy, atoms that are excited by the γ radiation may leave their crystallographic site, may induce damage in the solid, and then behave as free to recoil atoms. Second, if the recoil energy is smaller than the atomic binding energy but larger than the vibrational energy of approximately 10^{-3} to 10^{-1} eV, the recoil energy is dissipated in lattice vibrations, increasing the temperature of the crystal. Resonant absorption is not possible because emission and absorption occur at an energy that is too different from the nuclear transition energy, E_0. Third, finally, if the free-atom recoil energy is smaller than the quantized energy of a one-phonon excitation, a fraction of the photons may be emitted or absorbed without phonon excitation or deexcitation. This process is called a zero-phonon γ transition. When an average is taken over many emission processes, the energy transferred per event is exactly the free-atom recoil energy.

The probability, f, that the nuclear transition occurs without any recoil or change in the phonon state of the crystal is called the *Lamb-Mössbauer factor*. It is a function of the lattice properties of the solid and of temperature.

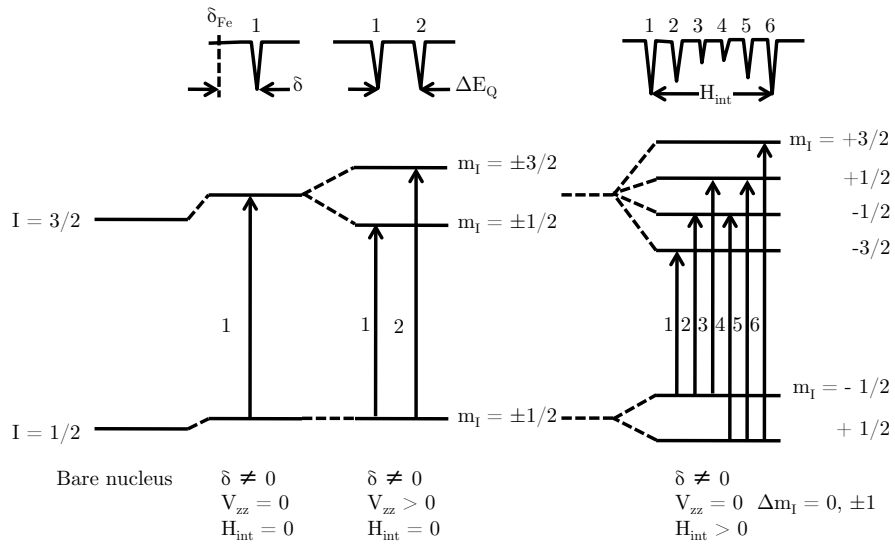

Figure B.5 Schematic diagram of the nuclear energy level shift and splitting of ^{57}Fe isotope as a function of chemical environment, electric field gradient, and internal magnetic hyperfine field. Reproduced from [130].

The Mössbauer effect has been observed for approximately 100 elements. Iron-57 is the most commonly used isotope in Mössbauer spectroscopy for three reasons, the Lamb-Mössbauer factor is large between 4.2 and *ca.* 1200 K, the iron-57 isotope has a relatively large natural abundance of 2 %, and cobalt-57 may be used as a source with a long life-time.

Because of the observed narrow natural line width of the nuclear transition, the hyperfine interactions, *i.e.*, the interactions between the nucleus and its environment, may be measured by Mössbauer spectroscopy. There are three hyperfine interactions, the isomer shift, the quadrupole splitting, and the nuclear Zeeman effect. The first two interactions are of electric origin, whereas the third is of magnetic origin.

The isomer shift results from the non-point nuclear charge distribution and, hence, its overlap with the electronic distribution. Because only the s-electrons have a non-zero density probability at the nucleus, the isomer shift is essentially a measure of the s-electron density at the nucleus. The perturbation of the nuclear energy level diagram by the isomer shift is shown in Figure B.5. Because the nuclear radius is different in the excited and ground states of the iron-57 nucleus, both levels are shifted by different amounts and the energy of the transition is

shifted relative to a conventional zero, taken in practice as the center of the α-iron Mössbauer spectrum, noted δ_{Fe} in Figure B.5. The isomer shift is given in SI units [182] by

$$\delta = \frac{1}{5\epsilon_0} Z e^2 R_{\mathrm{eff}}^2 \frac{\Delta R}{R_{\mathrm{eff}}} [|\psi_a(0)|^2 - |\psi_{st}(0)|^2], \tag{B.13}$$

where ϵ_0 is the vacuum permittivity, Z the atomic number, and e the charge of electron. In the nuclear factor of equation B.13, R_{eff} is the mean nuclear radius for the ground and excited states and $\Delta R/R_{\mathrm{eff}}$ is the relative radius change between the ground and the excited state. In the electronic factor of equation B.13, $|\psi_a(0)|^2$ and $|\psi_{st}(0)|^2$ are the electron density probability at the iron nucleus in the absorber and standard material, respectively.

The quadrupole splitting, ΔE_Q, results from the interaction between the nuclear quadrupole moment, Q, and the electric field gradient created at the nucleus by the surronding electric charges. The nuclear quadrupole moment, Q, reflects the deviation of the nucleus from spherical symmetry. Nuclei with a spin 0 or 1/2 are spherical and hence the I = 1/2 ground state of iron-57 has a zero quadrupole moment, whereas the I = 3/2 excited state of iron-57 has a quadrupole moment of 0.16 ± 0.02 barn. The electric field gradient is a tensor, $\partial^2 V/\partial x_i \partial x_k$ that can be reduced to its principal components in an appropriate coordinate system, $V_{xx} = \partial^2 V/\partial x^2$, $V_{yy} = \partial^2 V/\partial y^2$, $V_{zz} = \partial^2 V/\partial z^2$. These three components must obey Laplace's equation,[3]

$$V_{xx} + V_{yy} + V_{zz} = 0. \tag{B.14}$$

Further, in the case of axial symmetry, such as in an axially distorted pseudo-octahedral complex,

$$V_{xx} = V_{yy} = -\frac{1}{2} V_{zz} = -\frac{1}{2} qe = -\frac{1}{2} \left(\frac{\partial^2 V}{\partial z^2} \right). \tag{B.15}$$

The effect of the quadrupole interaction on the nuclear levels of iron-57 is shown in Figure B.5. The degeneracy of the excited I = 3/2 level is partially removed by the quadrupole interaction and the two pairs of sublevels, $m_I = \pm 3/2$ and $m_I = \pm 1/2$ are separated by an energy, $\Delta E_Q = e^2 qQ/2$. Two transitions from the ground state to the two excited states are now possible and a doublet with a quadrupole splitting, ΔE_Q, is observed. Many examples of doublets are found in this thesis. All the relevant details for the quadrupole interaction may be found in [130] and [182].

The third hyperfine interaction results from the magnetic interaction between the nuclear magnetic moment and the magnetic field at the nucleus created by

[3] Laplace's equation says $\Delta f = \partial^2 f/\partial x^2 + \partial^2 f/\partial y^2 + \partial^2 f/\partial z^2 = 0$.

the electrons. This interaction completely removes the degeneracy of the nuclear levels, as shown in Figure B.5. Six transitions are allowed in agreement with the selection rules for a magnetic dipole transition, $\Delta m_I = 0, \pm 1$. The observed Mössbauer spectrum is a sextet, the most commonly observed sextet is that of a calibration spectrum with an α-iron foil. No further discussion of the magnetic interaction will be given herein because no sextet spectrum is presented in this thesis.

The hyperfine interactions are easily measured in an iron-57 Mössbauer spectrum because of the narrow natural line width of the transition. Typically the energies associated with the hyperfine interactions are of the order of a few to 50 times the line width. As we will see in the next section, the energy scale in a Mössbauer spectrum is given in mm/s. The natural linewith for an iron-57 Mössbauer spectral absorption is 0.195 mm/s and this line width sets an appropriate lower detection limit for any hyperfine interaction.

Experimental spectrometer

A schematic of a typical Mössbauer spectrometer is shown in Figure B.6. Mössbauer spectroscopy is actually a resonant absorption experiment in which a source emits a γ radiation that is absorbed by an absorber. In the case of iron-57 Mössbauer spectroscopy, the source is cobalt-57 diffused in a rhodium matrix. As is shown in Figure B.7, cobalt-57 decays by electron capture to an excited level of iron-57, which itself decays to the excited level with spin 3/2 at an energy of 14.41 keV above the ground state with spin 1/2. The 14.41 keV transition is the emitted Mössbauer radiation, that is absorbed by the iron-57 nuclei present in the absorber. Because the iron-57 nuclei present in the source and in the absorber are in different electric and magnetic environments, the energy of the emitted radiation is different from that required for absorption. Hence, the emitted energy must be modulated to restore resonance. This modulation is achieved through Doppler shifting the radioactive source relative to a stationary absorber. For a velocity, $\pm v$, of the source, the energy of the emitted radiation is modulated by $\Delta E = \pm v E_{em}/c$. A modulation in energy of 10^{-7} to 10^{-8} eV is comparable to the energies involved in the hyperfine interactions and corresponds to a velocity of a few mm/s in the case of iron-57. Most spectrometers function in constant-acceleration mode, *i.e.*, the velocity linearly varies with time between $-v_{max}$ and $+v_{max}$. The γ-rays transmitted through the absorber are counted by a detector, *e.g.*, a gas proportional counter, and counts are stored in a multichannel analyzer or a computer memory as a function of the velocity of the source. The use of the Doppler shift for the modulation of the emitted energy explains the unusual usage of mm/s as a unit of energy in Mössbauer spectroscopy.

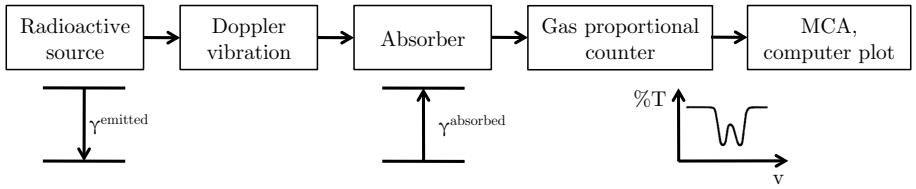

Figure B.6 General scheme of Mössbauer spectrometer. Reproduced from [130].

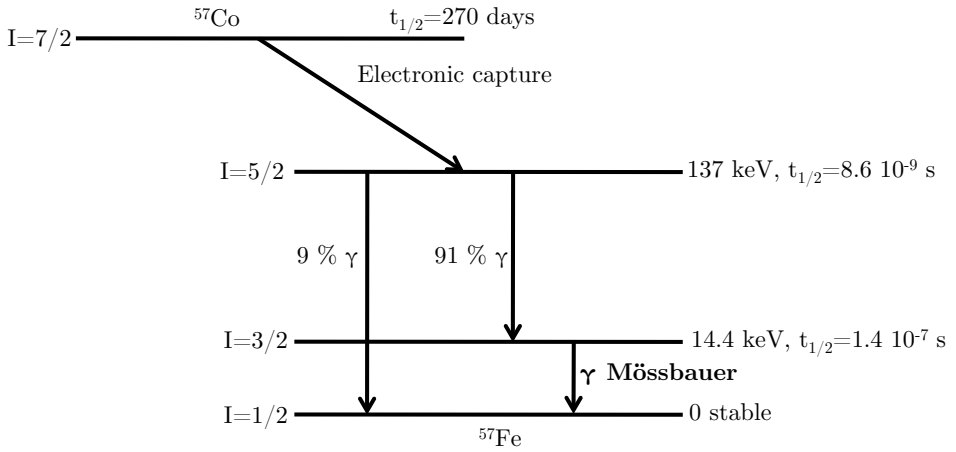

Figure B.7 ^{57}Fe Mössbauer source obtained from ^{57}Co by electronic capture. Reproduced from [182].

The Mössbauer spectrometer used in this thesis is located at the University of Liège. It is a a constant-acceleration spectrometer equipped with a Janis Supervaritemp cryostat to allow low-temperature measurements. The Mössbauer spectral absorbers were prepared with 10 to 15 mg/cm^2 of powdered Prussian blue mixed with boron nitride, which is transparent to γ radiation. The acquisition time typically lasted one day but it was slightly increased as the source became less intense with time. The spectrometer was calibrated at 295 K with α-iron powder. The Mössbauer spectra were fitted with Lorentzian lines, using the Levenberg-Marquardt algorithm.

B.2.4 Optical microscopy

An optical microscope essentially consists of an ocular and an objective and permits the magnification of images of small samples. The spatial resolution is restricted by the diffraction limit imposed by the wavelength of the probe light. The basic principles of the optical microscope are well known and will not be further detailed herein.

Two optical microscopes were used in this thesis, an Olympus BX51 optical microscope located at the European Center of Archaeometry at the University of Liège and an Zeiss Axioplan optical microscope, located at the Royal Institute for Cultural Heritage, Brussels. Both are equipped with two different light sources, a visible light source and a UV light source. The UV light source was used to image cross-sections, in order to evidence fluorescent areas. Three types of illumination modes, selected by means of appropriate filters, are available, the bright field illumination, the dark field illumination, and the cross-polarized light illumination. In the bright illumination, all the direct light, either diffracted or not by the object, reaches the objective, resulting in an weakly contrasted image composed of the object image superimposed on an uniform bright background. In the case of the dark field illumination, the direct light that is not diffracted by the sample is suppressed and only the diffracted light is collected, resulting in an object image superimposed on an uniform dark background. Finally, the cross-polarized illumination is obtained by using polarizers and can provide detailed information on the structure and composition of the sample. The polarized light was used to image cross-sections because it eliminates surface irregularities in case of rough polishing.

The experimental conditions – use of visible/UV light and dark/bright field/polarized illumination – under which the optical micrographs were obtained, are indicated in the legend of the figures in the body of this thesis.

B.2.5 Particle induced X-ray emission studies

The particle induced X-ray emission measurements were performed at the cyclotron located at the IPNAS laboratory, at the University of Liège.

Basic principles

The particle induced X-ray emission, PIXE, method is an elemental analytical technique based on the detection of X-rays emitted by the deexcitation of the atoms in a material. When a sample is irradiated by a beam of charged particles, usually protons, the charged particles excite the electrons in the innermost shells of the atoms. The inner shell vacancies that are produced by this ionization are

then filled by electrons from an outermost shell. The excess of energy is released by the emission of an X-ray of a characteristic energy of the element.

An X-ray spectrum consists of a continuous background, referred as to the *Brehmsstrahlung* and which is produced by the deceleration of deflected charged particles, and characteristic X-ray lines of the atoms present in the sample. The surface area of each peak in the spectrum is related to the concentration of the corresponding element in the sample. If the number of incident particles is known, an absolute quantification can be calculated on the basis of the X-ray production cross-sections, the efficiency of the detector, and experimental geometry. The PIXE method is extremely sensitive with a detection limit down to one part per million, in mass units.

Experimental equipment

The PIXE measurements reported in this thesis were carried out by using an external hydrogen proton beam of approximately 3.12 MeV, produced by the cyclotron at the IPNAS laboratory. The experimental PIXE experimental arrangement is shown in Figure B.8. Description and recent improvements of the PIXE line and extraction nozzle can be found in the papers by Weber [185], Mathis [186], and Dupuis [187].

The emitted X-rays are detected by two energy dispersive semiconductor detectors. The low energy X-ray detector is a lithium drifted silicon Si(Li) Sirius detector equipped with a 1 μm carbon foil. The lower quantification limit in energy is approximately 1 keV and therefore, all Z elements above sodium can be detected by means of their K, L, or M X-ray lines. A system of helium injection is placed between the proton beam spot and the detector for two reasons, first in order to avoid the energy loss of the incident particles as well as their energetic and spatial dispersion, and second, to reduce the absorption in air of low-energy K X-rays, such as the sodium K_α X-ray of 1.041 keV. The heavy Z-element X-ray detector is a low energy Germanium (LEGe) Canberra detector. Because iron is the main metal in Prussian blue, the detector is supplied with a 5 μm chromium absorber in order to reduce the iron X-ray intensity.

The external proton beam is collimated by a collimator of 0.5 mm in diameter, resulting in a spot of approximately 1 mm in diameter on the sample. The analysis spot is pin-pointed by a laser beam and visualized on a CCD camera placed in the beam axis. Because the X-ray production yield is extremely high, the intensity of the proton beam can be very low and did not exceed 5 nA. The beam dose is monitored by counting the protons that are backscattered by a gold-covered collimator. These backscattered protons are detected by using a silicon surface

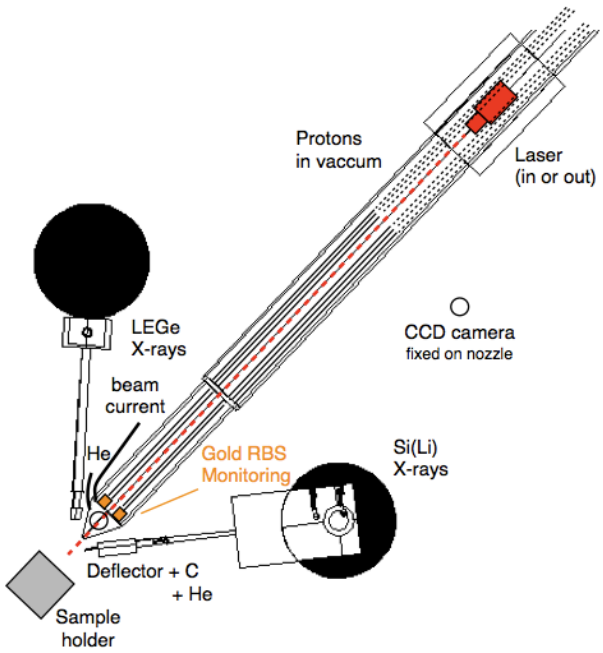

Figure B.8 The PIXE experimental set-up.

barrier PIPS Canberra detector positioned just in front of the extraction window.

The PIXE spectra were analyzed with the *GUPIXWIN* software [188]. This program consists of the non-linear least-squares fitting of PIXE spectra and the derivation of element concentrations from the X-ray peak areas in the spectrum.

The quantification of the elemental concentrations requires the calibration in energy of the spectrum, the adjustment of experimental parameters, such as absorber attenuation and relative detector efficiencies, and the consideration of matrix effects. Calibration and adjustment of the experimental parameters are achieved by fitting a standard of known concentration, such as a diorite, DR-N, standard. The matrix effects, which are related to the deceleration of the incident protons and the absorption of the emerging X-rays in the bulk sample, depend on the composition of the sample. Prussian blue powders were analyzed in the form of pressed pellets and were therefore considered as thick targets. The elemental concentration determination has been resolved by an *iterative matrix element solution* mode. The matrix corrections and invisible elements, *i.e.*, the light elements that are known to be present in the sample but whose X-rays are not visible, are taken into account. In Prussian blue, the cyanide ions, which are not detected,

were included in the elemental quantification as stoichiometrically tied to iron in the Fe:C:N ratio of 1:3:3 because soluble and insoluble Prussian blues contain approximately two iron ions for six cyanide groups. The water molecules were not taken into account for the quantification. Finally, the elemental concentrations are calculated by normalizing the total mass concentration to 100 %. The error on the elemental concentration is evaluated from the statistical error, which is the standard deviation based on Poisson statistics, and the fit error determined for the principal line from the final linear least squares fit [188].

No heavy Z-elements were detected in the PIXE spectra recorded at high-energy with the LEGe detector. Therefore, these high-energy spectra were not fitted because the low-energy PIXE spectra were sufficient to fully describe the elemental composition of Prussian blue.

B.2.6 Raman spectroscopy

Most of the Raman spectroscopy measurements were performed at the Laboratory of Analytical Chemistry at the University of Liège in collaboration with Prof. Bernard Gilbert. Measurements on genuine art samples were carried out at the Royal Institute for Cultural Heritage, Brussels, under the supervision of Dr. Jana Sanyova.

Basic principles

Raman spectroscopy is a vibrational spectroscopy based on the inelastic scattering of a monochromatic light, see Figure B.9. When a molecule is exposed to a monochromatic radiation of frequency ν_0 its diffusion spectrum consists both of an intense line at the frequency ν_0, which corresponds to the elastic Rayleigh scattering, and of two sets of weak lines on both sides of ν_0. These weak lines, with an intensity of less than 10^{-6} that of the Rayleigh intensity, are called Raman peaks and are characterized by frequencies $\nu_R = \Delta\nu = \nu \pm \nu_0$. Raman peaks with a negative shift are referred to as *Stokes scattering* whereas Raman peaks with a positive shift are referred to as *anti-Stokes*. Because there are fewer molecules in an excited state than in the ground state the anti-Stokes scattering is less intense than the Stokes scattering.

The Raman effect results from the electric dipolar interaction between monochromatic radiation and the molecules. The electric field, $\vec{E}$, of the monochromatic radiation of frequency ν_0 creates an induced dipole moment, $\vec{p}$, in the molecule, a dipole moment that oscillates at frequency ν_0 and is given by the expression

$$\vec{p} = [\alpha]\vec{E}, \tag{B.16}$$

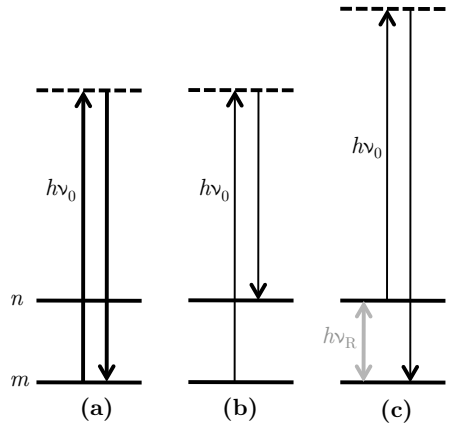

Figure B.9 Interaction between an incident photon characterized by an energy $h\nu_0$ and a molecule with two vibrational states m and n; **a**, the Rayleigh scattering, **b**, Stokes scattering, and, **c**, anti-Stokes scattering. Reproduced from [116].

where $[\alpha]$ is the *polarizability tensor*. The electric field, $\vec{E}$, oscillates at the frequency ν_0, and is thus given by

$$\vec{E} = \vec{E}_0 \cos 2\pi\nu_0 t. \tag{B.17}$$

Because the molecule is vibrating at the frequency ν_R, the polarizability tensor is modulated at this frequency and is given by the expression

$$[\alpha] = [\alpha]_0 + [\alpha'] \cos 2\pi\nu_R t, \tag{B.18}$$

where $[\alpha]_0$ is the polarizability tensor of the molecule in the ground state and $[\alpha']$ is the modulation amplitude. The insertion of equations B.17 and B.18 in equation B.16 yields

$$\vec{p} = ([\alpha]_0 + [\alpha'] \cos 2\pi\nu_R t)\vec{E}_0 \cos 2\pi\nu_0 t. \tag{B.19}$$

By applying elementary trigonometric relationships, $\vec{p}$ may be written as

$$\vec{p} = \vec{E}_0([\alpha]_0 \cos 2\pi\nu_0 t + \frac{1}{2}[\alpha'] \cos 2\pi(\nu_0 + \nu_R)t + \frac{1}{2}[\alpha'] \cos 2\pi(\nu_0 - \nu_R)t. \tag{B.20}$$

Equation B.20 clearly shows that the modulation of the induced dipole moment, $\vec{p}$, results in the emission of peaks at the frequencies, ν_0, *i.e.*, Rayleigh scattering, $\nu_0 + \nu_R$, *i.e.*, anti-Stokes scattering, and $\nu_0 - \nu_R$, *i.e.*, Stokes scattering.

The selection rules for active vibrations in a Raman spectrum are derived from quantum mechanics. A vibration is Raman-active *if the polarizability of the molecule is modified by the vibration.* In the case of a polyatomic molecule with a center of symmetry, the so-called *mutual exclusion rule* applies and active modes in Raman spectroscopy are inactive in infrared spectroscopy and vice-versa.

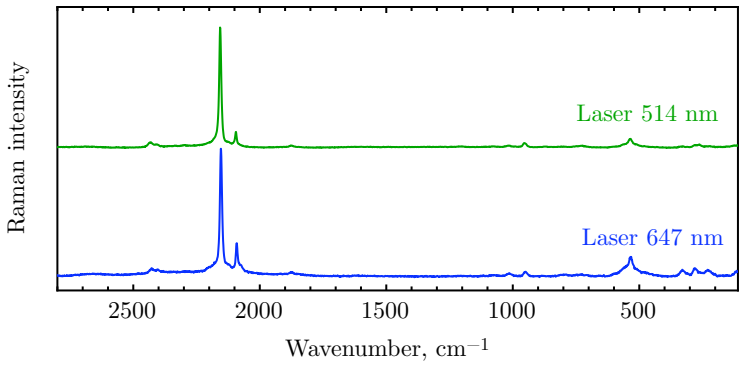

Figure B.10 Raman spectra of a commercial Prussian blue obtained with a 514 nm laser, green, and a 647 nm laser, blue.

Experimental spectrometer

The experimental set-up for Raman spectroscopy usually consists of an intense monochromatic source, such as a laser, an optical system used to collect the light scattered by the sample and an interferometric or dispersive spectrometer coupled with a sensitive detection system.

The instrument located at the Royal Institute for Cultural Heritage is a Renishaw inVia multiple laser dispersive Raman spectrometer equipped with a Peltier-cooled near-infrared enhanced, deep-depletion CCD detector (576×384 pixels) and a direct-coupled Leica DMLM microscope. A 785 nm laser made by Toptica Photonics XTRA, Graefelfing, Munich, Germany, was used. Neutral density filters can be used to reduced the laser power on the sample. The instrument is calibrated using the silicon peak.

The apparatus at the Laboratory of Analytic Chemistry and Electrochemistry is a home-made performance computerized Raman spectrometer. Samples were analyzed using either a He-Ne laser at a wavelength of 647 nm or an Ar laser at a wavelength of 514 nm. Raman spectra of a commercial Prussian blue obtained with both lasers are shown in Figure B.10. The 647 nm-laser enhances by resonance the Raman band intensities of Prussian blue, because Prussian blue absorbs light by electronic transitions in this spectral region. The choice of the laser also depends on the detector that is coupled to the laser. The detection efficiency varies with the type of detector and, furthermore, is not constant over the entire spectral range. The spectra were analyzed with the software developed by Prof. Gilbert. The baseline was corrected with a polynomial function.

B.2.7 Scanning electron microscopy

The scanning electron microscopy measurements were obtained with a JEOL JSM-7500F field-emission electronic scanning microscope located at the University of Namur, Belgium. Scanning electron microscopy coupled with energy-dispersive X-ray spectroscopy experiments on genuine cross-sections were carried out at the Royal Institute of Cultural Heritage, Brussels. Basic information on scanning electron microscopy can be found in the book by Goldstein *et al.* [189].

Basic principles

Scanning electron microscopy provides imaging and elemental analytical information on a nanometer to micrometer scale. The sample is irradiated by a sharply focused electron beam, which can either scan the surface of the sample to form images or be fixed to obtain an analysis at one spot. The interaction between the electrons and the sample produces a variety of signals, such as secondary electrons, backscattered electrons, and characteristic X-rays.

Secondary electrons are the low energy, less than 50 eV, electrons that are ejected of the sample by inelastic scattering interactions. These low-energy electrons originate within a few nanometers from the sample surface. The brightness of the signal depends on the number of secondary electrons reaching the scintillator-photomultiplier detector, and hence, on the surface topography. Secondary electrons can thus be used to form topographic images of the surface with a resolution approximating the size of the focused electron beam. In addition to the shadow relief effect of the secondary electron contrast, the three-dimensional appearance of the image is also a result of the large depth of field of the scanning electron microscope.

Backscattered electrons are the high-energy electrons in the electron beam, that are reflected or back-scattered by elastic scattering interactions with the atoms in the sample interaction volume. Backscattered electrons can also be used for imaging. Because heavy Z-elements in the sample backscatter electrons more strongly than light Z-elements, the imaging contrast results from the differences in atomic number and indicates areas with different chemical compositions.

The analysis of the characteristic X-rays that are emitted as a result of electron bombardment yields elemental information about a sample region of *ca.* 1 μm in diameter and 1 μm in depth under normal operating conditions. The emitted X-rays are usually collected by an energy-dispersive lithium drifted silicon Si(Li) solid-state detector, which can detect X-rays from all elements above atomic number 4 with a limit of detection in bulk material of approximately 0.1 wt % at the

typical beam current used for secondary electron imaging in the scanning electron microscopy. This specific use of the scanning electron microscopy is often referred to as the energy dispersive X-ray analysis. The quantification of energy dispersive X-ray spectra is possible but requires accounting for the matrix effects in the sample and the detector efficiency, which varies upon elements. The energy dispersive X-ray analyses presented in this thesis were only qualitatively interpreted.

Experimental microscope

A scanning electron microscope consists of an electron column and a control console. In the case of a field-emission scanning electron microscope, the electrons are produced by a field emission cathode, which is usually a wire fashioned into a sharp point and submitted to a negative potential. The electrons leave the cathode by quantum tunnelling effect through the potential barrier. They are then accelerated by the electron gun to an energy in the range of 0.1 to 30 keV and focused through a system of electron lenses before reaching the sample surface. A deflection system inside the final lens shifts the beam to a series of discrete locations along a line in order to form an image. The electron beam is generated in an electron column at a pressure of approximately 10^{-4} Pa.

The scanning electron micrographs presented in this thesis were obtained with an emission current of 10 µA and a 15 keV electron beam. The micrographs were recorded in the secondary electron emission mode. The contrast is thus related to the topography of the sample surface. Powder Prussian blue samples were deposited on a double sided carbon tape on the sample holder and introduced in the microscope. Because of the semiconducting behavior of Prussian blue, no sample charging was observed during the measurements. In contrast, cross-sections embedded in resin were non-conductive and therefore, were sputter-coated with a gold layer of a few nanometers in an argon atmosphere in order to ensure conductivity.

B.2.8 Thermogravimetric analyses

Thermogravimetric analysis is a thermal technique for determining the composition of a material by measuring the amount and rate of mass change as a function of temperature in a controlled atmosphere. Differential scanning calorimetry measures the change of the difference in the heat flow rate to the sample and to a reference sample as a function of temperature.

The thermogravimetric analyses coupled with differential scanning calorimetry analyses were carried out by Magali Brisbois with a Netzsch STA 447 C instrument

located in the Chemistry Department at the University of Liège. The Prussian blue powder samples were placed in an alumina crucible and heated with a constant heating rate of 2°C/min in air. The TGA curves presented in this thesis were normalized, *i.e.*, divided by the sample mass, so that they begin at 100 %.

B.2.9 UV-visible spectroscopy

UV-visible spectroscopy is a suitable technique to characterize the optical and electronic properties of samples because the energy range of UV-visible radiation matches the energy range required to induce electronic excitations between molecular orbitals. UV-visible spectra appear as a continuous absorption band because the vibrational and rotational levels of the molecular orbitals are superimposed upon the electronic levels, producing a combination of overlapping lines.

In UV-visible absorption spectroscopy, the absorbance, A_λ, of a compound at a selected wavelength, λ, is given by the Lambert-Beer law [190]

$$A_\lambda = \epsilon_\lambda l C, \tag{B.21}$$

where A_λ is the unitless absorbance, ϵ_λ is the wavelength dependent molar absorption coefficient in units of L $\text{mol}^{-1}\text{cm}^{-1}$, l is the optical path length of the measurement in cm, and C is the concentration in mol/L. The Beer-Lambert law is strictly valid only for monochromatic radiation. Furthermore, at higher concentration, the molar absorption coefficient, ϵ is no longer independent of the concentration, C, because of interactions between absorbing molecules in the solvent [191].

UV-visible reflectance spectroscopy measures the reflectance as a function of wavelength, *i.e.*, the intensity ratio of the surface-reflected electromagnetic radiation to the incident radiation. Two types of reflection can be distinguished, specular[4] reflection, which is associated with smooth polished surfaces, and diffuse reflection, which is associated with reflection from mat or dull texture surfaces, such as powders or paint layers [192]. The diffuse reflected signal is usually attenuated by two phenomena, absorption and scattering, and is best described by the Kubelka-Munk theory. The latter links the absorption and scattering through the ratio of the absorption coefficient, K, and the scattering coefficient, S, to the reflectance, R, see **Appendix C** for details. A quantitative analysis of reflectance spectra necessarily requires using the Kubelka-Munk theory. However, in this thesis, the UV-visible reflectance spectra were only used to characterize the color and

[4]Specular reflection implies that the angle of incidence is equal to the angle of reflection.

the change in color. Such a qualitative interpretation does not require the application of Kubelka-Munk corrections.

UV-visible absorption spectroscopy experiments were carried out at the laboratory of biomedical spectroscopy in the Physics Department at the University of Liège, in collaboration with Dr. Pierre-Henry Guelluy. The instrument is a Kontron Uvikon 941 double-beam spectrophotometer. Prussian blue colloidal solutions of 0.001 M were prepared by dispersing appropriate amount of powdered Prussian blue in 10 mL of deionized water. The solutions were then placed for fifteen minutes in ultrasonic bath. Each solution was finally poured in a quartz cell. The percentage of radiation that is absorbed by the sample was recorded as a function of wavelength, between 350 and 900 nm.

For UV-visible reflectance spectroscopy, two types of instruments were employed, a BYK-Gardner color guide and a StellarNet EPP2000C UV/visible reflectance spectrometer. The BYK-Gardner color guide has a $45°/0°$ geometry and a 4 mm aperture. A visible spectrum was recorded between 400 and 700 nm with a resolution of 20 nm, and automatically converted to the Commission Internationale de l'Eclairage 1976 unitless L^*, a^*, and b^* parameters by using the standard illuminant D65 as a reference. These parameters correspond to the lightness, red-greenness, and yellow-blueness, respectively, of the color and are derived from the XYZ tristimulus values of a reference white object and the colored object [135]. In order to evaluate the degree of fading of a sample, the color difference, ΔE^*, between the unexposed and the aged exposed portion of the sample can be calculated from

$$\Delta E^* = [(\Delta L^*)^2 + (\Delta a^*)^2 + (\Delta b^*)^2]^{1/2}. \tag{B.22}$$

Typically, a ΔE^* color difference of less than one is imperceptible to the human eye.

The UV/visible reflectance spectrometer used was a StellarNet EPP2000C spectrometer equipped with a CCD detector. The optical-fiber probe consists of six illuminating fibers and a single fiber that collets the reflected light. The sample is illuminated over a surface area of approximately 4 mm^2 at an angle of $45°$ in order to avoid direct reflection; a Halon D50 white reference was used for calibration. The spectra were recorded in reflection mode between 350 and 880 nm, with a resolution of 1 nm. The absorbance spectra were then calculated with the SpectraWiz software.

B.2.10 X-ray powder diffraction

The X-ray powder diffraction experiments were carried out in the Geology Department at the University of Liège. The measurements were performed by Dr. Frédéric Hatert.

Basic principles

X-ray diffraction is based on the interference of coherent X-rays that are scattered by the electron clouds of atoms in the sample. The analysis of the diffraction pattern, *i.e.*, the spatial distribution of the diffracted intensity, provides information on the structure of the studied compound.

The direction of the diffracted radiation is given by Bragg law. A set of reticular planes with Miller indices (h, k, l) is represented in Figure B.11. Simple trigonometry shows that the path length difference between two scattered X-rays is

$$AB + CB = 2d \sin\theta. \tag{B.23}$$

To ensure coherent scattering this path length difference must be equal to an integer number of wavelength, *i.e.*,

$$AB + CB = n\lambda \tag{B.24}$$

where λ is the wavelength of the incident diffracted X-ray radiation and d, the inter-reticular distance between two (h, k, l) planes.

In the case of a cubic crystal, such as Prussian blue, the inter-reticular distance, d, is given by

$$d = \frac{a}{\sqrt{h^2 + k^2 + l^2}}. \tag{B.25}$$

The intensity, I, of the diffraction lines depends on several parameters, namely the intensity scattered by an electron with the polarization factor, P, the Lorentz factor, L, which is a function of the geometry of the experiment, the structure factor, F, calculated from the atomic positions, the Debye factor, which is caused by the thermal excitation of electrons around their equilibrium position, the multiplicity factor, j_k, of reflection k, and the absorption factor of the radiation in the crystal [94][194]. The intensity, I, is related to these parameters by

$$I \propto \frac{1}{R} D \frac{1}{\mu^*} \frac{V}{v^2} j_k L p |F|^2, \tag{B.26}$$

where R is the distance between the sample and the detector, V, the irradiated volume of the sample, v, the lattice volume, and μ^*, the linear absorption coefficient.

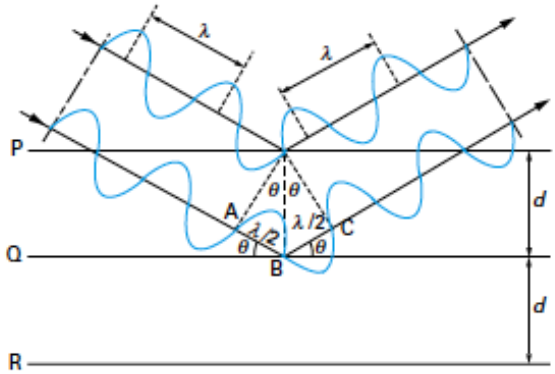

Figure B.11 Interference of waves scattered by atoms in a crystal: Bragg law demonstration [193].

Experimental diffractometer

A diffraction experiment consists in measuring the diffracted intensity as a function of the diffraction angle. The instrument used in this thesis is a PANalytical PW-3710 diffractometer. It is equipped with an iron K_α X-ray tube with a wavelength of 1.9373 Å.[5]

The diffraction pattern contains the structural information of the sample but also the instrumental contribution. Therefore the sample profile, $f(x)$, must be deconvoluted from the experimental profile, $h(x)$, and instrumental profile, $g(x)$,

$$h(x) = f(x) \otimes g(x) = \int_{-\infty}^{+\infty} f(y)g(x-y)\mathrm{d}y. \tag{B.27}$$

There are several deconvolution methods. Only the method based on an *a priori* knowledge of the profile shape function is presented here. Nowadays the profile shape function for a X-ray diffraction line is usually taken as a simple analytical function, such as a *pseudo-Voigt* profile [195][196]. This is an approximation of the normalized Voigt profile, which is the convolution product between a Lorentzian function, L, and a Gaussian function, G. The pseudo-Voigt profile is described as follows

$$\Omega(2\theta) = \eta L(2\theta, H) + (1-\eta)G(2\theta, H), \tag{B.28}$$

where η is the mixing parameter and 2θ, the diffraction angle and H, the full

[5] Actually the iron K_α tube emits iron $K_\alpha 1$ as well as iron $K_\alpha 2$ radiation of wavelength of 1.93604 and 1.93998 Å in an intensity ratio of 0.5.

width at half maximum.

Using a pseudo-Voigt profile makes the deconvolution of equation B.27 easier. Indeed, due to the convolution properties of Lorentzian and Gaussian functions,

$$H_L^f = H_L^h - H_L^g \tag{B.29}$$

and

$$(H_G^f)^2 = (H_G^h)^2 - (H_G^g)^2, \tag{B.30}$$

where H_L and H_G are the Lorentzian and Gaussian full width at half maximum of the sample profile referred to as f, the experimental profile, h, and the instrumental profile, g.

The decomposition of the X-ray powder diffraction patterns with a pseudo-Voigt profile function was carried out by using the software *Peakoc* developed by Masson [97]. Each diffraction line was then characterized by a 2θ diffraction angle, a full-width at half-maximum, H^h, and a mixing parameter, η.

The full width at half maximum of the Lorentzian and the Gaussian components, H_L^h and H_G^h, can be extracted from the integral width of the pseudo-Voigt profile, H_{pV}^h, by the empirical relations [196],

$$\frac{H_L^h}{H_{pV}^h} = 0.72928\eta + 0.19289\eta^2 - 0.07783\eta^3 \tag{B.31}$$

and

$$\frac{H_G^h}{H_{pV}^h} = (1 - 0.74417\eta - 0.24781\eta^2 - 0.00810\eta^3)^{1/2}. \tag{B.32}$$

The full width at half maximum for both Gaussian and Lorentzian experimental contributions, H_L^g and H_G^g, at a given angle were calculated from the modified Caglioti-type equations,

$$H_G^g = [U.\tan^2\theta + V\tan\theta + W]^{1/2} \tag{B.33}$$

and

$$H_L^g = X\tan\theta + Y/\cos\theta + Z. \tag{B.34}$$

The parameters U, V, W, X, Y, and Z characteristic of the PANalytical diffractometer used for the measurements were determined by Rietveld refinement on the standards NAC, $Na_2Ca_3Al_2F_{14}$ and LaB_6. The instrumental Gaussian and Lorentzian profile functions are shown in Figure B.12.

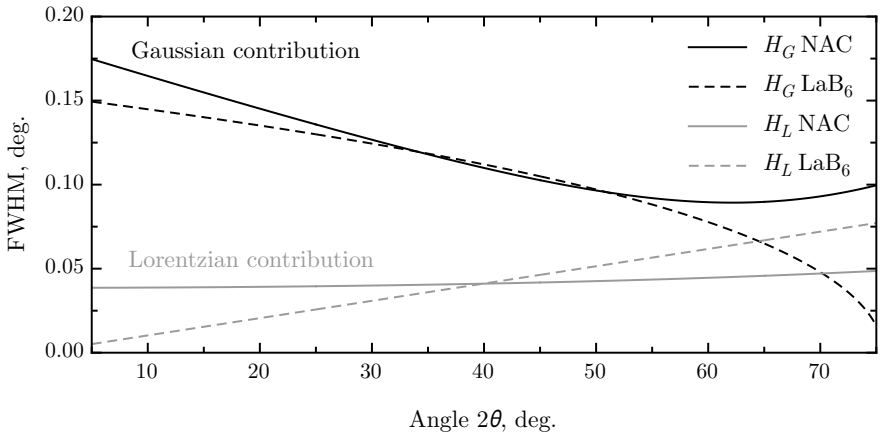

Figure B.12 Instrumental resolution Gaussian and Lorentzian full widths at half maximum, H_G and H_L, of the PANalytical diffractometer determined on the NAC, $Na_2Ca_3Al_2F_{14}$, and LaB_6 standards.

The Gaussian and Lorentzian broadening of the sample profile, H_G^f and H_L^f, were obtained by using equations B.29 and B.30. Then, the pure full width at half maximum of the pseudo-Voigt profile, H_{pV}^f, was calculated from H_G^f and H_L^f by using the polynomial approximation

$$H_{pV}^f = [(H_G^f)^5 + 2.69269(H_G^f)^4 H_L^f + 2.42843(H_G^f)^3(H_L^f)^2 + 4.47163(H_G^f)^2(H_L^f)^3 + 0.07842 H_G^f (H_L^f)^4 + (H_L^f)^5]^{1/5}.$$

Finally, the pure integral width of the pseudo-Voigt profile, β_{pV}^f, is related to the full width at half maximum, H_{pV}^f, by the relation [195]

$$\beta_{pV}^f = \pi \frac{H_{pV}^f/2}{[\eta + (1-\eta)(\pi \ln 2)]^{1/2}}. \tag{B.35}$$

The Williamson-Hall method and the Scherrer's relation are then applied on the pure integral width, β_{pV}^f, see **Chapter 2, Section 2.2.4**.

B.3 Synchrotron radiation-based techniques

Because of the specific characteristics of the synchrotron radiation, *i.e.*, high brilliance, high flux, and tunable energy, the synchrotron radiation-based techniques provide information that could not be obtained by laboratory techniques. In the recent years interest for the use of synchrotron radiation in archaeometry has

grown because synchrotron radiation is particularly suitable to study paintings and cultural heritage objects, because of their inherent complexity [197] [198].

A brief description of the synchrotron radiation and synchrotron facility design is first given. Next, the two synchrotron radiation-based techniques used in this thesis, *i.e.*, X-ray absorption spectroscopy and high-energy X-ray diffraction, are presented.

B.3.1 Synchrotron radiation

Synchrotron were originally used to accelerate charged particles up to relativistic speeds, *i.e.*, speeds close to the speed of light, in order to perform high-energy physics experiments. In 1947 particle physicists observed that accelerated electrons emitted an electromagnetic radiation tangentially to the electron beam path, as they were directed around curved paths by magnetic fields. This radiation was called *synchrotron radiation*, since it was observed for the first time in a synchrotron. First considered as a nuisance because it steals energy from the particle beam, synchrotron radiation was then found in the 1960's to be extremely useful for X-ray experiments.

As a result of the relativistic speed of the charged particles, the emitted synchrotron radiation has particular properties. It is highly directional and its electromagnetic spectrum is shifted to much higher energies. Moreover, synchrotron radiation is characterized by an extremely high flux and brilliance. The term *flux* represents the total number of photons/sec in a beam whereas the *brilliance* is expressed in photons/sec/(source area mm^2)/(source angular divergence $mrad^2$). This quantity is an invariant in ideal optical systems. The high flux of synchrotron radiation allows fast experiments and its brilliance, which is many orders of magnitude greater than that of conventional X-ray sources, results in a photon beam with a small size and a small angular divergence. Consequently the photons can be easily collected and focussed by X-ray optics of reasonable size, such as mirrors and monochromators. Moreover the synchrotron light source offers a high stability of the beam and allows pulsed time structure resolved experiments, because of the bunch structure of the electron beam.

A synchrotron light source consists of an injection system and a storage ring. The general scheme and details of the storage ring of the European Synchrotron Facility Research, ESRF, Grenoble, are shown in Figure B.13. The charged particles are usually electrons because they radiate much more efficiently for a given particle energy than the much more massive protons. The injection system generally comprises a linear accelerator, *linac*, and a booster synchrotron. The electrons

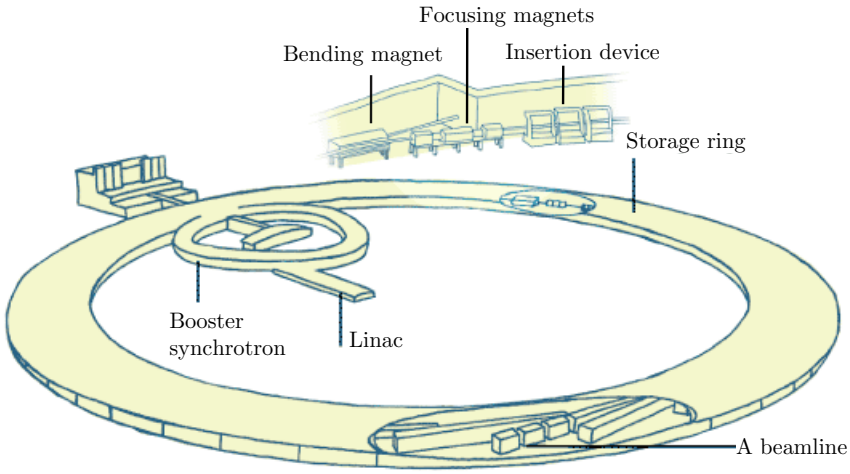

Figure B.13 General scheme of the ESRF, Grenoble. The electrons are accelerated in the linac and in the booster synchrotron up to an energy range of 6 GeV. The high-energy electrons are then transferred to a storage ring of 844 meters in circumference. Adapted from [199].

emitted by an electron gun are first accelerated in the linac and then transmitted to the booster synchrotron. The kinetic energy of the electron beam is increased as it passes through conducting cavities, *RF cavities*, in which a radio frequency electromagnetic standing wave is maintained. The series of the RF cavities have a phase relation between them such that the average phase advance of the radio frequency field equals the velocity of the accelerated particles, providing an accelerating field. The groups of electrons, called *bunches*, are finally transferred in the storage ring. The storage ring consists of evacuated pipes under ultrahigh vacuum, bend magnets, and insertion devices. The relativistic electrons travel in straight lines until they encounter a strong magnetic field in the vertical direction produced by bend magnets, a magnetic field that causes the electrons to move in arc with a radius curvature on the order of tens of meters, after which they continue travelling in straight line until the next bend magnet. The storage ring is thus not circular but rather polygonal, with rounded corners. After radiation, the electron beam pass through RF cavities to replenish the particle energy and focusing magnets, in order to keep the electron beam size as small as possible. In addition to the bend magnets, required to deflect the beam around the storage ring, another type of magnetic structure, called *insertion devices* can be inserted into the straight sections between the bend magnets. These insertion devices, such as wigglers and undulators, consist of periodic arrays of magnets which force the

electron beam to oscillate back and forth, resulting in the emission of enhanced synchrotron radiation. Insertion devices are optimized to produce radiation that fulfills experimental requirements. In third generation synchrotron light sources, such as the ESRF or Soleil, the insertion devices are an integral part of the design, in contrast with second generation synchrotron light sources. The X-rays produced by the electron beam are finally directed towards beamlines, which are dedicated for a specific technique or type of research. A beamline includes an optics cabin, in which the X-ray beam can be collimated, filtered, splitted, monochromated, shuttered, or focussed using X-ray optics, an experimental cabin, and a control cabin, where the user sets up and controls the experiment, collects, and evaluates data. Further details on the synchrotron design and operation can be found in the books of Bunker [113] and of Winick [200].

B.3.2 High-energy synchrotron X-ray diffraction

The high-energy synchrotron X-ray diffraction experiments were performed at the beamline ID11 at the ESRF in Grenoble, France and at the beamline CRISTAL, at Soleil, Paris, in collaboration with the Department MCMF at the Institut Néel, Grenoble.

Pair distribution function

Conventional structure determination, such as the Rietveld method, is based on the analysis of the intensities and positions of Bragg reflections and only provides a long range average structure of the crystal. However, many materials, such as Prussian blue, have an inherent disorder and, consequently, their local atomic arrangements can not be accurately described by the average structure. This disorder causes deviation from the average structure that results in the occurrence of diffuse scattering [201]. This diffuse scattering contains information about two-body interactions and can be studied by the pair distribution function analysis. Different formalisms and definitions of the pair distribution function exist. The discussion herein is based on the formalism developed by Billinge, Egami, and Proffen, which is used in the PDFFIT and PDFGui softwares [109][202].

The pair distribution function is obtained from the powder diffraction data by a Fourier transform of the normalized scattering intensity $S(Q)$,

$$G(r) = 4\pi r[\rho(r) - \rho_0] = \frac{2}{\pi}\int_0^\infty Q[S(Q) - 1]\sin Qr\mathrm{d}Q, \tag{B.36}$$

where $\rho(r)$ is the microscopic pair density, ρ_0 the atomic number density, and Q is the magnitude of the scattering vector. For elastic scattering, $Q = 4\pi\sin\theta/\lambda$,

where 2θ is the scattering angle and λ the wavelength of the radiation used.

The function $G(r)$ in equation B.36 refers to as the *reduced pair distribution function*. The pair distribution function is related to the latter function by

$$g(r) = 1 + \frac{G(r)}{4\pi\rho_0}. \tag{B.37}$$

In practice, the reduced pair distribution function, $G(r)$, is the function that is extracted from X-ray diffraction data and then fitted.

Extraction and refinement of the PDF

In order to obtain the experimental atomic pair distribution function, $G(r)$, the normalized scattering intensity, $S(Q)$, must be first extracted from the X-ray diffraction data. The observed X-ray scattering intensity, $I^{obs}(Q)$, results from the sum of several scattering contributions [203]

$$I^{obs}(Q) = PAG[I^c(Q) + I^i(Q) + I^m(Q)] + B, \tag{B.38}$$

where P, A, G and B account for polarization, absorption, geometrical, and background corrections, respectively, I^c is the coherent scattering, I^i is the incoherent scattering, and I^m is the multiple scattering.

The normalized scattering intensity, $S(Q)$, contains the coherent scattering intensities from the sample and is given by the relation [203][204]

$$S(Q) = 1 + \left[\frac{I^c(Q) - \langle|b|^2\rangle}{|\langle b\rangle|^2}\right], \tag{B.39}$$

where $\langle|b|^2\rangle = \sum_{i=1}^{n} a_i|b_i(Q)|^2$ and $\langle b\rangle = \sum_{i=1}^{n} a_i b_i(Q)$, in which $b_i(Q)$ is the scattering factor for atom i, which is dependent on the scattering angle, 2θ, for X-rays, and a_i is the atomic fraction of atom i.

The pair distribution function is extracted by using the PDFgetX2 software [108]. Figure B.14 summarizes the different steps of the PDF extraction from the scattering signal obtained on a commercial Prussian blue sample. First the scattering signal coming from the container is subtracted from the total scattering signal, see Figure B.15.a. The scattering intensity, $I(Q)$, can then be corrected to exclude incoherent and inelastic contributions, absorption effects, and multiple scattering. Next the scattering intensity is normalized in order to obtain the function $S(Q)$, see Figure B.15.b. The normalization by the factor $|\langle b\rangle|^2$ results in a data amplification at high Q. The function $F(Q) = Q[S(Q) - 1]$ is calculated

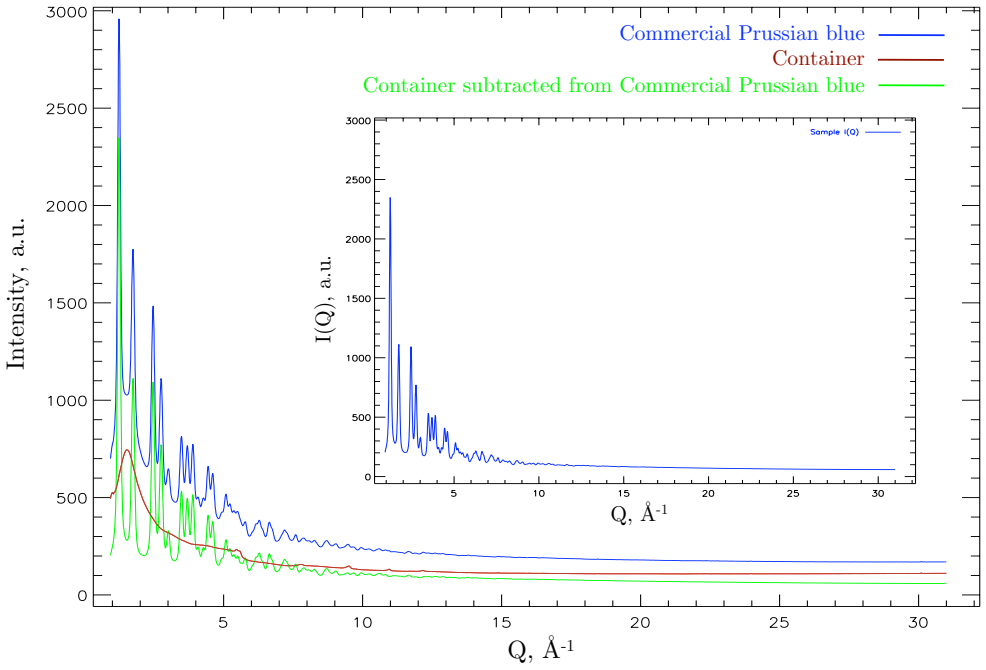
Commercial Prussian blue
Container
Container subtracted from Commercial Prussian blue
Intensity, a.u.
Q, Å-1
Sample I(Q)
I(Q), a.u.
Q, Å-1

(a)

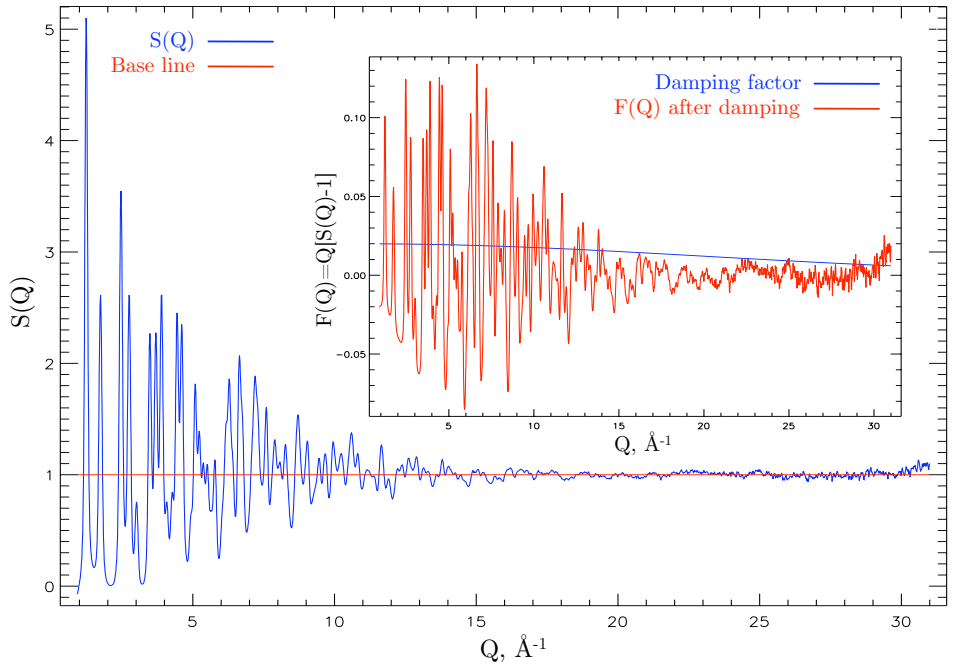
S(Q)
Base line
Damping factor
F(Q) after damping
S(Q)
F(Q)=Q[S(Q)-1]
Q, Å-1
Q, Å-1

(b)

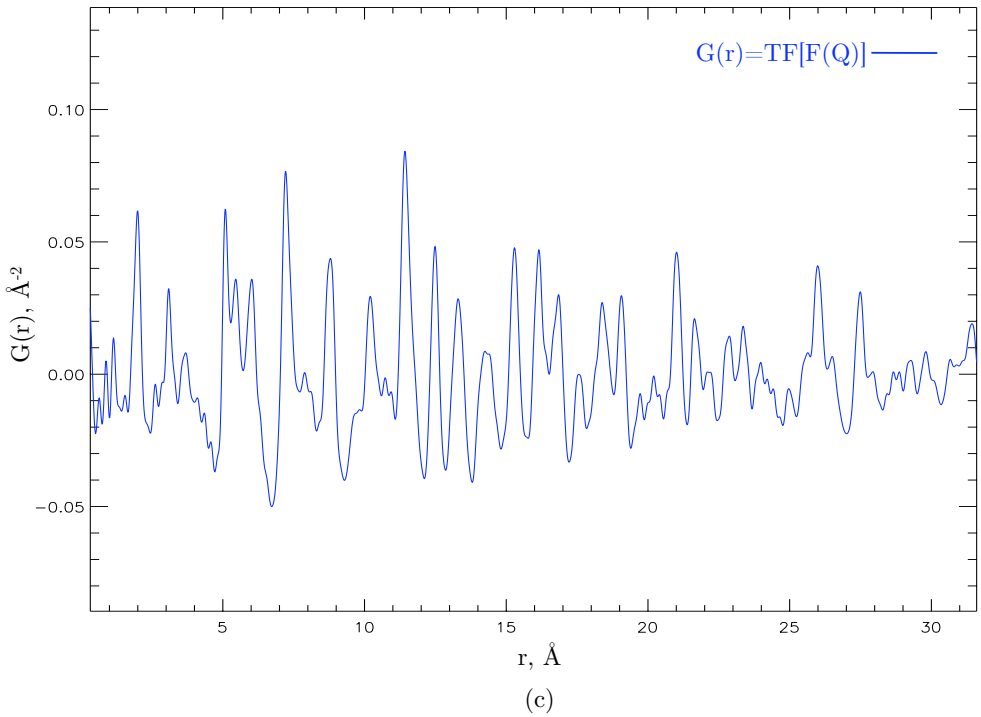

Figure B.14 The PDF extraction from the total scattering signal of a Prussian blue sample encapsulated in a capillary. **a**, Subtraction of the scattering signal of the container from the total scattering signal, **b**, normalization of the scattering intensity and calculation of the function F(Q), and **c**, Fourier transform of the damped $F(Q)$ function with a $Q_{max} = 30$ Å^{-1}.

and can be damped by a Gaussian function of adjustable width, 20 Å^{-1} in this case, centered around zero, in order to reduce the statistical noise at high Q. Finally the pair distribution function, $G(r)$, is obtained by Fourier transform of the damped $F(Q)$ to a maximum Q-value, Q_{max}, of 30 Å^{-1}, see Figure B.15.c.

The software PDFGui [109] was used for the PDF refinement. This software is actually a modified and re-designed version of the profile fitting refinement program PDFfit [202]. The refinement is based on the least squares minimization in the direct space of the experimental PDF with a structural periodic model. This structural model of the pair distribution function can be seen as a bond-length distribution between all pairs of atoms i and j within the crystal, up to a maximum distance. Each contribution is weighted according to the product of the

scattering factor of the atoms i and j. This model is calculated by [109]

$$G_{calc}(r) = \frac{1}{r} \sum_{i} \sum_{j \neq i} \left[\frac{b_i b_j}{\langle b \rangle^2} \delta(r - r_{ij}) \right] - 4\pi r \rho_0, \tag{B.40}$$

where b_i is the scattering power of atom i, $\langle b \rangle$ is the average scattering power of the sample, r_{ij} is the distance between atoms i and j.

The structural, atomic, and experimental parameters can be refined to adjust the model to the experimental data. In the PDF analysis of the Prussian blue samples, the lattice parameter, a, the scale factor for each phase, and the position, the occupancy, and anisotropic thermal parameters for each atom in each phase were refined. The resolution damping factor was determined on a LaB_6 standard sample and was fixed for the refinement of the Prussian blue samples. This factor accounts for the progressive decrease of the amplitude of the PDF peaks at larger distances due to the resolution of the diffraction experiment.

Experimental facilities

The pair distribution function is best obtained by using high energy synchrotron radiation, which permits to record the scattering signal at high Q. The PDF experiment was carried out at the beamline ID11, ESRF, Grenoble. This beamline allows one to work at high flux at an energy range between 29 to 140 keV. It is equipped with a Si(111) double crystal monochromator and a X-ray transfocator. The beam size was approximately 50×200 µm area. The Prussian blue samples were stored in quartz capillaries of 0.3 mm in diameter and placed in front of the detector. The X-ray energy was 99.428 keV, *i.e.*, a wavelength of 0.124968 Å. A total of 81 2D diffraction images per sample, with a acquisition time of 20 seconds per image, were collected. The 2D diffraction images were then averaged and integrated into a linear scattering signal with the software fit2D [107]. The distance between the sample and the detector was determined with a LaB_6 standard.

The X-ray powder diffraction data used for the Rietveld refinement were collected at the CRISTAL beamline, Soleil, Paris. The beamline is located at a undulator port and provides a beam in the energy range of 4 to 30 keV, with a relative energy resolution, $\Delta E/E$, of approximately 10^{-4}. The beam scross-section on the sample is *ca.* 450×100 µm2. The X-ray powder diffraction data on the commercial soluble, C02, and insoluble, C03, were collected at a wavelength of 0.442930 Å.

B.3.3 X-ray absorption spectroscopy

The iron K-edge X-ray near edge absorption spectroscopy, XANES, and extended X-ray fine structure spectroscopy, EXAFS, experiments were performed at the DUBBLE Dutch-Belgian beamline at the European Synchrotron Radiation Facility, in Grenoble, France. The measurements and the data interpretation were carried out in collaboration with the X-ray Microspectroscopy and Imaging, XMI, research group of the Department of Analytical Chemistry at the Ghent University.

Basic principles

X-ray absorption spectroscopy consists of measuring the absorption coefficient $\mu(E)$ as a function of X-ray energy, near the absorption edge of a given element present in the sample. The intense incident X-ray photon ejects a photoelectron from an inner atomic orbital, a photoelectron whose wave function is scattered by neighboring atoms, see Figure B.15. Interferences between the ejected and scattered fractions of the photoelectron wave-function occur and result in an energy-dependent variation in the X-ray absorption coefficient, $\mu(E)$. The measurement and analysis of the energy dependence of the X-ray absorption coefficient provide information on the local structure around the absorbing atom or ion. An expression of the EXAFS formula is derived below.

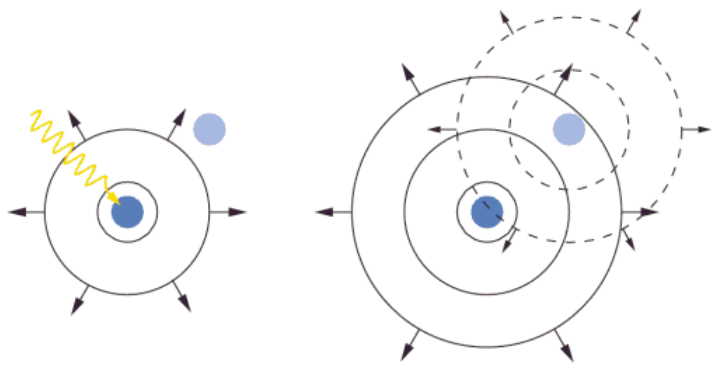

Figure B.15 The origin of EXAFS. An X-ray photon is absorbed by an atom, resulting in promotion of a core-level electron to an unoccupied continuum state. As the electron wave, represented in solid circles, propagates out from the excited atom, it can be scattered by neighboring atoms. The scattered waves, in dashed circles, interfere with the outgoing waves, thereby modulating the absorption cross-section as a function of photon energy. Reproduced from [205].

When an atom absorbs an X-ray photon with an energy larger than the binding energy of a core electron, this electron is transferred to the continuum. If the energy of the X-ray photon, $\hbar\omega$, is only slightly larger than the binding energy, E_0, of the core electron, the absorption involves only one electron. The kinetic energy, E_e, of the photoelectron is thus $E_e = \hbar\omega - E_0$.

The absorption probability, μ, of a transition between a core level and the final states that is induced by a time-dependent perturbation, must be evaluated. In the following the discussion is restricted to the K-edge absorption, for which the initial state is the deep $1s$ core level. The Fermi golden rule states that the absorption cross-section, $\mu(\hbar\omega)$, is proportional to the square of the modulus of the transition amplitude, *i.e.*,

$$\mu(\hbar\omega) = C^{st}|\langle\psi_i|\hat{e}\cdot\vec{r}e^{i\vec{\kappa}\cdot\vec{r}}|\psi_f\rangle|^2\rho(E_f - E_i - \hbar\omega), \tag{B.41}$$

where $|\psi_i\rangle$ and $|\psi_f\rangle$ are the initial and final electron wave functions of energy E_i and E_f, respectively, ρ is the density of states, $\hat{e}\cdot\vec{r}e^{i\vec{\kappa}\cdot\vec{r}}$ represents the interaction between the electromagnetic field and the electrons with $\hat{e}$, the X-ray electric polarization vector and $\vec{\kappa}$, the wave vector given by the expression $\vec{\kappa} = \vec{p}/\hbar$, where $\vec{p}$ is the X-ray photon momentum, and, finally, $\hbar\omega$ is the X-ray energy.

The matrice element $\langle\psi_i|\hat{e}\cdot\vec{r}e^{i\vec{\kappa}\cdot\vec{r}}|\psi_f\rangle$ can be written as

$$\langle\psi_i|\hat{e}\cdot\vec{r}e^{i\vec{\kappa}\cdot\vec{r}}|\psi_f\rangle \approx \langle\psi_i|\hat{e}\cdot\vec{r}|\psi_f\rangle + i\langle\psi_i|(\hat{e}\cdot\vec{r})(\vec{\kappa}\cdot\vec{r})|\psi_f\rangle + \ldots. \tag{B.42}$$

The first term is the dipolar term and the second one, the quadrupolar term. In the *dipolar approximation*, the quadrupolar term is neglected, because it is much smaller than the dipolar term. The equation B.41 thus becomes

$$\mu(\hbar\omega) = C^{st}\sum_{i,f}\langle\psi_i|\hat{e}\cdot\vec{r}|\psi_f\rangle|^2\delta(E_f - E_i - \hbar\omega), \tag{B.43}$$

where $\delta(E_f - E_i - \hbar\omega)$ is the Dirac function indicating the conservation of energy.

As previously stated the initial state, $\langle\psi_i|$, is the $1s$ core level. Such a deep core level is screened by the other higher energy electron shells and can be assumed to be independent of the local structure around the absorbing atom. Other weakly bound electrons contribute to a lesser extent to the absorption. The final state, $|\psi_f\rangle$, *i.e.*, the free electron wave function, is less trivial to evaluate.

The EXAFS oscillations are obtained by measuring the absorption cross-section

$$\mu(E_e) = \mu_0(E_e)[1 + \chi(E_e)], \tag{B.44}$$

where E_e is the kinetic energy of the photoelectron, $\mu_0(E_e)$, the absorption cross-section of the isolated atom, and $\chi(E_e)$, the function that describes the EXAFS oscillations.

The function, $\chi(E_e)$, reflects the modulation of the absorption coefficient resulting from the scattering by the neighboring atoms or ions. In the single scattering approximation and for K-edge excitations, χ is given as a function of the electron momentum, $k = \sqrt{(}2m(E - E_0)/\hbar^2)$, by the expression:

$$\chi(k) = -S_0^2 \sum_i \frac{3\cos^2\theta_i}{kr_i^2} |f_i(k)| e^{-2r_i/\lambda_e} \sin[2kr_i + 2\delta_1(k) + arg(f_i(k))], \quad \text{(B.45)}$$

where S_0^2 is a parameter that accounts for the loss of coherence resulting from multi-electron processes, r_i is the vector connecting the absorber to the scatterer, θ_i is its angle with the X-ray polarization vector $\hat{e}$, $|f_i(k)|$ is the complex electron backscattering amplitude, λ_e is the mean free path of the photoelectron, and δ_1 is the partial wave phase shift resulting from the scattering by the potential of the central absorbing atom.

Equation B.45 is referred to as the *standard EXAFS equation* and takes into account the contribution of each atom i at a relative distance r_i from the absorbing atom in the EXAFS oscillations.

Atoms of the same type situated at approximately the same distance from the absorbing atom form *coordination shells*. Equation B.45 can thus be rewritten as

$$\chi(k) = -\sum_j \left(\frac{S_0^2(k) e^{-2R_j/\lambda_e}}{kR_j^2} N_j |f_j(k)| e^{-2k^2\sigma_j^2} \right) \sin[2kR_j + 2\delta_1(k) + arg(f_j(k))], \quad \text{(B.46)}$$

where N_j is the number of atoms in the j^{th} coordination shell, and σ_j^2 is the mean square variation in distances around the average R_j, between the absorbing atom and atoms in the j^{th} shell. The factor $e^{-2k^2\sigma^2}$ is referred to as the *Debye-Waller* factor and accounts for disorder.

In conclusion, the EXAFS equation provides information about the coordination number, N_j, the bond distances, R_j, and the structural disorder, σ_j^2. The extraction of this information implies the knowledge of the phase shift, $\phi(k) = 2\delta_1(k) + arg(f_j(k)$, the backscattering amplitudes, $|f_j(k)|$, and the mean free path, λ_e, in equation B.46. Fortunately, in the case of an identical absorber-scatterer pair, the backscattering amplitude, and phase shifts are chemically transferable from a reference compound to the compound of interest [206].

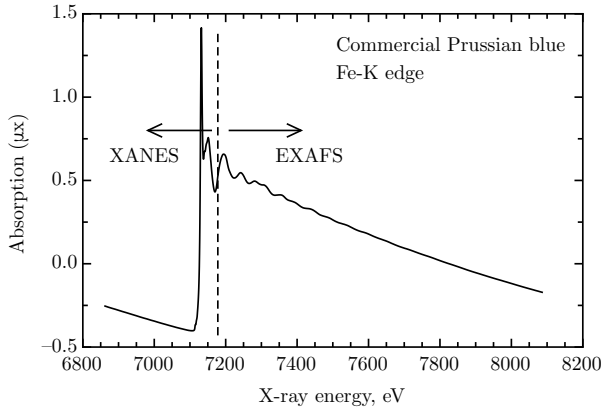

Figure B.16 Raw iron K-edge XAS signal of a commercial Prussian blue. By convention, the XANES energy range extends from *ca.* 50 eV below to *ca.* 50 eV above the absorption edge and the EXAFS energy range extends from *ca.* 50 eV to a few hundred eV above the absorption edge.

Data analysis

X-ray absorption spectroscopy, XAS, consists of two parts, the X-ray absorption near-edge spectroscopy, XANES, and the Extended X-ray Absorption Fine Structure, EXAFS, spectroscopy. Data extraction and analyses of XANES and EXAFS are separately performed. Figure B.16 shows the experimental XAS signal given by a commercial Prussian blue. By convention, the XANES energy range extends from *ca.* 50 eV above the edge and the EXAFS energy range extends from *ca.* 50 eV to a few hundred eV above the absorption edge.

Both XANES and EXAFS data reduction and analysis were performed with the XDAP software [207] under the supervision of Dr. Geert Silversmit, from the Ghent University. The starting fitting model for Prussian blue was determined by Dr. Geert Silversmit.

A modified Victoreen curve [208] was used for the pre-edge background subtraction in the X-ray absorption spectra obtained in transmission mode and a linear function or a constant was used for the same subtraction in the spectra obtained in fluorescence detection mode. A cubic spline routine [209]. was used for the atomic background, μ_0, subtraction. The pre-edge background subtracted spectra were normalized to the edge jump, which was taken to be the value of the atomic background at 50 eV above the K-edge.

Because the EXAFS equation B.46 is a sum of damped sinusoidal waves with

amplitudes depending on the type and number of neighboring atoms and their distribution, the EXAFS reduced data $\chi(k)$ can be presented either in k-space, as in equation B.46, or Fourier transformed into the R-space, as

$$FT(R) = \frac{1}{\sqrt{2\pi}} \int_{k_{min}}^{k_{max}} k^n \chi(k) e^{-2ikR} dk. \tag{B.47}$$

The $\chi(k)$ function can be weighed by a factor k^n in order to counterbalance the damping of $\chi(k)$ at large k resulting from the decrease in the scattering amplitude. In addition, a high k^n-weighting, *e.g.*, $k = 3$, promotes the contribution of the heavy Z-scatterers, because heavy Z-elements have larger scattering amplitudes at higher k-values than do the light Z-elements.

The fit parameters were determined by multiple shell fitting in R-space, by applying the difference file technique using Fourier transforms [210]. The phase shifts and backscattering amplitudes were obtained from FEFF8.0 calculations [211] on the insoluble Prussian blue crystal structure, by taking the iron(II) ion as the central iron site. The FEFF output for the shortest single scattering path, $Fe^{II}-C$, was used to model the first coordination shell around both iron sites in the Prussian blue structure, *i.e.*, $Fe^{II}-C$ or $Fe^{III}-N$. Identical scattering and amplitude functions were used for N and C, because the scattering properties of atoms, which are first-neighbors in the periodic table are similar. Because of the linear geometry of the $Fe^{II}-C-N-Fe^{III}$ path in the Prussian blue structure, the multiple scattering contributions for the second and third shells are larger than the single scattering contributions for these shells [212]. Therefore, the multiple scattering paths with the highest probability were retained to model the second and third shells. For the second shell, $Fe^{II}-N$ or $Fe^{III}-C$, this multiple scattering path was a 3-leg path, $Fe^{II}-C-N-Fe^{III}$ and for the third shell, $Fe^{II}-Fe^{III}$, this path was a 4-leg path, $Fe^{II}-Fe^{III}-N-C-Fe^{II}$. X-ray absorption spectroscopy probes an average coordination for the two Fe^{II} and Fe^{III} sites, in Prussian blue. This average coordination for commercial and laboratory-synthesized soluble Prussian blue is given in Table B.1 [12].

The accuracy of the phase shifts and backscattering amplitudes for the first and second shells obtained from the above procedure was evaluated with a fit of the first two coordination shells in a $K_4[Fe(CN)_6]$ powder sample measured in transmission. The FEFF8.0 calculations were uploaded into the XDAP software and the parameter, S_0^2, and the Debye-Waller factors were optimized to obtain an agreement with the known crystallographic coordination numbers. The Debye-Waller factors reported in this work for the Prussian blue samples are, therefore, relative to the $K_4[Fe(CN)_6]$ structure and expressed as $\Delta\sigma^2$.

Table B.1 The average bond distances, R, coordination numbers, N, relative Debye-Waller factors $\Delta\sigma^2$, and inner potential corrections, ΔE_0, for the EXAFS fits of six reference Prussian blue powder samples

	Crystal structure		EXAFS fit values[b]			
Absorber-scatterer	R, Å	N[a]	R, Å	N	$\Delta\sigma^2$, Å^2	ΔE_0, eV
Fe(II)-C	1.92(1)	3	1.90(1)	2.8(1)	0.0002(2)	-4.1(3)
Fe(III)-N	2.04(1)	3	2.06(1)	3.1(1)	0.0002(2)	2.2(5)
Fe(II)-N	3.04(1)	3	3.04(1)	2.9(1)	0.0002(2)	1.7(5)
Fe(III)-C	3.16(1)	3	3.15(1)	3.0(2)	0.0002(2)	4.3(6)
Fe(II)-Fe(III)	5.08(1)	6	5.10(1)	6.1(2)	-0.0005(2)	-4.6(3)

[a]Average theoretical iron coordination number for the defect-free soluble Prussian blue structure. [b]The values given in parentheses are the standard deviations of the fit values for six samples.

The fit on the Prussian blue structure was performed on the average EXAFS spectra of six different soluble and insoluble reference Prussian blue powders, *i.e.*, the commercial insoluble C01 and C03 and soluble C02 and C04 Prussian blues, the laboratory-synthesized soluble A148 Prussian blue, as well as an additional commercial insoluble Prussian blue purchased from the artist's materials supplier, Pébéo, Gemenos, France. The bond distances were optimized in the fit and deviated by at most 0.01 Å from the average bond distances reported for the $K_4[Fe(CN)_6]$ crystal structure [213]. A similar procedure was followed for the third shell in soluble Prussian blue, by fitting the iron-iron shell with a coordination number, N, of 6 for the averaged spectrum of the three soluble Prussian blue powder samples.

In the crystal structure of both soluble and insoluble Prussian blue, a fraction of the iron(II) sites are vacant. The probability of having the central iron(II) site missing is given by the occupancy parameter, p, in the $Pm3m$ crystal structure, see **Section 2.2.4**. This probability was determined to be higher for the insoluble C03 Prussian blue than for the soluble C02 Prussian blue, resulting in a lower theoretical iron-iron coordination number for the insoluble C03 Prussian blue. However, attempt to fit the iron-iron coordination number in this insoluble sample did not lead to a significantly deviation from that observed for the six average spectra.

In conclusion, the EXAFS spectra of both soluble and insoluble Prussian blue powder samples could be fit with the above procedure and resulted in bond distances and coordination numbers close to the X-ray crystal structure values, see Table B.1. A single Debye-Waller factor was fitted for the four contributions within the first two coordination shells. For all EXAFS fits, the coordination numbers for the two contributions in the second $Fe^{II}-N$ and $Fe^{III}-C$ shells were constrained to the same value of three. Because these contributions are fit with the 3-leg mul-

tiple scattering paths involving both the carbon and nitrogen atoms in the first and second shell, the two different 3-leg paths will both disappear as soon as a carbon or nitrogen atom in the first or second coordination shell is missing. Hence, the same coordination number for the two 3-leg paths may be assumed. The coordination numbers for the contributions in the first coordination shell however were not constrained.

Experimental facilities

The DUBBLE Dutch-Belgian beamline BM26 is located at a bending magnet port of the ESRF electron storage ring, a magnet with a magnetic field induction of 0.4 T. This beamline, which is equipped with a Si(111) double crystal monochromator, delivers an X-ray beam with an energy of 9.6 keV and a relative energy resolution, $\Delta E/E$, of *ca.* 2×10^{-4} [214]. The higher harmonics were suppressed with a silicon reflecting strip on a mirror behind the monochromator.

The energy scale was calibrated with a 4 μm thick iron foil, whose spectrum was recorded in transmission mode and the energy of the first maximum in the derivative of the absorption around the iron K-edge was taken at 7112 eV. In transmission mode, the intensities of the incident and transmitted X-ray beams were measured with Oxford Instrument ionization detectors. In fluorescence mode, the spectra were collected with a liquid nitrogen cooled energy dispersive nine channel monolithic Ge detector. Powders of both the laboratory-synthesized and commercial Prussian blue samples have been measured in transmission mode. After appropriate mixing and grinding with boron nitride, the powders were pressed into self-supporting pellets in a stainless steel sample holder. The iron K-edge spectra of paint layers were recorded in fluorescence mode because of the low concentration of iron in the diluted samples. Schematics of the equipment and the detection line are shown in Figures B.17 and B.18.

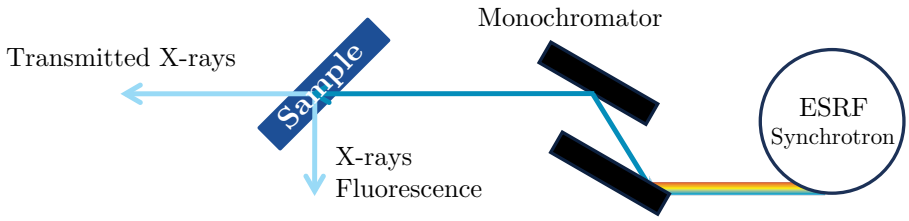

Figure B.17 Schematic overview of the experimental set-up of the DUBBLE beamline.

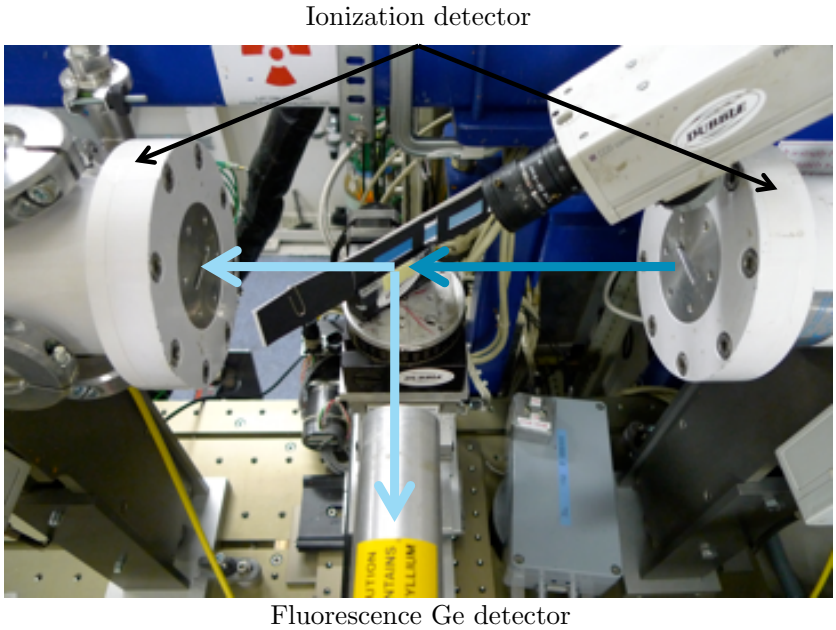

Figure B.18 The detection line at the DUBBLE beamline. The XAS signal is recorded either in transmission mode by an ionization detector, or in fluorescence mode, by a Ge detector.

Appendix C

Absorption and Scattering Theories

Color results from the interaction between matter and light. It is not an intrinsic property of a material because, in order to appear colored, an object must be illuminated and observed by a receptor, such as the eyes. Three types of colors[1] are usually distinguished, (1) the *physical colors*, which arise from the scattering, diffraction, or interferences of light in the matter, (2) the *chemical colors*, resulting from the absorption of certain wavelengths by the matter, and (3) the *physiological colors*, which are described as sensations and are related to the nature of the visual organ.

The physical colors are produced in a transparent medium, where no dissipation occurs, whereas the chemical colors depend on the intrinsic properties of the compound and are *durable* in opposition with the transitory character of the physical colors. The tinctorial properties of a pigment greatly depend on its absorption and scattering properties. The absorption of light in a pigmented medium is governed by the *Lambert-Beer law* whereas the scattering of light by pigments particles can be described by the *Mie* scattering, which is more general than the *Rayleigh* scattering. The Kubelka-Munk model combines both absorption and scattering properties. The physiological aspects of the pigment color will not be discussed herein.

Lambert-Beer law

When light radiation passes through a material, the light intensity, I, decreases with the optical path length, l, and the concentration, C, of the absorbing com-

[1] This classification dates back from the eighteenth century and was elaborated by Johann W. von Goethe (1749-1832). It is still used nowadays in books about color science [51].

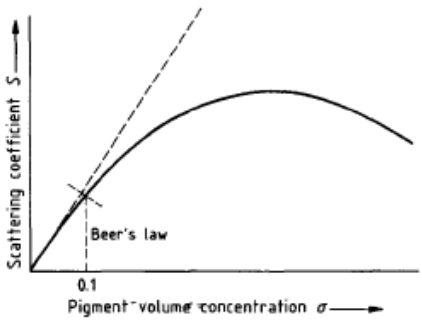

Figure C.1 Scattering coefficient, S, as a function of pigment volume concentration, σ [52].

pound, according to the relation

$$I = I_0 e^{-\alpha l} = I_0 e^{-\epsilon l C}, \tag{C.1}$$

where I_0 is the incident light intensity, α is the absorption coefficient of the substance, and $\epsilon = \alpha/C$ is the extinction coefficient or absorption molar coefficient. Equation C.1 is the so-called *Lambert-Beer law*[2] and can be found under the form

$$A = \log \frac{I_0}{I} = \epsilon l C, \tag{C.2}$$

where A is the absorbance. The Lambert-Beer law only applies to chromatic radiation [191].

In the case of an absorbing and scattering medium, such as paint layers, the absorption coefficient, α, is replaced by the addition of the absorption coefficient, K, and the scattering coefficient, S [88]. Equation C.1 becomes

$$I = I_0 e^{-(K+S)l}. \tag{C.3}$$

The absorption and scattering coefficients, K and S, are wavelength dependent and describe the attenuation of the radiation per unit path for a specific system. They have the dimensions of reciprocal length. The absorption coefficient, K, is proportional to the pigment volume concentration,[3] whereas the scattering coefficient, S, is proportional to the pigment volume concentration only for low

[2]The Lambert-Beert law is also known as Beer's law, Beert-Lambert law, or Beer-Lambert-Bouguer law.

[3]The pigment volume concentration is defined as the ratio of the pigment volume to the total volume, *i.e.*, the volume of both the pigment and the medium.

pigment volume concentration [52], see Figure C.1. At higher concentration the scattering coefficient is smaller than the value extrapolated from the Lambert-Beer law because the pigment particles are too close to each other, resulting in interaction and hindrance between the light scattered waves by individual particles [52].

Rayleigh and Mie scattering

Besides the absorption, the color of a pigment is influenced by the scattering of light by the pigment particles. The scattering also determines the optical properties of a paint layer, which is a highly heterogeneous and granular system.

The Rayleigh scattering deals with the scattering caused by particles that are much smaller than the wavelengths of the incident light. A fraction of the absorbed light is re-emitted by the particles in all directions at the same wavelength. The scattered radiation is produced by the dipoles that are induced by the primary radiation in each particle. The model assumes that the particles are far enough apart to exclude any interactions between them and that the density fluctuations between two distinct points in the medium are independent. These conditions are fulfilled in an ideal gas, for example. In such a case, the scattering intensity, I_s, is related to that of the incident light, I_0, of wavelength λ by the relation [24]

$$\frac{I_s}{I_0} = \frac{\text{constant}}{\lambda^4}. \tag{C.4}$$

Because of the dependence to the inverse fourth power of the wavelength in equation C.4, the scattering intensity is stronger for short wavelengths than for long wavelengths. The Rayleigh scattering thus explains the blue appearance of the sky because the blue fraction of the visible light is more strongly scattered by the molecules in the atmosphere than the red fraction. In case of unpolarized incident radiation the Rayleigh scattering also depends on the angle of observation. The scattering intensities at the angles of 0° and 180° are maximal and equal in the forward and backward directions relative to the direction of propagation of the primary radiation.

In contrast with the Rayleigh scattering, the Mie scattering deals with scattering particles that are no longer small in comparison with the incident radiation wavelength. With such particles, the dipoles induced by the incident light do no longer emit in phase from either extreme of the particle. Destructive interference among the scattered light waves occurs, reducing the scattered intensity. The German physicist Mie solved Maxwell's equations for spherical particles using the complex refractive index and found a very complex expression for the scattered intensity [89]. According to the Mie theory, the scattered intensity by large particles is much less strongly dependent on the wavelength than shown by equation

C.4 for small particles. This difference is the reason why the water droplets that form fog, mist, and low cloud appear white. The Mie theory also provides the values of the absorption cross-section, Q_A, and the scattering cross-section, Q_S. These dimensionless parameters depend on the geometric diameter of the particle size. For both the absorption and scattering cross-sections, Q_A and Q_S, an optimum particle size exists for which the cross-sections reach a maximum value. The optimum particle size for scattering and absorption do not usually coincide.

Although the assumptions of the Mie and Rayleigh theories are not valid for pigments, it has been shown that these theories provide a satisfactory interpretation of the optical properties of pigmented systems [88][90]. The Rayleigh scattering can be seen as a particular case of the Mie scattering. Both types of scattering can be distinguished by the Mie scattering parameter, q, defined as the ratio of the perimeter of a sphere of radius r to the wavelength in the medium of refractive index, n_M

$$q = \frac{2\pi r}{\lambda_M} = \frac{2\pi r}{\lambda / n_M}. \tag{C.5}$$

If $q < 1$, the scattering of light corresponds to Rayleigh scattering; if $1 < q < 2$ it lies in the transition range between Rayleigh and Mie scattering, and finally, if q>2, it can be described by the Mie scattering.

The color of Prussian blue containing paint layers as a function of particle size was qualitatively discussed in **Section 2.2.3**. A quantitative interpretation, such as the determination of the optimum size for both scattering and absorption, requires to know the wavelength dependent complex refractive index, $n^* = n(1 - \mathrm{i}\kappa)$, where n is the real refractive index and κ, the absorption index. Unfortunately, reliable values for the absorption index, κ, of Prussian blue pigment are not available and can not be easily determined because no direct method exists for measuring the optical indices in colored inorganic pigments.

Kubelka-Munk theory

The Kubelka Munk theory takes into account both absorption and scattering and is particularly suitable to study heterogeneous scattering media exposed to a diffuse isotropic light, such as paint layers. In a paint layer, the photons do not travel in straight line but are rather scattered by the heterogeneities of the system. It has been shown that photons travel an average distance of $2\mathrm{d}x$ in a $\mathrm{d}x$ film thickness. Consequently, the value of the absorption coefficient, which is referred to as the loss of photons by absorption in a $\mathrm{d}x$ thickness, is taken as $2K$ instead of K, which is the absorption coefficient for a homogeneous medium without scattering. The scattering of the incident light is assumed to be isotropic in a heterogeneous

scattering medium and is described by an averaged parameter, β.

The reflectance coefficient, R_∞, of an opaque, *i.e.*, infinitely thick, film is related to the absorption and scattering coefficients by

$$\frac{2K}{\beta} = \frac{(1 - R_\infty)^2}{2R_\infty}. \tag{C.6}$$

Equation C.6 shows that the reflectance depends on the ratio of the absorption and scattering coefficients, and not on their individual values. Equation C.6 is the fundamental equation of the Kubelka-Munk model. A simple example can help to better understand this equation. Let us consider a paint layer composed of a very absorbing pigment in high concentration so that the $2K/\beta$ ratio is greater than 1, *i.e.*, $2K/\beta > 1$. Consequently, equation C.6 becomes

$$R_\infty \approx \frac{\beta}{4K} < 1. \tag{C.7}$$

Because of this low reflectance coefficient, this paint layer poorly reflects the colored light. In order to improve the color, *i.e.*, enhance the light reflection, β/K can be increased by adding an extender composed of transparent, non absorbing particles. This will favor the scattering processes. This example can be applied to the case of Prussian blue, which is a highly absorbing pigment. In paint layers Prussian blue was often mixed with an extender or a white pigment to enhance light reflection.

Appendix D

Integral Text of Ancient Recipes for Producing Prussian Blue

The original eighteenth century recipes that were prepared in this thesis are integrally reproduced below.

D.1 Dossie, 1758

« The Prussian blue may be prepared in perfection by the following process. Take of blood any quantity; and evaporate it to perfect dryness. Of this dry blood, powdered, take six pounds, and of the best pearl-ashes two pounds: mix them well together in a glass or stone mortar; and then put the mixt matter into large crucibles or earthen-pots; and calcine it in the furnace described, p.22; the top of the crucible or pot being covered with a tile, or other such convenient thing, but no luted. The calcination should be continued, so long as any flame appears to issue from the matter; or rather till it become very slender and blue; for if the fire be very strong, a small flame would arise for a very long time. When the matter has been sufficiently calcined, take the vessels which contain it out of the fire; and, as quickly as possible, throw it into two or three gallons of water; and, as it soaks there, break it with a wooden spatula, that no lumps may remain. Put it then in a proper tin-vessel, and boil it for the space of three quarters of an hour or more; and filter it while hot through paper in the tin cullenders described, p.27; and pass some water through the filter when it is run dry, to wash out the remainder of the lixivium of the blood and pearl-ashes; the earth remaining in the filter may be then thrown away. In the mean time, dissolve of clean alum four pounds, and of green vitriol or copperas two pounds, in three gallons of water. Add this solution

gradually to the filtered lixivium, so long as any effervescence appear to arise on the mixture; but, when no ebullition or ferment follows the admixture, cease to put in more. Let the mixture then stand at rest, and a green powder will be precipitated: from which, when it has thoroughly subsided, the clear part of the fluid must be poured off, and fresh water put in its place, and stirred well about with the green powder: and, after a proper time of settling, poured off like the first. Take then of spirit of salt double the weight of the green vitriol which was contained in the quantity of solution of vitriol and alum added to the lixivium, which will soon turn the green matter to a blue colour; and, after some time, add a proper quantity of water, and wash the colour in the same manner, as has been directed for lake; and when properly washed, proceed in the same manner to dry it in lumps of convenient size. »

In Dossie R., *The Handmaid for the Arts*, Nourse, J., London, 78-80 (1757).

D.2 Le Pileur d'Apligny, 1779

« Le bleu de Prusse est une couleur animale, qui a néanmoins le fer pour base. Voici la manière de faire cette couleur. On prend une livre de potasse bien sèche, qu'on mêle à autant de sang de bœuf desséché et pulvérisé : on met ce mélange dans un creuset, et on le fait calciner doucement. Il faut avoir attention que le creuset ne soit plein qu'aux deux tiers, afin que la matière qui se gonfle ne se répande pas. Dans les commencemens [*sic*], il s'élève beaucoup de fumée et de flamme; lorsque la flamme cesse, on augmente le feu, pour faire rougir la matière et pour qu'en cet état elle ne laisse plus paroître qu'une flamme légère et bleuâtre. On ôte alors le creuset du feu, et on le laisse refroidir. On ramasse avec une cuiller de fer la pâte rouge qu'il contient, et on jette dans six pintes d'eau bouillante : on filtre la lessive qui en provient, et l'on repasse de l'eau chaude sur le marc, pour achever de le dessaler, et ensuite on réunit les lessives, qu'on fait réduire sur le feu, si l'on veut donner plus d'activité. D'un autre côté, on fait dissoudre ensemble dans une suffisante quantité d'eau chaude six onces de vitriol de Mars et huit onces d'alun de roche et l'on verse dans cette dissolution la lessive susdite chaude. Après une vive effervescence, il se précipite une fécule verdâtre : on remue le mélange et on le verse sur une toile serrée ; la liqueur passe au travers et le précipité reste sur le linge : on l'enlève avec une cuiller, pour le mettre dans une terrine de grès, l'on verse par dessus huit onces d'acide marin, qui lui fait prendre aussitôt

une belle couleur bleue ; mais ce précipité reste toujours chargé d'une colle tenace qui lui ôte sa vivacité : on l'en débarrasse par des lotions répétées. L'usage a appris que l'eau de puits, ou toute eau dure avoit pour cela plus d'efficacité que l'eau de rivière. Ce lavage exige de la patience ; car il faut trois à quatre semaines, en changeant d'eau ce bleu deux fois par jour : au bout de ce temps, on le passe au travers d'un linge serré ; on le laisse égoutter, et on en forme des gâteaux ou tablettes, qu'on fait sécher à l'ombre et à l'abri de la poussière. »

In Le Pileur d'Apligny, M., *Traité des couleurs matérielles et de la manière de colorer relativement aux différents arts et métiers*, Saugrain et Lamy, Paris, France, 36-38 (1779).

Bibliography

[1] John Wiley & Sons. (2011). Archaeometry, Online, <http://www.wiley.com/bw/journal.asp?ref=0003-813x>. Lastchecked on September 26, 2011.

[2] Elias, M. and Cotte, P. *Appl. Opt.* **47**(12), 2146 (2008).

[3] de Viguerie, L., Walter, P., Laval, E., Mottin, B., and Solé, V. *Angewandte Chemie* **122**(35), 6261–6264 (2010).

[4] Delamare, F. *Bleus en poudres, De l'Art à l'Industrie, 5000 ans d'innovations.* Ecole des Mines de Paris, Paris, p. 181-234, (2007).

[5] Google. (2011). Google search, Online, <http://www.google.be/search>. Lastchecked on September 26, 2011.

[6] Elsevier. (2011). Prussian blue, Online, <http://www.sciencedirect.com/>. Lastchecked on September 26, 2011.

[7] Thomson Reuters. (2011). Prussian blue search in Web of Knowledge, Online, <http://www.webofknowledge.com/>. Lastchecked on September 26, 2011.

[8] Bartoll, J. and Bärbel, J. *Z. f. Kunsttechnologie u. Konservierung* **24**, 88 (2010).

[9] Ware, M. *J. Chem. Educ.* **85**(5), 612 (2008).

[10] Dean, J. A. *Lange's Handbook of Chemistry.* McGraw-Hill, New York, fourteenth edition, (1992).

[11] Keggin, J. F. and Miles, F. D. *Nature* **137**, 2 (1936).

[12] Buser, H. J., Schwarzenbach, D., Petter, W., and Ludi, A. *Inorg. Chem.* **16**(11), 2704 (1977).

[13] Herren, F., Fischer, P., Ludi, A., and Haelg, W. *Inorg. Chem.* **19**(4), 956 (1980).

[14] Bueno, P. R., Ferreira, F. F., Giménez-Romero, D., Setti, G. O., Faria, R. C., Gabrielli, C., Perrot, H., Garcia-Jareno, J. J., and Vicente, F. *J. Phys. Chem. C* **112**(34), 13264 (2008).

[15] Macquer, P. J. In *Histoire de l'Académie Royale des Sciences de l'année 1752*, 60–77. Paris (1756).

[16] Cuvier, G. *Histoire des progrès des sciences naturelles: depuis 1789 jusqu'à ce jour*, volume 1. Verboeckhoven et Cie, Paris, (1864).

[17] Chadwick, B. M. and Sharpe, A. G. In *Advances in Inorganic Chemistry and Radiochemistry,* Emeléus, H. J. and Sharpe, A. G., editors, volume 8, 83–176. Academic press, New York and London (1966).

[18] Robin, M. B. *Inorg. Chem.* **1**(2), 337 (1962).

[19] Huheey, J. E., Keiter, E. A., and Keiter, R. L. *Chimie Inorganique.* HarperCollins College Publishers, (1996).

[20] Shriver, D. F. and Atkins, P. W. *Inorganic Chemistry.* Oxford University Press, third edition, (1999).

[21] Meissler, G. L. and Tarr, D. *Inorganic Chemistry.* Pearson Education, Inc., third edition, (2004).

[22] Day, P. *Molecules into Materials, Case Studies in Materials Chemistry - Mixed Valency, Magnetism and Superconductivity.* World Scientific Publishing Co. Pte. Ltd., (2007).

[23] Fung, S. C. and Drickamer, H. G. *J. Chem. Phys.* **51**(10), 4353 (1969).

[24] Nassau, K. *The Physics and Chemistry of Color, The Fifteen Causes of Color.* John Wiley & Sons, second edition, (2001).

[25] Robin, M. and Day, P. *Mixed-Valence chemistry : A Survey and Classification*, volume 10 of *Advances in Inorganic Chemistry and Radiochemistry.* Academic Press, (1967).

[26] Ito, A., Suenaga, M., and Ono, K. *J. Chem. Phys.* **48**(8), 3597 (1968).

[27] Maer, K. *J. Am. Chem. Soc.* **90**(12), 3201 (1968).

[28] Neff, V. and Neff, V. D. *J. Electrochem. Soc.* **125**(6), 886 (1978).

[29] Mortimer, R. J. *Annu. Rev. Mater. Res.* **41**(1), 147 (1997).

[30] Duncan, J. F. and Wigley, P. W. R. *J. Chem. Soc.* , 1120 (1963).

[31] Bueno, P. R., Gimenez-Romero, D., Ferreira, F. F., Setti, G. O., Garcia-Jareno, J. J., Agrisuelas, J., and Vicente, F. *J. Phys. Chem. C* **113**(22), 9916 (2009).

[32] Agrisuelas, J. *ECS trans.* **16**(24), 151 (2009).

[33] Xidis, A. and Neff, V. D. *J. Electrochem. Soc.* **138**(12), 3637 (1991).

[34] Kulesza, P. J., Malik, M. A., Denca, A., and Strojek, J. *Anal. Chem.* **68**(14), 2442 (1996).

[35] de Tacconi, N. R., Rajeshwar, K., and Lezna, R. O. *Chem. Mater.* **15**, 3046 (2003).

[36] Puganova, E. A. and Karyakin, A. A. *Sens. Actuators, B* **109**(1), 167 (2005).

[37] Chi, Q. and Dong, S. *Anal. Chim. Acta* **310**(3), 429 (1995).

[38] Koncki, R. and Wolfbeis, O. S. *Sens. Actuators, B* **51**(1-3), 355 (1998).

[39] Flomenbaum, N., Goldfrank, L., Hoffman, R., Howland, M. A., Lewin, N., and Nelson, L. *Goldfrank's Toxicologic Emergencies.* The McGraw-Hill Companies, Inc., eighth edition, (2006).

[40] Technical Report 65, National Council of Radiation Protection and Measurements, (1980).

[41] Faustino, P. J., Yang, Y., Progar, J. J., Brownell, C. R., Sadrieh, N., May, J. C., Leutzinger, E., Place, D. A., Duffy, E. P., Houn, F., Loewke, S. A., Mecozzi, V. J., Ellison, C. D., Khan, M. A., Hussain, A. S., and Lyon, R. C. *J. Pharm. Biomed. Anal.* **47**(1), 114 (2008).

[42] Pyrasch, M., Toutianoush, A., Jin, W., Schnepf, J., and Tieke, B. *Chem. Mater.* **15**(1), 245 (2003).

[43] Verdaguer, M., Bleuzen, A., Marvaud, V., Vaissermann, J., Seuleiman, M., Desplanches, C., Scuiller, A., Train, C., Garde, R., Gelly, G., Lomenech, C., Rosenman, I., Veillet, P., Cartier dit Moulin, C., and Villain, F. *Coord. Chem. Rev.* **190-192**, 1023 (1999).

[44] Ferlay, S. *Nature* **378**(6558), 701 (1995).

[45] Bleuzen, A., Lomenech, C., Escax, V., Villain, F., Varret, F., Cartier dit Moulin, C., and Verdaguer, M. *J. Am. Chem. Soc.* **122**(28), 6648 (2000).

[46] Einaga, Y., Yamamoto, T., Sugai, T., and Sato, O. *Chem. Mater.* **14**(11), 4846 (2002).

[47] Bocharova, V., Gorodyska, G., Kiriy, A., Stamm, M., Simon, P., Nch, I., Elefant, D., Lou, X., Stoffelbach, F., Detrembleur, C., and Jerome, R. *Prog. Colloid Polym. Sci.* **132** (2006).

[48] Vaucher, S., Li, M., and Mann, S. *Angew. Chem., Int. Ed.* **39**(10), 1793 (2000).

[49] Zhou, P. H. and Xue, D. S. *J. Appl. Phys.* **96**(1), 610 (2004).

[50] Shen, X., Wu, S., Liu, Y., Wang, K., Xu, Z., and Liu, W. *J. Colloid Interface Sci.* **329**(1), 188 (2009).

[51] Zuppiroli, L. and Bussac, M.-N. *Traité des couleurs.* Presses polytechniques et universitaires romandes, Lausanne, (2003).

[52] Buxbaum, G. and Pfaff, G. *Industrial Inorganic Pigments.* Wiley-VCH, third edition, (2005).

[53] Béguin, A. *Dictionnaire technique de la peinture A-B*, volume 1. Paris, (1978).

[54] Berrie, B. H. In *Artist's Pigments, A Handbook of Their History and Characteristics,* FitzHugh, E. W., editor, volume 3. Oxford University Press, New York (1997).

[55] Perego, F. *Dictionnaire des matériaux du peintre.* Belin, (2005).

[56] Ware, M. *Cyanotype: The History, Science and Art of Photographic Printing in Prussian blue.* Science Museum, London, (1999).

[57] Kirby, J. *National Gallery Technical Bulletin* **14**, 62 (1993).

[58] Kirby, J. and Saunders, D. *National Gallery Technical Bulletin* **25**, 73 (2004).

[59] Levison, H. W. *Artists' Pigments Lightfastness Tests and Ratings.* Colorlab, Hallandale, Florida, (1976).

[60] Field, G. *Chromatography; or, A Treatise on Colours and Pigments and of their Powers in Painting.* Tilt and Bogue, (1841).

[61] Chevreul, M. *Revue scientifique et industrielle* **5**(3), 74 (1849).

[62] Ellis, D., Eckhoff, M., and Neff, V. D. *J. Phys. Chem.* **85**(9), 1225 (1981).

[63] Taguchi, M., Yagi, I., Nakagawa, M., Iyoda, T., and Einaga, Y. *J. Am. Chem. Soc.* **128**(33), 10978 (2006).

[64] Dostal, A., Kauschka, G., Reddy, S. J., and Scholz, F. *J. Electroanal. Chem.* **406**(1-2), 155 (1996).

[65] Vilmos, G. and Beck, M. T. *Polyhedron* **2**(5), 387 (1983).

[66] Balzani, V. and Carassiti, V. *Photochemistry of Coordination Compounds.* Academic press, London, (1970).

[67] Nechitayilo, V. B., Styopkin, V. I., Tkachenko, Z. A., Goltsov, Y. G., Sherstyuk, V. P., and Zhilinskaya, V. V. *Electrochim. Acta* **40**(15), 2501 (1995).

[68] Woodward, J. *Philosophical Transactions* **XXXIII**(381), 15 (1724).

[69] Krafft, S. In *Description des machines et procédés pour lesquels des brevets d'invention ont été pris sous le régime de la loi du 5 juillet 1844*, volume 17, 159. Paris, France (1850).

[70] Wilde, R. E., Nath, G. S., and Marshall, B. J. *Inorg. Chem.* **9**(11), 2512 (1970).

[71] Google. December (2011). Google Patents, Online, <http://www.google.com.br>. Lastchecked on December 4, 2011.

[72] PatentStorm. (2011). PatentStorm, Online, <http://www.patentstorm.us/>. Lastchecked on December 4, 2011.

[73] Morrison, J. O., Chatham, N. J., and Perkins, B. H. *Manufacture of iron blue pigments*, Patent Version Number 2592169. E. I. du Pont de Nemours & Compagny, Wilmingthon, Delaware, July 24 (1946).

[74] Krüger, J. *Procédé de production de pigments bleus au cyanure de fer fortement colorés et de teinte pure*, Brevet d'invention n° 1487299. VEB KALI-CHEMIE, Paris, France, Mai 22 (1967).

[75] Patil, A. S., Bantjes, J. H., and Ouderkirk, J. T. *Process for preparing ferriferrocyanide pigments*, Patent Version Number 4414033. BASF Wyandotte Corporation, Michigan, United States, November 8 (1983).

[76] Gratzfeld, E., Clausen, E., Reinhardt, H., and Schaefer, H. *Iron blue pigment, process for its pigmentation and use*, Patent Version Number 4915742. Degussa Aktiengesellschaft, Frankfurt, Germany, (1983).

[77] Reinhardt, H., Trebinger, K., and Kallrath, G. *Process for the production of Berlin blue*, Patent Version Number 3985571. Deutsche, Gold-Und Silbert-scheideanstalt vormals Roessler, Frankfurt (Main), Germany, October 12 (1976).

[78] Gratzfeld, E., Clausen, E., Reinhardt, H., and Schaefer, H. *Iron blue pigment, process for making the same and use*, Patent Version Number 4378995. Degussa Aktiengesellschaft, Frankfurt am Main, Germany, (1983).

[79] Schiek, R. C. *Iron blue pigments and process for preparation*, Patent Version Number 4681638. Ciba-Geigy Corporation, Ardsley, N. Y., May 2 (1986).

[80] Reinhardt, H., Trebinger, K., and Kallrath, G. *Process for the production of alkali ferrocyanide*, Patent Version Numbers 3864453. Deutsche, Gold-Und Silbert-scheideanstalt vormals Roessler, Frankfurt (Main), Germany, February 4 (1975).

[81] Reinhardt, H., Trebinger, K., and Kallrath, G. *Process for the production of Berlin blue*, Patent Version Numbers 3915733. Deutsche, Gold-Und Silbert-scheideanstalt vormals Roessler, Frankfurt (Main), Germany, October 28 (1975).

[82] Epstein, L. M. *J. Chem. Phys.* **36**(10), 6 (1961).

[83] Ganguli, S. and Bhattacharya, M. *J. Chem. Soc. Faraday T.* **79**(7), 1513 (1983).

[84] Bal, B., Ganguli, S., and Bhattacharya, M. *J. Phys. Chem. B* **88**(20), 4575 (1984).

[85] Imanishi, N., Morikawa, T., Kondo, J., Takeda, Y., Yamamoto, O., Kinugasa, N., and Yamagishi, T. *J. Power Sources* **79**(2), 215 (1999).

[86] Inoue, H., Nakazawa, T., Mitsuhashi, T., Shirai, T., and Fluck, E. *Hyperfine Interact.* **46**(1), 723 (1989).

[87] Eastaugh, N., Walsh, V., Chaplin, T., and Siddal, R. *Pigment Compendium, A Dictionnary of Historical Pigments.* Elsevier Butterworth Heinemann, Oxford, (2008).

[88] Oyarzùn, J. M. *Pigment Processing, Physico-chemical Principles.* European coatings literature. Vincentz Verlag, Hannover, Germany, (2000).

[89] Mie, G. *Annalen der Physik* **330**(3), 377 (1908).

[90] Maikowski, M. A. *Prog. Colloid Polym. Sci.* **59**, 70 (1976).

[91] Reinhardt, H. *Process for the production of ferrocyanide blue*, Patent Version Number 4046861. Deutsche, Gold-Und Silbert-scheideanstalt Vormals Roessler, October 28 (1975).

[92] Rosseinsky, D. R., Lim, H., Jiang, H. J., and Chai, J. W. *Inorg. Chem.* **42**(19), 6015 (2003).

[93] Taft, W. S. J. and Mayer, J. W. *The Science of Paintings.* Springer, New York, (2000).

[94] Guinebretière, R. *Diffraction des rayons X sur échantillons polycristallins, instrumentation et étude de la microstructure.* Hermes Science and Lavoisier, Paris, (2006).

[95] Stokes, A. R. and Wilson, A. J. C. *Proc. Camb. Phil. Soc.* **38**, 313 (1942).

[96] Williamson, G. K. and Hall, W. H. *Acta Metallurgica* **1**(1), 22 (1953).

[97] Masson, O. *Etude des défauts de structure par diffraction des rayons X sur poudres. Utilisation d'un montage en réflexion asymétrique équipé d'un détecteur courbe à localisation.* PhD thesis, Université de Limoges, (1998).

[98] Stokes, A. R. and Wilson, J. C. *Proc. Phys. Soc. London* **56**(3), 174 (1944).

[99] Rietveld, H. M. *Acta Crystallogr.* **22**, 151 (1967).

[100] Rodriguez-Carvajal, J. *Phys. B* **192**, 55 (1993).

[101] Kulesza, P. J., Zamponi, S., Berrettoni, M., Marassi, R., and Malik, M. A. *Electrochim. Acta* **40**(6), 681 (1995).

[102] Reguera, E. *Z. Phys. Chem.* **223**(6), 701 (2009).

[103] Garcia-Jareno, J. *Electrochim. Acta* **44**(2), 395 (1998).

[104] Billinge, S. J. L. *Retrieved from http://arxiv.org/abs/cond-mat/0210559* , 17 (2002).

[105] Proffen, T., Petkov, V., Billinge, S. J. L., and Vogt, T. *Z. Kristallogr.* **217**, 47 (2002).

[106] Bordet, P. *Etude de la Structure Locale par la Fonction de Distribution de Paires.* Ecole Thématique 10-14 Mai 2007 (Maubuisson), (2007).

[107] Hammersley, A. P., Svensson, S. O., Hanfland, M., Fitch, A. N., and Haüsermann, D. *Journal of High Pressure Research* **14**, 235 (1996).

[108] Qiu, X., Thompson, J. W., and Billinge, S. J. L. *J. Appl. Crystallogr.* **37**, 678 (2004).

[109] Farrow, C. L., Juhas, P., Liu, J. W., Bryndin, D., Božin, E. S., Bloch, J., Proffen, T., and Billinge, S. J. L. *J. Phys.: Condens. Matter* **19**(33), 335219 (2007).

[110] Martinetto, P. and Bordet, P. *C02 PDF [electronic mail]. Addressee: Louise Samain.*, Personal communication. December 21, 2011.

[111] Ludi, A. In *Mixed-Valence Compounds: Theory and Applications in Chemistry, Physics, Geology, and Biology,* Brown, D. B., editor, volume 58 of *NATO Advanced Study Institutes*, 25–47, (1979).

[112] Bevington, P. R. and Robinson, D. K. *Data reduction and error analysis for the physical sciences.* WCB/McGraw-Hill, USA, second edition, (1992).

[113] Bunker, G. *Introduction to XAFS, A Practical Guide to X-ray Absorption Fine Structure Spectroscopy.* Cambridge University Press, Cambridge, (2010).

[114] Samain, L., Silversmit, G., Sanyova, J., Vekemans, B., Salomon, H., Gilbert, B., Grandjean, F., Long, G. J., Hermann, R. P., Vincze, L., and Strivay, D. *J. Anal. At. Spectrom.* **26**(5), 930 (2011).

[115] Nakamoto, K. *Infrared and Raman Spectra of Inorganic and Coordination Compounds.* Wiley-Interscience Publication, New York, fourth edition, (1978).

[116] Poilblanc, R. and Crasnier, F. *Spectroscopies infrarouge et raman.* Grenoble Sciences, Les Ulis, France, (2006).

[117] Kettle, S. F. A., Aschero, G. L., Diana, E., Rossetti, R., and Stanghellini, P. L. *Inorg. Chem.* **45**(13), 4928 (2006).

[118] Kettle, S. F. A., Diana, E., Marchese, E. M. C., Boccaleri, E., and Stanghellini, P. L. *J. Raman Spectrosc.* , 4928 (2011).

[119] Barsan, M. M., Butler, I. S., Fitzpatrick, J., and Gilson, D. F. R. *J. Raman Spectrosc.* **42**(9), 1820 (2011).

[120] Jolivet, J., Henry, M., and Livage, J. *Metal Oxide Chemistry and Synthesis : From Solution to Solid State.* (2000).

[121] Asai, C. *Z. f. Kunsttechnologie u. Konservierung* **18**, 261 (2005).

[122] Sanyova, J. *Contribution à l'étude de la structure et des propriétés des laques de garance.* PhD thesis, Université Libre de Bruxelles, Bruxelles, Belgique, (2000/2001).

[123] Dossie, R. *The Handmaid to the Arts.* Nourse, J., London, (1758).

[124] Le Pileur d'Apligny, M. *Traité des couleurs matérielles et de la manière de colorer relativement aux différents arts et métiers.* Saugrain et Lamy, Paris, France, (1779).

[125] Murad, E. and Johnston, J. H. In *Mössbauer Spectroscopy Applied to Inorganic Chemistry,* Long, G. J., editor, volume 2, p. 507. Plenum Press (1987).

[126] Michel, F. M., Ehm, L., Antao, S. M., Lee, P. L., Chupas, P. J., Liu, G., Strongin, D. R., Schoonen, M. A. A., Phillips, B. L., and Parise, J. B. *Science* **316**(5832), 1726 (2007).

[127] Mikutta, C., Mikutta, R., Bonneville, S., Wagner, F., Voegelin, A., Christl, I., and Kretzschmar, R. *Geochim. Cosmochim. Acta* **72**(4), 1111 (2008).

[128] Yamaguchi, G., Yanagida, H., and Ono, S. *Bull. Chem. Soc. Jpn.* **37**(10), 1555 (1963).

[129] Hwang, S. L., Shen, P. Y., Chu, H. T., and Yui, T. F. *International Geology Review* **48**(8), 754 (2006).

[130] Long, G. J., editor. *Mössbauer Spectroscopy Applied to Inorganic Chemistry*, volume 1 of *John P. Fackler, Jr.* volume 1, Plenum Press, New York, (1984).

[131] Wilke, M., Farges, F., Petit, P.-E., Brown Jr, G. E., and Martin, F. *Am. Mineral.* **86**, 714 (2001).

[132] Xia, L. and McCreery, R. L. *J. Electrochem. Soc.* **146**(10), 3696 (1999).

[133] Laver, M. In *Artist's Pigments, A Handbook of Their History and Characteristics,* FitzHugh, E. W., editor, volume 3, 310. Oxford University Press, New York (1997).

[134] International Organization for Standardization. *General methods of test for pigments and extenders - Part 15: comparison of resistance of light of coloured pigments of similar types.* ISO 787-15:1986 (1986).

[135] Wyszecki, G. and Stiles, W. *Color Science, Concepts and Methods, Quantitative Data and Formulae.* John Wiley & Sons, New York, second edition, (2000).

[136] Atlas. (2009). Suntest, Xenon Test Instruments, <http://atlas-mts.com/shop/Products/Laboratory-Weathering-Testing/Xenon-Arc-Instruments/SUNTEST-CPS-CPS/c001001001/p7>. Lastchecked on January 12, 2012.

[137] Winsor & Newton. (2011). Winsor & Newton, The World's Finest Artists' Materials, Color information, Online, <http://www.winsornewton.com/products.aspx?PageID=154&ProductID=462>. Lastchecked on January 14, 2012.

[138] Egerton, G. and Egerton, G. S. *J. Soc. Dyers Colour.* **86**(6), 242 (1970).

[139] Kumar, A., Yusuf, S. M., and Keller, L. *Phys. Rev. B: Condens. Matter Mater. Phys.* **71**(5), 054414 (2005).

[140] de Wet, J. F. and Rolle, R. *Z. Anorg. Allg. Chem.* **336**(1), 96 (1965).

[141] Walker, R. G. and Watkins, K. O. *Inorg. Chem.* **7**(5), 885 (1968).

[142] Itaya, K., Ataka, T., Toshima, S., and Shinohara, T. *J. Phys. Chem.* **86**(13), 2415 (1982).

[143] Yusuf, S. M. *Re: Questions on PRB71(2005)054414 [electronic mail]. Addressee: Fernande Grandjean, Louise Samain, Gary J. Long.*, Personal communication. February 5, 2010.

[144] Ng, C. W., Ding, J., Shi, Y., and Gan, L. M. *J. Phys. Chem. Solids* **62**(4), 767 (2001).

[145] Agnihotry, S. A., Singh, P., Joshi, A. G., Singh, D. P., Sood, K. N., and Shivaprasad, S. M. *Electrochim. Acta* **51**(20), 4291 (2006).

[146] Ayers, J. B. and Waggoner, W. H. *J. Inorg. Nucl. Chem.* **33**(3), 721 (1971).

[147] Hamnett, A., Christensen, P. A., and Higgins, S. J. *Analyst* **119**, 735 (1994).

[148] Zhao, J., Zhang, Y., Shi, C., Chen, H., Tong, L., Zhu, T., and Liu, Z. *Thin Solid Films* **515**(4), 1847 (2006).

[149] Reguera, E., Fernández-Bertrán, J., Dago, A., and Díaz, C. *Hyperfine Interact.* **73**(3), 295 (1992).

[150] Shenoy, G. K., Wagner, F. E., and Kalvius, G. M. In *Mössbauer Isomer Shift,* Shenoy, G. K. and Wagner, F. E., editors, p. 49. Amsterdam (1978).

[151] Dostal, A., Hermes, M., and Scholz, F. *J. Electroanal. Chem.* **415**(1-2), 133 (1996).

[152] Gullikson, E. (2010). X-ray Attenuation Length, Online, <http://henke.lbl.gov/optical_constants/atten2.html>. Lastchecked on January 22, 2012.

[153] Henke, B. L., Gullikson, E. M., and David, J. C. *Atomic Data and Nuclear Data Tables* **54**(2), 181 (1993).

[154] Nomura, K. In *Mössbauer Spectroscopy in Materials Science,* Miglierini, M. and Petridis, D., editors, p. 63–78. Kluwer Academic (1999).

[155] Gilbert, B. *Profondeur d'analyse*, Personal communication. January 27, 2012.

[156] Gettens, R. J., Kühn, H., and Chase, W. T. In *Artists' Pigments, A Handbook of Thier History and Characteristics,* Roy, A., editor, volume 2, p. 69–70. Oxford University Press, New York (1993).

[157] Van der Weerd, J., Van Loon, A., and Boon, J. J. *Stud. Conserv.* **50**(1), 20 (2005).

[158] Meilunas, R. J., Bentsen, J. G., and Steinberg, A. *Stud. Conserv.* **35**(1), 33 (1990).

[159] Nakamoto, K. *Infrared Spectra of Inorganic and Coordination Compounds.* Wiley-Interscience Publication, New York, second edition, (1970).

[160] Herington, E. F. and Kynaston, W. *Journal of Chemical Society* , 3555 (1955).

[161] Arbizzani, R., Casellato, U., Fiorin, E., Nodari, L., Russo, U., and Vigato, P. A. *J. Cult. Herit.* **5**(2), 167 (2004).

[162] Kühn, H. In *Artists' Pigments, A Handbook of Their History and Characteristics,* Feller, R. L., editor, volume 1, p. 169. Oxford University Press, New York (1985).

[163] Laver, M. In *Artist's Pigments, A Handbook of Their History and Characteristics,* FitzHugh, E. W., editor, volume 3. Oxford Universtiy Press, New York (1997).

[164] Rowe, S. *Stud. Conserv.* **49**, 259 (2004).

[165] Bueno, P. R., Giménez-Romero, D., Gabrielli, C., Garcia-Jareno, J. J., Perrot, H., and Vicente, F. *J. Am. Chem. Soc.* **128**(51), 17146 (2006).

[166] Cotte, M., Checroun, E., Susini, J., and Walter, P. *Appl. Phys. A: Mater. Sci. Process.* **89**(4), 841 (2007).

[167] Cession, C., Sanyova, J., and Van Bos, M. *Bulletin de l'Institut Royal du Patrimoine Artistique* **26**, 163 (1994-1995).

[168] Gordon Clark, J. *Wallpaper in Decoration.* Frances Lincoln Limited, London, (2001).

[169] Saunders, G. *Wallpaper in Interior Decoration.* Watson-Guptill Publications, Michigan, (2002).

[170] Claes, M.-C. and Augustyniak, A.-S. (2008). Service for the study of historic monuments and wall paintings section: ongoing projects, Online, <http://www.kikirpa.be/EN/65/415/Recherches+en+cours.htm?>. Lastchecked on January 27, 2012.

[171] Claes, M.-C. *Papiers peints de l'hôtel Dewez*, Personal communication. December 23, 2011.

[172] Arijs, H. *Paul Cauchie (1875-1952): tussen feit en fictie. Biografische aanzet: beginjaren en carrière als decorateur-entrepreneur tijdens de art-nouveauperiod.* Vrije Universiteit Brussel, Brussels, (2010-2011).

[173] Hill, J. *Immaterial Architecture.* Routledge, p. 176, (2006).

[174] Sanyova, J. and Decq, L. *Villa Germaine*, Rapport d'analyses 2011_11087, Royal Institute for Cultural Heritage. (2011).

[175] Bell, I. M., Clark, R. J. H., and Gibbs, P. J. *Spectrochim. Acta, Part A* **53**(12), 2159 (1997).

[176] Service des Collections artistiques. (2010). Exposition "Reflets de la peinture vietnamienne des années 1965 à 1985. Donation Joseph Poncin" (Liège, 2010), Online, <http://www.wittert.ulg.ac.be/fr/expo/2010/poncin.html>. Lastchecked on January 31, 2012.

[177] Saunders, D. and Kirby, J. *National Gallery Technical Bulletin* **25**, 62 (2004).

[178] Lauricella, M. *La synthèse, l'utilisation et la dégradation du bleu de Prusse sur support papier.* Université de Liège, Liège, (2010-2011).

[179] Khopkar, S. M. *Basic Concepts of Analytical Chemistry.* New Age International Publishers, New Delhi, second edition, (1998).

[180] Rouessac, F. and Rouessac, A. *Chemical Analysis, Modern Instrumentation Methods and Techniques.* John Wiley & Sons, West Sussex, England, (2007).

[181] Smith, B. C. *Fundamentals of Fourier Transform Infrared Spectroscopy.* CRC Press and Taylor & Francis Group, USA, second edition, (2011).

[182] Janot, C. *L'effet Mössbauer et ses applications à la physique du solide et à la métallurgie physique.* Published by Aigrain, P. and Blanc-Lapierre, A. and Friedel, J. and Lévy, M., Paris, (1972).

[183] Grandjean, F. *TP 1re Licence: Fluorescence résonnante sans recul de photons γ.* Université de Liège, (2001).

[184] Gütlich, P., Bill, E., and Trautwein, A. X. *Mössbauer Spectroscopy and Transition Metal Chemistry, Fundamentals and Applications.* Springer, Berlin, (2011).

[185] Weber, G., Martinot, L., Strivay, D., Garnir, H. P., and George, P. *X-Ray Spectrom.* **34**(4), 297 (2005).

[186] Mathis, F., Othmane, G., Vrielynck, O., del Castillo, H. C., Chêne, G., Dupuis, T., and Strivay, D. *Nucl. Instrum. Methods Phys. Res., Sect. B* **268**(11-12), 2078 (2010).

[187] Dupuis, T., Chêne, G., Mathis, F., Marchal, A., Philippe, M., Garnir, H.-P., and Strivay, D. *Nucl. Instrum. Methods Phys. Res., Sect. B* **268**(11-12), 1911 (2010).

[188] Weatherstone, A., Vormwald, M., Boyd, N., and Campbell, I. *The GUPIXWIN manual and user guide.* University of Guelph, version 2.1, (2000).

[189] Goldstein, J., Newbury, D., Joy, D., Lyman, C., Echlin, P., Lifshin, E., Sawyer, L., and Michael, J. *Scanning Electron Microscopy and X-Ray Microanalysis.* Plenum Press, New York, third edition, (2003).

[190] Liauw, M. A., Baylor, L. C., and O'Rourke, P. E. In *Process Analytical Technology,* Bakeev, K. A., editor, chapter 4. John Wiley & Sons (2010).

[191] Biémont, E. *Spectroscopie moléculaire, Structures moléculaires et analyse spectrale.* De Boeck, Bruxelles, Belgium, (2008).

[192] Blitz, J. P. In *Modern Techniques in Applied Molecular Spectroscopy,* Mirabella, F. M., editor, Techniques in analytical chemistry, chapter 5. John Wiley & Sons, USA (1998).

[193] Broll, N. *Caractérisation de solides cristallisés par diffraction X.* Techniques de l'Ingénieur, traité Analyse et Caractérisation. Weka, Paris (1996).

[194] Bordet, P. *Affinement des diagrammes de diffraction de poudres par la méthode de Rietveld.* Institut des matériaux de Nantes, Unité Mixte de Recherche - CNRS-Université, September (2010).

[195] Welcomme, E. *Développements de techniques combinées de microanalyse par rayonnement synchrotron pour l'étude des pigments à base de carbonates de plomb.* PhD thesis, Université Pierre et Marie Curie - Paris VI, Paris, France, (2007).

[196] Jouanneaux, A. *Formation permanente du CNRS: Techniques d'analyse des diagrammes de diffraction des rayons X et des neutrons par les poudres.* Institut des matériaux de Nantes, Unité Mixte de Recherche - CNRS-Université, September (1996).

[197] Cotte, M., Susini, J., Sole, V. A., Taniguchi, Y., Chillida, J., Checroun, E., and Walter, P. *J. Anal. At. Spectrom.* **23**, 820 (2008).

[198] Janssens, K. *J. Anal. At. Spectrom.* **26**, 883 (2011).

[199] ESRF. (2012). ESRF, virtual tour, Online, <http://www.esrf.eu/AboutUs/ GuidedTour>. Lastchecked on January 5, 2012.

[200] Winick, H. *Synchrotron radiation sources, a primer*, volume 1 of *Synchrotron Radiation Techniques and Applications.* World Scientific Publishing Co., Singapore, (1994).

[201] Frey, F. *Acta Crystallogr., Sect. B: Struct. Sci.* **51**(4), 592 (1995).

[202] Proffen, T. and Billinge, S. J. L. *J. Appl. Crystallogr.* **32**(3), 572 (1999).

[203] Kramer, M. J. *J. Appl. Crystallogr.* **40**, 77 (2007).

[204] Bordet, P. Formation permanente, Diffraction par les matériaux polycristallins, (2010).

[205] Willmott, P. *An Introduction to Synchrotron Radiation, Techniques and Applications.* John Wiley & Sons, United Kingdom, (2011).

[206] Silversmit, G. *EXAFS, Extended X-ray Absorption Fine Structure.* In course notes of the second master course on *Advanced X-ray Spectroscopic Mehtods of Analysis*, Ghent University, (2010-2011).

[207] Vaarkamp, M., Linders, J., and Koningsberger, D. *Phys. B* **208-209**, 159 (1995).

[208] Vaarkamp, M., Dring, I., Oldman, R., Stern, E., and Koningsberger, D. *Phys. Rev. B: Condens. Matter Mater. Phys.* **50**, 7872 (1994).

[209] Cook, J. and Sayers, D. *J. Appl. Phys.* **52**, 5024 (1981).

[210] Koningsberger, D., Mojet, B., van Dorsen, G., and Ramaker, D. *Top. Catal.* **10**, 143 (2000).

[211] Ankudinov, A., Ravel, B., Rehr, J., and Conradson, S. *Phys. Rev. B: Condens. Matter Mater. Phys.* **58**, 7565 (1998).

[212] Glatzel, P., Jacquamet, L., Bergmann, U., de Groot, F. M. F., and Cramer, S. P. *Inorg. Chem.* **41**(12), 3121 (2002).

[213] Willans, M. J., Wasylishen, R. E., and McDonald, R. *Inorg. Chem.* **48**(10), 4342 (2009).

[214] Nikitenko, S., Beale, A. M., van der Eerden, A. M. J., Jacques, S. D. M., Leynaud, O., O'Brien, M., Detollenaere, D., Kaptein, R., Weckhuysen, B. M., and Bras, W. *J. Synchrotron Radiat.* **15**, 632 (2008).

Résumé

Le bleu de Prusse est un pigment moderne synthétique qui fut découvert à Berlin au début du XVIII^{e} siècle. Il s'agit d'un complexe hydraté d'hexacyanoferrate(II) de fer(III). Sa couleur bleue est produite par un transfert de charge entre les ions de fer d'étage d'oxydation différent, lors de l'absorption de la lumière vers 700 nm. Grâce à son pouvoir colorant important et son faible coût, le bleu de Prusse connut une popularité immédiate et fut largement utilisé par les artistes jusqu'en 1970. Cependant, dès le milieu du XVIII^{e} siècle, sa tenue à la lumière fut remise en cause; le pigment a en effet tendance à se décolorer et à verdir. En outre, la méthode de préparation du pigment semble jouer un rôle déterminant dans sa permanence à la lumière. L'objectif principal de cette thèse consistait à identifier les mécanismes de dégradation du pigment de bleu de Prusse en milieu pictural.

Le bleu de Prusse a été synthétisé selon les méthodes de préparation anciennes et modernes. Une analyse approfondie des pigments a révélé une variation de la taille des cristallites ainsi que du taux de lacunes selon le type de synthèse utilisée. Ces deux propriétés influencent fortement les configurations locales électroniques et structurales des ions de fer dans le bleu de Prusse. Dans certains bleus de Prusse synthétisés selon les méthodes du XVIII^{e} siècle, la présence de ferrihydrite nanocrystallisée a été mise en évidence. Ce composé, indésirable, est produit lors de la synthèse. Les couches de peinture préparées avec du bleu de Prusse ont ensuite été décolorées par vieillissement accéléré à la lumière. Alors que le bleu de Prusse pur en ton plein est extrêmement permanent, ce même pigment pâlit lorsqu'il est appliqué en teinte claire ou mélangé avec un pigment blanc. La décoloration du bleu de Prusse a été attribuée à la réduction des ions de fer(III) en surface de la couche picturale. De plus, une oxydation partielle du bleu de Prusse est observée dans l'entièreté de la couche. L'analyse d'objets du patrimoine culturel a confirmé ces réactions d'oxydation et de réduction des ions de fer dans le bleu de Prusse vieilli.

L'étude des mécanismes d'altération des pigments et des matériaux picturaux est primordiale pour la conservation ainsi que pour les études historiques afin de préserver au mieux notre patrimoine artistique et culturel tout en respectant les intentions originales de l'artiste.

Abstract

Prussian blue is a modern synthetic pigment discovered in Berlin at the beginning of the eighteenth century. Prussian blue is a hydrated iron(III) hexacyanoferrate(II) complex and its color results from an intervalence charge transfer between the iron(II) and iron(III) ions when light is absorbed at *ca.* 700 nm. Because of both its highly intense color and its low cost, Prussian blue enjoyed immediate popularity among artists and was widely used as a pigment in paintings until the 1970's. However, the permanence of Prussian blue had already been questioned by the mid-eighteenth century, because it exhibits a tendency to fade in light and to turn green. The preparative methods were rapidly recognized as a contributory factor in the fading of the pigment. The main objective of this thesis is the identification of the degradation mechanisms of Prussian blue pigments in paint layers.

Prussian blue was synthesized according to both ancient and modern preparation methods. A thorough analysis of the pigments revealed a dependency upon the type of synthesis, the crystallite size, and vacancy content, all properties that influence the local electronic and structural configurations of the iron ions in Prussian blue. The presence of nanocrystalline ferrihydrite as an undesirable iron containing reaction product was identified in Prussian blue pigments prepared according to eighteenth-century recipes. Discoloration upon light exposure in Prussian blue paint layers was induced by accelerated ageing. Pure Prussian blue painted in a dark shade is extremely light fast but fades when either painted in a lighter shade or mixed with white pigments. The fading of Prussian blue was attributed to a reduction of the iron(III) ions at the surface of the paint layer. A partial oxidation of Prussian blue in the entire paint layer was also observed. The analysis of works of art containing Prussian blue confirmed the combined oxidation and reduction of Prussian blue iron ions upon ageing.

The study of alteration mechanisms in a painting pigment is essential both for conservation and historical studies in order to best preserve our cultural and artistic heritage with respect to an artist's original intentions.